SIEMENS

MAGNETOM Flash

The Magazine of MRI

Issue Number 2/2015 | ISMRM Edition

Not for distribution in the US

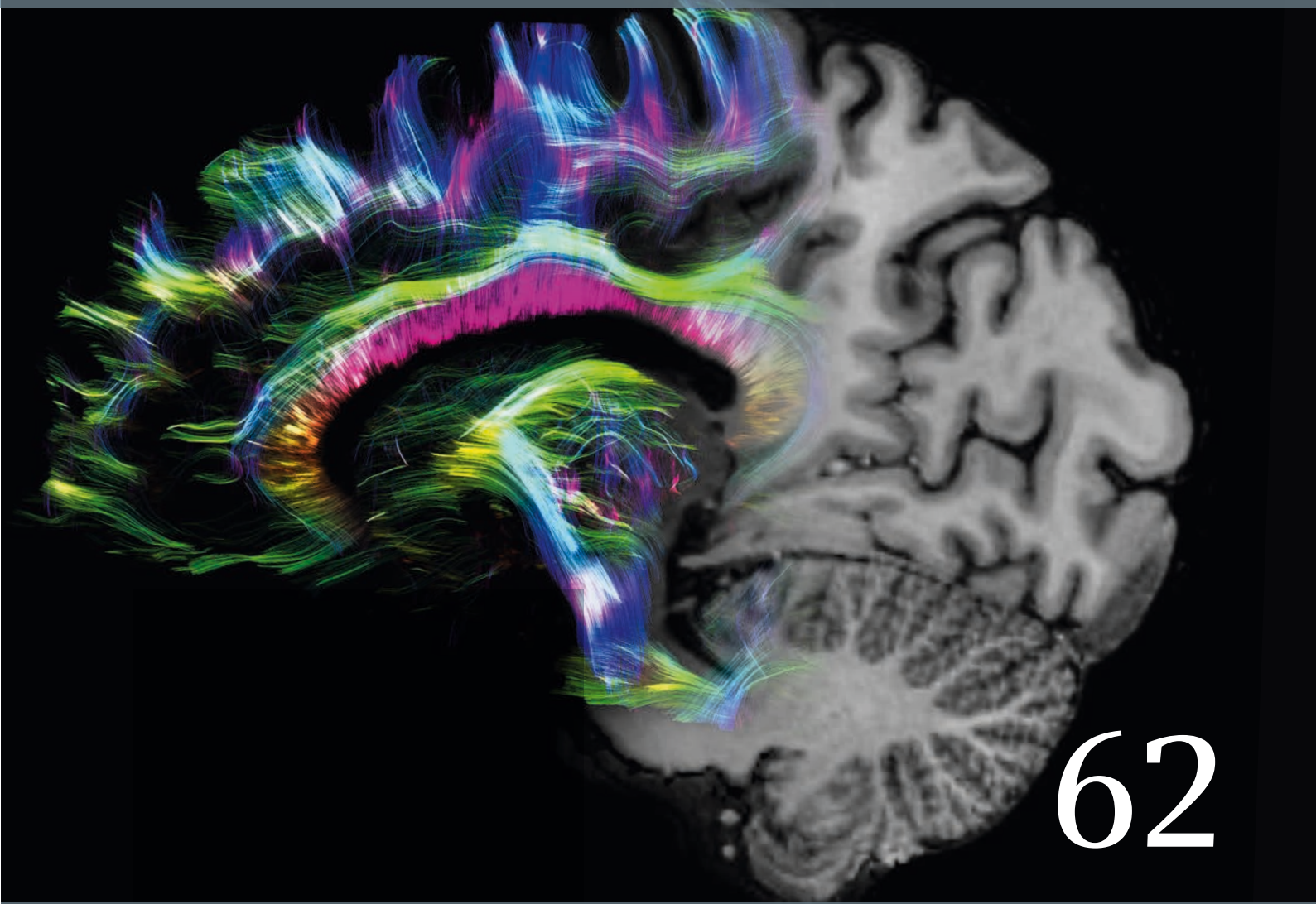

62

7T Image Gallery: Translate MRI Research Power into Clinical Care
Page 8

fit-Upgrade: A Success Story
Stephan Zangos, Thomas J. Vogl
Page 16

Hepatic Fat Quantification in Pediatric Patients
Jie Deng, Cynthia K. Rigsby, et al.
Page 23

Dot Configuration with the Dot Cockpit
Bart Schraa
Page 38

4D-MRI: Radiotherapy of Moving Targets
Kinga B. Bernatowicz, Antony J. Lomax, et al.
Page 74

Michael Schaaf has been Head of the Technology and Research Department of the business unit MR within Siemens Healthcare since November 2013. He is responsible for every MRI System with a field strength higher than 3T, and for all non-clinical MR projects.

Michael has worked in MR since 1996 in different functions. After several years working in the gradient development team, he spent four years in Shenzhen, China, helping to set up the Siemens MR factory there.

Back at MR headquarters, Michael is now working with his team on the next generation of 7T MRI systems from Siemens Healthcare.

Dear MAGNETOM Flash reader,

"Nothing is accepted until you prove it."

The forthcoming ISMRM will be a special one, because Siemens will publish its future plans for 7T. So I am very thankful for the opportunity to share my views on the 7T MRI segment here with MAGNETOM Flash readers and to talk a little bit about this segment which, for the time being, remains basically non clinical.

Over the last two decades the 7T MRI system has developed from a unique prototype technology, usable only by highly specialized experts, towards a serial product. It is true that in comparison with a high-end 3T clinical scanner there are still a number of challenges to overcome before one gets to see the amazing results unlocked by the fieldstrength of 7T. However, its increased signal-to-noise ratio leads to an increase in spatial resolution, enabling you to see structures that have never been seen before. A 7T system supplies additional information on functional images, which enables, for example, work with low-sensitivity nuclei.

Sometimes I am asked whether all the effort is justified. It is my strong belief that it is. I have no doubt that 7T will find its place in the clinical research arena. And whilst the number of installations of 7T systems may not rival those of the 3T – at least not in the foreseeable future – the effort and commitment of an extremely active ultra-high-field community is helping to demonstrate that even today diagnoses and treatment strategies may change thanks entirely to the additional information offered by the 7T. The enthusiasm and motivation of our 7T users encourages us to develop 7T further. To explain this in more detail, I would like to look a little bit back in the history and describe the origins of this ultra-high-field segment.

The first systems were brought to the field part by part even before the turn of the century. This required research centers to buy the equipment they needed directly from the different component suppliers. For example, the 7T magnet came from Magnex; the gradient system from either Magnex or Varian; and the RF-System – including the amplifier – from CPC or Analogic. The first systems were therefore built from separate components not specifically developed to be integrated with each other, with the result that interfaces sometimes did not match. These research institutes faced a big challenge in integrating all these different components to create a running 7T MRI system. Nevertheless, mechanical and electrical challenges were met, a working software (SW) developed, and necessary surface coils designed and built by highly motivated teams.

The first *in vivo* images with these machines were so promising that companies like Siemens decided to offer the complete MRI console (gradients, RF chain, and SW) in order to foster this segment further. What stayed the same in the early days, however, was the need for the customer to purchase the magnet separately: indeed, this remains true today in respect of an MRI system with field strength higher than 7T.

The components used by Siemens came from the 3T shelf. Siemens took the best, most reliable parts from the latest existing 3T platform and adapted them for the needs of 7T. By using such components it was possible to provide the good service, application packages, and SW updates already associated with the 3T systems. This significantly improved reliability and repeatability, since Siemens could provide the right spare parts where required. By providing these benefits to the research institutes, the number of installed Siemens 7T systems has increased steadily by up to five installations per year for each of the last two years.

Nevertheless, each 7T system was and remains a project in its own right. Knowing this, Siemens made the business decision that serving the ultra-high-filed segment by providing the necessary solutions for different user visions was only possible if it could look at these installations as single projects, in contrast to the well-developed and organized product business associated with the 1.5T and 3T systems. A separate department was created to work very closely with each ultra-high-field customer. Siemens has always offered close support as a partner from the first idea right until hand over, and beyond. In parallel, this small group of experts began developing functionalities according to specific user requirements.

An example of this is the parallel transmit (pTX) technology. This new feature was first announced as add on to the 7T at the ISMRM in 2006. The need for special transmit technology is based on the B_1 inhomogeneity, which is more severe at 7T than, for example, at 3T. Alongside existing prototypes, developed and built by research institutes themselves, Siemens offers an 8-channel parallel transmit system for the 7T, by duplicating the single transmit channel eight times. The first image, after a successful integration of the pTX system, either together with a new or already existing 7T system, was the logo of the institute in a phantom.

While conducting the first research studies, including the pTX system, the understanding and need for sophisticated SAR supervision grew clearer and became the focal point of parallel transmit imaging. Today, because of its obvious strong advantages, the pTX technology is becoming indispensible for every 7T user, especially now that the focus is shifting towards 7T body imaging. Because Siemens strongly believes in the vision and entrepreneurship of the largest ultra-high-field community (>65% of the worldwide installed ultra-high-field systems are from Siemens) the development of the pTX system is ongoing. The target is clear: We aim to provide the right equipment to enable reliable and safe clinical imaging with pTX technology in the future.

Early in 2013 Agilent (the UHF magnet manufacturer) revealed that it would no longer support the growing ultra-high-field segment with human whole body magnets. This commercial decision from the core magnet supplier in this field created a vacuum for some time. Before the decision, the main talk was of the number of transmit or receive channels, gradient performance and special shimming technologies. Since then, the talk now focuses on the simple question: Do you have a magnet?

Only a few people outside of Siemens know that more than a year before Agilent made this announcement, Siemens had already decided to develop and manufacture its own human whole body 7T magnet. I believe it is only a matter of time before the 7T is used in a clinical setting. Siemens is now so strong in this growing field that we do not want to miss this unique opportunity to be the vendor of choice. As a consequence, we made the strategic decision to take this path only if we have full control of all of our major components, such as the magnet. Siemens' strategy was proved correct and the experience and ability of Siemens Magnet Technology (SMT) – the largest human MRI magnet supplier in the world – brought us to the position where we could announce at the ISMRM 2014 that we were developing our own 7T magnet. Just one year later, we are proud to reveal that the first magnet is not only up and running, but that it has also been successfully installed at Friedrich-Alexander University of Erlangen-Nuremberg (FAU) in Erlangen, Germany.

Right now 7T is almost at the point of clinical usage. I would still not claim that 7T will make 1.5T or 3T obsolete in the future. 7T will stay special and it will be exciting to see how the ongoing changes in the research field and especially in the clinical environment of MRI will influence this development. My own fascination for the ultra-high-field segment is based on the technology used, the research projects which are set up, and – especially – the people running the already installed systems. Working together with the largest ultra-high-field community in the world is a great pleasure and an ongoing positive challenge to my team and myself. Alongside this technical fascination, we always ask ourselves: What are the ultimate benefits for patients, and is this tremendous effort all worthwhile?

As a supplier for imaging equipment Siemens will not be able to answer this question alone. It is the research community, our existing and upcoming collaboration partners, whom we count on to provide the fact-based answers to this question. What Siemens can do and will do is show strong commitment to, and provide the necessary support for, the research community with the necessary equipment. Siemens will provide the right tooling: It is up to you to develop the vision.

I would like to end by expressing sincere thanks to the ultra-high-field community, my great team at Siemens, and to wish you an exciting and inspiring ISMRM 2015.

With best regards

MAGNETOM 7T is still under development and not commercially available yet. Its future availability cannot be ensured. MAGNETOM 7T is not yet licensed for sale in Canada, in accordance with Canadian Law. Performance claims have not been reviewed by Health Canada, and are subject to change. Its future availability cannot be guaranteed.

Editorial Board

We appreciate your comments.
Please contact us at magnetomworld.med@siemens.com

Antje Hellwich
Editor-in-chief

Wellesley Were
MR Business Development Manager Australia and New Zealand

Ralph Strecker
MR Collaborations Manager, São Paulo, Brazil

Sven Zühlsdorff, Ph.D.
Clinical Collaboration Manager, Chicago, IL, USA

Gary R. McNeal, MS (BME)
Advanced Application Specialist, Cardiovascular MR Imaging Hoffman Estates, IL, USA

Peter Kreisler, Ph.D.
Collaborations & Applications, Erlangen, Germany

Review Board

Lisa Chuah, Ph.D.
Global Segment Manager Neurology, Neurosurgery, Pediatrics, and Orthopedics

Robin Heidemann, Ph.D.
UHF Global Marketing Manager

Berthold Kiefer, Ph.D.
Head of Oncological and Interventional Applications

Sunil Kumar S.L., Ph.D.
Senior Manager Applications

Matthias Lichy, M.D., M.Sc.
Clinical Competence Center

Reto Merges
Head of Scientific Marketing

Heiko Meyer, Ph.D.
Head of Neuro Applications

Gregor Thörmer, Ph.D.
Global Segment Manager Men's and Women's Health

Christina Triantafyllou, Ph.D.
Director of Global UHF Product Relationship Management

Heike Weh
Clinical Data Manager

The MAGNETOM World

Your portal to talks, articles and case studies on 7T MRI*

Siemens' global MRI community offers peer-to-peer support and information. Radiologists, physicists cardiologists, and technologists, have all contributed with publications, presentations, training documents, case studies, and more – all freely available to you via this unique network.

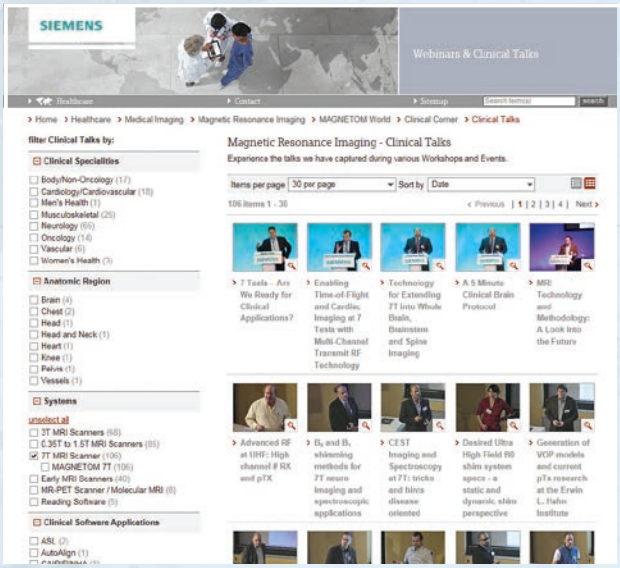

Don't miss the >100 lectures and presentations by international and renowned experts in the field on all aspects of ultra high field MRI that will allow you to be exposed to new ideas and alternative approaches.

The centerpiece of the MAGNETOM World Internet platform consists of MAGNETOM users' results. Here you will find case reports, articles and application tips allowing you to optimize your daily work.

Put the advantages of the MAGNETOM World to work for you!

www.siemens.com/magnetom-world

Content

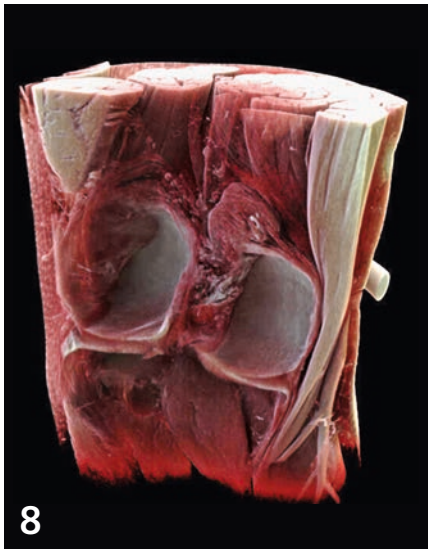

7T[1] Image Gallery

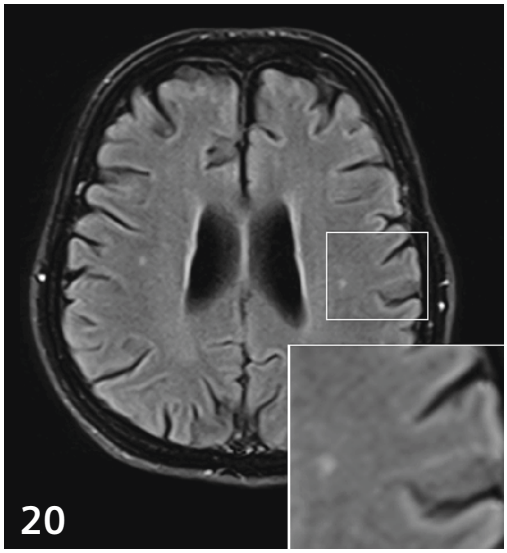

Quiet Imaging with *syngo* MR E11

Editorial

2 Nothing is accepted until you prove it
Michael Schaaf
Siemens Healthcare, Erlangen, Germany

7T[1] Image Gallery

8 Translate MRI Research Power into Clinical Care

Business

16 fit-Upgrade: A Success Story
Stephan Zangos, Thomas J. Vogl, University Hospital Frankfurt/Main, Germany

Product News

20 *syngo* MR E11 on a MAGNETOM Aera
Martin Reiss-Zimmermann, Radiologische Gemeinschaftspraxis Erfurt, Germany

Pediatric[2] Imaging

23 Hepatic Fat Quantification in Pediatric Patients using Multi-echo Dixon VIBE
Jie Deng, et al., Ann & Robert H. Lurie Children's Hospital of Chicago, Chicago, IL, USA

Abdominal Imaging

26 Case Report: ^{18}F-FDG PET/MRI of Hepatic Cholangiocarcinoma
Shetal N. Shah, et al., Cleveland Clinic, Cleveland, OH, USA

34 First Experiences with the Whole-Body Dot Engine[3]
Stephan Zangos, et al., University Hospital Frankfurt, Frankfurt/Main, Germany

[1] MAGNETOM 7T is still under development and not commercially available yet. Its future availability cannot be ensured. MAGNETOM 7T is not yet licensed for sale in Canada, in accordance with Canadian Law. Performance claims have not been reviewed by Health Canada, and are subject to change. Its future availability cannot be guaranteed.

[2] MR scanning has not been established as safe for imaging fetuses and infants under two years of age. The responsible physician must evaluate the benefit of the MRI examination in comparison to other imaging procedures.

[3] WIP, the product is currently under development and is not for sale in the US and in other countries. Its future availability cannot be ensured. The product is not yet licensed for sale in Canada, in accordance with Canadian Law. Performance claims have not been reviewed by Health Canada, and are subject to change. Its future availability cannot be guaranteed.

The information presented in MAGNETOM Flash is for illustration only and is not intended to be relied upon by the reader for instruction as to the practice of medicine. Any health care practitioner reading this information is reminded that they must use their own learning, training and expertise in dealing with their individual patients. This material does not substitute for that duty and is not intended by Siemens Medical Solutions to be used for any purpose in that regard. The treating physician bears the sole responsibility for the diagnosis and treatment of patients, including drugs and doses prescribed in connection with such use. The Operating Instructions must always be strictly followed when operating the MR System. The source for the technical data is the corresponding data sheets.

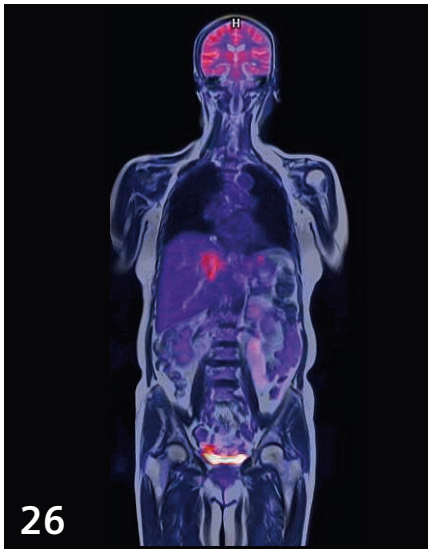

^{18}F-FDG PET/MRI of Hepatic Cholangiocarcinoma

Improved Visualization of Neuroforamina

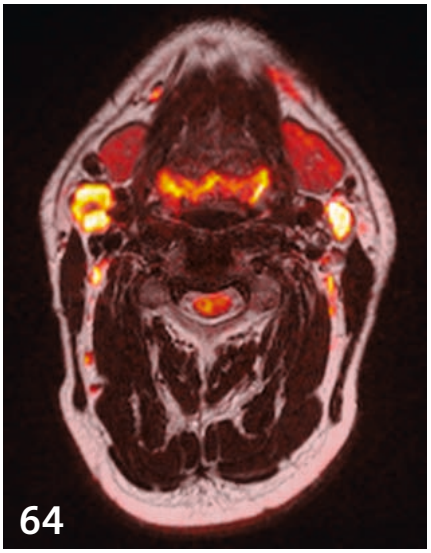

RESOLVE DWI for RT Planning for Head & Neck cancers

How-I-do-it

38 Dot Configuration with the Dot Cockpit
Bart Schraa, Siemens Canada Limited, Oakville, ON, Canada

44 fMRI Made Easy with an Integrated Siemens and NordicNeuroLab Solution
Marte Thuen, NordicNeuroLab, Bergen, Norway

Neurology

48 Contrast-free Quantitative CBF and Bolus Arrival Time using Multi-delay Arterial Spin Labeling Perfusion MRI in Moyamoya Disease
Qiao Penggang, et al., Affiliated Hospital of the Academy of Military Medical Sciences, Beijing, China

Orthopedic Imaging

52 Practical Considerations for the Evaluation of the Neuroforamina in Routine Spine Imaging at 3T
Marc-André Weber, et al., University Hospital Heidelberg, Germany

58 Can MRI Estimate the Cortical Bone Quality? A Feasibility Study Employing Short-TE MRI
Hamidreza Saligheh Rad, et al., Tehran University of Medical Sciences, Tehran, Iran

Radiation Therapy

64 Anatomical and Functional MRI for Radiotherapy Planning of Head and Neck Cancers
Maria A. Schmidt, et al., Royal Marsden NHS Foundation Trust and Institute of Cancer Research, Sutton, UK

70 Development of MR-only Planning for Prostate Radiation Therapy Using Synthetic CT
Peter Greer, et al., University of Newcastle, Newcastle, New South Wales, Australia

74 4D-MRI: Future of Radiotherapy of Moving Targets?
Kinga B. Bernatowicz, et al., Paul Scherrer Institut (PSI), Villigen, Switzerland

78 Technical Aspects of MR-only Radiotherapy
Tufve Nyholm, et al., Umeå University, Sweden

84 *syngo*.via RT Image Suite: Empower Radiation Therapy with MRI Information
Elena Nioutsikou, Siemens Healthcare, Forchheim, Germany

Men's Health

88 Case Series: 3T Prostate MRI With and Without the Use of an Endorectal Coil
Josephin Otto, et al., Leipzig University Hospital, Leipzig, Germany

90 60-Channel Body Coil for 1.5T and 3T
Gregor Thörmer, Siemens Healthcare, Erlangen, Germany

Translate MRI Research Power into Clinical Care

With over 25 years of experience in ultra-high field MRI, and with more than 40 systems installed or planned, Siemens Healthcare fosters research and collaboration in the 7T arena with leading research institutions around the world. With the strongest and most active 7T community across the globe, Siemens' collaboration partners translate MRI research into better diagnostic outcomes, as shown in this image gallery.

MAGNETOM 7T is ongoing research. All data shown are acquired using a non-commercial system under institutional review board permission. MAGNETOM 7T is still under development and not commercially available yet. Its future availability cannot be ensured. MAGNETOM 7T is not yet licensed for sale in Canada, in accordance with Canadian Law. Performance claims have not been reviewed by Health Canada, and are subject to change. Its future availability cannot be guaranteed.

Calcification of the globus pallidus

- Arrows demonstrate calcification of the globus pallidus

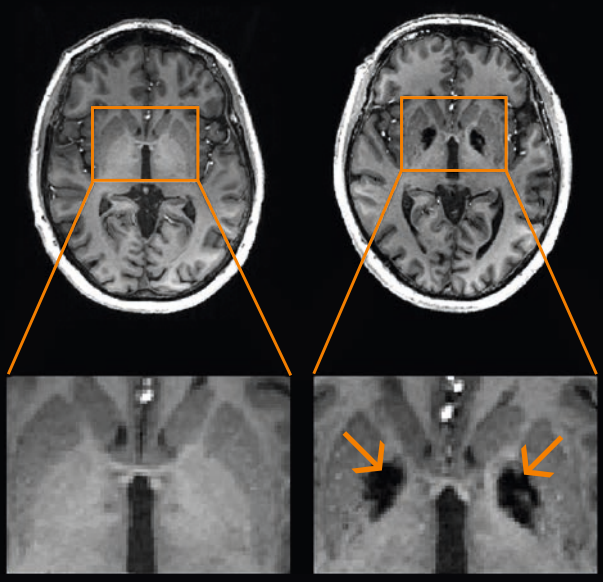

Normal control | Bilateral calcification

Courtesy of Deutsches Zentrum für Neurodegenerative Erkrankungen (DZNE), Bonn, Germany

Ultra-high resolution Diffusion of the right occipital lobe (axial slice)

- 800 µm isotropic resolution
- Robust reconstruction of multiple fiber directions per voxel
- Sub-millimeter resolution:
  - following the fiber trajectory at the interface between the white matter and the cortex
  - Trajectories entering the cortex of the parietal lobe

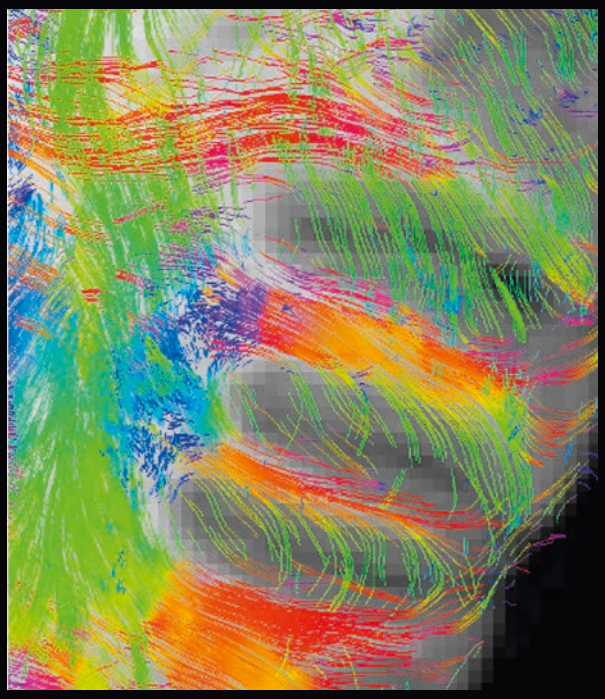

Courtesy of Max-Planck-Institute (MPI), Leipzig, Germany

Characterizing pathologic features of Multiple Sclerosis lesions

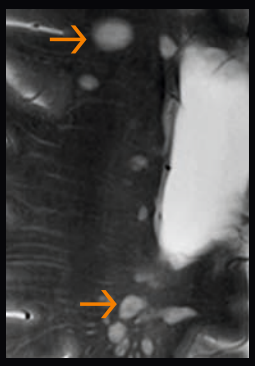

TSE, TR 7000 ms,
TE 69 ms, TA 3:23 min

SWI, TR 27 ms,
TE 15 ms, TA 5:15 min

Courtesy of Medical University Vienna (MUV), Vienna, Austria

Glioblastoma Multiforme: Susceptibility-Weighted Imaging (SWI); 3T vs. 7T

- GBM under antiangiogenic therapy
- 7T SWI provides superior assessment of microvasculature allowing better understanding of tumor-associated neoangionesis and therapy monitoring

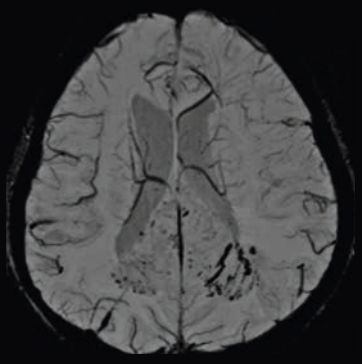

3T

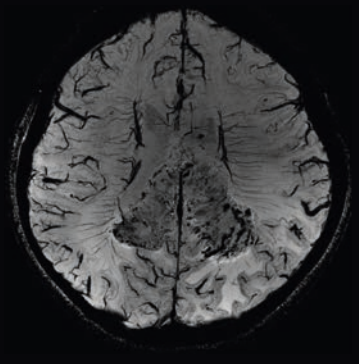

7T

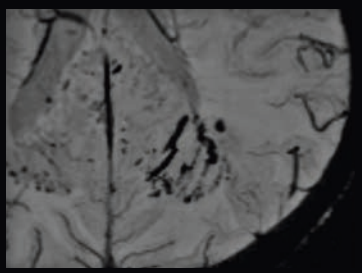

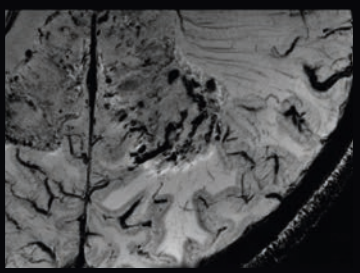

Courtesy of Essen University Hospital, Erwin L. Hahn Institute for MRI, Essen, Germany

Tumor visualization

- Patient with Glioblastoma at the left temporal lobe
- 200 µm inplane resolution

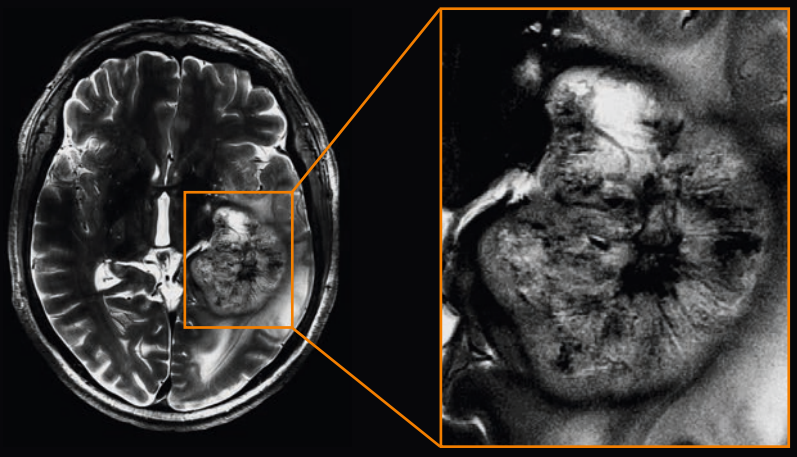

Courtesy of German Cancer Research Center, DKFZ, Heidelberg, Germany

Non-contrast enhanced angiography Time-of-Flight (ToF)

- 300 micron isotropic resolution
- TA 8:13 min, iPAT 3
- 1 TX/32 RX channel coil
- Maximum Intensity Projection (MIP)

Courtesy of Massachusetts General Hospital (MGH), Boston, MA, USA

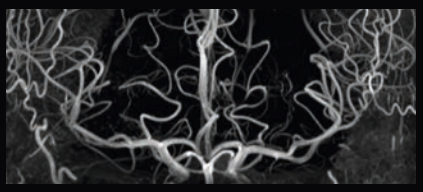

Coronal

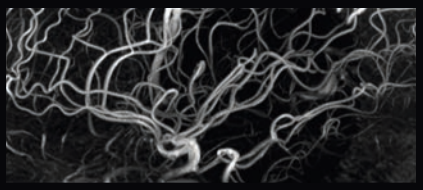

Sagittal

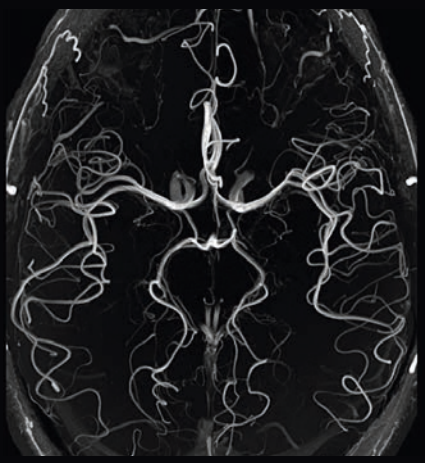

Axial

Diffuse axonal injury

- Improved depiction of small traumatic microbleeds (arrows) with 7T SWI

3T
0.7 x 0.8 x 2.6 mm³

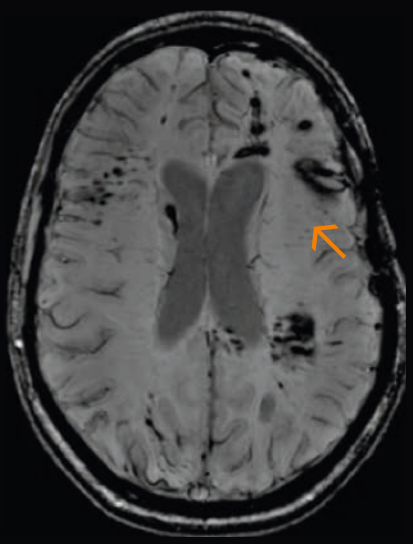

7T high resolution
0.25 x 0.25 x 1.5 mm³

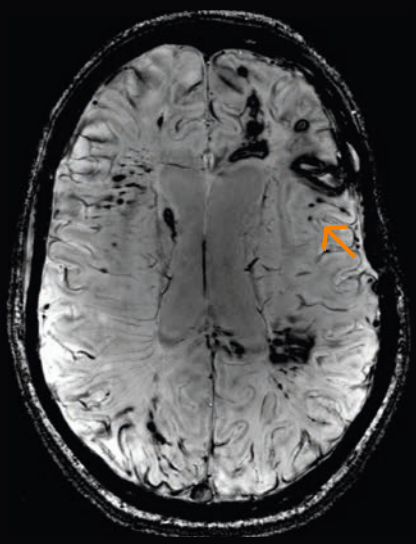

High-resolution quantitative mapping

- High-resolution quantitative imaging at 7T of an early-stage Multiple Sclerosis patient. 0.75 x 0.75 x 0.9 mm³

Courtesy of LREN-LTS5/CHUV-CIBM, Lausanne, Switzerland

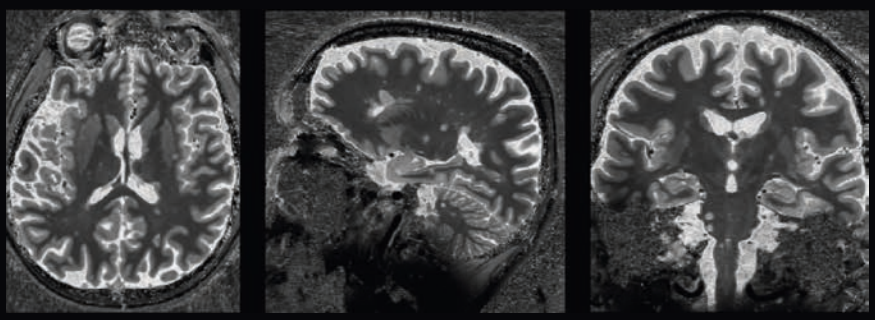

T1 map

Epilepsy imaging

- Hippocampus
  0.25 x 0.25 x 1 mm³ TSE;
  average of 3 acquisitions

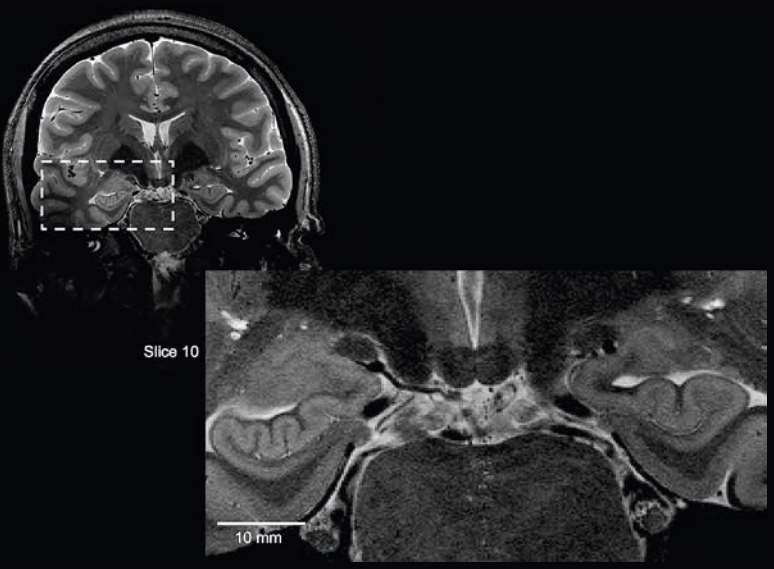

Courtesy of Maastricht University (UM), Maastricht, The Netherlands

Potential of 'new' contrasts: T2*-weighted

Courtesy of MGH, Boston, MA, USA

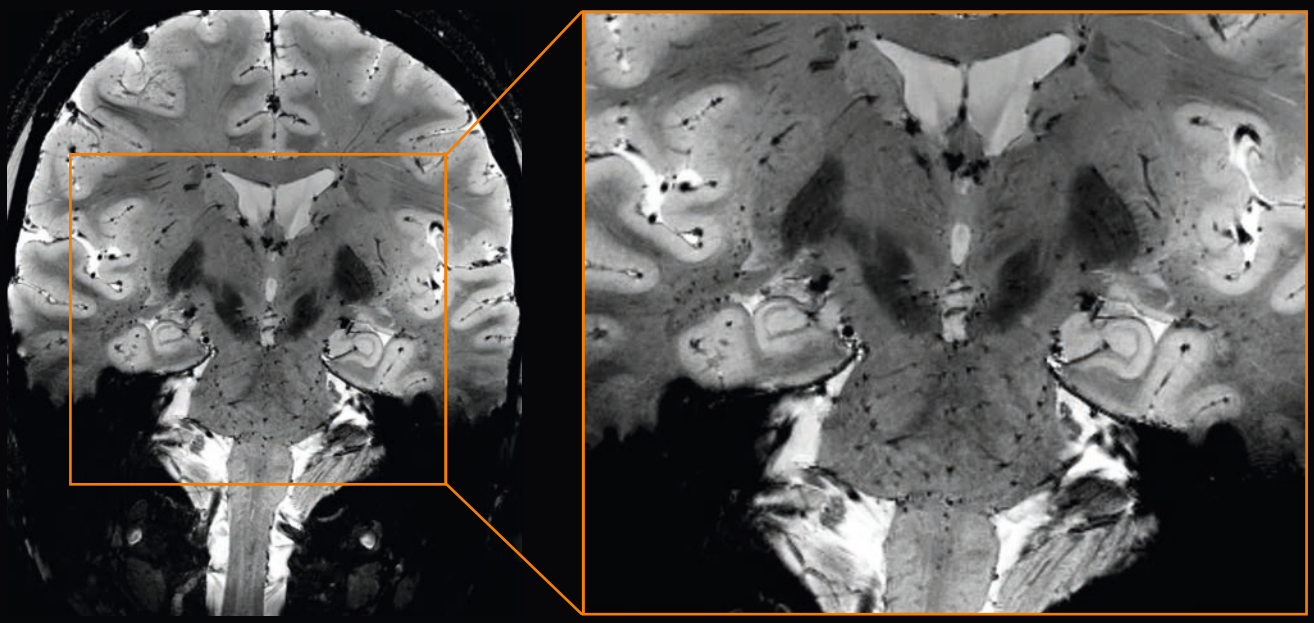

Small bowel using TrueFISP

- 0.7 x 0.7 x 2.0 mm³
  TA 20 sec

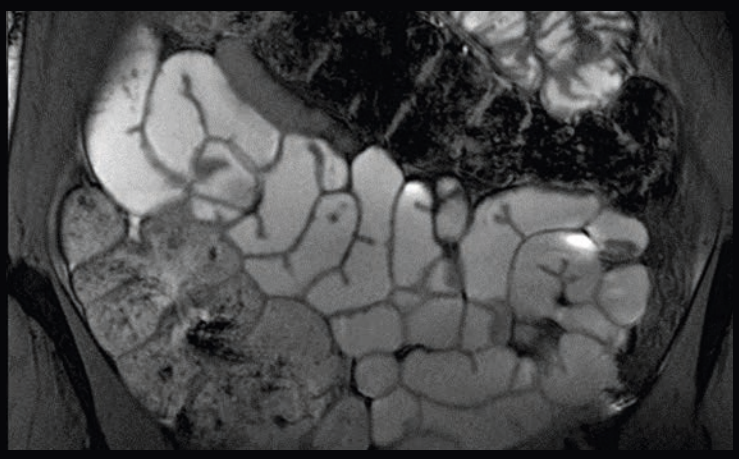

Courtesy of Essen University Hospital, Erwin L. Hahn Institute for MRI, Essen, Germany

Cardiac imaging at 7T

- B_1-shimming over cardiac cycle

Short axis view

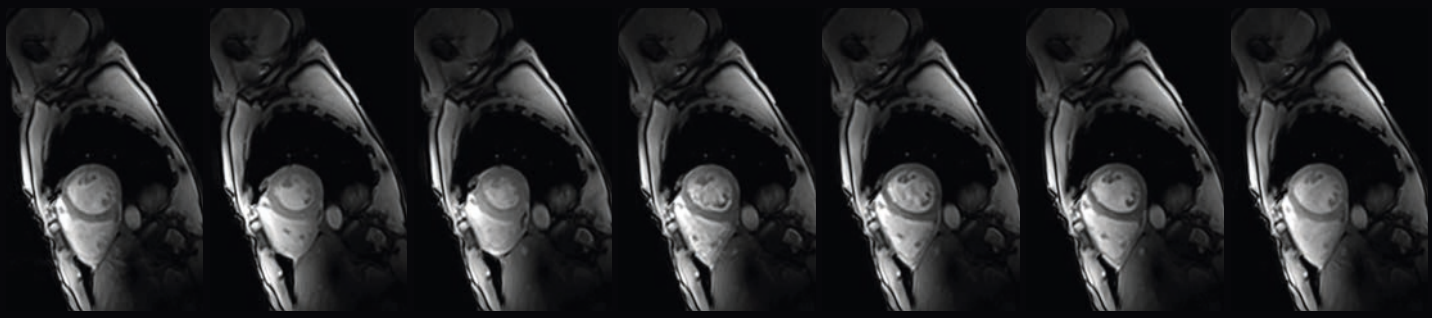

phase 1 | phase 5 | phase 9 | phase 13 | phase 17 | phase 21 | phase 28

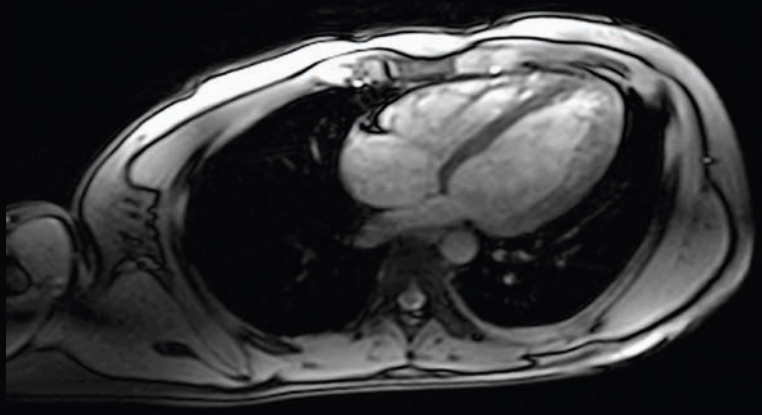

Pseudo 4-chamber view

- 2.3 x 2.3 x 5 mm^3
- Temporal resolution 42/45 ms
- TE 2.9/3.1 ms; BW 554 Hz/pixel
- 8 segments; up to 32 cardiac phases

Courtesy of Center for Magnetic Resonance Research (CMRR), Minneapolis, MN, USA

Aortic valve cine imaging FLASH

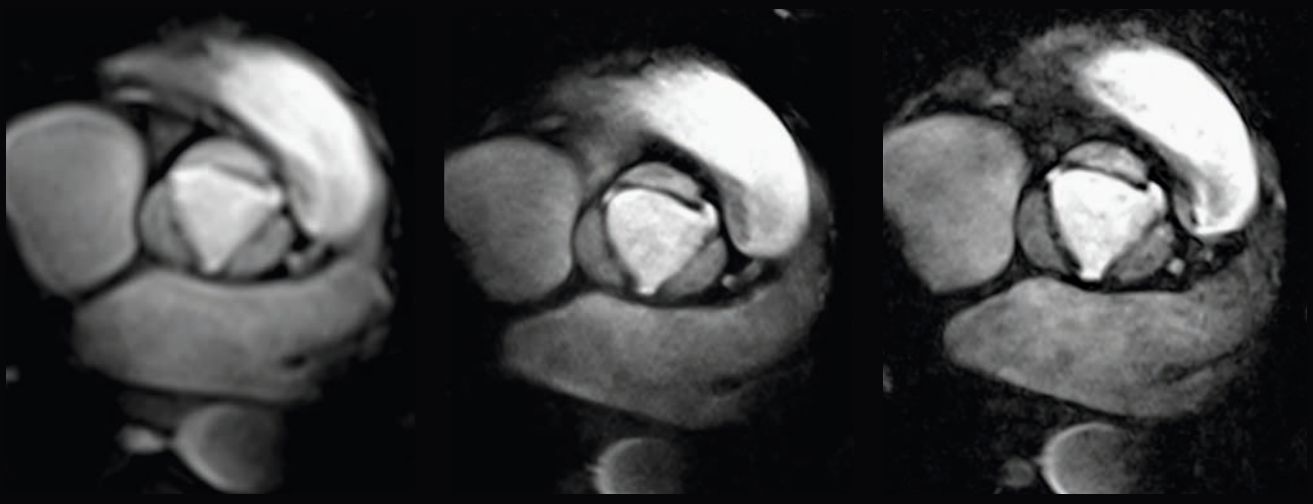

1.4 x 1.4 x 4.0 mm^3 | 1.4 x 1.4 x 3.0 mm^3 | 1.4 x 1.4 x 1.5 mm^3

Courtesy of Essen University Hospital, Erwin L. Hahn Institute for MRI, Essen, Germany

High resolution breast imaging

- In breast MRI 0.6 mm isotropic imaging has potential for the visualization of small structures such as ligaments that are not visible in standard resolution images.

Courtesy of New York University (NYU), New York, NY, USA

Cervical cancer

- T1-weighted FLASH-2D ce transversal:
  0.6 x 0.6 x 2.0 mm^3
  TA 1:25 min

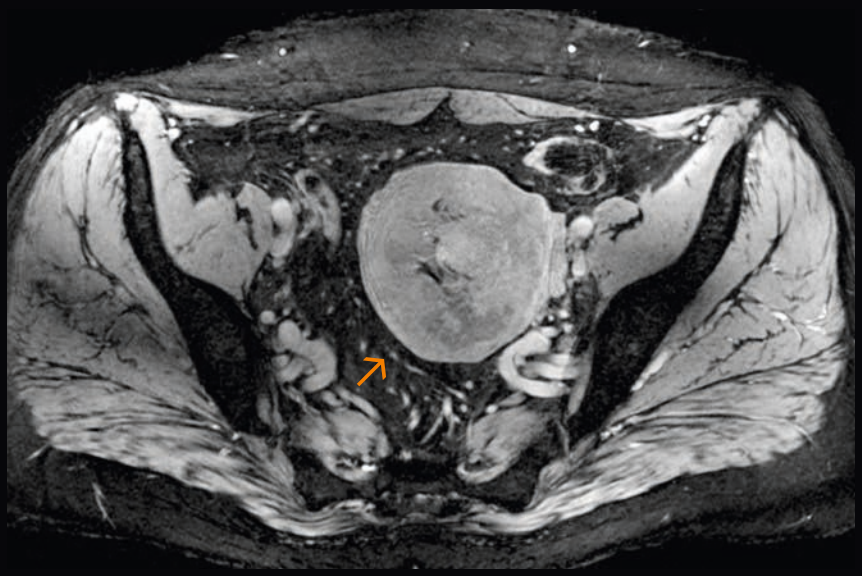

Courtesy of Essen University Hospital, Erwin L. Hahn Institute for MRI, Essen, Germany

Prostate cancer

- T2-weighted fast spin echo axial images at 0.75 x 0.75 x 3 mm^3 from 2 patients using parallel transmit and 8 refocusing pulses. Targeted MR guided biopsy in Patient 1, confirmed a prostate adenocarcinoma (hypointense region – red circle). In Patient 2, a hypointense lesion is visible in the right peripheral zone (yellow circle) confirmed by a whole-mount prostatectomy to be an adenocarcinoma of the prostate.

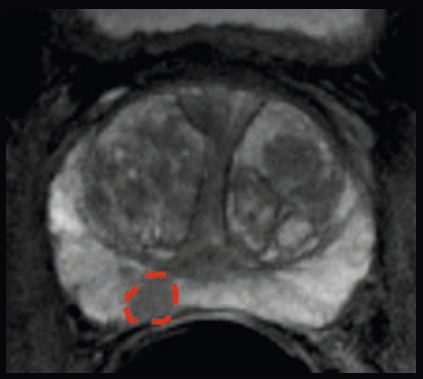

Patient 1

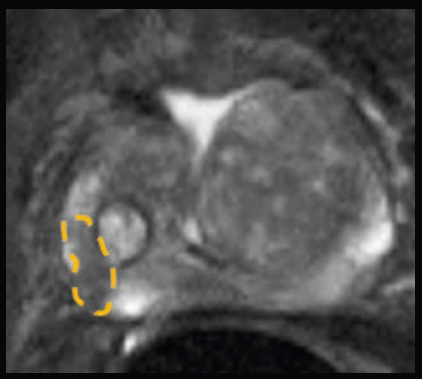

Patient 2

Courtesy of University Nijmegen Medical Centre, Radiology Department, Nijmegen, The Netherlands

Imaging the cervical spine, spinal injury

- Increased signal might indicate dorsal-column Wallerian degeneration
- Hyposignal might indicate localized hemosiderin to specific dorsal-horn laminae
- T2*-weighted FLASH 0.37 x 0.37 x 3 mm³

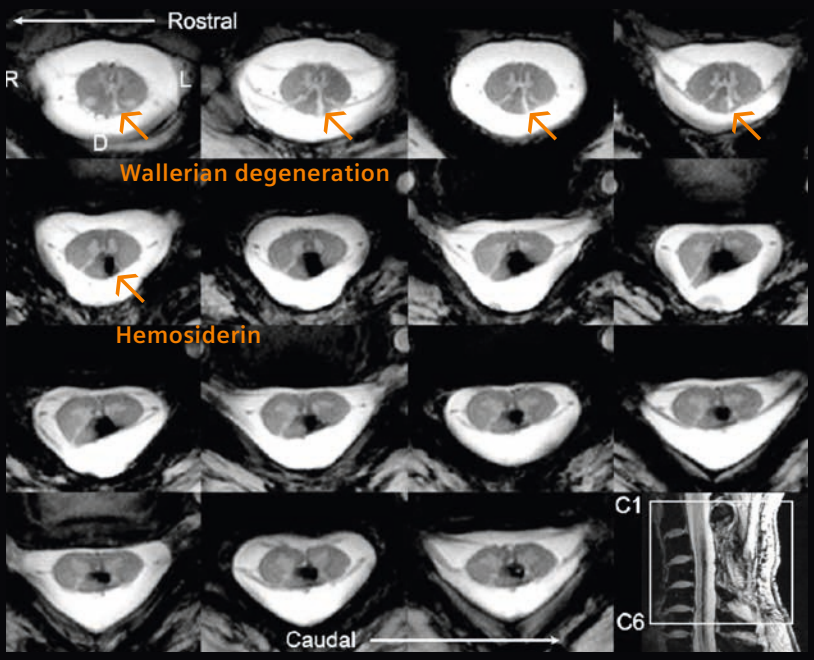

Courtesy of Massachusetts General Hospital (MGH), Boston, MA, USA

Cervical spine imaging, ALS patient

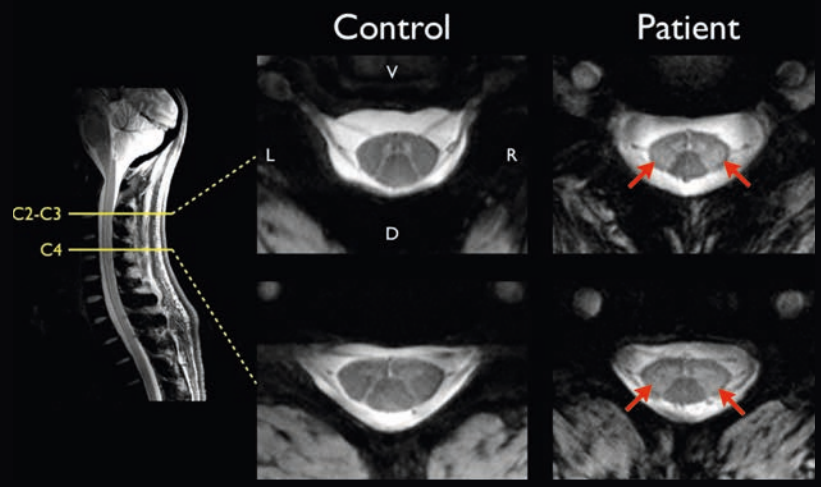

Courtesy of Massachusetts General Hospital (MGH), Boston, MA, USA

Quantitative hip cartilage imaging

- T1- **(A)**, T2- **(B)** and T2*- **(C)** relaxation time maps of the hip joint in sagittal view, with enlarged views of the joint space above. Note the clear differentiation between acetabular and femoral cartilage.
- T1 mapping: 0.4 x 0.4 x 2.0 mm³
- T2 and T2* mapping: 0.5 x 0.5 x 2.5 mm³

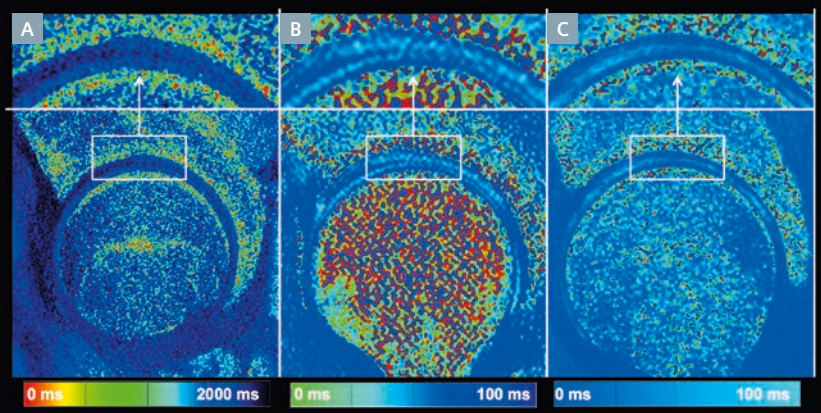

Courtesy of Essen University Hospital, Erwin L. Hahn Institute for MRI, Essen, Germany

T1 dGEMRIC
0.4 x 0.4 x 2.0 mm³

T2
0.5 x 0.5 x 2.5 mm³

T2*
0.5 x 0.5 x 2.5 mm³

Meniskus fracture

- **(A)** TSE with fat sat 0.4 x 0.4 x 2.5 mm^3
- **(B)** TSE 0.3 x 0.3 x 2.5 mm^3

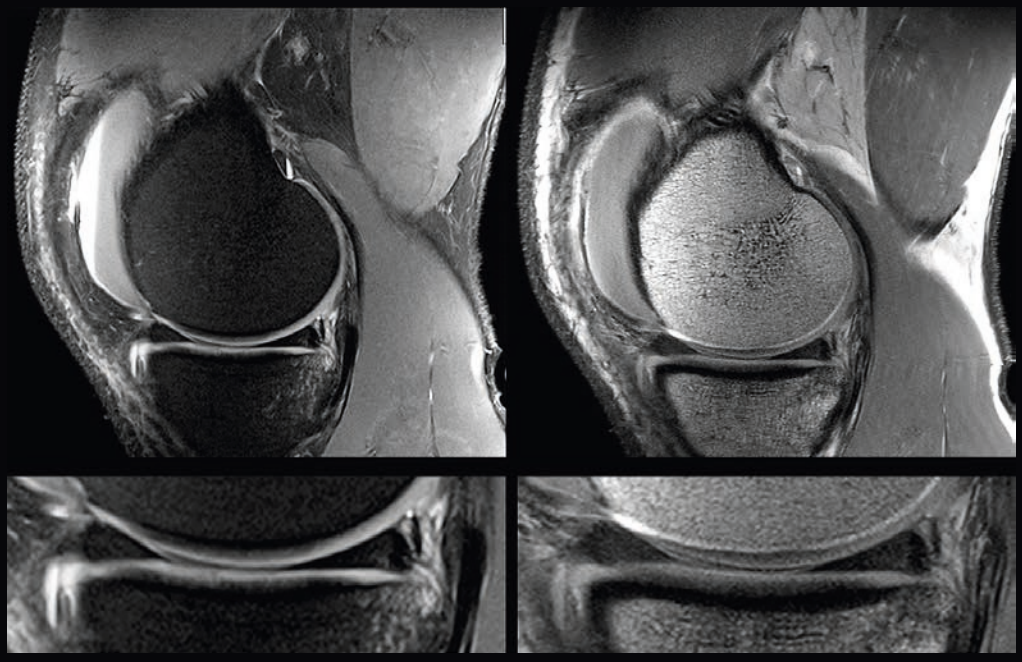

A B

Courtesy of Medical University Vienna (MUW), Vienna, Austria

Cinematic rendering of 7T knee images using *syngo*.via Frontier[1]

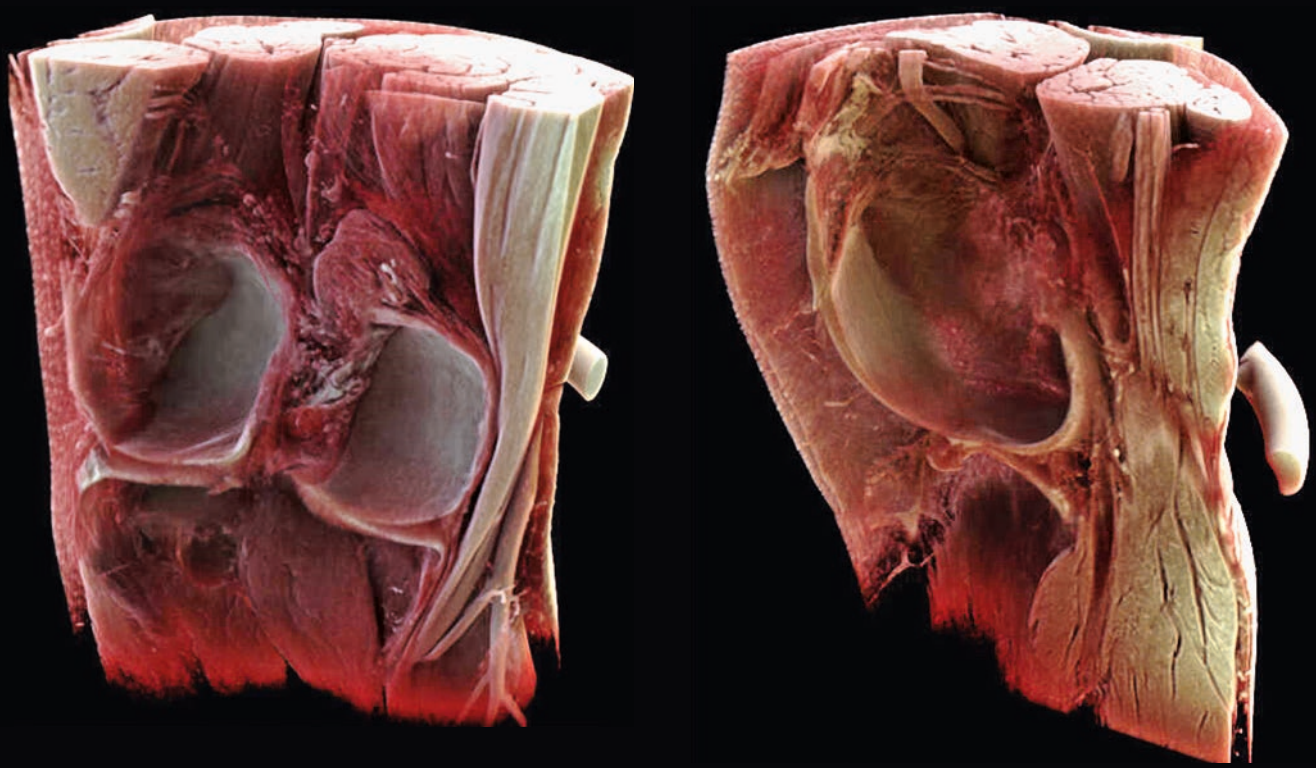

Courtesy of Medical University Vienna (MUV), Vienna, Austria

[1] WIP, the product is currently under development and is not for sale in the US and in other countries. Its future availability cannot be ensured. The product is not yet licensed for sale in Canada, in accordance with Canadian Law. Performance claims have not been reviewed by Health Canada, and are subject to change. Its future availability cannot be guaranteed.

fit-Upgrade: A Success Story

Stephan Zangos; Thomas J. Vogl

Institute for Diagnostic and Interventional Radiology, University Hospital Frankfurt, Frankfurt/Main, Germany

We reported on our first experiences with fit-upgrades on the MAGNETOM Avanto^{fit} and MAGNETOM Prisma^{fit} in MAGNETOM Flash [1] a year ago. This article is an update of this experience. fit-upgrades to both MR systems were carried out, problem-free, in only 15 days, without additional rebuilding measures. The magnet remained in the scanner room while all other components were replaced. The fit-upgrades gave us access to the latest MRI technology, including a new gradient system, Tim 4G architecture, and day optimizing throughput (Dot) workflow engines on both systems. Both systems are currently operating without problems and without unscheduled downtime.

These upgrades should help improve workflow and image quality, and ultimately lead to an increase in the number of examinations.

In addition, the new Dot engines provide improved examinations through fast and reproducible imaging. These are now routinely used for all liver, spine, cranial, and heart examinations in our clinic, where examinations can be adapted easily to answer specific questions at decision points.

When financing new devices today, we see a widening gap between the high costs of the system and lower revenue per exam. Today, radiologists aim to develop their own departments, with high quality services at acceptable prices.

Various strategies could be utilized to increase the number of examinations within the same number of working hours. The new systems enable a significant reduction in examination times as a result of better system performance, giving the same image quality. Indeed, the new systems can often provide improved image quality in shorter examination times.

Inexperienced staff can be led through examinations using the guidance features of the new Dot engines, reducing unnecessary or repetitive images. As a result, training time can be significantly reduced and consistent imaging quality achieved. This is an important factor, particularly in teaching hospitals, where inexperienced staff must often be deployed. The additional use of the Dot engines with their built-in automation assists the technologist during the examinations.

In a retrospective analysis[1] (Table 1), we showed that with the fit-upgrades, exam frequency could be increased in our department by 20.6% to 697 examinations/year using the Avanto^{fit}, and by 13.2% to 469 examinations/year using the Prisma^{fit}. After upgrades, changes in the number of examinations are often multifactorial and cannot be accurately broken down to individual causes. The increased system performance allows us to provide improved image quality to our referring physicians.

After the upgrade we could increase the number of examinations without any conscious change to our examination strategies, or by extending our working hours. In particular, we found that better performance of the new systems and use of the Dot engines were the primary contributors to the increase in number of investigations. Improvement in image quality has also been recognized by our clinical partners, which has led to good acceptance of our MRI examinations in the hospital.

Table 1

	01.01.-31.12.2012	01.01.-31.12.2014
Workdays	252	252
	MAGNETOM Avanto	**MAGNETOM Avanto^{fit}**
Cases total	3377	4074
Cases/day	13,4	16,2
	MAGNETOM Trio Tim	**MAGNETOM Prisma^{fit}**
Cases total	3543	4012
Cases/day	14,1	15,9

A retrospective analysis[1] shows that the fit-upgrades increased exam frequency in our department. 697 more cases with Avanto^{fit} and 469 more cases with Prisma^{fit}.

Conclusion

The fit-upgrade remains an economically attractive approach for an aged MR system. By improving system performance and workflow using the system software, the number of examinations can be increased, together with improved image quality, with little effort.

[1] The statements by Siemens' customers described herein are based on results that were achieved in the customer's unique setting. Since there is no 'typical' setting and many variables exist there can be no guarantee that other customers will achieve the same results.

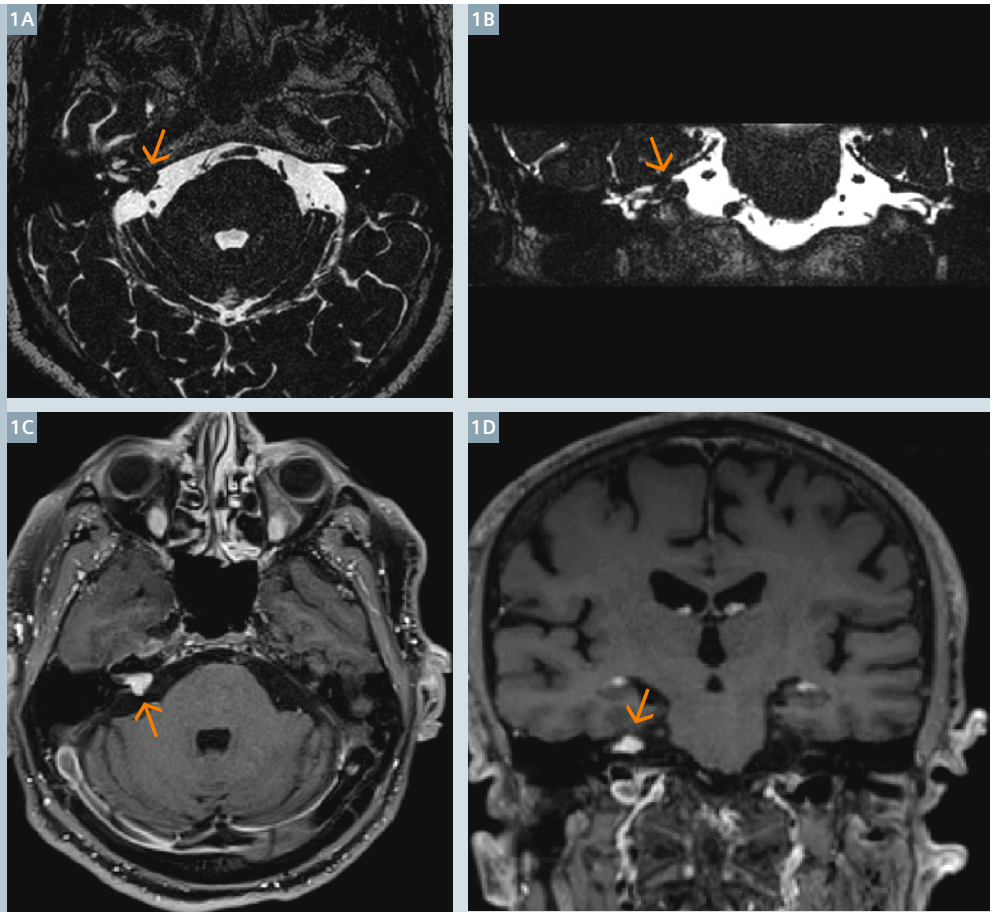

1 **(1A, B)** Representation of an acoustic neurinoma (arrow) on the MAGNETOM Avanto[fit]. T2-weighted SPACE transversal (TR 1200 ms, TE 264 ms, slice thickness 0.6 mm) and reconstructed coronal slice orientations. **(1C, D)** Contrast-enhanced T1-weighted MPRAGE (TR 1800 ms, TE 2.6 ms, slice thickness 1 mm) with automatically calculated coronal MPR.

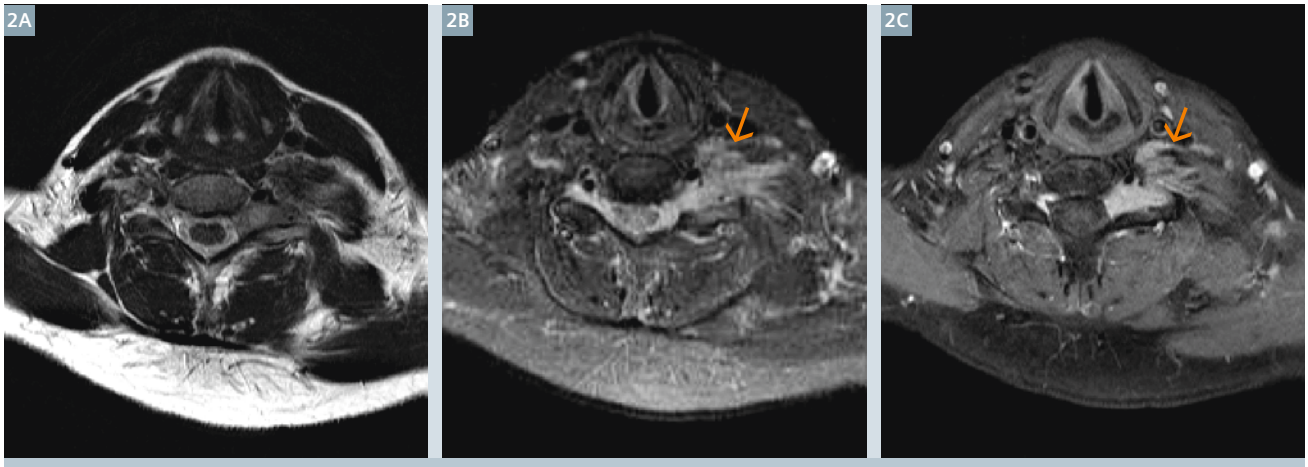

2 Relapse of B-NHL (arrow) on the Avanto[fit].
Comparison of the T2w TSE (TR 4000 ms, TE 79 ms; slice thickness 5 mm), T2w TIRM (TR 4140 ms, TE 32 ms; slice thickness 6 mm) and contrast-enhanced T1w TSE FS-Dixon sequences (TR 520 ms, TE 14 ms; slice thickness 5 mm). The images show homogeneous fat saturation in this problem area, facilitating diagnosis.

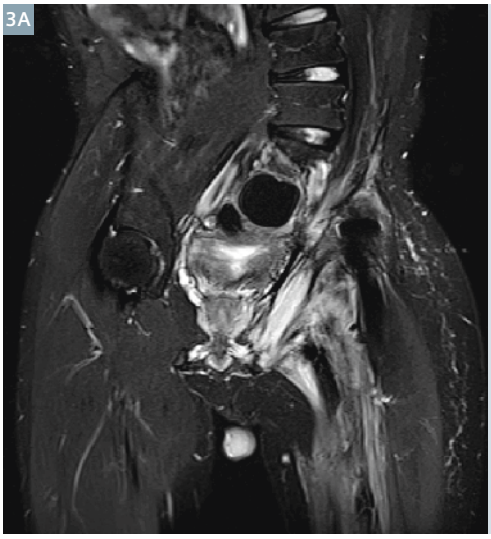

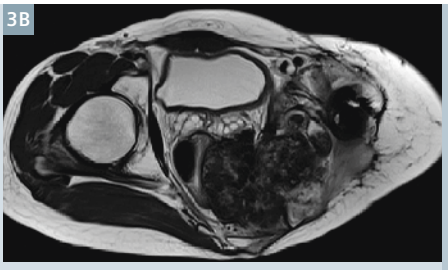

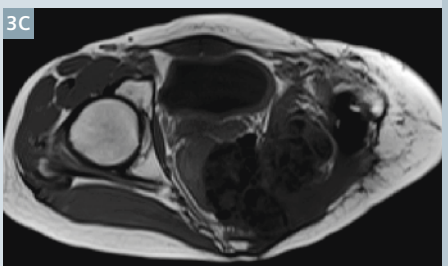

3 Recurrence after resection of osteosarcoma of the ilium on the MAGNETOM Avanto[fit]. T2w TIRM WARP (TR 4670 ms, TE 39 ms; slice thickness 5 mm), T2w TSE WARP (TR 5530 ms, TE 77 ms; slice thickness 6 mm), T1w TSE WARP (TR 500 ms, TE 7 ms; slice thickness, 6 mm), and T1w TSE WARP sequences show the reduction of metal artifacts of tumor prosthesis.

4 MIP (maximum intensity projection) of a TWIST angiography in neutral and provocation positions on the MAGNETOM Avanto[fit]. The images show an entrapment on the left side.

References

1 Zangos S, Vogl TJ. MAGNETOM Trio upgrade to Prisma[fit] better imaging technique ccombined with higher throughput in clinical practice. MAGNETOM Flash no. 58, 3(2014): 32-38.

Thomas J. Vogl

Stephan Zangos

Contact

Prof. Dr. med. Stephan Zangos
Institute for Diagnostic and Interventional Radiology
University Hospital Frankfurt
Theodor-Stern-Kai 7
Haus 23c
60590 Frankfurt am Main
Germany
Phone: + 49 (0)69 6301-87287
Fax: +49 (0)69 6301-7288
zangos@em.uni-frankfurt.de

Expert Talks

Don’t miss the talks of experienced and renowned experts on all aspects of MR imaging.

MRI Technology and Methodology: A Look into the Future

Peter Jezzard
University of Oxford (Oxford, UK)

Whole-Body MRI: Changing Cancer Patient Managment

Anwar R. Padhani
Mount Vernon Cancer Centre (London, UK)

Future Trends in Breast MRI: TWIST-VIBE for Breast Cancer Staging in 2 Minutes

Ritse Mann
Radboud University Medical Center (Nijmegen, The Netherlands)

A 5 Minute Clinical Brain Protocol

Lawrence Wald
Massachusetts General Hospital (Boston, MA, USA)

Body MRI and Whole-Body Staging in Pediatric* Patients

Günther Schneider
Saarland University Hospital (Homburg, Germany)

Visit us at **www.siemens.com/magnetom-world**

Go to **Clinical Corner > Clinical Talks**

* MR scanning has not been established as safe for imaging fetuses and infants under two years of age.
The responsible physician must evaluate the benefit of the MRI examination in comparison to other imaging procedures.

syngo MR E11 on a MAGNETOM Aera: First Impressions

Dr. Martin Reiss-Zimmermann, M.D.

Radiologische Gemeinschaftspraxis Erfurt, Germany

The decision to purchase a new or replacement MR scanner is always based on various factors, such as investment/reimbursement costs, necessary building space, innovative technology (e.g. image quality, patient throughput, specialized examinations) and patient comfort.

The restrictions of the building in terms of space and load capacity limited us to the footprint of the pre-existing MAGNETOM Harmony and a 1.5 Tesla MR scanner system. While these unavoidable limitations certainly reduced the range of potential scanners, our considerations focused mainly on technical advances resulting in increased image quality and patient comfort, and also on running expenses. A wide-bore system was considered essential, since our diagnostic spectrum is based not only on musculoskeletal (MSK) and neurological (Neuro) imaging, but also includes whole-spine/whole-body and MR angiography examinations.

The MAGNETOM Aera met our requirements and more: It even featured additional benefits, such as zero-Helium-boil-off technology, which reduces running costs, especially during this worldwide shortage of Helium. Furthermore, the offer included an upgrade from *syngo* MR D13 to *syngo* MR E11 shortly after the installation of the scanner.

Having worked with *syngo* MR B17/19 before, the switch to D13, and later on to E11 was rather easy. While the main character and philosophy of the graphical user interface stayed the same, the new features were easy to understand. In our view, a minor downside of D13 was the replacement of the trashcan in the lower left corner, which was re-introduced in E11. Being used to this feature, the missing option led to several sequence stops in the beginning (although this is something one can get used to). The new MAGNETOM Aera also provided new Tim 4G coils with higher coil element density and new sequence features, resulting in an improved image quality (Fig. 1). Two of the features we would like to discuss in more detail are Quiet and WARP sequences.

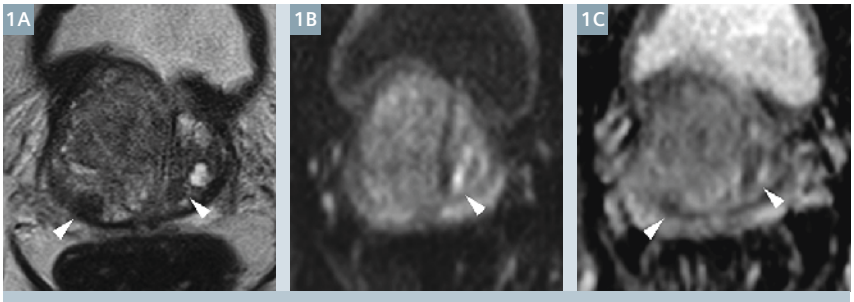

1 Multifocal prostate cancer (Gleason score 7a) in segment 5p and 11p with hypointense depiction in axial T2-weighted imaging **(1A, B)** and hypointense signal values in ADC **(1C)**. Note that only the tumor in segment 11p is hyperintense in b800. Imaging was performed only with surface coils, without the use of an endorectal coil.
Sequence parameters:
T2w TSE: FOV 200 mm², slice 3 mm, TR 6500 ms, TE 108 ms, matrix 320, 3 averages, TA 3:47 min;
DWI: FOV 200 mm², slice 3 mm, TR 3600 ms, TE 71 ms, matrix 112, b-values (averages) 0 (4 avg), 50 (5 avg) and 800 (20 avg), TA 5:04 min.

At first we were rather skeptical about the performance of the Quiet sequences in real live practice. It seems understandable that a less steep slew rate reduces noise. But we asked ourselves how this could be done with virtually no additional scan time or without degradation of image quality? And furthermore, were there any differences in various sequences or examination regions? During system setup we tested those sequences extensively, especially for MSK and Neuro examinations. The sequences were slightly modified by the Siemens application specialist, resulting in minimal increase of scan time and with visually little to no image degradation (Fig. 2). In our preliminary experience, the new Quiet feature is no real push-button technique but consists of several important steps with variable parameter settings and can be seen as a trade-off triangle between noise reduction, image quality and acquisition time (Table 1).

When using the new PETRA sequence for the first time, we were astonished that one could hardly hear the sequence [1]. Compared to a conventional MPRAGE sequence the PETRA images exhibit a softer differentiation between grey and white matter (Fig. 3). In our view, further studies are clearly needed to evaluate the impact of this altered contrast as well as the marginal increase in acquisition time (e.g. time versus noise in examinations of children) [2]. Also, the PETRA sequence inherently covers a large field-of-view in z-axis, generating a set of images above the cranium and without essential information.

Table 1

TSE	SE	GRE
'Noise Reduction' on	'Noise Reduction' on	'Noise Reduction' on
↑ bandwidth	↑ bandwidth	↑ bandwidth
↑ echospacing	↑ TR	↑ TR
'Gradient Motion Refoc' off	↑ TE	↑ TE
RF pulse type 'Fast'	RF pulse type 'Fast'	RF pulse type 'Fast'
↑ TR and/or ↓ no. of slices		'Asymmetric Echo' on

Parameter settings for noise reduction – please note that there are no definitive values for parameter modification.
Consider 10-15 % change as a good start to experiment. (Parameters can be changed on Routine card and Sequence card Part 1 & 2).

Great progress is being made in artifact reduction caused by surgical implants[1], which includes modification of the composition of modern implants[1] as well as data acquisition. Nevertheless, especially in cases of endoprosthesis (e.g. knee or hip joint) and in older implants[1], examinations can be degraded by severe distortions. High-bandwidth sequences, but even more WARP and SEMAC, can help to reduce these artifacts [3]. While high-bandwidth sequences usually go along with SNR reduction and SEMAC sequences are very time consuming, our favorite tool is the WARP technique. In fact, we use WARP sequences for all spine examinations in patients with known metal implants with excellent results (Fig. 4). Compared to 3T imaging with increased susceptibility artifacts, WARP sequences are able to provide diagnostic image quality in almost all cases [4]. Therefore in our daily routine, SEMAC sequences are used almost only in cases of full-joint replacement, which are demanding for every imaging technique. Certainly, SEMAC cannot bypass elementary laws of MR physics, but it helps to bring light into the area adjacent to the joint replacement (Fig. 5).

To shortly summarize our impressions after three months of usage: The new *syngo* MR E11 software improved our daily practice, which is mainly focused on MSK and Neuro imaging, in

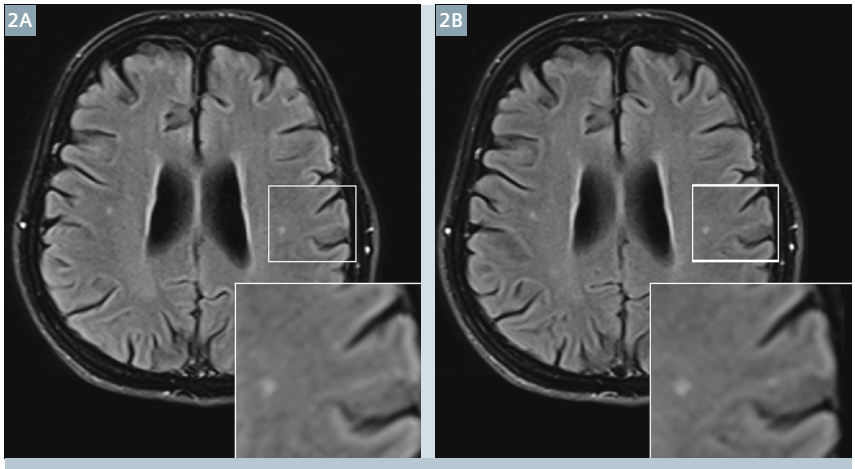

2 Axial FLAIR imaging of a 56-year-old man with history of headache. Note, there are no visible differences between the Quiet and the regular sequence.
Sequence parameters:
Quiet (2A): TR 8700 ms, TE 87 ms, bandwidth 210, TA 3:15 min.
Regular (2B): TR 8500 ms, TE 87 ms, bandwidth 190, TA 3:06 min.

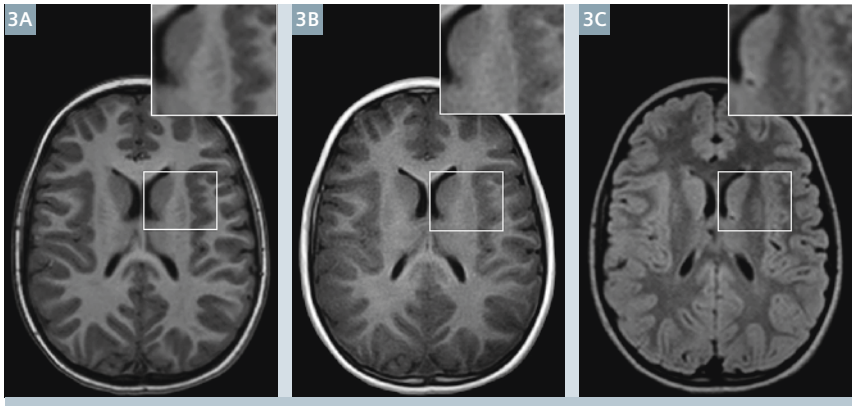

3 Imaging of a 7-year-old girl with suspected epilepsy, using isotropic 3D sequences **(3A)** MPRAGE, **(3B)** PETRA, **(3C)** FLAIR-SPACE. Note the slightly blurred differentiation of grey and white matter of the caudate head, the insular cortex and the superior aspect of the caudolenticular grey bridges in PETRA compared to the standard MPRAGE and FLAIR-SPACE sequence.
Sequence parameters:
PETRA: FOV 288 mm², TR 3.32 ms, TE 0.07 ms, IR 1300 ms, TA 5:49 min.
MPRAGE: FOV 250 mm², TR 2200 ms, TE 2.88 ms, TI 900 ms, TA 4:56 min.
FLAIR-SPACE: FOV 231 x 265 mm, TR 5000 ms, TE 336 ms, TI 1800 ms, TA 4:55 min.

[1] The MRI restrictions (if any) of the metal implant must be considered prior to patient undergoing MRI exam. MR imaging of patients with metallic implants brings specific risks. However, certain implants are approved by the governing regulatory bodies to be MR conditionally safe. For such implants, the previously mentioned warning may not be applicable. Please contact the implant manufacturer for the specific conditional information. The conditions for MR safety are the responsibility of the implant manufacturer, not of Siemens.

terms of diagnostic imaging quality and (probably) patient comfort. WARP sequences are routinely performed in all patients with metal implants and result in diagnostic quality in almost every case. SEMAC sequences are a great, but more time demanding backup tool for individual cases. We believe that noise reduction increases patient comfort, as well as other aspects of modern imaging such as wide-bore scanners, reduced scan times and scanner room light installations. Therefore, we are planning to assess the impact of Quiet sequences on subjective patient comfort in a separate statistical survey.

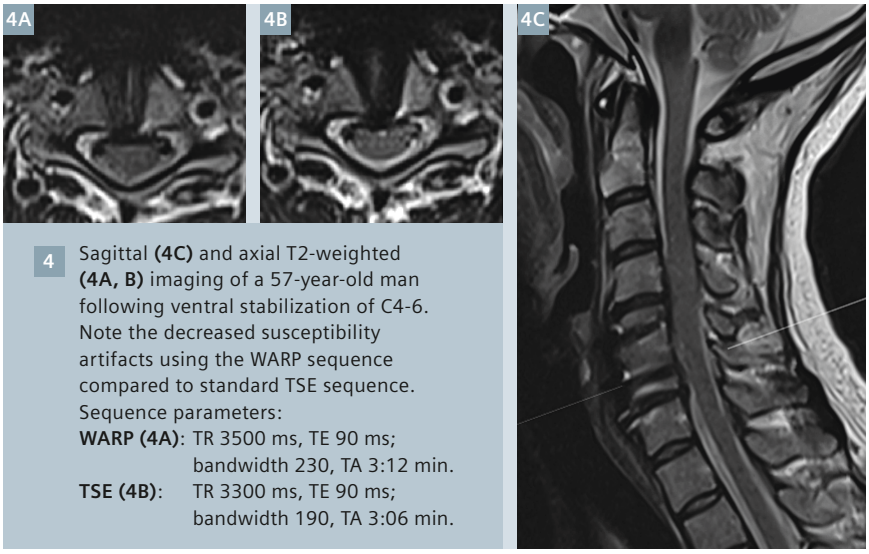

4 Sagittal **(4C)** and axial T2-weighted **(4A, B)** imaging of a 57-year-old man following ventral stabilization of C4-6. Note the decreased susceptibility artifacts using the WARP sequence compared to standard TSE sequence. Sequence parameters:
WARP (4A): TR 3500 ms, TE 90 ms; bandwidth 230, TA 3:12 min.
TSE (4B): TR 3300 ms, TE 90 ms; bandwidth 190, TA 3:06 min.

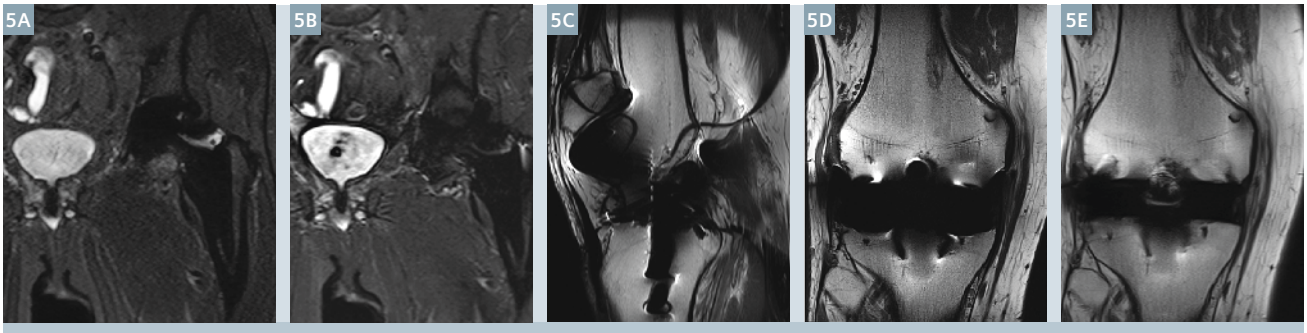

5 Images of two different patients. **(5A, B)** show a 63-year-old patient with bilateral full hip replacement, scheduled for MRA of the lower extremities (5A: PD-w FS SEMAC, 5B: standard PD-w FS). Note the markedly decreased susceptibility artifacts adjacent to the left hip implant in SEMAC imaging (TR 5340 ms, TE 37 ms, bandwidth 780, TA 05:36 min), which allow for detection of effusion within the articular capsule. In standard imaging the artifacts even extend within the pelvic floor (TR 3500 ms, TE 33 ms, bandwidth 160, TA 01:41 min).
(5C-E) depict a 53-year-old female with knee replacement. Note the severe distortions in sagittal PD-w imaging (5C). Distortions are also found in coronal imaging. Compared to the standard T1 TSE sequence (5D) the PD-w SEMAC sequence exhibits a softer contrast with slightly less details. Note that in SEMAC the artifact reductions allows for evaluation of the intercondylar fossa (TR 3480 ms, TE 28 ms, bandwidth 650, TA 04:06 min).

syngo MR E11 comes with even more improvements such as StarVIBE and FreezeIt, which we did not focus on yet.

Contact

Dr. Martin Reiss-Zimmermann, M.D.
Radiologische Gemeinschaftspraxis Erfurt
Brühlerwallstr. 4
99084 Erfurt
Germany
Phone: +49 (0)361 - 220 900
MRZ@neuroradiologie-erfurt.de

References

1 Grodzki DM, Jakob PM, Heismann B (2012) Ultrashort echo time imaging using pointwise encoding time reduction with radial acquisition (PETRA). Magnetic Resonance in Medicine 67:510-518.

2 Ida M, Wakayama T, Nielsen ML, Abe T, Grodzki DM (2014) Quiet T1-weighted imaging using PETRA: Initial clinical evaluation in intracranial tumor patients. Journal of Magnetic Resonance Imaging. 10.1002/jmri.24575.

3 Bachschmidt T, Lipps F, Nittka M (2012) syngo WARP - Metal Artifact Reduction Techniques in Magnetic Resonance Imaging. MAGNETOM Flash 2/2012:24-25.

4 Lee YH, Lim D, Kim E, Kim S, Song HT, Suh JS (2013) Usefulness of slice encoding for metal artifact correction (SEMAC) for reducing metallic artifacts in 3-T MRI. Magnetic Resonance Imaging 31:703-706.

[1] The statements by Siemens' customers presented here are based on results that were achieved in the customer's unique setting. Since there is no 'typical' hospital and many variables exist (e.g., hospital size, case mix, level of IT adoption), there can be no guarantee that other customers will achieve the same results.

Hepatic Fat Quantification in Pediatric Patients using Multi-echo Dixon VIBE: Early Experience

Jie Deng, Ph.D.[1,2]; Xiaodong Zhong, Ph.D.[4]; Mark Fishbein, M.D.[3]; Marci Messina, RT(R)(MR)[1]; Brian Reilly, RT (R)[1]; Shivraman Giri, Ph.D.[5]; Stephan Kannengiesser, Ph.D.[6]; Marcel Nickel, Ph.D.[6]; Cynthia K. Rigsby M.D.[1,2]

[1] Department of Medical Imaging, Ann & Robert H. Lurie Children's Hospital of Chicago, Chicago, IL, USA
[2] Department of Radiology, Feinberg School of Medicine, Northwestern University, Chicago, IL, USA
[3] Division of Gastroenterology, Hepatology, and Nutrition, Ann & Robert H. Lurie Children's Hospital of Chicago, Chicago, IL, USA
[4] MR R&D Collaborations, Siemens Healthcare, Atlanta, GA, USA
[5] MR R&D Collaborations, Siemens Healthcare, Chicago, IL, USA
[6] Siemens Healthcare, Erlangen, Germany

Introduction

Non-alcoholic fatty liver disease (NAFLD) is a co-morbidity of obesity and potential precursor of cirrhosis and hepatocellular carcinoma. Liver biopsy is the standard of care for diagnosis and to establish disease severity but is an invasive approach that provides limited sampling locations and is not suitable for screening or frequent monitoring. Non-invasive imaging modalities such as ultrasound and CT are helpful to identify hepatic fat, however, these techniques provide less optimal soft tissue contrast and the radiation from CT has become a heightened concern, particularly in children. Besides excellent soft tissue contrast, MRI can provide quantitative measurements of hepatic fat without radiation risks, a particularly appealing feature in the assessment of pediatric[1] patients.

The multi-echo Dixon VIBE technique, part of the new application package LiverLab, enables comprehensive liver fat quantification through mapping of fat and water percentages and R2*. This methodology creates new opportunities for diagnostics that until recently had been felt to be overly cumbersome or not feasible to perform in children.

[1] MR scanning has not been established as safe for imaging fetuses and infants under two years of age. The responsible physician must evaluate the benefit of the MRI examination in comparison to other imaging procedures.

Case 1:

12-year-old, male.
Clinical indication: mixed hyperlipidemia.

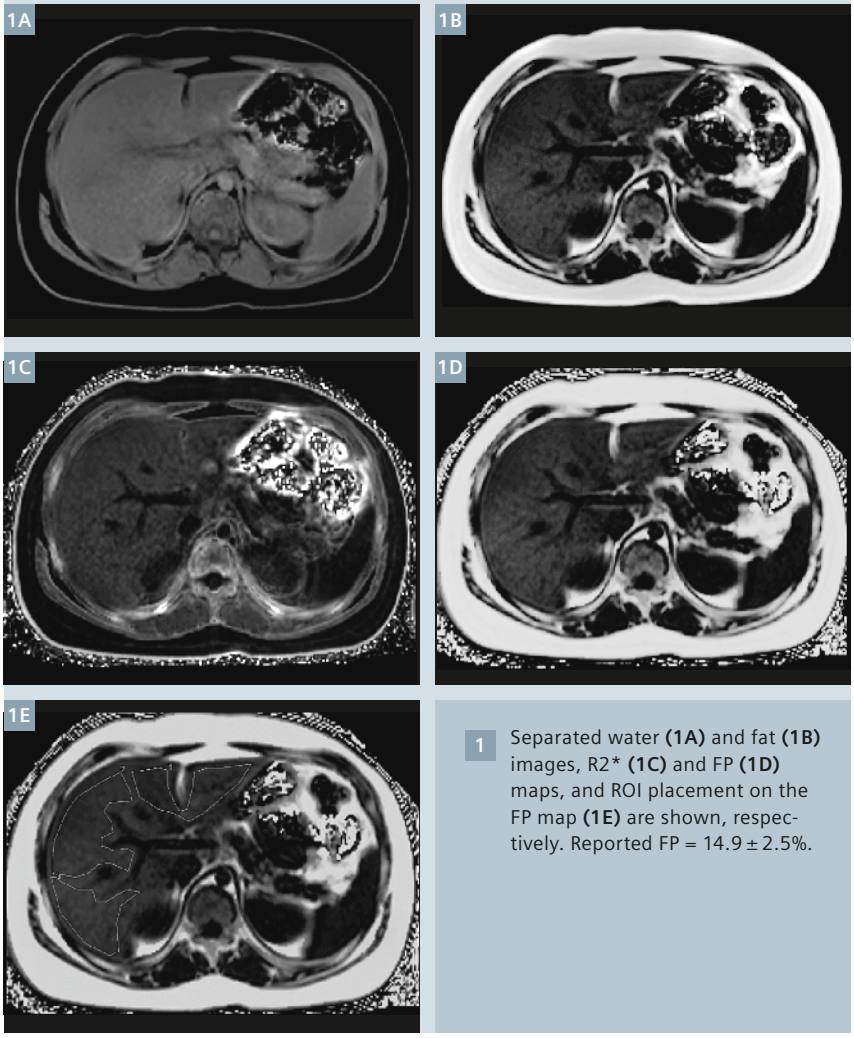

1 Separated water **(1A)** and fat **(1B)** images, R2* **(1C)** and FP **(1D)** maps, and ROI placement on the FP map **(1E)** are shown, respectively. Reported FP = 14.9 ± 2.5%.

Accurate liver fat quantification is confounded by many factors, including but not limited to, T2* signal decay, field inhomogeneities, and T1 effects. The multi-echo Dixon VIBE sequence addresses these challenges systematically. First, the sequence is designed to include algorithms or strategies to compensate for all the above confounding effects to provide accurate results, i.e. using low flip angle to reduce T1 effects, and nonlinear fitting for simultaneous estimation of fat and R2* (1/ T2*) [1]. Second, the sequence is based on a 3D GRE acquisition compatible with CAIPIRINHA acceleration [2, 3], permitting whole liver coverage in a single breathhold (appealing for children). Finally, the scanner console displays scan results instantaneously including inline images of water signal and fat signal, and parametric maps of fat percentage (FP) and R2*, allowing for rapid region-of-interest (ROI) analysis.

In this trial, we demonstrate the potential utility of multi-echo Dixon VIBE sequence for hepatic fat quantification in pediatric subjects. It shall be noted that the multi-echo Dixon VIBE sequence evaluated in this article was a prototype, where the features of the final product version may vary.

Method

Imaging Protocols in our Institution

The typical fatty liver imaging protocol in our institution consists of a 3-plane single shot HASTE sequence with fat saturation, followed by the multi-echo Dixon VIBE. HASTE images are used for ruling out significant diseases in liver, bile duct, pancreas, kidney, spleen, adrenal glands, abdominal lymphadenopathy, and bone marrow abnormality.

Exams are performed on our 1.5T MAGNETOM Aera scanners. The imaging parameters of multi-echo Dixon VIBE include TR 15 ms, flip angle 6°, matrix 256×168, field-of-view 400 mm × 87.5%, 20% phase oversampling, phase direction A-P, slice thickness 5 mm, 40 partitions, bandwidth 1085 Hz/Pixel, bipolar

Case 2:

14-year-old, male.
Clinical indication: chronic non-alcoholic fatty liver disease.

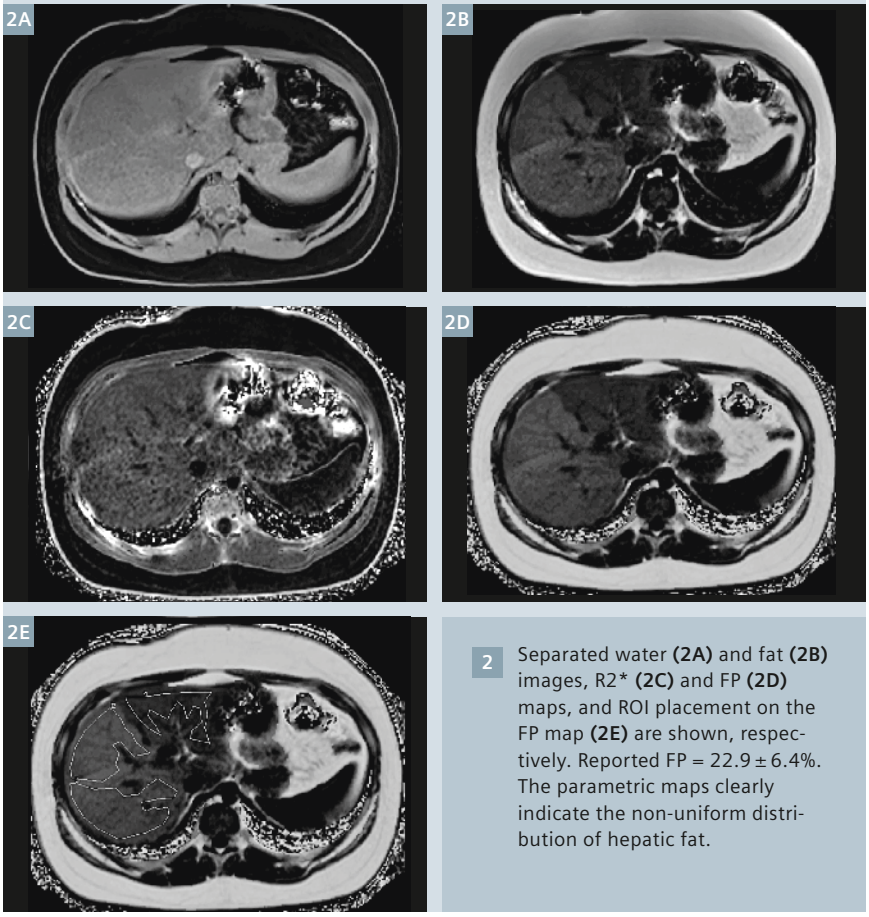

2 Separated water **(2A)** and fat **(2B)** images, R2* **(2C)** and FP **(2D)** maps, and ROI placement on the FP map **(2E)** are shown, respectively. Reported FP = 22.9 ± 6.4%. The parametric maps clearly indicate the non-uniform distribution of hepatic fat.

Case 3:

17-year-old, male.
Clinical indication: an increase in weight and BMI and history of fatty liver disease.

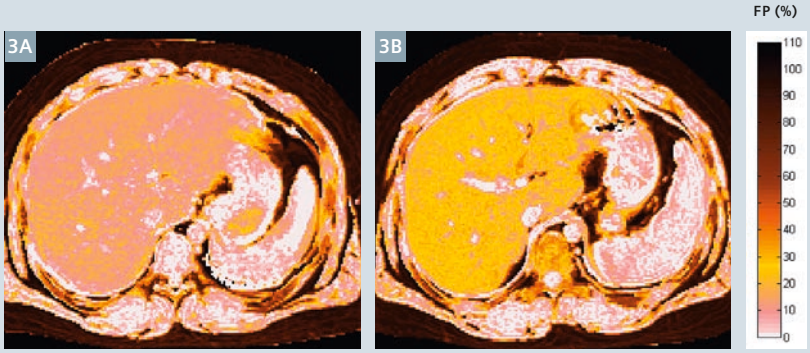

3 FP maps measured in November, 2013 **(3A)** and August, 2014 **(3B)** demonstrate that FP increased from 15.9±0.63% to 22.7±1.3%. The color-coded FP maps of the patient's liver are provided in the personalized education material with fat percentage information regarding the disease progression.

readout, the first TE 2.3 ms, and 6 echoes collected with ΔTE 2.3 ms. CAIPIRINHA acceleration is used with factors of 2 in both phase encoding and partition directions, leading to an acquisition time of 18 s.

Three liver ROIs are placed on the FP maps of four center slices, and care is taken to avoid large vessel areas. If inhomogeneous fat distribution is observed, more ROIs will be drawn on these areas. Mean and standard deviation of FP values are reported and documented in PACS. FP is compared with each patient's previous numbers to monitor the liver fat change.

Children attending the NAFLD clinic at our institution are initially evaluated by a hepatologist. Children with suspected NAFLD then undergo MRI using fatty liver protocols to establish the presence of fatty liver. Aside from diagnostic purposes, the images are also useful for patient education. Personalized images of the child's liver combined with a brief interpretation are used to promote weight loss and liver fat reduction.

Conclusion

The multi-echo Dixon VIBE technique is highly useful in the evaluation of pediatric NAFLD. Its advantages include accurate whole liver fat quantification and short scan time of a single breathhold. This technique generates detailed mapping of the fat deposition within the liver that may be implemented for diagnostics and patient education. There is potential utility for follow-up due to ease of administration and demonstrative results.

References

1 Zhong X, Nickel MD, Kannengiesser SA, Dale BM, Kiefer B, Bashir MR. Liver fat quantification using a multi-step adaptive fitting approach with multi-echo GRE imaging. Magn Reson Med 2014;72:1353-1365.

2 Rofsky NM, Lee VS, Laub G, Pollack MA, Krinsky GA, Thomasson D, Ambrosino MM, Weinreb JC. Abdominal MR imaging with a volumetric interpolated breath-hold examination. Radiology 1999;212:876-884.

3 Breuer FA, Blaimer M, Mueller MF, Seiberlich N, Heidemann RM, Griswold MA, Jakob PM. Controlled aliasing in volumetric parallel imaging (2D CAIPIRINHA). Magn Reson Med 2006;55:549-556.

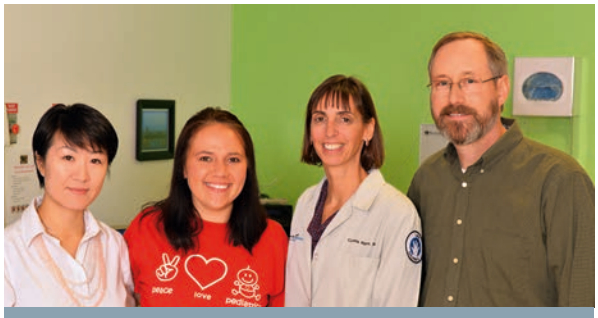

Jie Deng Marci Messina Cynthia K. Rigsby Brian Reilly

Mark Fishbein

Contact

Jie Deng, Ph.D., DABMP
MR Physicist, MR Safety Officer, Medical Imaging
Ann & Robert H. Lurie Children's Hospital of Chicago
Research Assistant Professor, Radiology
Feinberg School of Medicine
Northwestern University
225 East Chicago Avenue, Box 9
Chicago, Illinois 60611-2605,
USA
Phone: +1 312.227.3394
Fax: +1 312.227.9786
jdeng@luriechildrens.org

Case Report: ^{18}F-FDG PET/MRI of Hepatic Cholangiocarcinoma

Sean Gallagher, BA; Bandar Safar, M.D.; Shetal N. Shah, M.D.

Cleveland Clinic, Cleveland, OH, USA

Case summary

A 63-year-old Korean women with unexplained weight loss, appetite loss, 'pink' stools, and weakness presented with an alkaline phosphatase of 843 U/L and a poorly defined liver mass without morphologic evidence of liver cirrhosis or portal hypertension on Computed Tomography (CT) scan done at an outside hospital. Liver function tests were within normal limits and no jaundice was noted on exam at presentation. Based on initial workup which included endoscopic retrograde cholangiopancreatography (ERCP) with stenting of left and right biliary tree and bile duct brushings which showed adenocarcinoma, ^{18}F-FDG* PET/MRI with diagnostic MRI of the liver was requested for initial treatment strategy. This imaging was requested for mass characterization, evaluation of disease extent, and pre-surgical planning.

Imaging findings

Simultaneous ^{18}F-FDG PET/MRI scan from skull vertex to thighs and a diagnostic contrast enhanced (Gadavist®, Bayer Schering Pharma, Leverkusen, Germany) MRI of the liver obtained on a 3T Siemens Biograph mMR scanner reveal a 6.7 x 4.6 x 4.9 cm (AP, Lat, CC) T1 hypointense, T2 hyperintense liver mass occupying segments VIII and V, centered around the intra-hepatic ductal confluence (Figs. 1A, B). The lesion is complex with a central non-enhancing intense T2 bright signal consistent with cystic change that is not FDG avid suggesting region of necrosis or bile lake, as well as a peripherally enhancing nodular soft tissue tumor rind which is mildly hyperintense on T2 as well as relatively FDG avid (maximum SUV 5.5). Following gadolinium administration the tumor rim demonstrates delayed enhancement (Fig. 1C). The region of necrosis or bile lake demonstrates restricted diffusion consistent with malignancy.

*The full prescribing information for the Fludeoxyglucose F^{18} injection can be found at the end of the article.

1 63-year-old Asian female with liver mass on prior CT scan was referred for a staging ^{18}F-FDG PET/MRI exam. Whole-body (vertex to thigh) ^{18}F-FDG PET/MRI with diagnostic contrast enhanced liver MRI (Gadovist®) were performed.

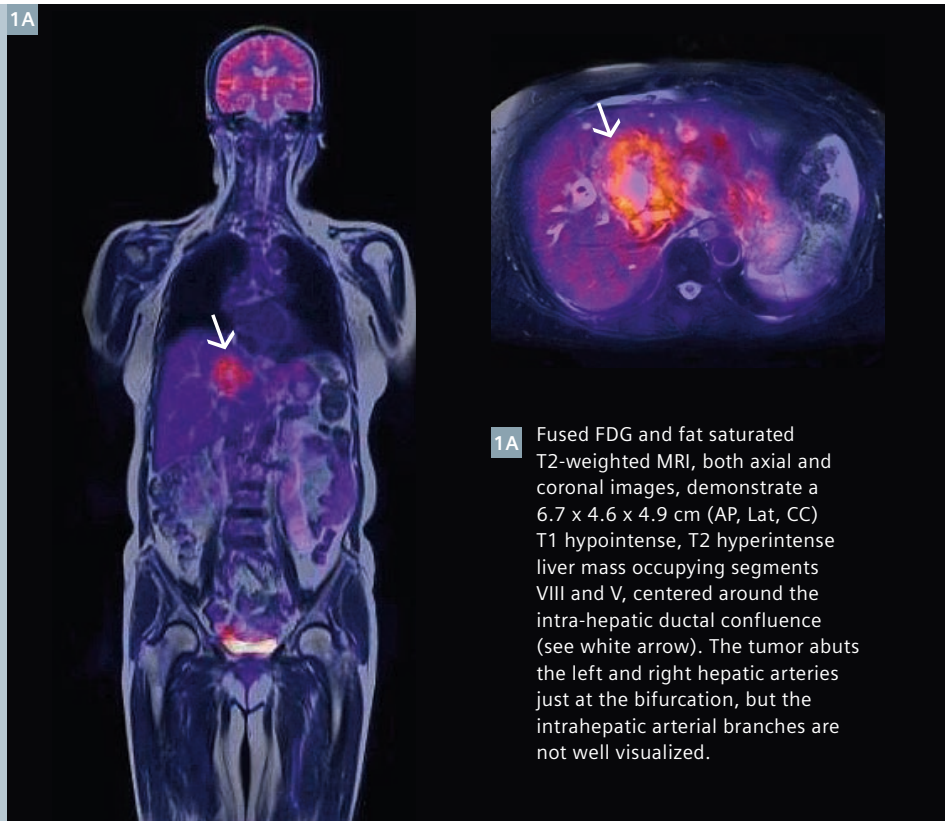

1A Fused FDG and fat saturated T2-weighted MRI, both axial and coronal images, demonstrate a 6.7 x 4.6 x 4.9 cm (AP, Lat, CC) T1 hypointense, T2 hyperintense liver mass occupying segments VIII and V, centered around the intra-hepatic ductal confluence (see white arrow). The tumor abuts the left and right hepatic arteries just at the bifurcation, but the intrahepatic arterial branches are not well visualized.

1B

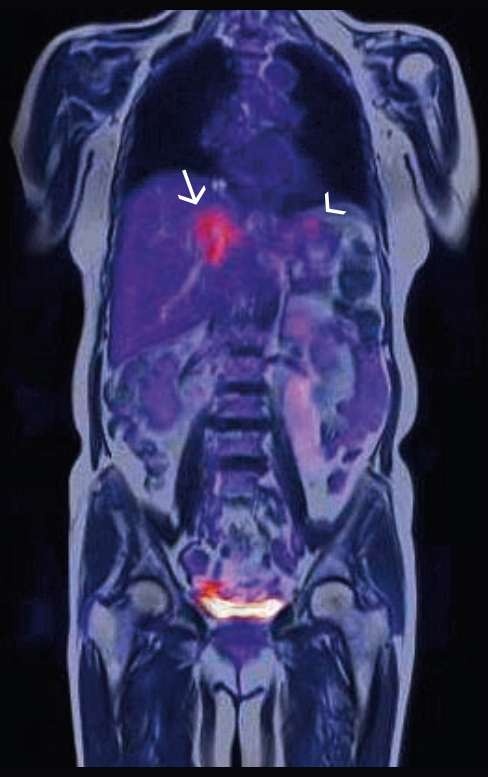

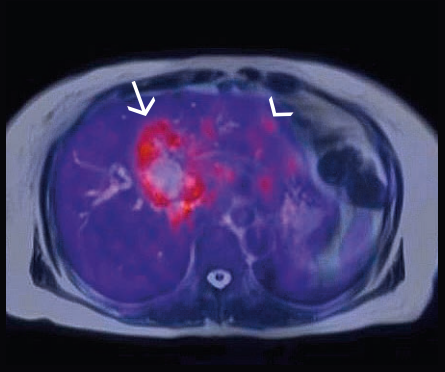

1B Fused FDG and T2w MRI, both axial and coronal images, demonstrate a 6.7 x 4.6 x 4.9 cm (AP, Lat, CC) T1 hypointense, T2 hyperintense liver mass occupying segments VIII and V, centered around the intra-hepatic ductal confluence (see white arrow). The tumor abuts the left and right hepatic arteries just at the bifurcation, but the intrahepatic arterial branches are not well visualized. Also demonstrated are mildly T2 hyperintense, FDG-avid enhancing hepatic lesions with restricted diffusion within segment II (see arrowhead).

1C

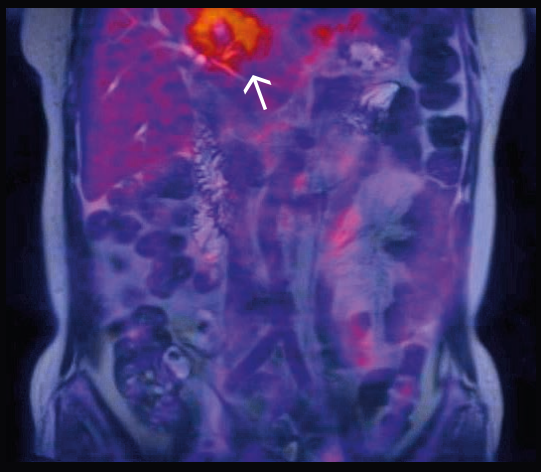

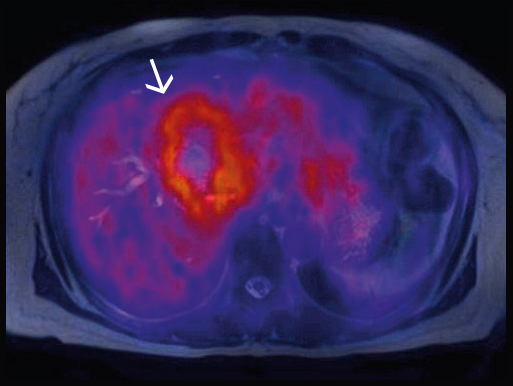

1C Fused FDG and T2w MRI, both axial and coronal images, demonstrate a 6.7 x 4.6 x 4.9 cm (AP, Lat, CC) T1 hypointense, T2 hyperintense liver mass occupying segments VIII and V, centered around the intra-hepatic ductal confluence (see white arrow). The tumor abuts the left and right hepatic arteries just at the bifurcation, but the intrahepatic arterial branches are not well visualized. The lesion is complex with a central non-enhancing intense T2 bright signal consistent with cystic change that is not FDG avid suggesting region of necrosis or bile lake, as well as a peripherally enhancing, mildly T2 bright signal nodular soft tissue tumor rind that is relatively FDG avid (maximum SUV 5.5), that following gadolinium administration demonstrates delayed enhancement.

1D Fused FDG and T2w MRI, both axial and coronal images, demonstrate mildly T2 hyperintense, FDG-avid enhancing hepatic lesions with restricted diffusion within segment II (max. SUV 3.4) that are highly suspicious for metastatic sites (see arrowhead showing most hypermetabolic lesion in segment II – max. SUV 3.4).

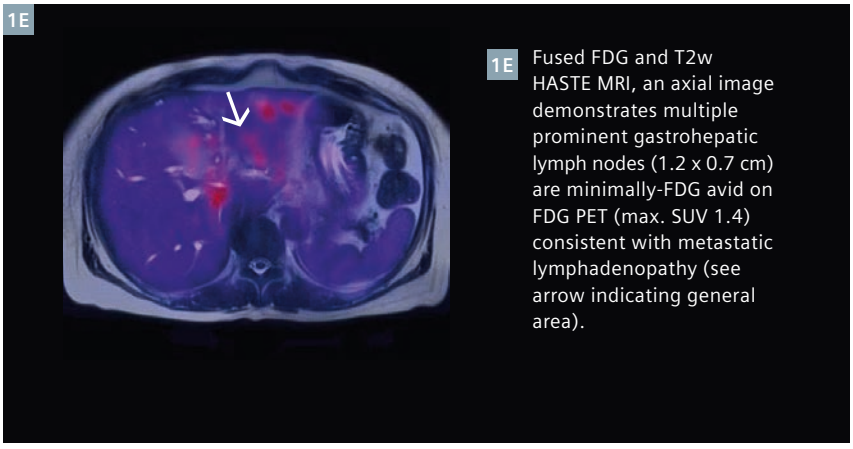

1E Fused FDG and T2w HASTE MRI, an axial image demonstrates multiple prominent gastrohepatic lymph nodes (1.2 x 0.7 cm) are minimally-FDG avid on FDG PET (max. SUV 1.4) consistent with metastatic lymphadenopathy (see arrow indicating general area).

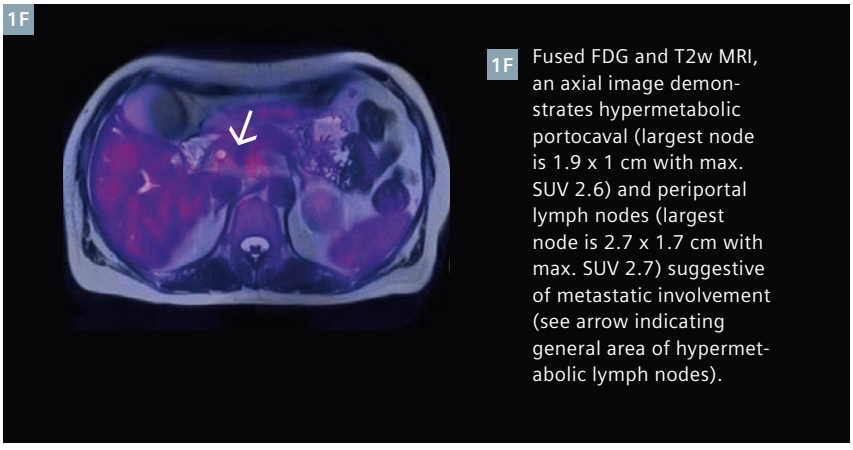

1F Fused FDG and T2w MRI, an axial image demonstrates hypermetabolic portocaval (largest node is 1.9 x 1 cm with max. SUV 2.6) and periportal lymph nodes (largest node is 2.7 x 1.7 cm with max. SUV 2.7) suggestive of metastatic involvement (see arrow indicating general area of hypermetabolic lymph nodes).

The tumor involves the biliary confluence, left main bile radical and to a lesser extent the main right biliary radical. There is mild right lobe and moderate left lobe upstream intrahepatic biliary ductal dilation peripheral to the lesion. There is also moderate intrahepatic biliary dilation of a branch draining the caudate lobe. Incidental note is made of mild concentric intra- and extra hepatic biliary wall thickening with peri-biliary enhancement consistent with cholangitis (Fig. 1D). The distal CBD measures about 0.7 cm with mural enhancement and CBS stent *in situ* (Fig. 1E).

The tumor abuts the left and right hepatic arteries just at the bifurcation (Figs. 1A-C), but the intrahepatic arterial branches are not well visualized. Tumor encases the proximal middle hepatic vein and encases and narrows the left hepatic vein, but they are patent based on contrast enhanced images. Tumor also encases and narrows the left portal vein, particularly the branch supplying the medial left hepatic lobe. The tumor does not efface or encase the patent right

portal, right anterior and right posterior portal venous branches.

Simultaneous PET/MRI also shows at least two mildly T2 hyperintense, FDG-avid enhancing hepatic lesions with restricted diffusion within segments II (max. SUV 3.4) and V (max. SUV 2.3) that are highly suspicious for metastatic sites (Figs. 1B, D).

Multiple prominent gastrohepatic lymph nodes (1.2 x 0.7 cm) are minimally-FDG avid on FDG PET (max. SUV 1.4) consistent with metastatic lymphadenopathy (Fig. 1E) There are also hypermetabolic portocaval (largest node is 1.9 x 1 cm with max. SUV 2.6) and periportal lymph nodes (largest node is 2.7 x 1.7 cm with max. SUV 2.7) also suggestive of metastatic involvement (Fig. 1F).

Diagnosis

Surgically unresectable cholangiocarcinoma (Klatskin's tumor) with hepatic metastases and regional metastatic lymphadenopathy.

Conclusion

Our case demonstrates characteristic hilar cholangiocarcinoma on FDG PET/MRI. On intial review at our institution (after biopsy and ^{18}F-FDG PET/MRI), it was classified as an unresectable hilar cholangiocarcinoma (likely stage IV and Bismuth-Corlette type IV) due to central location with likely second order bile duct involvement, presence of additional metastatic lesion in the liver, likely regional lymphatic node spread. Due to the unresectability of the tumor, this patient did not undergo any surgical intervention. The patient was started on gemcitabine and cisplatin and underwent symptomatic treatment via bile duct stenting. As of the writing of this case, her disease has unfortunately progressed while on this therapy.

Cholangiocarcinoma is a relatively rare cancer with a poor prognosis upon diagnosis due to the high likelihood of unresectability [1]. Management of this entity is multidisciplinary and based on a multimodal approach. Cholangiocarcinoma is staged both via a TNM system and also using the Bismuth-Corlette classification. The Bismuth-Corlette classification allows the physician to get a good idea of the amount of liver that would need to be resected to excise the tumor and therefore can help determine the practical resectability of the tumor. Typically, Bismuth-Corlette type III and above tumors are considered unresectable [2]. Assessment of lymph node status and metastases is needed in order to determine resectability [3]. Allowing for pre-surgical determination of unresectability allows for avoidance of unneeded morbidity in the event that a tumor thought to be resectable before surgery is found to be unresectable during surgery [2]. It should be noted that resection of this cancer is needed to obtain even at least marginally promising outcomes.

Cholangiocarinoma presents an imaging challenge due to the abdominal soft tissue structures that must be discriminated amongst each other in a radiological image. If imaging is able to exquisitely delineate soft-tissue structures to a greater extent than with current standard of care imaging, then both decreased iatrogenic surgical patient morbidity and increased identification of disease extent can be realized. Currently, FDG PET/CT with MRI scans of specific body parts (if needed) has been of great benefit in complete assessment of malignancies. FDG PET/CT has been shown to be helpful in evaluating response to therapy, with changes in FDG-positive lesions as an accurate indication of favorable response at 12 months, irrespective of changes on MRI. Whole-body MRI, on the other hand, has been shown to be more optimally suited to assess overall disease activity. With the advent of combining FDG PET and MRI in one, particularly with simultaneous acquisition, a new gold standard 'one stop shop' scan can be performed. ^{18}F-FDG PET/MRI can show not only the overall disease activity, but it also can show a comparable assessment of treatment response when compared to other imaging modalities. ^{18}F-FDG PET/MRI has shown promise and is being used clinically at our institution for both staging and treatment decision implications. PET/MRI appears to be excellent for evaluation of soft tissue involvement of solid tumors, especially that of adjacent vital structures to enable surgical resection as well as to assess for loco-regional and systemic metastatic disease. There is significant dose reduction by omitting CT and it has the potential for increased optimization of appropriate healthcare resources.

References

1 Deoliveira ML, Cunningham SC, Cameron JL, et al. Cholangiocarcinoma: thirty-one-year experience with 564 patients at a single institution. Ann Surg. 2007;245(5):755-62.

2 Chung, Yong Eun, Myeong-Jin Kim, Young Nyun Park, Yoon-Hee Lee, and Jin-Young Choi. "Staging of extrahepatic cholangiocarcinoma." European radiology18, no. 10 (2008): 2182-2195.

3 Castellano-megías VM, Ibarrola-de andrés C, Colina-ruizdelgado F. Pathological aspects of so called "hilar cholangiocarcinoma". World J Gastrointest Oncol. 2013;5(7):159-70.

The statements by Siemens' customers presented here are based on results that were achieved in the customer's unique setting. Since there is no 'typical' hospital and many variables exist (e.g., hospital size, case mix, level of IT adoption), there can be no guarantee that other customers will achieve the same results.

Contact

Shetal N. Shah, M.D.
Cleveland Clinic Main Campus
Diagnostic Radiology / Nuclear Medicine
Mail Code JB3
9500 Euclid Avenue
Cleveland, OH 44195
USA
Phone: +1 216.445.8168

HIGHLIGHTS OF PRESCRIBING INFORMATION

These highlights do not include all the information needed to use Fludeoxyglucose F 18 Injection safely and effectively. See full prescribing information for Fludeoxyglucose F 18 Injection.
Fludeoxyglucose F 18 Injection, USP
For intravenous use
Initial U.S. Approval: 2005

RECENT MAJOR CHANGES

Warnings and Precautions (5.1, 5.2)	7/2010
Adverse Reactions (6)	7/2010

INDICATIONS AND USAGE

Fludeoxyglucose F18 Injection is indicated for positron emission tomography (PET) imaging in the following settings:

- Oncology: For assessment of abnormal glucose metabolism to assist in the evaluation of malignancy in patients with known or suspected abnormalities found by other testing modalities, or in patients with an existing diagnosis of cancer.
- Cardiology: For the identification of left ventricular myocardium with residual glucose metabolism and reversible loss of systolic function in patients with coronary artery disease and left ventricular dysfunction, when used together with myocardial perfusion imaging.
- Neurology: For the identification of regions of abnormal glucose metabolism associated with foci of epileptic seizures (1).

DOSAGE AND ADMINISTRATION

Fludeoxyglucose F 18 Injection emits radiation. Use procedures to minimize radiation exposure. Screen for blood glucose abnormalities.

- In the oncology and neurology settings, instruct patients to fast for 4 to 6 hours prior to the drug's injection. Consider medical therapy and laboratory testing to assure at least two days of normoglycemia prior to the drug's administration (5.2).
- In the cardiology setting, administration of glucose-containing food or liquids (e.g., 50 to 75 grams) prior to the drug's injection facilitates localization of cardiac ischemia (2.3).

Aseptically withdraw Fludeoxyglucose F 18 Injection from its container and administer by intravenous injection (2).

The recommended dose:

- for adults is 5 to 10 mCi (185 to 370 MBq), in all indicated clinical settings (2.1).
- for pediatric patients is 2.6 mCi in the neurology setting (2.2).

Initiate imaging within 40 minutes following drug injection; acquire static emission images 30 to 100 minutes from time of injection (2).

DOSAGE FORMS AND STRENGTHS

Multi-dose 30mL and 50mL glass vial containing 0.74 to 7.40 GBq/mL (20 to 200 mCi/mL) Fludeoxyglucose F 18 Injection and 4.5mg of sodium chloride with 0.1 to 0.5% w/w ethanol as a stabilizer (approximately 15 to 50 mL volume) for intravenous administration (3).

CONTRAINDICATIONS

None

WARNINGS AND PRECAUTIONS

- Radiation risks: use smallest dose necessary for imaging (5.1).
- Blood glucose adnormalities: may cause suboptimal imaging (5.2).

ADVERSE REACTIONS

Hypersensitivity reactions have occurred; have emergency resuscitation equipment and personnel immediately available (6).
To report SUSPECTED ADVERSE REACTIONS, contact PETNET Solutions, Inc. at 877-473-8638 or FDA at 1-800-FDA-1088 or www.fda.gov/medwatch.

USE IN SPECIFIC POPULATIONS

Pregnancy Category C: No human or animal data. Consider alternative diagnostics; use only if clearly needed (8.1).

- Nursing mothers: Use alternatives to breast feeding (e.g., stored breast milk or infant formula) for at least 10 half-lives of radioactive decay, if Fludeoxyglucose F 18 Injection is administered to a woman who is breast-feeding (8.3).
- Pediatric Use: Safety and effectiveness in pediatric patients have not been established in the oncology and cardiology settings (8.4).

See 17 for PATIENT COUNSELING INFORMATION

Revised: 1/2011

FULL PRESCRIBING INFORMATION: CONTENTS*

1 INDICATIONS AND USAGE
1.1 Oncology
1.2 Cardiology
1.3 Neurology
2 DOSAGE AND ADMINISTRATION
2.1 Recommended Dose for Adults
2.2 Recommended Dose for Pediatric Patients
2.3 Patient Preparation
2.4 Radiation Dosimetry
2.5 Radiation Safety – Drug Handling
2.6 Drug Preparation and Administration
2.7 Imaging Guidelines
3 DOSAGE FORMS AND STRENGTHS
4 CONTRAINDICATIONS
5 WARNINGS AND PRECAUTIONS
5.1 Radiation Risks
5.2 Blood Glucose Abnormalities
6 ADVERSE REACTIONS
7 DRUG INTERACTIONS
8 USE IN SPECIFIC POPULATIONS
8.1 Pregnancy
8.3 Nursing Mothers
8.4 Pediatric Use
11 DESCRIPTION
11.1 Chemical Characteristics
11.2 Physical Characteristics
12 CLINICAL PHARMACOLOGY
12.1 Mechanism of Action
12.2 Pharmacodynamics
12.3 Pharmacokinetics
13 NONCLINICAL TOXICOLOGY
13.1 Carcinogenesis, Muta-genesis, Impairment of Fertility
14 CLINICAL STUDIES
14.1 Oncology
14.2 Cardiology
14.3 Neurology
15 REFERENCES
16 HOW SUPPLIED/STORAGE AND DRUG HANDLING
17 PATIENT COUNSELING INFORMATION

* Sections or subsections omitted from the full prescribing information are not listed.

FULL PRESCRIBING INFORMATION

1 INDICATIONS AND USAGE

Fludeoxyglucose F 18 Injection is indicated for positron emission tomography (PET) imaging in the following settings:

1.1 Oncology

For assessment of abnormal glucose metabolism to assist in the evaluation of malignancy in patients with known or suspected abnormalities found by other testing modalities, or in patients with an existing diagnosis of cancer.

1.2 Cardiology

For the identification of left ventricular myocardium with residual glucose metabolism and reversible loss of systolic function in patients with coronary artery disease and left ventricular dysfunction, when used together with myocardial perfusion imaging.

1.3 Neurology

For the identification of regions of abnormal glucose metabolism associated with foci of epileptic seizures.

2 DOSAGE AND ADMINISTRATION

Fludeoxyglucose F 18 Injection emits radiation. Use procedures to minimize radiation exposure. Calculate the final dose from the end of synthesis (EOS) time using proper radioactive decay factors. Assay the final dose in a properly calibrated dose calibrator before administration to the patient [see Description (11.2)].

2.1 Recommended Dose for Adults

Within the oncology, cardiology and neurology settings, the recommended dose for adults is 5 to 10 mCi (185 to 370 MBq) as an intravenous injection.

2.2 Recommended Dose for Pediatric Patients

Within the neurology setting, the recommended dose for pediatric patients is 2.6 mCi, as an intravenous injection. The optimal dose adjustment on the basis of body size or weight has not been determined [see Use in Special Populations (8.4)].

2.3 Patient Preparation

- To minimize the radiation absorbed dose to the bladder, encourage adequate hydration. Encourage the patient to drink water or other fluids (as tolerated) in the 4 hours before their PET study.
- Encourage the patient to void as soon as the imaging study is completed and as often as possible thereafter for at least one hour.
- Screen patients for clinically significant blood glucose abnormalities by obtaining a history and/or laboratory tests [see Warnings and Precautions (5.2)]. Prior to Fludeoxyglucose F 18 PET imaging in the oncology and neurology settings, instruct patient to fast for 4 to 6 hours prior to the drug's injection.
- In the cardiology setting, administration of glucose-containing food or liquids (e.g., 50 to 75 grams) prior to Fludeoxyglucose F18 Injection facilitates localization of cardiac ischemia

2.4 Radiation Dosimetry

The estimated human absorbed radiation doses (rem/mCi) to a newborn (3.4 kg), 1-year old (9.8 kg), 5-year old (19 kg), 10-year old (32 kg), 15-year old (57 kg), and adult (70 kg) from intravenous administration of Fludeoxyglucose F 18 Injection are shown in Table 1. These estimates were calculated based on human[2] data and using the data published by the International Commission on Radiological Protection[4] for Fludeoxyglucose ^{18} F. The dosimetry data show that there are slight variations in absorbed radiation dose for various organs in each of the age groups. These dissimilarities in absorbed radiation dose are due to developmental age variations (e.g., organ size, location, and overall metabolic rate for each age group). The identified critical organs (in descending order) across all age groups evaluated are the urinary bladder, heart, pancreas, spleen, and lungs.

Table 1. Estimated Absorbed Radiation Doses (rem/mCi) After Intravenous Administration of Fludeoxyglucose F-18 Injection[a]

Organ	Newborn (3.4 kg)	1-year old (9.8 kg)	5-year old (19 kg)	10-year old (32 kg)	15-year old (57 kg)	Adult (70 kg)
Bladder wall[b]	4.3	1.7	0.93	0.60	0.40	0.32
Heart wall	2.4	1.2	0.70	0.44	0.29	0.22
Pancreas	2.2	0.68	0.33	0.25	0.13	0.096
Spleen	2.2	0.84	0.46	0.29	0.19	0.14
Lungs	0.96	0.38	0.20	0.13	0.092	0.064
Kidneys	0.81	0.34	0.19	0.13	0.089	0.074
Ovaries	0.80	0.8	0.19	0.11	0.058	0.053
Uterus	0.79	0.35	0.19	0.12	0.076	0.062
LLI wall *	0.69	0.28	0.15	0.097	0.060	0.051
Liver	0.69	0.31	0.17	0.11	0.076	0.058
Gallbladder wall	0.69	0.26	0.14	0.093	0.059	0.049
Small intestine	0.68	0.29	0.15	0.096	0.060	0.047
ULI wall **	0.67	0.27	0.15	0.090	0.057	0.046
Stomach wall	0.65	0.27	0.14	0.089	0.057	0.047
Adrenals	0.65	0.28	0.15	0.095	0.061	0.048
Testes	0.64	0.27	0.14	0.085	0.052	0.041
Red marrow	0.62	0.26	0.14	0.089	0.057	0.047
Thymus	0.61	0.26	0.14	0.086	0.056	0.044
Thyroid	0.61	0.26	0.13	0.080	0.049	0.039
Muscle	0.58	0.25	0.13	0.078	0.049	0.039
Bone surface	0.57	0.24	0.12	0.079	0.052	0.041
Breast	0.54	0.22	0.11	0.068	0.043	0.034
Skin	0.49	0.20	0.10	0.060	0.037	0.030
Brain	0.29	0.13	0.09	0.078	0.072	0.070
Other tissues	0.59	0.25	0.13	0.083	0.052	0.042

[a] MIRDOSE 2 software was used to calculate the radiation absorbed dose. Assumptions on the biodistribution based on data from Gallagher et al.1 and Jones et al.2

[b] The dynamic bladder model with a uniform voiding frequency of 1.5 hours was used. *LLI = lower large intestine; **ULI = upper large intestine

2.5 Radiation Safety – Drug Handling

- Use waterproof gloves, effective radiation shielding, and appropriate safety measures when handling Fludeoxyglucose F 18 Injection to avoid unnecessary radiation exposure to the patient, occupational workers, clinical personnel and other persons.
- Radiopharmaceuticals should be used by or under the control of physicians who are qualified by specific training and experience in the safe use and handling of radionuclides, and whose experience and training have been approved by the appropriate governmental agency authorized to license the use of radionuclides.
- Calculate the final dose from the end of synthesis (EOS) time using proper radioactive decay factors. Assay the final dose in a properly calibrated dose calibrator before administration to the patient [see Description (11.2)].
- The dose of Fludeoxyglucose F 18 used in a given patient should be minimized consistent with the objectives of the procedure, and the nature of the radiation detection devices employed.

2.6 Drug Preparation and Administration

- Calculate the necessary volume to administer based on calibration time and dose.
- Aseptically withdraw Fludeoxyglucose F 18 Injection from its container.
- Inspect Fludeoxyglucose F 18 Injection visually for particulate matter and discoloration before administration, whenever solution and container permit.
- Do not administer the drug if it contains particulate matter or discoloration; dispose of these unacceptable or unused preparations in a safe manner, in compliance with applicable regulations.
- Use Fludeoxyglucose F 18 Injection within 12 hours from the EOS.

2.7 Imaging Guidelines

- Initiate imaging within 40 minutes following Fludeoxyglucose F 18 Injection administration.
- Acquire static emission images 30 to 100 minutes from the time of injection.

3 DOSAGE FORMS AND STRENGTHS

Multiple-dose 30 mL and 50 mL glass vial containing 0.74 to 7.40 GBq/mL (20 to 200 mCi/mL) of Fludeoxyglucose F 18 Injection and 4.5 mg of sodium chloride with 0.1 to 0.5% w/w ethanol as a stabilizer (approximately 15 to 50 mL volume) for intravenous administration.

4 CONTRAINDICATIONS

None

5 WARNINGS AND PRECAUTIONS

5.1 Radiation Risks

Radiation-emitting products, including Fludeoxyglucose F 18 Injection, may increase the risk for cancer, especially in pediatric patients. Use the smallest dose necessary for imaging and ensure safe handling to protect the patient and health care worker [see Dosage and Administration (2.5)].

5.2 Blood Glucose Abnormalities

In the oncology and neurology setting, suboptimal imaging may occur in patients with inadequately regulated blood glucose levels. In these patients, consider medical therapy and laboratory testing to assure at least two days of normoglycemia prior to Fludeoxyglucose F 18 Injection administration.

6 ADVERSE REACTIONS

Hypersensitivity reactions with pruritus, edema and rash have been reported in the post-marketing setting. Have emergency resuscitation equipment and personnel immediately available.

7 DRUG INTERACTIONS

The possibility of interactions of Fludeoxyglucose F 18 Injection with other drugs taken by patients undergoing PET imaging has not been studied.

8 USE IN SPECIFIC POPULATIONS

8.1 Pregnancy

Pregnancy Category C

Animal reproduction studies have not been conducted with Fludeoxyglucose F 18 Injection. It is also not known whether Fludeoxyglucose F 18 Injection can cause fetal harm when administered to a pregnant woman or can affect reproduction capacity. Consider alternative diagnostic tests in a pregnant woman; administer Fludeoxyglucose F 18 Injection only if clearly needed.

8.3 Nursing Mothers

It is not known whether Fludeoxyglucose F 18 Injection is excreted in human milk. Consider alternative diagnostic tests in women who are breast-feeding. Use alternatives to breast feeding (e.g., stored breast milk or infant formula) for at least 10 half-lives of radioactive decay, if Fludeoxyglucose F 18 Injection is administered to a woman who is breast-feeding.

8.4 Pediatric Use

The safety and effectiveness of Fludeoxyglucose F 18 Injection in pediatric patients with epilepsy is established on the basis of studies in adult and pediatric patients. In pediatric patients with epilepsy, the recommended dose is 2.6 mCi. The optimal dose adjustment on the basis of body size or weight has not been determined. In the oncology or cardiology settings, the safety and effectiveness of Fludeoxyglucose F 18 Injection have not been established in pediatric patients.

11 DESCRIPTION

11.1 Chemical Characteristics

Fludeoxyglucose F 18 Injection is a positron emitting radiopharmaceutical that is used for diagnostic purposes in conjunction with positron emission tomography (PET) imaging. The active ingredient 2-deoxy-2-[^{18}F]fluoro-D-glucose has the molecular formula of $C_6H_{11}{}^{18}FO_5$ with a molecular weight of 181.26, and has the following chemical structure:

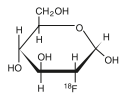

Fludeoxyglucose F 18 Injection is provided as a ready to use sterile, pyrogen free, clear, colorless solution. Each mL contains between 0.740 to 7.40GBq (20.0 to 200 mCi) of 2-deoxy-2-[^{18}F]fluoro-D-glucose at the EOS, 4.5 mg of sodium chloride and 0.1 to 0.5% w/w ethanol as a stabilizer. The pH of the solution is between 4.5 and 7.5. The solution is packaged in a multiple-dose glass vial and does not contain any preservative.

11.2 Physical Characteristics

Fluorine F 18 decays by emitting positron to Oxygen O 16 (stable) and has a physical half-life of 109.7 minutes. The principal photons useful for imaging are the dual 511 keV gamma photons, that are produced and emitted simultaneously in opposite direction when the positron interacts with an electron (Table 2).

Table 2. Pricipal Radiation Emission Data for Fluorine F18

Radiation/Emission	% Per Disintegration	Mean Energy
Positron (b+)	96.73	249.8 keV
Gamma (±)*	193.46	511.0 keV

*Produced by positron annihilation

From: Kocher, D.C. Radioactive Decay Tables DOE/TIC-I 1026, 89 (1981)

The specific gamma ray constant (point source air kerma coefficient) for fluorine F 18 is 5.7 R/hr/mCi (1.35 x 10-6 Gy/hr/kBq) at 1 cm. The half-value layer (HVL) for the 511 keV photons is 4 mm lead (Pb). The range of attenuation coefficients for this radionuclide as a function of lead shield thickness is shown in Table 3. For example, the interposition of an 8 mm thickness of Pb, with a coefficient of attenuation of 0.25, will decrease the external radiation by 75%.

Table 3. Radiation Attenuation of 511 keV Photons by lead (Pb) shielding

Shield thickness (Pb) mm	Coefficient of attenuation
0	0.00
4	0.50
8	0.25
13	0.10
26	0.01
39	0.001
52	0.0001

For use in correcting for physical decay of this radionuclide, the fractions remaining at selected intervals after calibration are shown in Table 4.

Table 4. Physical Decay Chart for Fluorine F18

Minutes	Fraction Remaining
0*	1.000
15	0.909
30	0.826
60	0.683
110	0.500
220	0.250

*calibration time

12 CLINICAL PHARMACOLOGY

12.1 Mechanism of Action

Fludeoxyglucose F 18 is a glucose analog that concentrates in cells that rely upon glucose as an energy source, or in cells whose dependence on glucose increases under pathophysiological conditions. Fludeoxyglucose F 18 is transported through the cell membrane by facilitative glucose transporter proteins and is phosphorylated within the cell to [18F] FDG-6-phosphate by the enzyme hexokinase. Once phosphorylated it cannot exit until it is dephosphorylated by glucose-6-phosphatase. Therefore, within a given tissue or pathophysiological process, the retention and clearance of Fludeoxyglucose F 18 reflect a balance involving glucose transporter, hexokinase and glucose-6-phosphatase activities. When allowance is made for the kinetic differences between glucose and Fludeoxyglucose F 18 transport and phosphorylation (expressed as the „lumped constant" ratio), Fludeoxyglucose F 18 is used to assess glucose metabolism. In comparison to background activity of the specific organ or tissue type, regions of decreased or absent uptake of Fludeoxyglucose F 18 reflect the decrease or absence of glucose metabolism. Regions of increased uptake of Fludeoxyglucose F 18 reflect greater than normal rates of glucose metabolism.

12.2 Pharmacodynamics

Fludeoxyglucose F 18 Injection is rapidly distributed to all organs of the body after intravenous administration. After background clearance of Fludeoxyglucose F 18 Injection, optimal PET imaging is generally achieved between 30 to 40 minutes after administration.

In cancer, the cells are generally characterized by enhanced glucose metabolism partially due to (1) an increase in activity of glucose transporters, (2) an increased rate of phosphorylation activity, (3) a reduction of phosphatase activity or, (4) a dynamic alteration in the balance among all these processes. However, glucose metabolism of cancer as reflected by Fludeoxyglucose F 18 accumulation shows considerable variability. Depending on tumor type, stage, and location, Fludeoxyglucose F 18 accumulation may be increased, normal, or decreased. Also, inflammatory cells can have the same variability of uptake of Fludeoxyglucose F 18.

In the heart, under normal aerobic conditions, the myocardium meets the bulk of its energy requirements by oxidizing free fatty acids. Most of the exogenous glucose taken up by the myocyte is converted into glycogen. However, under ischemic conditions, the oxidation of free fatty acids decreases, exogenous glucose becomes the preferred myocardial sub strate, glycolysis is stimulated, and glucose taken up by the myocyte i s metabolized immediately instead of being converted into glycogen. Under these conditions, phosphorylated Fludeoxyglucose F 18 accumulates in the myocyte and can be detected with PET imaging.

In the brain, cells normally rely on aerobic metabolism. In epilepsy, the glucose metabolism varies. Generally, during a seizure, glucose metabolism increases. Interictally, the seizure focus tends to be hypometabolic.

12.3 Pharmacokinetics

Distribution: In four healthy male volunteers, receiving an intravenous administration of 30 seconds in duration, the arterial blood level profile for Fludeoxyglucose F 18 decayed triexponentially. The effective half-life ranges of the three phases were 0.2 to 0.3 minutes, 10 to 13 minutes with a mean and standard deviation (STD) of 11.6 (±) 1.1 min, and 80 to 95 minutes with a mean and STD of 88 (±) 4 min.

Plasma protein binding of Fludeoxyglucose F 18 has not been studied.

Metabolism: Fludeoxyglucose F 18 is transported into cells and phosphorylated to [^{18}F]-FDG-6- phosphate at a rate proportional to the rate of glucose utilization within that tissue. [F18]-FDG-6-phosphate presumably is metabolized to 2-deoxy-2-[F18]fluoro-6-phospho-D-mannose([F 18]FDM-6-phosphate).

Fludeoxyglucose F 18 Injection may contain several impurities (e.g., 2-deoxy-2-chloro-D-glucose (ClDG)). Biodistribution and metabolism of ClDG are presumed to be similar to Fludeoxyglucose F 18 and would be expected to result in intracellular formation of 2-deoxy-2-chloro-6-phospho-D-glucose (ClDG-6-phosphate) and 2-deoxy-2-chloro-6-phospho-D-mannose (ClDM-6-phosphate). The phosphorylated deoxyglucose compounds are dephosphorylated and the resulting compounds (FDG, FDM, ClDG, and ClDM) presumably leave cells by passive diffusion. Fludeoxyglucose F 18 and related compounds are cleared from non-cardiac tissues within 3 to 24 hours after administration. Clearance from the cardiac tissue may require more than 96 hours. Fludeoxyglucose F 18 that is not involved in glucose metabolism in any tissue is then excreted in the urine.

Elimination: Fludeoxyglucose F 18 is cleared from most tissues within 24 hours and can be eliminated from the body unchanged in the urine. Three elimination phases have been identified in the reviewed literature. Within 33 minutes, a mean of 3.9% of the administrated radioactive dose was measured in the urine. The amount of radiation exposure of the urinary bladder at two hours post-administration suggests that 20.6% (mean) of the radioactive dose was present in the bladder.

Special Populations:

The pharmacokinetics of Fludeoxyglucose F 18 Injection have not been studied in renally-impaired, hepatically impaired or pediatric patients. Fludeoxyglucose F 18 is eliminated through the renal system. Avoid excessive radiation exposure to this organ system and adjacent tissues.

The effects of fasting, varying blood sugar levels, conditions of glucose intolerance, and diabetes mellitus on Fludeoxyglucose F 18 distribution in humans have not been ascertained [see Warnings and Precautions (5.2)].

13 NONCLINICAL TOXICOLOGY

13.1 Carcinogenesis, Mutagenesis, Impairment of Fertility

Animal studies have not been performed to evaluate the Fludeoxyglucose F 18 Injection carcinogenic potential, mutagenic potential or effects on fertility.

14 CLINICAL STUDIES

14.1 Oncology

The efficacy of Fludeoxyglucose F 18 Injection in positron emission tomography cancer imaging was demonstrated in 16 independent studies. These studies prospectively evaluated the use of Fludeoxyglucose F 18 in patients with suspected or known malignancies, including non-small cell lung cancer, colo-rectal, pancreatic, breast, thyroid, melanoma, Hodgkin's and non-Hodgkin's lymphoma, and various types of metastatic cancers to lung, liver, bone, and axillary nodes. All these studies had at least 50 patients and used pathology as a standard of truth. The Fludeoxyglucose F 18 Injection doses in the studies ranged from 200 MBq to 740 MBq with a median and mean dose of 370 MBq.

In the studies, the diagnostic performance of Fludeoxyglucose F 18 Injection varied with the type of cancer, size of cancer, and other clinical conditions. False negative and false positive scans were observed. Negative Fludeoxyglucose F 18 Injection PET scans do not exclude the diagnosis of cancer. Positive Fludeoxyglucose F 18 Injection PET scans can not replace pathology to establish a diagnosis of cancer. Non-malignant conditions such as fungal infections, inflammatory processes and benign tumors have patterns of increased glucose metabolism that may give rise to false-positive scans. The efficacy of Fludeoxyglucose F 18 Injection PET imaging in cancer screening was not studied.

14.2 Cardiology

The efficacy of Fludeoxyglucose F 18 Injection for cardiac use was demonstrated in ten independent, prospective studies of patients with coronary artery disease and chronic left ventricular systolic dysfunction who were scheduled to undergo coronary revascularization. Before revascularization, patients underwent PET imaging with Fludeoxyglucose F 18 Injection (74 to 370 MBq, 2 to 10 mCi) and perfusion imaging with other diagnostic radiopharmaceuticals. Doses of Fludeoxyglucose F 18 Injection ranged from 74 to 370 MBq (2 to 10 mCi). Segmental, left ventricular, wall-motion assessments of asynergic areas made before revascularization were compared in a blinded manner to assessments made after successful revascularization to identify myocardial segments with functional recovery.

Left ventricular myocardial segments were predicted to have reversible loss of systolic function if they showed Fludeoxyglucose F 18 accumulation and reduced perfusion (i.e., flow-metabolism mismatch). Conversely, myocardial segments were predicted to have irreversible loss of systolic function if they showed reductions in both Fludeoxyglucose F 18 accumulation and perfusion (i.e., matched defects).

Findings of flow-metabolism mismatch in a myocardial segment may suggest that successful revascularization will restore myocardial function in that segment. However, false-positive tests occur regularly, and the decision to have a patient undergo revascularization should not be based on PET findings alone. Similarly, findings of a matched defect in a myocardial segment may suggest that myocardial function will not recover in that segment, even if it is successfully revascularized. However, false-negative tests occur regularly, and the decision to recommend against coronary revascularization, or to recommend a cardiac transplant, should not be based on PET findings alone. The reversibility of segmental dysfunction as predicted with Fludeoxyglucose F 18 PET imaging

depends on successful coronary revascularization. Therefore, in patients with a low likelihood of successful revascularization, the diagnostic usefulness of PET imaging with Fludeoxyglucose F 18 Injection is more limited.

14.3 Neurology

In a prospective, open label trial, Fludeoxyglucose F 18 Injection was evaluated in 86 patients with epilepsy. Each patient received a dose of Fludeoxyglucose F 18 Injection in the range of 185 to 370 MBq (5 to 10 mCi). The mean age was 16.4 years (range: 4 months to 58 years; of these, 42 patients were less than 12 years and 16 patients were less than 2 years old). Patients had a known diagnosis of complex partial epilepsy and were under evaluation for surgical treatment of their seizure disorder. Seizure foci had been previously identified on ictal EEGs and sphenoidal EEGs. Fludeoxyglucose F 18 Injection PET imaging confirmed previous diagnostic findings in 16% (14/87) of the patients; in 34% (30/87) of the patients, Fludeoxyglucose F 18 Injection PET images provided new findings. In 32% (27/87), imaging with Fludeoxyglucose F 18 Injection was inconclusive. The impact of these imaging findings on clinical outcomes is not known.

Several other studies comparing imaging with Fludeoxyglucose F 18 Injection results to subsphenoidal EEG, MRI and/or surgical findings supported the concept that the degree of hypometabolism corresponds to areas of confirmed epileptogenic foci. The safety and effectiveness of Fludeoxyglucose F 18 Injection to distinguish idiopathic epileptogenic foci from tumors or other brain lesions that may cause seizures have not been established.

15 REFERENCES

1. Gallagher B.M., Ansari A., Atkins H., Casella V., Christman D.R., Fowler J.S., Ido T., MacGregor R.R., Som P., Wan C.N., Wolf A.P., Kuhl D.E., and Reivich M. "Radiopharmaceuticals XXVII. 18F-labeled 2-deoxy-2-fluoro-d-glucose as a radiopharmaceutical for measuring regional myocardial glucose metabolism in vivo: tissue distribution and imaging studies in animals," J Nucl Med, 1977; 18, 990-6.
2. Jones S.C., Alavi, A., Christman D., Montanez, I., Wolf, A.P., and Reivich M. "The radiation dosimetry of 2 [F-18] fluoro-2-deoxy-D-glucose in man," J Nucl Med, 1982; 23, 613-617.
3. Kocher, D.C. "Radioactive Decay Tables: A handbook of decay data for application to radiation dosimetry and radiological assessments," 1981, DOE/TIC-I 1026, 89.
4. ICRP Publication 53, Volume 18, No. I-4,1987, pages 75-76.

16 HOW SUPPLIED/STORAGE AND DRUG HANDLING

Fludeoxyglucose F 18 Injection is supplied in a multi-dose, capped 30 mL and 50 mL glass vial containing between 0.740 to 7.40 GBq/mL (20 to 200 mCi/mL), of no carrier added 2-deoxy-2-[F 18] fluoro-D-glucose, at end of synthesis, in approximately 15 to 50 mL. The contents of each vial are sterile, pyrogen-free and preservative-free.

NDC 40028-511-30; 40028-511-50

Receipt, transfer, handling, possession, or use of this product is subject to the radioactive material regulations and licensing requirements of the U.S. Nuclear Regulatory Commission, Agreement States or Licensing States as appropriate.

Store the Fludeoxyglucose F 18 Injection vial upright in a lead shielded container at 25°C (77°F); excursions permitted to 15-30°C (59-86°F).

Store and dispose of Fludeoxyglucose F 18 Injection in accordance with the regulations and a general license, or its equivalent, of an Agreement State or a Licensing State.

The expiration date and time are provided on the container label. Use Fludeoxyglucose F 18 Injection within 12 hours from the EOS time.

17 PATIENT COUNSELING INFORMATION

Instruct patients in procedures that increase renal clearance of radioactivity.

Encourage patients to:

- drink water or other fluids (as tolerated) in the 4 hours before their PET study.
- void as soon as the imaging study is completed and as often as possible thereafter for at least one hour.

Manufactured by: PETNET Solutions Inc.
810 Innovation Drive
Knoxville, TN 37932

Distributed by: PETNET Solutions Inc.
810 Innovation Drive
Knoxville, TN 37932

PETNET Solutions

PN0002262 Rev. A

March 1, 2011

Indications

Fludeoxyglucose F^{18} Injection is indicated for positron emission tomography (PET) imaging in the following settings:

- **Oncology:** For assessment of abnormal glucose metabolism to assist in the evaluation of malignancy in patients with known or suspected abnormalities found by other testing modalities, or in patients with an existing diagnosis of cancer.
- **Cardiology:** For the identification of left ventricular myocardium with residual glucose metabolism and reversible loss of systolic function in patients with coronary artery disease and left ventricular dysfunction, when used together with myocardial perfusion imaging.
- **Neurology:** For the identification of regions of abnormal glucose metabolism associated with foci of epileptic seizures.

Important Safety Information

- **Radiation Risks:** Radiationemitting products, including Fludeoxyglucose F^{18} Injection, may increase the risk for cancer, especially in pediatric patients. Use the smallest dose necessary for imaging and ensure safe handling to protect the patient and healthcare worker.
- **Blood Glucose Abnormalities:** In the oncology and neurology setting, suboptimal imaging may occur in patients with inadequately regulated blood glucose levels. In these patients, consider medical therapy and laboratory testing to assure at least two days of normoglycemia prior to Fludeoxyglucose F^{18} Injection administration.
- **Adverse Reactions:** Hypersensitivity reactions with pruritus, edema and rash have been reported; have emergency resuscitation equipment and personnel immediately available.

Get your free copy of the PI-RADS Scoring Image Atlas

Visit us at
www.siemens.com/magnetom-world
Go to > Publications > Subscriptions > MRI Poster

Read the comprehensive article

"PI-RADS Classification: Structured Reporting for MRI of the Prostate"

by Matthias Röthke et al.
in MAGNETOM Flash 4/2013
page 30-38.

Available for download at
www.siemens.com/magnetom-world

SIEMENS

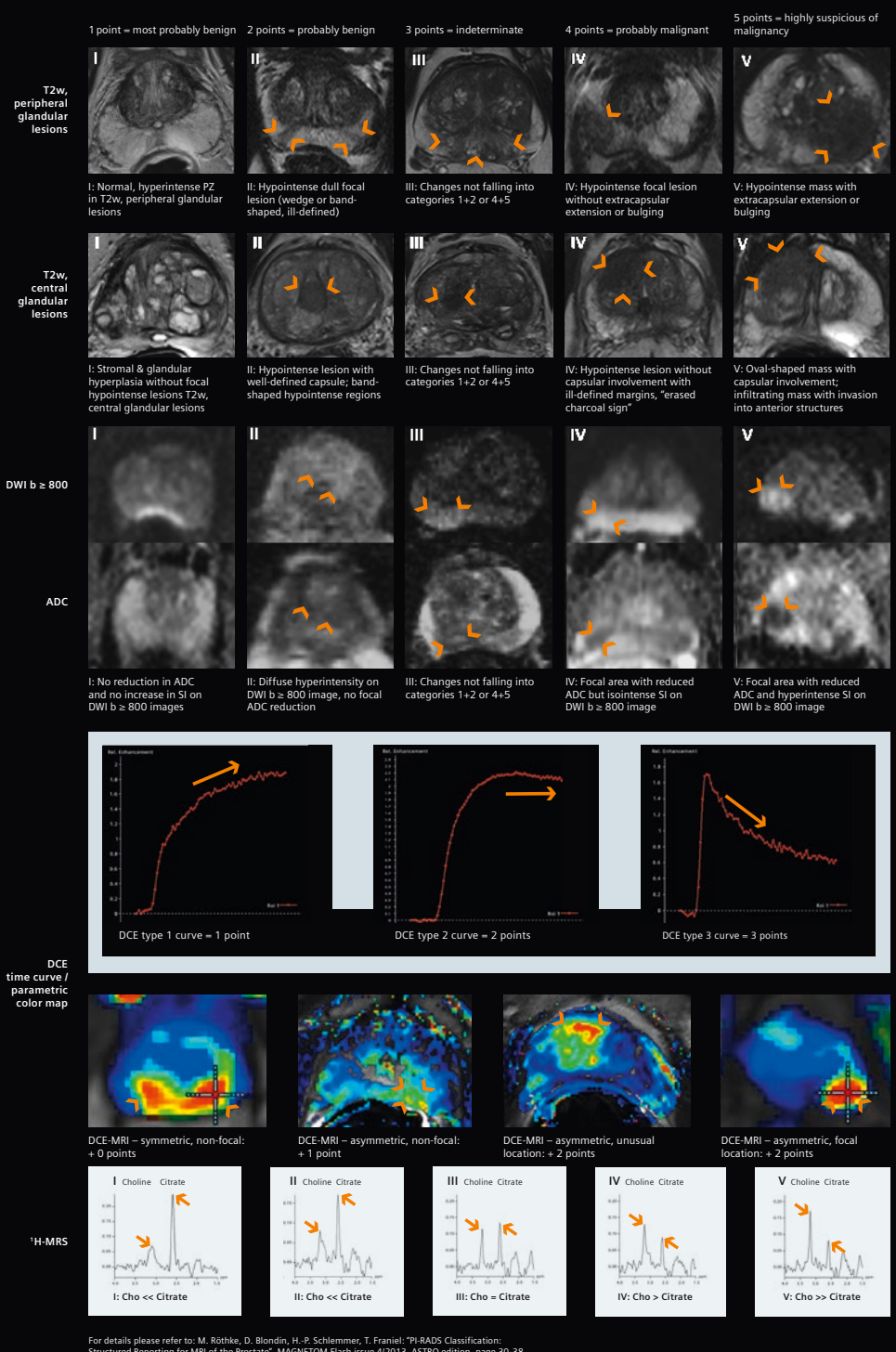

For details please refer to: M. Röthke, D. Blondin, H.-P. Schlemmer, T. Franiel: "PI-RADS Classification: Structured Reporting for MRI of the Prostate", MAGNETOM Flash issue 4/2013, ASTRO edition, page 30-38.

www.siemens.com/magnetom-world

PI-RADS SCORING Image Atlas

Prostate MRI

Answers for life.

First Experiences with the Whole-Body Dot Engine

Stephan Zangos; Daniel Alzmann; Boris Schulz; Thomas J. Vogl

Institute for Diagnostic and Interventional Radiology, University Hospital Frankfurt, Frankfurt/Main, Germany

In clinical routine, whole-body magnetic resonance (MR) imaging is highly beneficial in many scenarios, such as bone marrow alterations, infectious or rheumatic diseases, and evaluation of solid tumor spread-out. This technique reduces the need for separate, and therefore time-consuming dedicated examinations, and necessary therapy can be started earlier.

In the past, whole-body MR imaging within a single examination had not been feasible because of device-related limitations. One reason was the measurement volume of the scanner that was restricted by the number of coils and RF channels. Another reason was the repositioning of the patient and coils for a whole-body examination.

Subsequently, self-developed set-and-go protocols were used for whole-body examinations. However, this meant that all examination areas needed to be manually changed, which was time-consuming. Thus, the risk of incorrect adjustments leading to insufficient examinations increased.

With the latest scanner generation, however, such technical limitations are no longer relevant. Today, Tim 4G (Total imaging matrix technique), enables whole-body examinations of a scan range of up to 204 cm without any repositioning of the patient or coils. The patient is examined in the supine position with arms positioned tight against the body*.

Selection of dedicated coils is advisable according to the study regions: The head/neck coil, two body coils, and if necessary, the peripheral angio coil have to be positioned on top of the patient and are combined with the spine coils that are integrated in the table. In particular, the extensive use of strapped coils, especially in combination with the head/neck-coil, can cause discomfort in claustrophobic patients. Attaching the coils takes about two minutes.

Additionally, Dot (day optimizing throughput) workflow engines are available for various body regions. These are routinely used in our department, especially for neuro, spine, heart, and liver diagnostics. The Dot engines offer automatic adaptation of the study regarding anatomical and physical abilities of patients and dedicated sequences for an optimal imaging result. Because the field-of-view (FOV) is automatically adjusted, the number of slices and study region, as well as quick planning and execution of the examination, can be performed under standardized conditions. The intuitive graphical user interface of the Dot engines allows less experienced technologists to safely perform complex MR studies in our clinic.

* Please note that dangerous current loops may be generated when parts of the patient's body touch. These loops may lead to burns or increase the probability of simulations. In order to prevent potential current loops, ensure that the patient is positioned with proper distance between parts of the body.

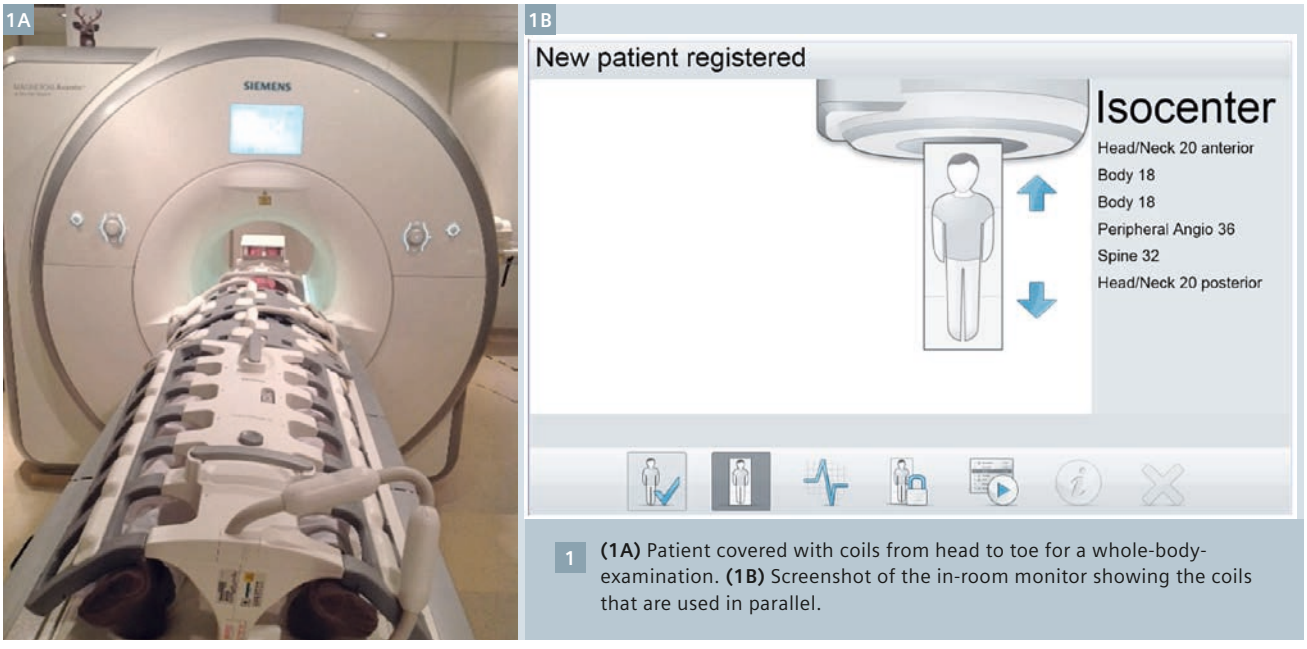

1 **(1A)** Patient covered with coils from head to toe for a whole-body-examination. **(1B)** Screenshot of the in-room monitor showing the coils that are used in parallel.

Whole-Body Dot Engine

Whereas in the past the Abdomen Dot Engine could perform auto-segmentation of only the liver, today the Whole-Body Dot Engine[1] covers a much larger examination field. It facilitates planning of multi-station examinations using extensions of the known AutoCoverage and AutoTiming mechanisms towards a multi-station examination. Once the patient is registered within the system, a fast view localizer is performed.

The localizer typically covers the anatomy from the head to the middle of the thighs and it is used to automatically segment different body regions such as chest, abdomen and pelvis. The localizer is performed with breath-holding and automatic breathhold commands. As a result of the segmentation the position and spatial extent of the different body regions are known and can be used to automatically adjust the FOV and number of slices of the multi-station examinations. The suggested coverage of the multi-station examinations is displayed in the graphical user interface of the scanner and can be modified by the technologist if necessary. The Whole-Body Dot Engine instantly estimates the optimal FOV in patients taller than 150 cm without the need for repositioning. But even with shorter patients, the study region can be easily adapted by using the graphical interface. In particular, the planning of thorax or abdomen examinations is now extremely easy and can be scheduled by the technologist intuitively in the same way as in computed tomography (CT). The simple adaptation of the study regions may significantly save time, in particular, during the planning of large study areas. Furthermore, an additional focus within a region can be chosen, and dedicated study protocols can be inserted. Multiple investigation strategies can be implemented in one protocol so that searching for the correct examination protocol in the sequence tree can be omitted. This includes, for example, dynamic examinations of the liver, MR angiography, or detailed regional study protocols to answer specific questions.

2 Screenshot showing the easy adaption of the examination coverage and the focus region using the new Whole-Body Dot Engine[1].

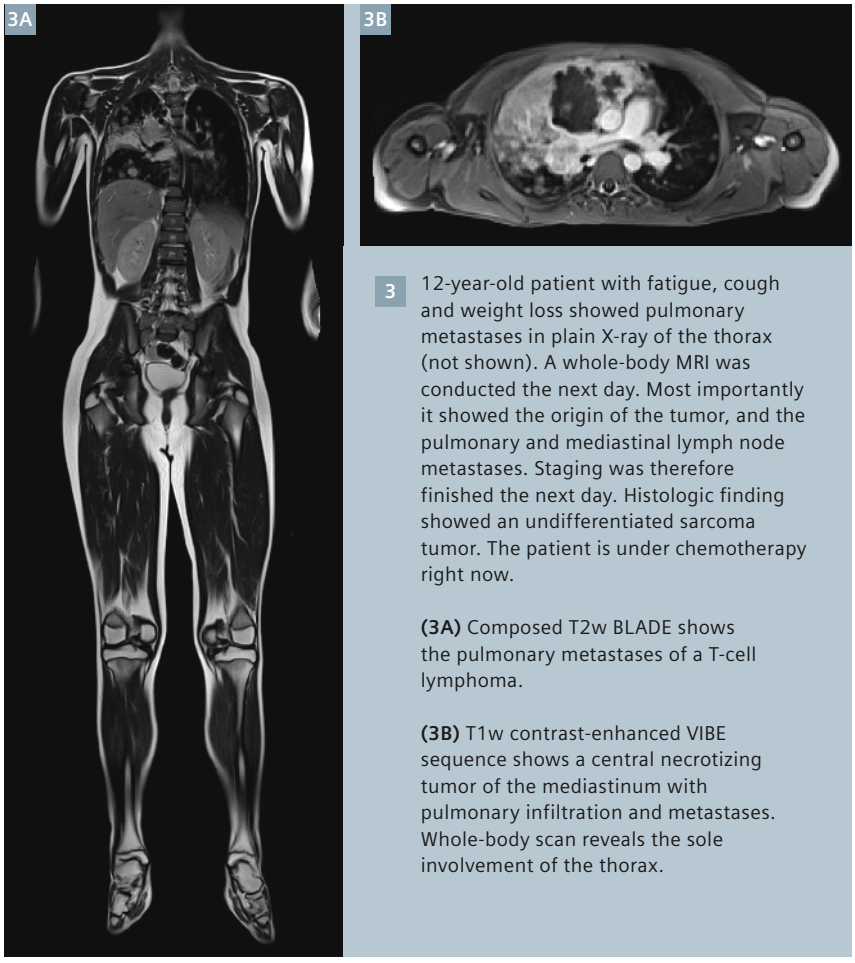

3 12-year-old patient with fatigue, cough and weight loss showed pulmonary metastases in plain X-ray of the thorax (not shown). A whole-body MRI was conducted the next day. Most importantly it showed the origin of the tumor, and the pulmonary and mediastinal lymph node metastases. Staging was therefore finished the next day. Histologic finding showed an undifferentiated sarcoma tumor. The patient is under chemotherapy right now.

(3A) Composed T2w BLADE shows the pulmonary metastases of a T-cell lymphoma.

(3B) T1w contrast-enhanced VIBE sequence shows a central necrotizing tumor of the mediastinum with pulmonary infiltration and metastases. Whole-body scan reveals the sole involvement of the thorax.

[1] WIP, the product is currently under development and is not for sale in the US and in other countries. Its future availability cannot be ensured. The product is not yet licensed for sale in Canada, in accordance with Canadian Law. Performance claims have not been reviewed by Health Canada, and are subject to change. Its future availability cannot be guaranteed.

The automatic voice commands allow an optimal scan process, ensuring the synchronized timing of breathing and scanning via breathholding techniques. Selection of language is possible, so that the

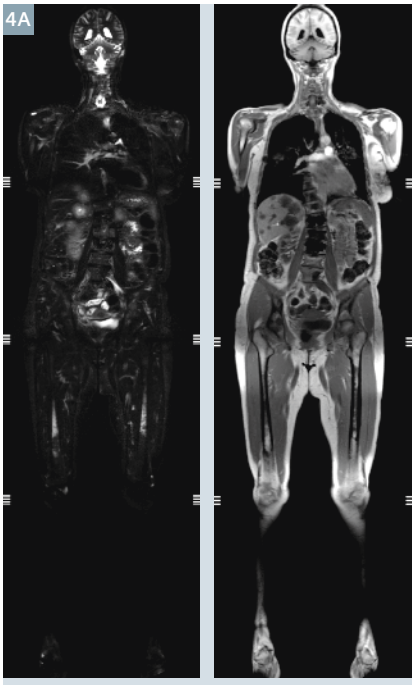

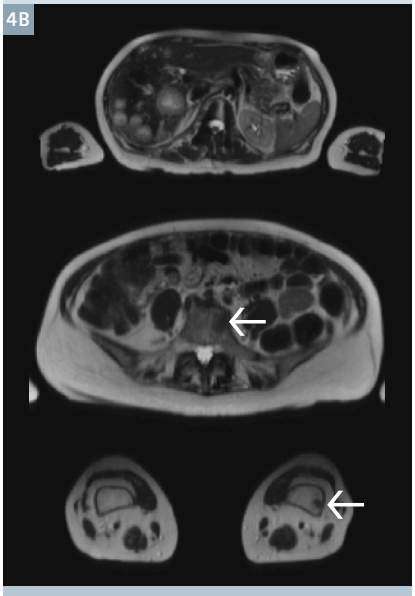

4 54-year-old female with newly diagnosed non-small cell lung cancer. Whole-body examination was performed for staging before systemic chemotherapy. These images were the basis for the follow-up after chemotherapy.

(4A) Coronal T2w HASTE TIRM and corresponding T1w FLASH sequences document liver and bone metastases in different areas.

(4B) Axial HASTE sequence shows liver and bone metastases of the lumbar vertebra and the femur.

breathing commands can be understood by all patients, thereby reducing respiratory artifacts. The timing after contrast administration is now performed in a way analogous to CT scanning by using automatic bolus detection. Therefore, image acquisition at the correct point in time for dynamic contrast phases is more reproducible.

The Whole-Body Dot Engine provides fast and robust image quality across all patients, with fewer errors or need of repeated examinations. It ensures that all stations of a multi-station examination are performed with consistent field-of-view and spatial resolution while simultaneously obeying the patient's breathhold capability. This offers more comparable results through standardization, especially for follow-up examinations. The Whole-Body Dot Engine was adapted to our specific departmental standards by inserting our routinely used and familiar sequence protocols.

Overall, the Whole-Body Dot Engine offers the technologist a much simpler and intuitive guidance, analogous to methods used in CT examinations. As a result, technologists no longer need to fear complex examinations.

Conclusion

The Whole-Body Dot Engine allows easy implementation and standardization and consistent MR imaging from head to toe. Furthermore, the study protocol performed can easily be adapted to individual clinical indications and MR-sequences.

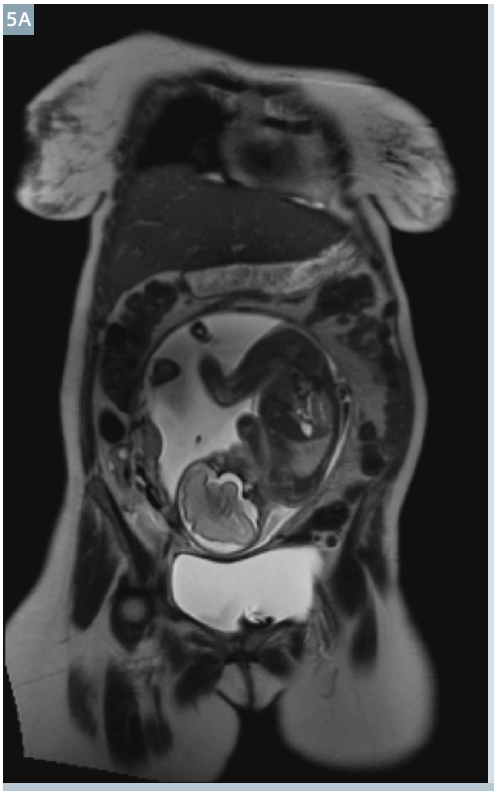

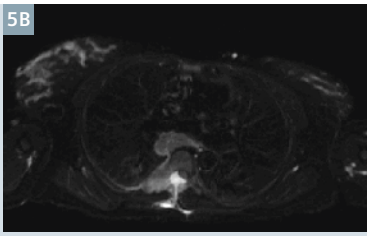

5 31-year-old female with 25 weeks gestation. The patient had a laminectomy after rapidly progressive paraparesis with spinal cord compression. Due to a still unclear histological finding whole-body MRI was performed to evaluate the spread. In the further course tuberculosis has been diagnosed and treated successfully.

(5A) Composed T2w HASTE sequence showed the current state of pregnancy with regularly developed fetus. **(5B)** Axial T2w HASTE TIRM sequence showed a residual infiltration of the costa and the posterior mediastinum. Whole-body MRI showed no further foci. **(5C)** Additionally conducted high-resolution study to assess the spine as a target region after surgery.

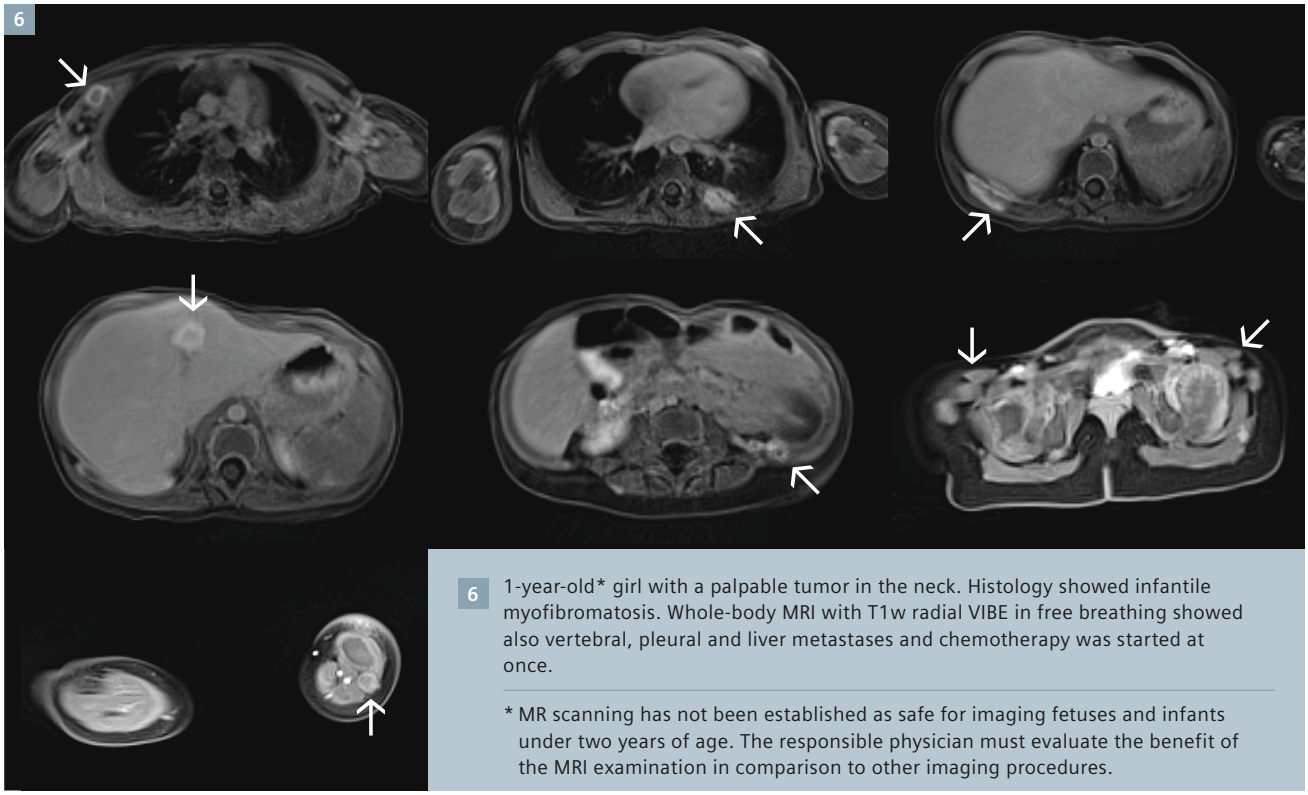

6 1-year-old* girl with a palpable tumor in the neck. Histology showed infantile myofibromatosis. Whole-body MRI with T1w radial VIBE in free breathing showed also vertebral, pleural and liver metastases and chemotherapy was started at once.

* MR scanning has not been established as safe for imaging fetuses and infants under two years of age. The responsible physician must evaluate the benefit of the MRI examination in comparison to other imaging procedures.

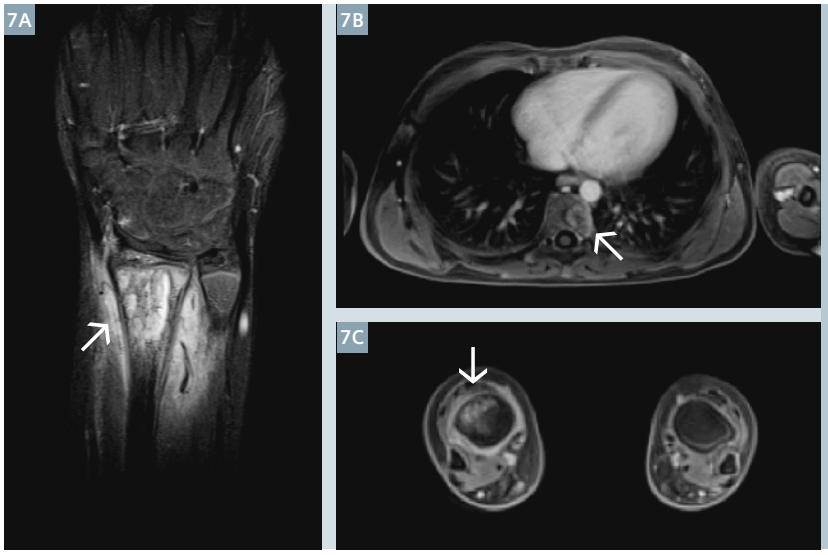

7 T1w SE FS sequence of a 10-year-old female with osteomyelitis of the radial bone of unknown origin.

Whole-body MRI with T1w radial VIBE in free breathing showed additional lesions in a vertebra **(7B)** and the right tibial bone **(7C)**. Based on the acquired images diagnosis of a chronic recurrent osteomyelitis could be made, and other foci of infect could be excluded.

Contact

Prof. Dr. med. Stephan Zangos
Institute for Diagnostic and Interventional Radiology
University Hospital Frankfurt
Theodor-Stern-Kai 7
Haus 23c
60590 Frankfurt am Main
Germany
Phone: + 49 (0)69 6301-87287
Fax: +49 (0)69 6301-7288
zangos@em.uni-frankfurt.de

Dot Configuration with the Dot Cockpit

Bart Schraa, MSc., Senior MR Application Specialist

Siemens Canada Limited, Oakville, ON, Canada

Introduction

Traditionally, protocols for patient examinations were mostly based on the expected pathology, for example in the brain: standard, MS, trauma, tumor and so on. There was a similar approach to the other body parts. Hence the protocols for each pathology were stored in a folder, in a more or less 'tree-like' structure. The image quality could be greatly hampered if patient movements were substantial, as with Parkinson's patients, or those with claustrophobia. It was up to the user to find appropriate protocols, to adjust the protocol or to find alternatives. In 2009 Siemens introduced a whole new approach to scanning patients with the release of the *syngo* MR D11 software for the MAGNETOM Aera and Skyra systems. This was the 3rd generation of automation in scanning software (see Fig. 1).

This also introduced a new way of configuring patient examinations. Before the *syngo* MR D11 software release, the set of protocols (program) used to examine a patient was solely based on the expected pathology, without taking into account the patient's condition, like level of cooperation or claustrophobia. With the introduction of Dot engines, the examination could be customized (personalized) based also on, for example, the patient's condition. With 'the flick of a switch' you could change, for example, from the standard to an uncooperative examination strategy. By using strategies within a Dot engine the exam could be easily tailored to the patient's condition if required. Furthermore, additional functionalities were introduced, such as AutoAlign in several body regions, or Auto Bolus detection. The main goals shared by the Dot engines are standardization, consistency and efficiency. All tools included in the Dot engines are designed to streamline the workflow throughout an examination.

DotGO

DotGO has been introduced in the latest release of the *syngo* MR E11 software and is based on the experiences of our customers with the Exam Explorer in the *syngo* MR software and in particular with the Dot engines in the previous software versions (D11 and D13). Standard now with the E11 software is the Dot Cockpit, which replaces the Exam Explorer. The Dot Cockpit overcomes the existing limitations of configuring patient examinations and Dot engines.

Because the initial release of the Dot engines was built on the existing Exam Explorer, there were some limitations/restrictions in the way we

1

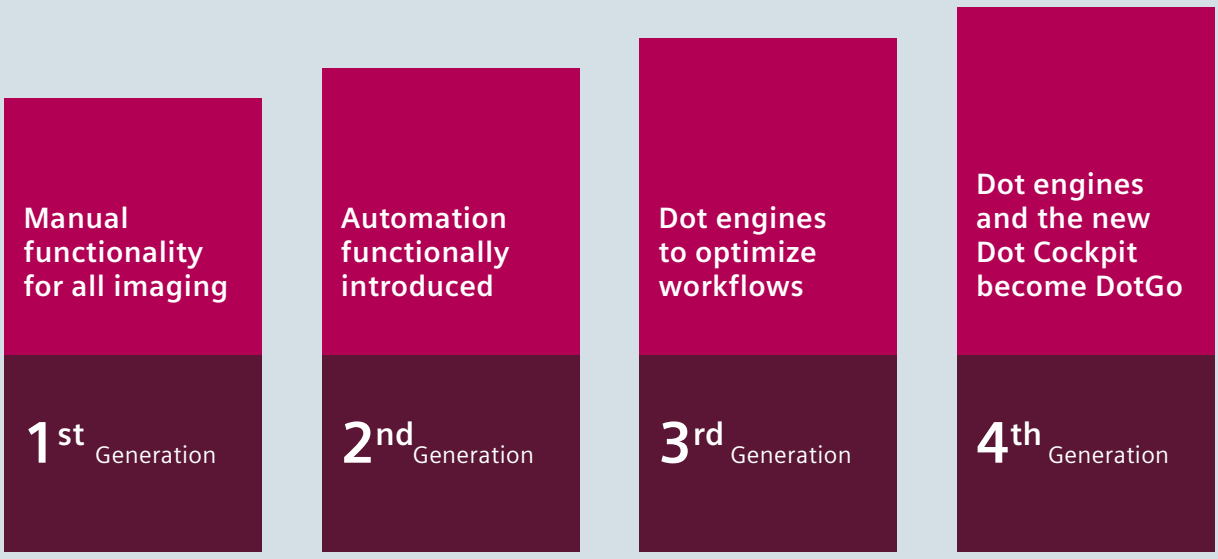

1 Generations of automation in MR.

could configure Dot engines. For many users this meant that their configuration was quite complicated and/or time consuming. Both the complexity and the time aspect have been addressed in the *syngo* MR E11 software. This article describes the way we configure Dot engines in the new E11 software as compared to the D13 software.

Dot Cockpit

The new Dot Cockpit is your central interface for all protocol management tasks. This includes flexible configuration of all Dot engines, according to your standards of care. The Dot Cockpit replaces the Exam Explorer and enables you to configure all of your MRI protocols – Dot or non-Dot protocols alike – and all of your Dot engines. You can create a Dot engine within minutes, with simple drag & drop. In the section headed "Dot configuration with *syngo* MR E11" we explain how to create a Dot engine step-by-step. But first let's briefly discuss how Dot engines were created with the *syngo* MR D13 software.

Dot Configuration with *syngo* MR D13

The steps describe the creation of the standard Brain Dot Engine as came with the 1.5T MAGNETOM Aera and 3T MAGNETOM Skyra scanners on the *syngo* MR D13 software. This standard Brain Dot Engine uses four different strategies and one patient context decision for contrast. Table 1 shows the different protocols per strategy.

These are the steps required to create such a Dot engine from the start:

1. Insert a Neuro patient view (creates the four strategies and patient context decision as described in table 1)
2. Add a Clinical Decision point called 'MPR Planning'
3. Insert six strategy branches for each protocol pre contrast (protocol 1–6)
4. Insert a Patient Context Decision for contrast administration
5. Insert a strategy branch for protocol 7–8
6. Insert a Clinical Decision called MPR Planning and attach the Dot AddIn 'MPR Planning' to it for the 3D protocols in the Resolution Focus strategy
7. Now copy all the different protocols in the respective folders
8. Attach a Generic View AddIn to all the protocols and make sure they are configured properly
9. As for the 3D protocols, make sure the MPR planning is configured properly and then assign the MPR assignment to the 3D protocols selecting the correct orientations
10. Test all the protocols in the 'simulation mode'

Table 1

Standard	Resolution Focus	Speed Focus	Motion-insensitive
AAHead_Scout	AAHead_Scout	AAHead_Scout	AAHead_Scout
t1_se_sag_320	t1_space_sag_iso	t1_fl2d_sag	t1_blade_sag_dark-fluid
t2_tse_tra_p2	t2_spc_sag_p2_iso	t2_haste_tra_p2	t2_blade_tra_p2
t2_tirm_tra_dark-fluid	t2_spc_da-fl_sag_p2_iso	t3_tirm_tra_dark-fluid_p3	t2_blade_tra_dark-fluid
ep2d_diff_3scan_trace_p2	ep2d_diff_3scan_trace_p2	ep2d_diff_3scan_trace_p2	ep2d_diff_3scan_trace_p2
t1_se_tra_320	Mpr planning for 3D	t1_fl2d_tra	t1_blade_tra_dark-fluid
contrast agent	contrast agent	contrast agent	contrast agent
t1_se_tra_320	t1_space_sag_iso	t1_fl2d_tra	t1_blade_tra_dark-fluid
t1_se_cor_320		t1_fl2d_cor	t1_blade_tra_dark-fluid

Overview protocols of the Dot engine.

2

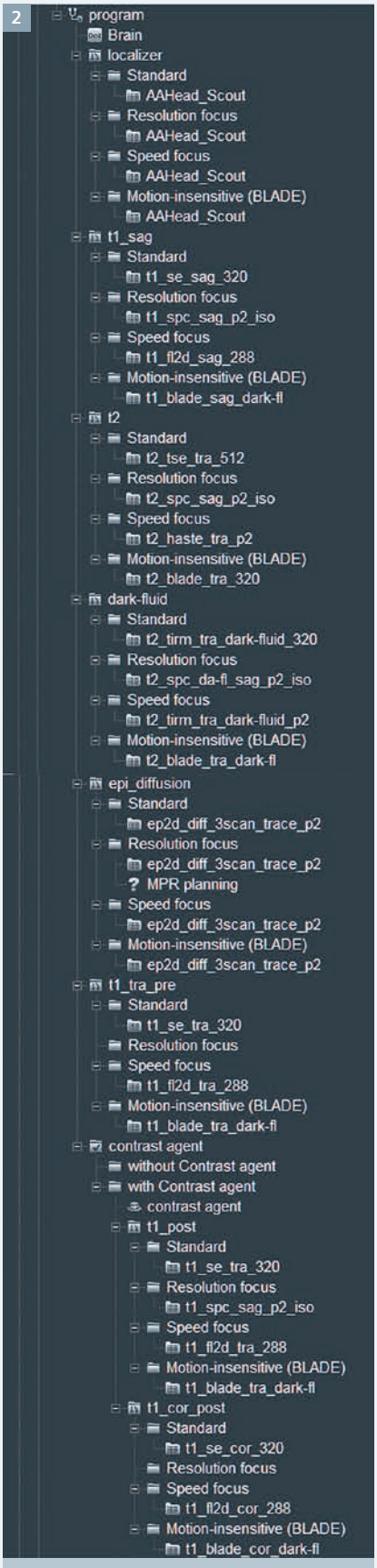

2 Overview Dot engine with *syngo* MR D13.

Figure 2 shows how the configuration would look like in the *syngo* MR D13 software.

Even for this relatively simple Dot engine it is difficult to present an easy overview of the complete Dot engine. In the next section we describe the configuration using the Dot Cockpit of software *syngo* MR E11.

Dot configuration with *syngo* MR E11

The new structogram view of the Dot Cockpit enables you to see the whole exam workflow. The different strategies, decisions, the branches and protocols are shown in a similar way as in table 1. Let's create the same Dot engine with *syngo* MR E11 as discussed in the previous section with *syngo* MR D13.

As a start we create four strategies by dragging a strategy into the program (Fig. 3), and rename the strategies 'Standard', 'Resolution focus', 'Speed focus' and 'Motion-insensitive (BLADE)'.

3

3 Inserting strategies.

4

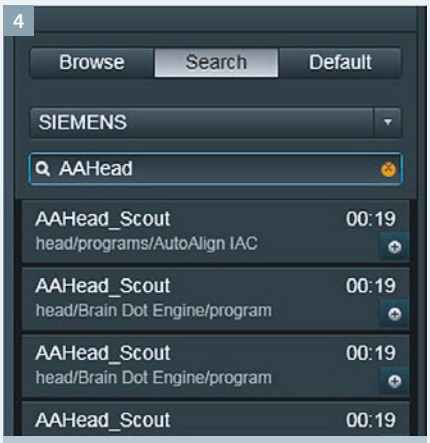

4 Using the Search functionality.

We need to insert the AAHead_Scout protocol, which can be found easily by using the built-in search functionality (Fig. 4). You can type in any string for the protocol you are looking for and it will show all protocols matching the keywords in the tree (SIEMENS) we are searching in. It will show also the program name where this protocol has been found. In this case it is AAHead for finding all the Auto Align scouts.

Now we can drag-and-drop this AAHead_Scout into the Standard strategy (Fig. 5).

5

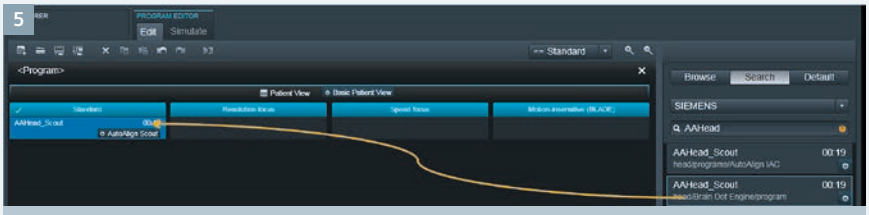

5 Drag-and-drop a protocol.

Since this is a protocol that we want to run in any of the strategies, we could use the Expand option (under the right mouse button) rather than copy the AAHead_Scout in each strategy (Fig. 6). This reduces the number of protocols in the Dot engine. The result is shown in figure 7. The AAHead_Scout is now a single protocol for all strategies. Now we can add all the other protocols (prior to contrast) into the respective strategies. This is achieved very quickly using the search option on the right side. Just by typing a few keywords, we can find the protocols that we need (Fig. 8).

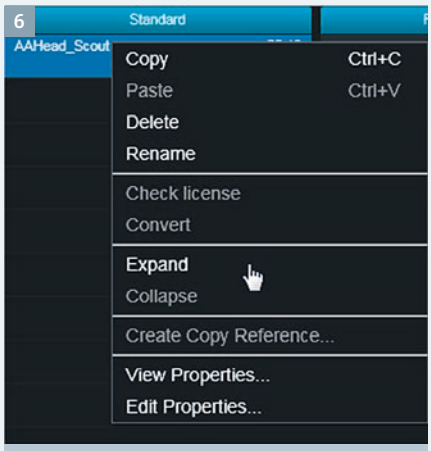

6 Expanding a protocol over all strategies.

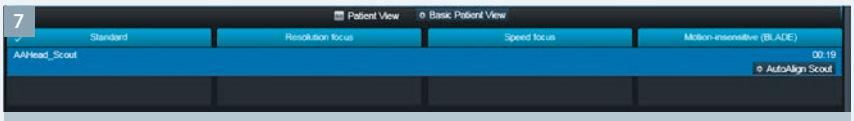

7 An expanded protocol.

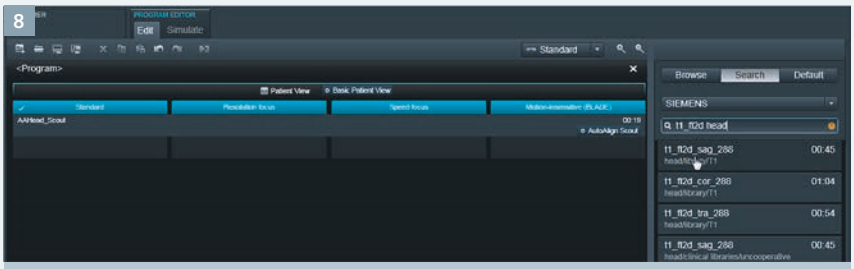

8 Searching for protocols.

After we have added all of the protocols the Dot engine looks like figure 9. Please note that the ep2d_diff_3scan_tra_p2 is also expanded since this protocol is used in all strategies just like the AAHead_Scout. In the 'Resolution focus' strategy an MPR planning has also been added. The MPR planning can be found using the Search functionality as well.

The next step in configuring the Dot engine is to configure the contrast agent administration. In *syngo* MR E11 we can also drag-and-drop decisions from another Dot engine by searching for the keywords 'head dot con', see figure 10. This contrast decision is then added to all four strategies.

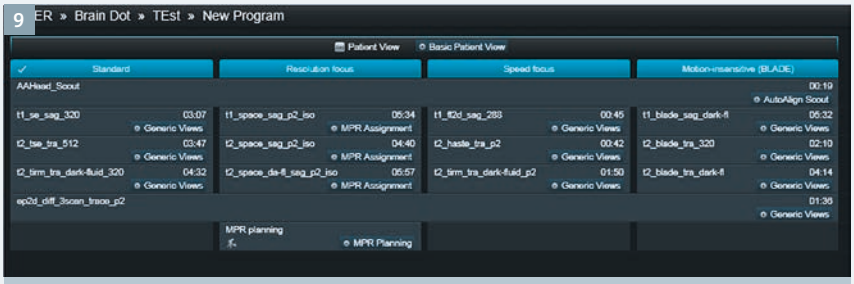

9 Dot engine configuration prior to contrast injection.

10 Searching for a decision.

After we have added the contrast decision in all four strategies, the Dot engine would look like what is shown in figure 11.

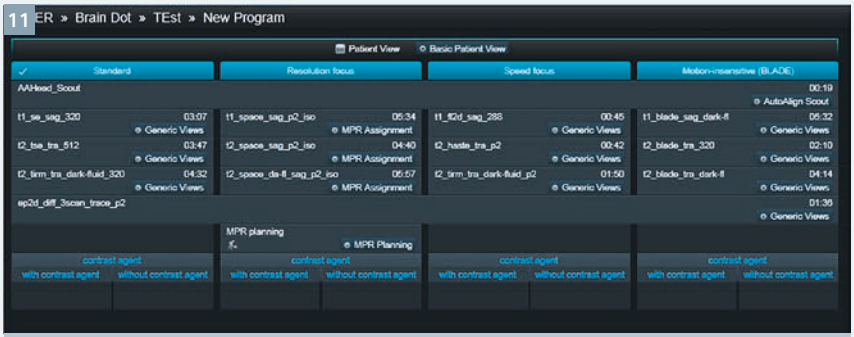

11 Dot engine with the contrast decision added.

Now that we have a contrast decision in all of the strategies, we put in the additional pre-contrast protocols, the 'inject contrast agent' pause and the post contrast protocols (Fig. 12). Please note that we leave empty 'cells' where there is no equivalent for a protocol in certain strategies, like MPR planning in the Resolution focus, but not in any of the others. Or the pre contrast t1 is not available (needed) in the 'Resolution focus' strategy, whereas there is one in all other strategies. This enables us to keep a clear overview of the Dot engine and identify the differences between the strategies.

What's left is to configure the MPR planning to have the presets that we normally want to have there, like FOV, slice thickness, spacing and the use of AutoAlign (Fig. 13).

Next, we need to select in the MPR Assignment of the 3D protocols the reconstruction that we require, in this case tra, cor or both (Fig. 14).

Now that we have configured everything we can switch to the simulation mode and see how everything will work when we select different strategies, without or with contrast selected. This can be easily controlled and viewed on the right side of the window or by selecting the strategy in the structogram including the contrast agent decision. Figure 15 shows the simulation mode for the Speed focus strategy and no contrast selected and figure 16 shows the same strategy (Speed focus) but now with the contrast selected. The structogram shows the selected strategy and protocols in a slightly brighter color than the others, whereas the right side of the screen shows which protocols would be visible in the queue, including the total time for the program.

One other feature to point out is that the Dot Cockpit recognizes which protocols have exactly the same configuration as the one we are editing. This is indicated by the "8 identical" in this case: Even if the name is different, identical protocols are found (Fig. 17). When we select this, a window on the right will appear with not only the

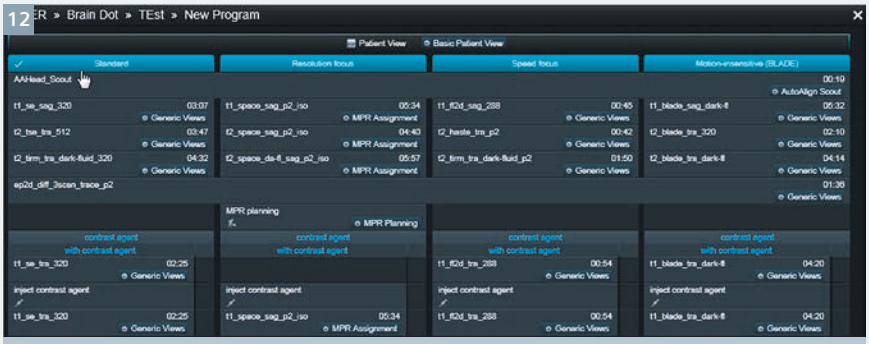

12 Dot engine with all protocols added.

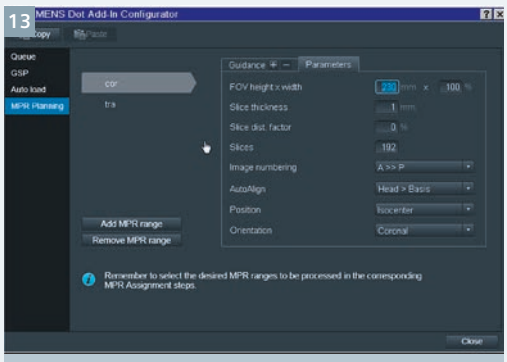

13 Configuration of the MPR planning step.

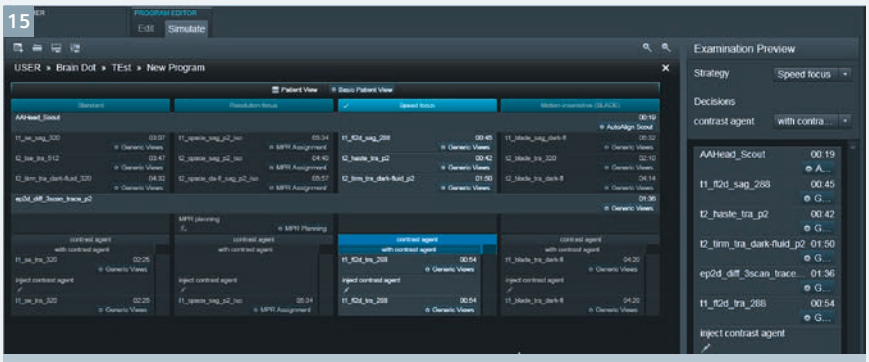

15 Simulation mode for the Speed focus strategy and no contrast selected.

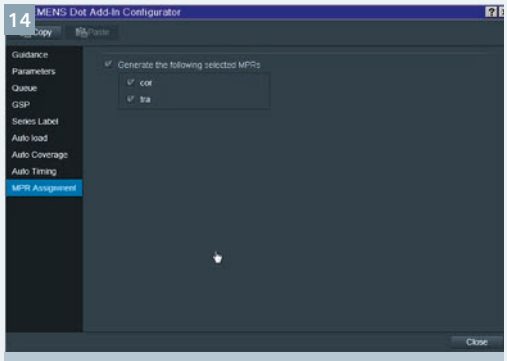

14 Configuration of the MPR assignment AddIn.

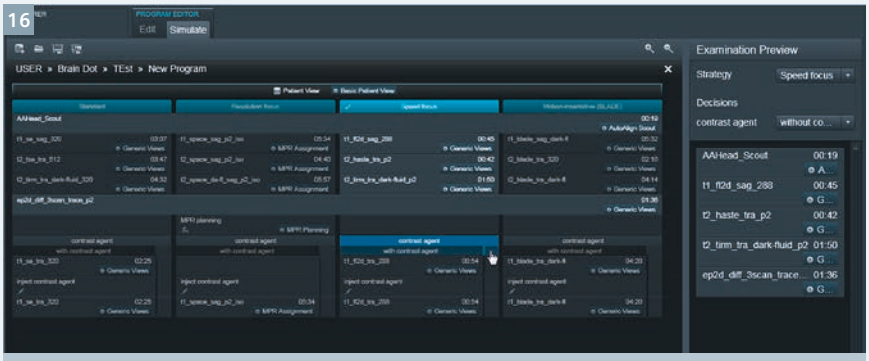

16 Simulation mode for the Speed focus strategy and with contrast selected.

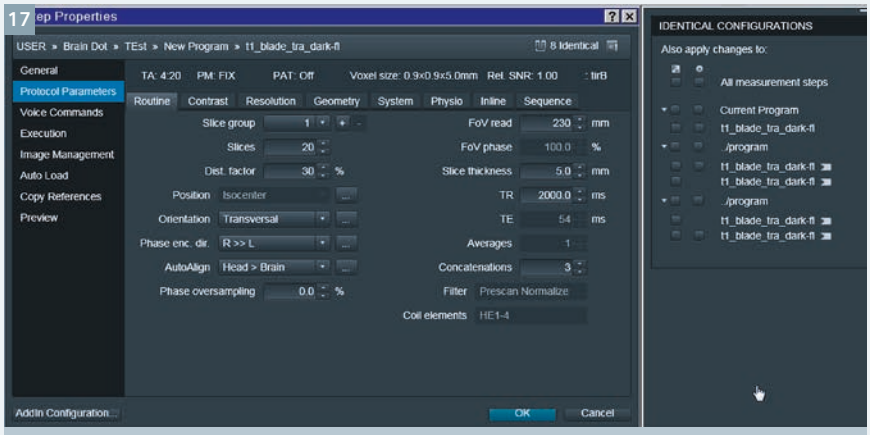

17 Identical configurations.

identical protocols (first column with checkboxes), but also the identical Dot AddIns (second column with check boxes). It could also be that whilst the protocol is identical, the Dot AddIn is not, or the protocol is different and the AddIn configuration is identical. By selecting the protocols or AddIns on the right, any changes that we make to either the protocol or the AddIn will also be applied to the selected protocols. This makes protocol management much easier and faster. Here we need to change just one protocol in order for eight other protocols and eight AddIns to be changed automatically.

Conclusion

In this article we have shown how the Dot Cockpit helps you to configure Dot engines in a much easier and faster way than before. The new Dot Cockpit allows for the creation of Dot engines within minutes. This would even allow for the creation or adjustment of Dot engines in between patients. The new structure overview gives a comprehensive overview of the complete Dot engine. In figure 18 it is shown how easy it is to obtain an overview of the entire Dot engine in *syngo* MR E11 as compared to *syngo* MR D13 (Fig. 19).

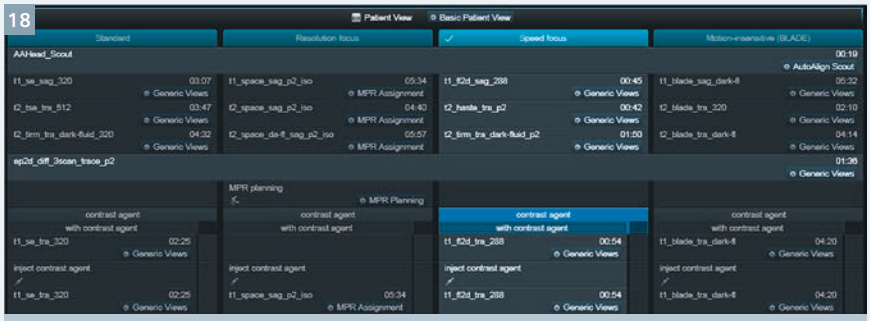

18 Dot engine overview in the *syngo* MR E11 software.

Contact

Bart Schraa
Siemens Canada Limited
HC CX NAM CA CX-CS APP
1577 North Service Road East Oakville
L6H 0H6 Oakville, ON
Canada
bart.schraa@siemens.com

19 Dot engine overview in the *syngo* MR D13 software.

fMRI Made Easy with an Integrated Siemens and NordicNeuroLab Solution

Marte Thuen, Ph.D.; Cathy Elsinger, Ph.D.

NordicNeuroLab, Bergen, Norway

BOLD fMRI is emerging as standard method of care for presurgical planning – mapping eloquent regions of the brain before brain surgery. What used to be a complicated setup available only to researchers is now available in the clinical radiology department. NordicNeuroLab provides a complete and easy-to-use fMRI solution – all necessary equipment for fMRI and nordicAktiva stimulus presentation software seamlessly integrated with the Siemens Numaris platform. This allows the user to run the paradigms directly from the Siemens Numaris interface, enhancing workflow for the MR technologist.

What is BOLD fMRI?

BOLD fMRI is the study of neuronal activity using MRI (Fig. 1). When a particular part of the brain becomes active as a response to a stimulus or task, there is increased flow of oxygen-rich blood into this region. Because of the difference in MR signal properties between the blood cells that carry oxygen compared to those that do not, this increase in blood supply can be detected using MRI. However, due to the level of sensitivity required to detect this signal difference, a specialized pulse sequence is needed on the MR scanner. This dynamic series measures the signal changes throughout the brain while a person is cued to perform a particular task. Task performance alternates with cycles of rest (20-30 seconds cycles), allowing a comparison of signal change in the brain due to the task. The description and timing of the cueing task are referred to as the fMRI paradigm.

Typical brain regions that can be mapped using fMRI are the motor cortex (finger tapping, toe movement, tongue movement), sensory regions (visual cortex, auditory cortex) and speech centers.

Why is fMRI important?

One goal of pre-operative surgical planning is to differentiate eloquent areas in the brain from pathology – those regions of the cortex in which injury produces cognitive or motor deficit – and to understand the relationship between eloquent cortex and pathology. The goal is to accurately delineate tissue pathology from surrounding eloquent cortex and vital connections between brain regions to aid in decision making that will maintain a balance between taking a more aggressive resection approach and reducing postoperative deficits. Furthermore, tumors and other pathologies can push brain activity regions out of their expected position, so mapping is critical to ensure maximum safe resection and for determining point of entry. This is of particular interest for determining language lateralization. Language representation can be investigated noninvasively using fMRI. This will reduce the risk of aphasia or other language deficits post surgery [1].

In addition to providing critical information in advance of the surgery, BOLD fMRI maps can be used within surgical navigation systems during brain surgery to guide intra-operative decision-making. The use of BOLD fMRI results preoperatively or intraoperatively has the potential to reduce neurological deficits by influencing the surgical approach, allowing for

1

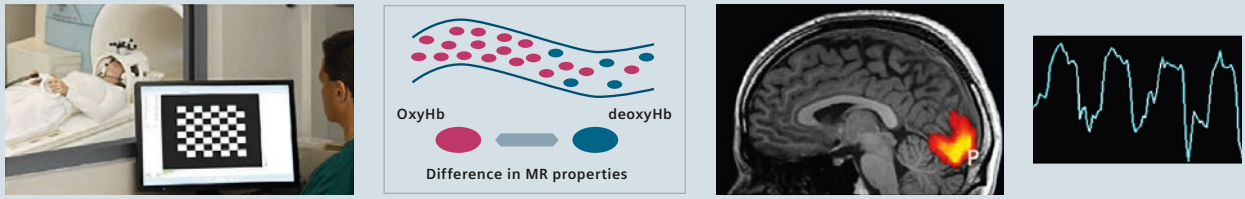

1 When a particular part of the brain becomes active, there will be an increased local blood flow. This can be detected using MRI, and will lead to an increased signal in the activated area.

more radical tumor resection while potentially reducing craniotomy size, reducing operating time and the need of awake surgery [1-4].

What equipment is needed for BOLD fMRI?

A high-quality fMRI study will require the patient to be cued to perform a particular cognitive or motor task while in the MR scanner. They can be presented with a visual stimulus (such as flickering checkerboard), be asked to read text (language study) or be cued to make finger movements using a response device. To present the stimuli, as well as inform the patient about whether they should perform a task or simply rest, a display needs to be available for the patient inside the MR bore. The patient can view the display via an MR compatible display attached to the head coil, NordicNeuroLab (NNL) VisualSystem, (Fig. 2A), or via a mirror mounted on top of the headcoil, which presents the image from an MR compatible monitor placed outside the MR scanner (NNL InroomViewingDevice, Fig. 2B). It is also possible to present stimuli to the patient via audio, using the NNL AudioSystem MR compatible headphones (Fig. 2A). These can also be used for patient communication. Patients can respond to language or motor tasks using the NNL ResponseGrip, which also provide a means of monitoring patient responses to various tasks (Fig. 2A).

All equipment used in the MR room must be MR compatible, that is, it must be able to operate safely in a strong magnetic field without causing distortions or artefacts in the MR image.

2 The NNL VisualSystem attached to the headcoil **(2A)**, or the NNL InroomViewingDevice **(2B)** are displaying the paradigm during fMRI. The NNL AudioSystem and ResponseGrip **(2A)** are used to provide audio stimuli and to collect patient response.

2A

2B

"We have been using the NNL fMRI equipment for about 10 years now in a clinical as well as a scientific setting. The efficiency using the products is very high, because of their easy usability and robustness.

We are very satisfied with our decision to use NNL equipment."

Professor Dr. Bernd Weber
Head of NeuroCognition, Imaging, Life&Brain Center, Bonn, Germany

The appropriate BOLD paradigm is presented using the nordicAktiva software, which contains a library of stimulus paradigms covering a wide range of cognitive, language and motor tasks. Enabling the BOLD Dot AddIn integration between the Siemens Numaris platform and nordicAktiva allows the paradigm to be selected and started from within the Numaris environment (Fig. 3). The MR acquisition must be synchronized with the timing of the paradigm, and this is taken care of by the NNL SyncBox which correlates the scanner's trigger pulse to the onset of the paradigm.

3 When enabling the BOLD Dot AddIn, the user can select the paradigm directly in Siemens Numaris **(3A)**. The lower image **(3B)** shows that a visual stimulation paradigm has been selected.

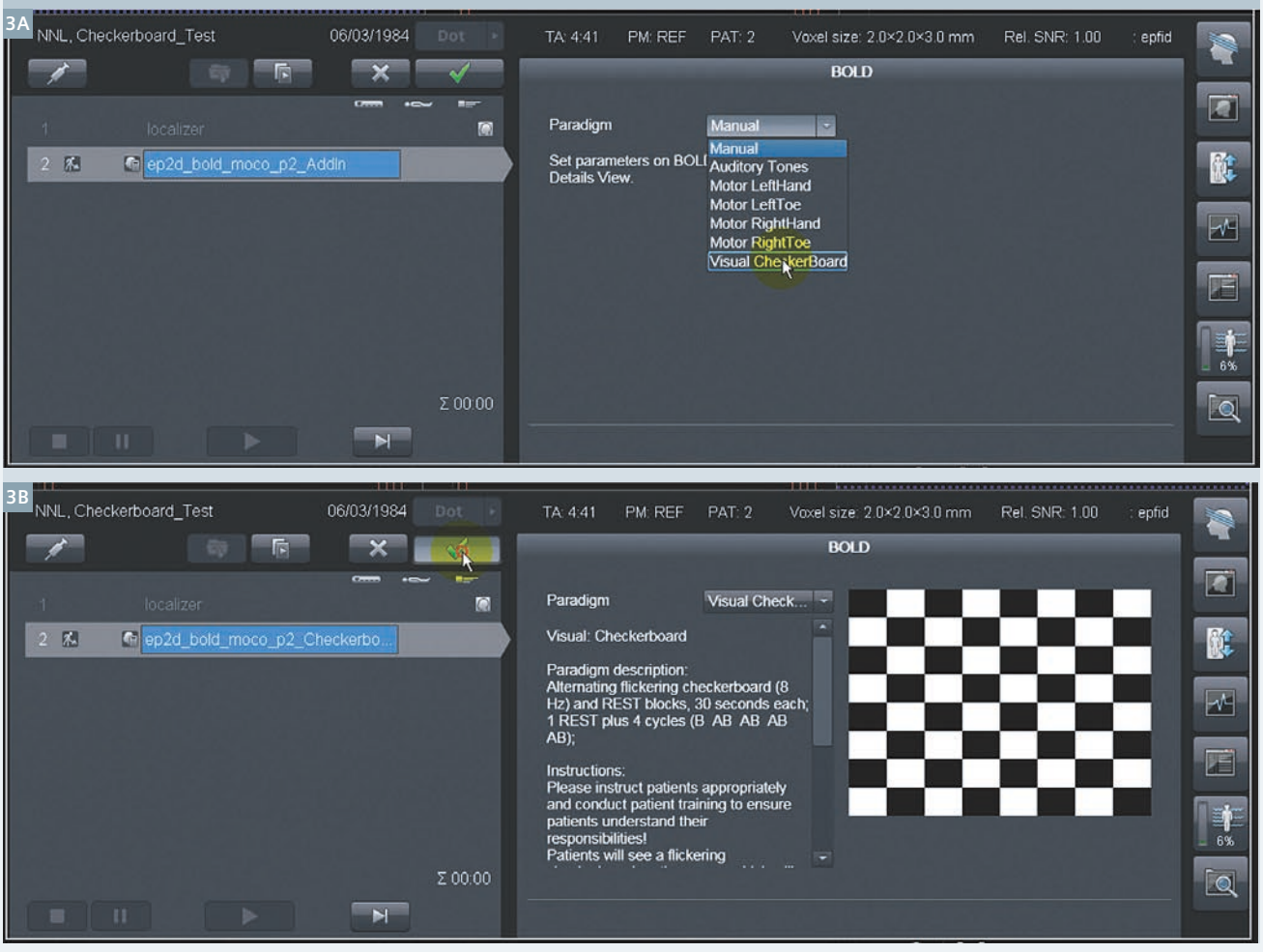

How to select the appropriate fMRI task?

The aim of presurgical fMRI is to map relevant regions surrounding pathology, so the type of paradigm to be done will be specific to the cortical region of interest (e.g. motor cortex). Tasks are selected that target the regions of interest and are possible for the patient to perform easily. The patient should be trained on each task to ensure that they completely understand the instructions and are able to perform the tasks well.

Task selection can be done directly from the Siemens Numaris workstation (Fig. 3). The paradigm will then be displayed visually on the device inside the MR scanner (NNL VisualSystem or NNL InroomViewingDevice), or aurally, via the headphones, depending on paradigm chosen. The NNL SyncBox will ensure that the paradigm presentation and MR image acquisition are synchronized precisely. A typical fMRI task alternates between a period of rest and activity (30 seconds, for approximately 4 cycles, about 5 minutes in total).

Once the fMRI session is complete, fMRI image data must be processed before the results can be sent to PACS or used for surgical planning (Fig. 4).

How to do fMRI:

1. Select paradigms based on location of pathology and functions to map.
2. Train patient to ensure they understand and can perform the tasks.
3. Select paradigm on Siemens Numaris.
4. Run the fMRI using the NNL fMRI equipment for displaying the paradigm to the patient.
5. After fMRI: send data to workstation dedicated for fMRI postprocessing.

4 BOLD fMRI results of left (red) and right (blue) finger tapping from a healthy volunteer.

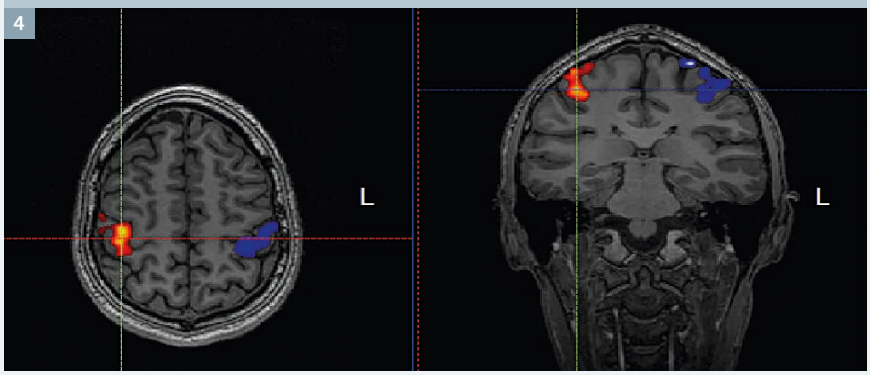

Contact

Marte Thuen, Ph.D.
Chief Technology Officer (CTO)
NordicNeuroLab AS
Møllendalsveien 65c
N-5009 Bergen
Norway
Phone +47 40 21 74 91
marte@nordicneurolab.com

References

1 Medina et al.: Seizure Disorders: Functional MR imaging for diagnostic evaluation and surgical treatment – Prospective study. Neuroradiology 236, 2005.

2 Petrella et al.: Preoperative functional MR imaging localization of language and motor areas: Effect on therapeutic decision making in patients with potentially resectable brain tumors. Radiology 240, 2006.

3 Håberg et al.: Preoperative blood oxygen level-dependent functional magnetic resonance imaging in patients with primary brain tumors: clinical applications and outcome. Neurosurgery 54, 2004.

4 Wilden et al.: Strategies to maximize resection of complex, or high surgical risk, low-grade gliomas. Neurosurg Focus 34, 2013.

Different NNL packages may be available for different MR systems in the US. Please contact your local sales representative for details.

Contrast-free Quantitative CBF and Bolus Arrival Time using Multi-delay Arterial Spin Labeling Perfusion MRI in Moyamoya Disease

Qiao Penggang[1]; Qian Tianyi[2]; Zuo Zhiwei[1]; Florian Fritz[3]; Josef Pfeuffer[3]; Li Gongjie[1]

[1] Department of Radiology, Affiliated Hospital of the Academy of Military Medical Sciences, Beijing, China
[2] Siemens Healthcare, MR Collaborations NE Asia, Beijing, China
[3] Siemens Healthcare, MR Neuro Applications, Erlangen, Germany

Introduction

Moyamoya disease (MMD) is a chronic cerebrovascular disease characterized by progressive stenosis and end-stage occlusion of terminal internal carotid arteries [1]. While MMD patients commonly experience frequent transient ischemic attacks (TIA), in most cases no infarction/ischemic lesions can be found on T1/T2/diffusion-weighted MR images. In these circumstances, dysfunctions of cerebral hemodynamics might provide unique information for diagnosis, surgery planning and outcome evaluation of MMD patients.

Currently there is no well-established gold standard for evaluating the complex cerebral hemodynamic patterns in MMD. Methods such as positron emission tomography (PET) [2], single photon emission computed tomography (SPECT) [3], computed tomography perfusion [4], and dynamic susceptibility contrast MRI (DSC-MRI) [5] all have the ability to assess cerebral perfusion. However, due to radiation dose and/or the use of contrast agents, these methods are not suitable for studies involving repeated examinations or long term follow-up research studies.

Arterial Spin Labeling (ASL) provides a non-invasive MRI alternative for measuring Cerebral Blood Flow (CBF), and has been applied for the study of a wide range of ischemic cerebrovascular diseases, such as acute ischemic stroke and MMD [6]. Commonly used ASL methods like PICORE Q2TIPS estimate CBF based on a single fixed delay/transit time, thus differences in time delay between the labeling of the feeding arteries and the arrival of labeled blood into brain tissue at different regions (as reflected e.g. by arterial transit time (ATT) or bolus arrival time (BAT)) introduce undesired variability to the measured signal and limit its interpretation in absolute terms. Therefore, by measuring the full inflow curve at multiple different inversion time points, a more accurately quantified CBF and precise timing information of blood flow (BAT map) can be obtained [7, 8].

In the following case studies, multi-delay ASL (MD-ASL) was used to measure CBF and BAT to evaluate the hemodynamic changes characteristic of MMD patients. The calculation of a CBF and BAT map for a multi-TI series is based on the original formulation of Buxton et al. [9] and is applying a voxel-wise fit. We then compared the performance of the technique with standard first-pass contrast-enhanced dynamic perfusion (DSC MRI).

Method

All patients were examined using a 3T MR system (MAGNETOM Skyra, Siemens Healthcare, Erlangen, Germany) with a 20-channel head-neck coil. The MD-ASL images were acquired using a prototype sequence 'Advanced 3D ASL'[1] with the following parameters: 3D GRASE imaging with FAIR Q2TIPS labeling, TR 4600 ms, TE 22 ms, slice thickness 4 mm, bolus duration 700 ms, 16 inversion times ranging from 480 to 4080 ms, total acquisition time 5 min including an M0 scan. DSC-MR images were post-processed though standard *syngo*.via pipeline using local AIF method.

Patient history and imaging findings

In these case studies, patterns of blood perfusion were bilaterally evaluated based on different blood circulation areas as shown in figure 1.

1 A = anterior circulation;
P = posterior circulation;
M1 = anterior middle cerebral artery (MCA) cortex;
M2 = MCA cortex lateral to insular ribbon;
M3 = posterior MCA cortex.

[1] Work in progress, the product is currently under development and is not for sale in the US and in other countries. Its future availability cannot be ensured. The product is not yet licensed for sale in Canada, in accordance with Canadian Law. Performance claims have not been reviewed by Health Canada, and are subject to change. Its future availability cannot be guaranteed.

Case 1:

49-year-old male patient, suffered intermittent numbness and weakness of right hand one year ago, accompanied by recurrent headache and dizziness. From the MRA and DSA images, we could identify a bilateral MCA occlusion and abnormal vascularity. The results of DSC-MRI showed long TTP (Fig. 2A) and MTT (Fig. 2C) in the bilateral hemispheric regions supplied by the MCA (M1, M2, M3) as well as in the right posterior circulation cortex (P), whereas CBV (Fig. 2D) was slightly increased and CBF (Fig. 2B) decreased bilaterally in M3. In the MD-ASL results, it can be observed that the topography of long BAT (Fig. 2E) matches TTP map very well, while the area with decreased CBF (Fig. 2F) is similar to DSC-MRI.

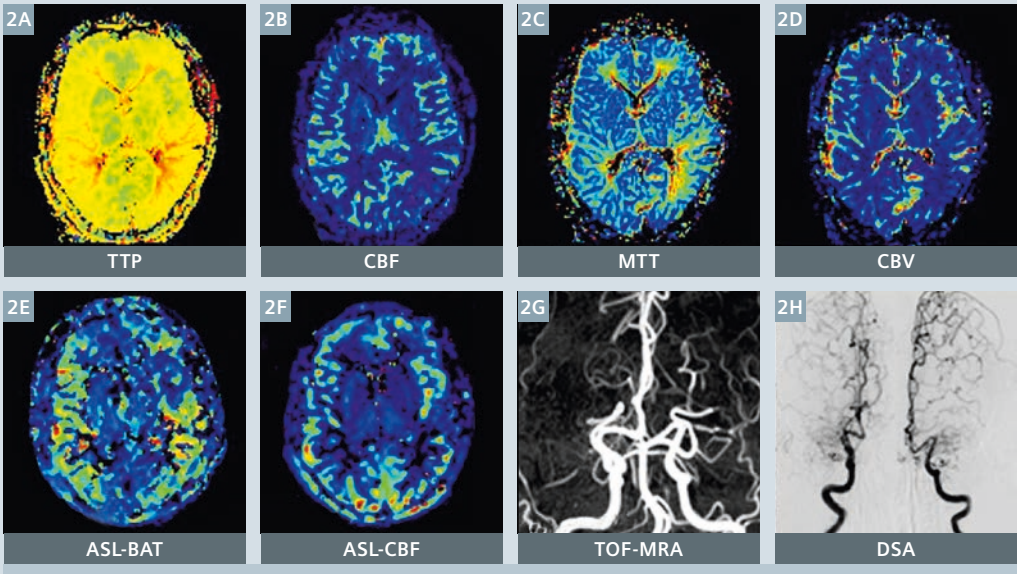

2 The upper row shows the results obtained by DSC-MRI: time to peak (TTP) **(2A)**, cerebral blood flow (CBF) **(2B)**, mean transit time (MTT) **(2C)**, cerebral blood volume (CBV) **(2D)**. The lower row shows the MD-ASL results including bolus arrival time (BAT, **2E**) and ASL-CBF **(2F)**, as well as brain vascular images collected by MR angiography (TOF-MRA) **(2G)**, and Digital Subtraction Angiography (DSA) **(2H)**.

Case 2:

49-year-old female patient who suffered of intermittent weakness of the right hand for the past four years. From the TOF-MRA and DSA images, we could see the bilateral MCA and ACA occlusion, as well as abnormal vascular structure. The results of DSC-MRI show long TTP (Fig. 3A) and MTT (Fig. 3C) bilaterally in brain regions supplied by MCA and ACA (A, M1, M2, M3), while CBV (Fig. 3D) and CBF (Fig. 3B) partly decreased. The results of MD-ASL showed an increased BAT (Fig. 3E) matching those observed in TTP and MTT as obtained with DSC-MRI. ASL-CBF images (Fig. 3F) also showed decreased CBF in the same area (bilateral M3) to DSC-MRI.

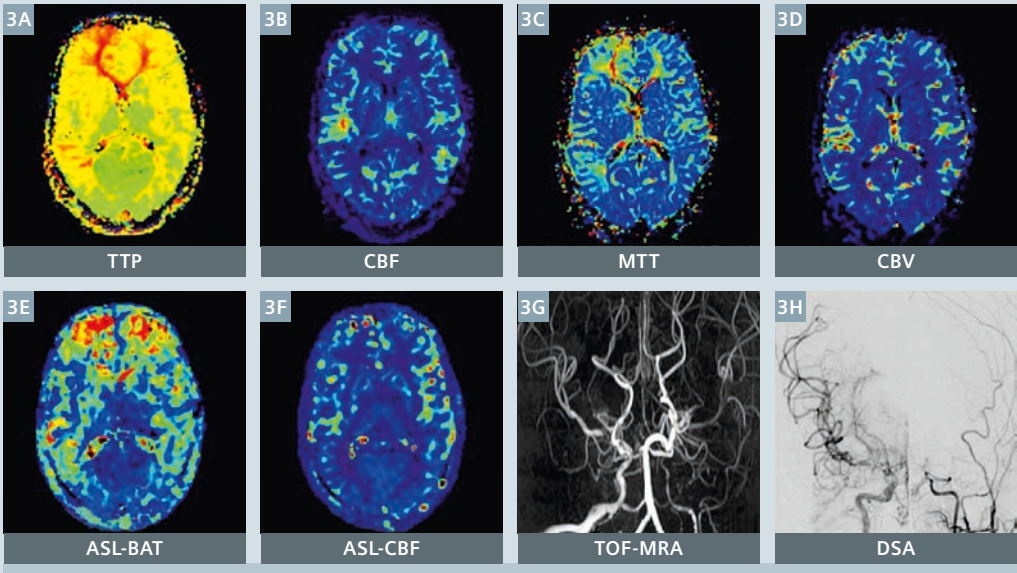

3 TTP **(3A)**, CBF **(3B)**, MTT **(3C)**, CBV **(3D)** obtained by DSC-MRI. BAT **(3E)**, CBF **(3F)** obtained using MD-ASL. Brain angiographic images obtained with TOF-MRA **(3G)** and DSA **(3H)**.

Case 3:

48-year-old female patient, suffered continuous weakness and numbness of left arm for the past seven years, and continuous weakness of left leg starting one year ago. From the MRA (Fig. 4G) and DSA (Fig. 4H) images, we could see the stenosis of bilateral MCA, ACA, left PCA and abnormal vascularity. The results of DSC-MRI show long TTP (Fig. 4A) and MTT (Fig. 4C) in areas A, M1, M2, M3, P of the left hemisphere, and areas A, M1, M2, M3 of the right hemisphere, while CBV (Fig. 4D) decreased in bilateral M3 and CBF (Fig. 4B)decreased in bilateral M1 and M3. In MD-ASL images, long BAT (Fig. 4E) areas were matched with the TTP map very well, and CBF (Fig. 4F) decreased in the similar area compared to DSC-MRI.

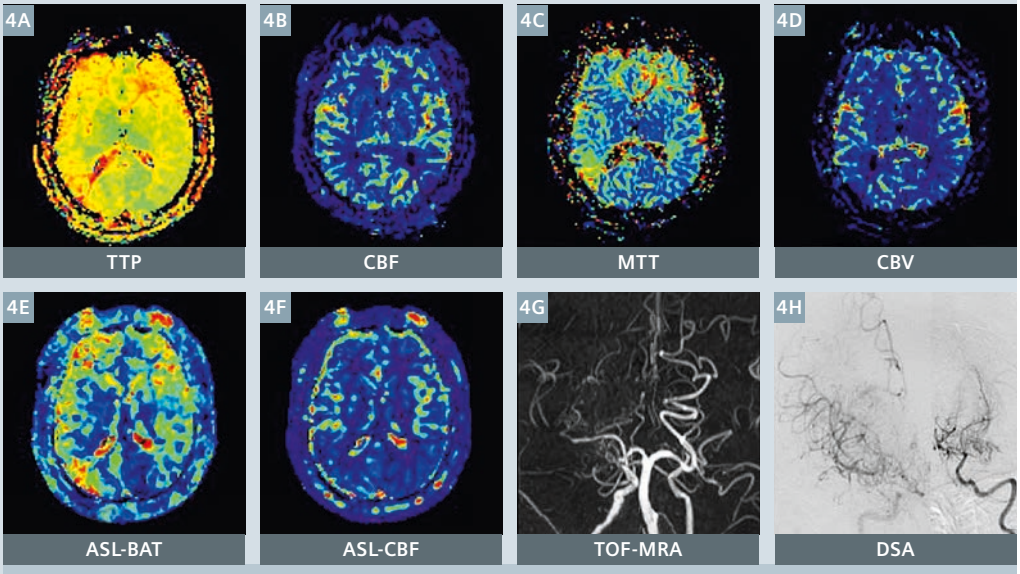

4 TTP **(4A)**, CBF **(4B)**, MTT **(4C)**, CBV **(4D)** obtained with DSC-MRI. BAT **(4E)**, CBF **(4F)** obtained using MD-ASL. Brain angiographic images obtained with TOF-MRA **(4G)** and DSA **(4H)**.

Conclusion

Our preliminary results demonstrate that the multi-delay 3D ASL method is able to robustly deliver both the arterial transition time and cerebral blood flow. By incorporating BAT information during the blood flow calculation, multi-delay ASL is capable of providing more accurate and less biased CBF, showing an equivalent performance to DSC-MRI in patients with Moyamoya disease. Because ASL is a non-invasive technique, there is high potential in using it to frequently monitor cerebrovascular diseases over long periods, or as a contrast-free quantitative measure of CBF in longitudinal studies.

References

1 Suzuki, J. & Kodama, N., 1983. Moyamoya disease--a review. Stroke, 14(1), pp.104–109.

2 Mihara, F. et al., 2003. Reliability of mean transit time obtained using perfusion-weighted MR imaging; comparison with positron emission tomography. Magnetic resonance imaging, 21(1), pp.33–39.

3 Yamada, I. et al., 1996. SPECT and MRI evaluations of the posterior circulation in moyamoya disease. Journal of nuclear medicine: official publication, Society of Nuclear Medicine, 37(10), pp.1613–1617.

4 Kang, K.H., Kim, H.S. & Kim, S.Y., 2008. Quantitative cerebrovascular reserve measured by acetazolamide-challenged dynamic CT perfusion in ischemic adult Moyamoya disease: initial experience with angiographic correlation. AJNR. American journal of neuroradiology, 29(8), pp.1487–1493.

5 Wityk, R.J. et al., 2002. Perfusion-weighted magnetic resonance imaging in adult moyamoya syndrome: characteristic patterns and change after surgical intervention: case report. Neurosurgery, 51(6), pp.1499–505– discussion 1506.

6 Detre, J.A. et al., 2009. Arterial spin-labeled perfusion MRI in basic and clinical neuroscience. Current Opinion in Neurology, 22(4), pp.348–355.

7 Wang DJ, et al., 2013. Multi-delay multi-parametric arterial spin-labeled perfusion MRI in acute ischemic stroke – Comparison with dynamic susceptibility contrast enhanced perfusion imaging. Neuroimage Clin., 3:1-7.

8 Wang R, et al., 2014, Multi-delay arterial spin labeling perfusion MRI in moyamoya disease--comparison with CT perfusion imaging. Eur Radiol. 24(5):1135-44.

9 R. B. Buxton, et al., 1998. A general kinetic model for quantitative perfusion imaging with arterial spin labeling. Magn Reson Med, 40(3):383_396.

Contact

Qiao Penggang
Department of Radiology, 307 Hospital
#8 Fengtai Dong Street, Fengtai District
Beijing, China 100071
qiaopenggang@sina.com

ESMRMB

European Society for Magnetic Resonance in Medicine and Biology

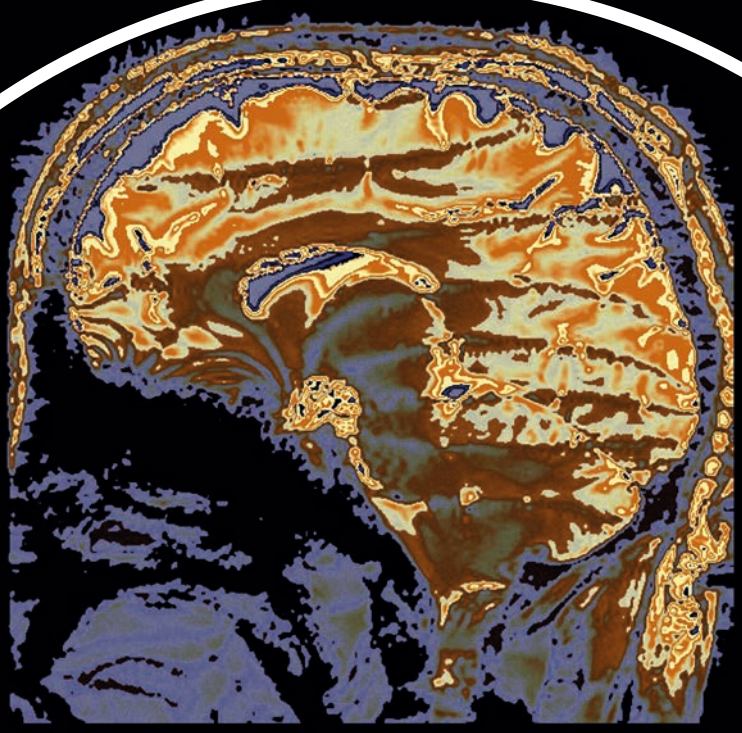

REGISTER NOW AT www.esmrmb.org

Lectures on MR 2015

Educational courses, exercises, and practical demonstrations on MR physics and engineering

RF coils:
Design, build and characterise your own
June 23–25, Berlin/DE

MRI simulation for sequence development, protocol optimisation, and education
June 29 – July 1, Copenhagen/DK

Resting state fMRI - basic concepts, methods & applications
September 2–4, Berlin/DE

Diffusion: What it means and how to measure it
September 28–30, Edinburgh/UK

www.esmrmb.org

Practical Considerations for the Evaluation of the Neuroforamina in Routine Spine Imaging at 3T. A Case Series

Thuy D. Do; Marc-André Weber

Clinic of Diagnostic and Interventional Radiology, University Hospital Heidelberg, Germany

Introduction

Pathologies of the neuroforamina are one of the most frequent indications for spine surgery. When imaging the neuroforamina usually sagittal and axial planes are acquired to delineate these pathologies. However, in a relatively small, but clinically not negligible, 29% of cases where root impingement was surgically confirmed, lateral root compression was underestimated in standard MRI with standard MR planes (axial/sagittal). Moreover, Bartynski et al. estimated the rate of successful prediction of a root impingement with such a standard MRI at only 72% [1]. Consequently there is a need to optimize the procedure for spine MRI to reliably evaluate nerve root impingement in a potential preoperative setting. By obtaining parasagittal sequences and by performing oblique image reconstructions, one can generate images that are strictly axial cuts through the neuroforamina. This allows for a better evaluation of the nerve enlargement, the disappearance of the nerve surrounding fat, and the provision of T2-neuropathy signals. The application of multiplanar reconstructions, e.g. for sacral nerves, has already been postulated and practiced on CT scans in clinical routine [2]. However, in clinical reality, MRI protocols often still use strictly axial and sagittal 2D planes, resulting in the above-mentioned challenges. In the following cases we present some practical aspects on the imaging protocols used to improve visualization of neuroforaminal pathologies.

Imaging of neuroforaminal pathologies at 3T

At our institute we mainly apply 3T MRI for evaluation of neurforaminal pathologies. The main advantage of imaging at 3T is the proportional increase of signal-to-noise ratio (SNR), enabling a clear reduction in slice thickness. Even in clinical realistic routine exams, the slice thickness can be reduced to even less than 3 mm for 2D T2-weighted MRI sequences. High SNR also provides better in-plane resolution as well as spatial resolution of the anatomical structures to be evaluated [5]. Although the disadvantages of MR imaging at 3T, such as dielectric shading effects, have to be taken into consideration, many of these limitations have been overcome, or are at least less pronounced, compared to the first clinical generation of 3T MR systems. Nevertheless, it should be emphasized that these dielectric shading effects do play a role in the application of 3T for spine imaging and must be addressed alongside other issues such as increased specific absorption rates. Most of the practical considerations in this case series, however, also apply for spine imaging at 1.5T.

All examinations presented in this article were performed on a 3T MRI scanner (MAGNETOM Verio, Siemens Healthcare, Erlangen, Germany) using the integrated multi-channel spine coil and – for imaging of the cervical spine – the head/neck coil.

Conclusion

Questions concerning pathologies of the neuroforamina, multiplanar reconstructions and/or additional angulated imaging sequences (at a 45° oblique view towards the standard sagittal plane) of the spine should particularly be included in routine examinations for improved delineation and depiction of neuroforaminal pathologies, especially if there is a need to evaluate surgical therapy. Whenever possible, a 3D sequence is preferred and thus post-imaging reconstructions can be compiled that not merely reduce examination time but also offers advantages for multiple planar reconstructions as well as simplifying the MR exam. In other cases, e.g. when dealing with metal instrumentation or motion artifacts due to pain, faster additional T2w sequences can be applied. Kinematic MRI might be beneficial for revealing disc bulges, which are not shown by traditional neutral views and should be considered also in a routine clinical setting for evaluation of the cervical spine.

Acknowledgment

The excellent technical assistance from Mrs. Sandra Kauczor and Joanna Weihrauch-Mohr is gratefully acknowledged.

Case 1: Parasagittal oriented T2-weighted sequences

An MRI exam of a 51-year-old male patient suffering pain within the cervical spine predominantly on the left side for the last four years. No focal neurologic symptoms were present. This case shows the value of parasagittal-oriented 2D MR sequences for improved confidence in diagnoses. In the parasagittal sequences, a focal mediolateral protrusion of the disc C3/C4-vertebra with compression of the left C3 spinal nerve can be easily delineated.

The disc herniation is less obvious due to partial volume effects and could have been missed on the standard sagittal planes, whereas the oblique parasagittal sequence nicely depicts the left sided protrusion (arrows). The parasagittal planes were planned as a 45° oblique angulated plane to the median and perpendicular to the neuroforamina. This case illustrates that by relying only on standard sagittal and axial 2D MRI for depicting the cervical spine and relatively thick slices (>3 mm), the diagnostic information may be limited for a proper evaluation of the nerve roots. In addition to the said protrusion, an old fracture of the spinous process C7 and Th1 was diagnosed.

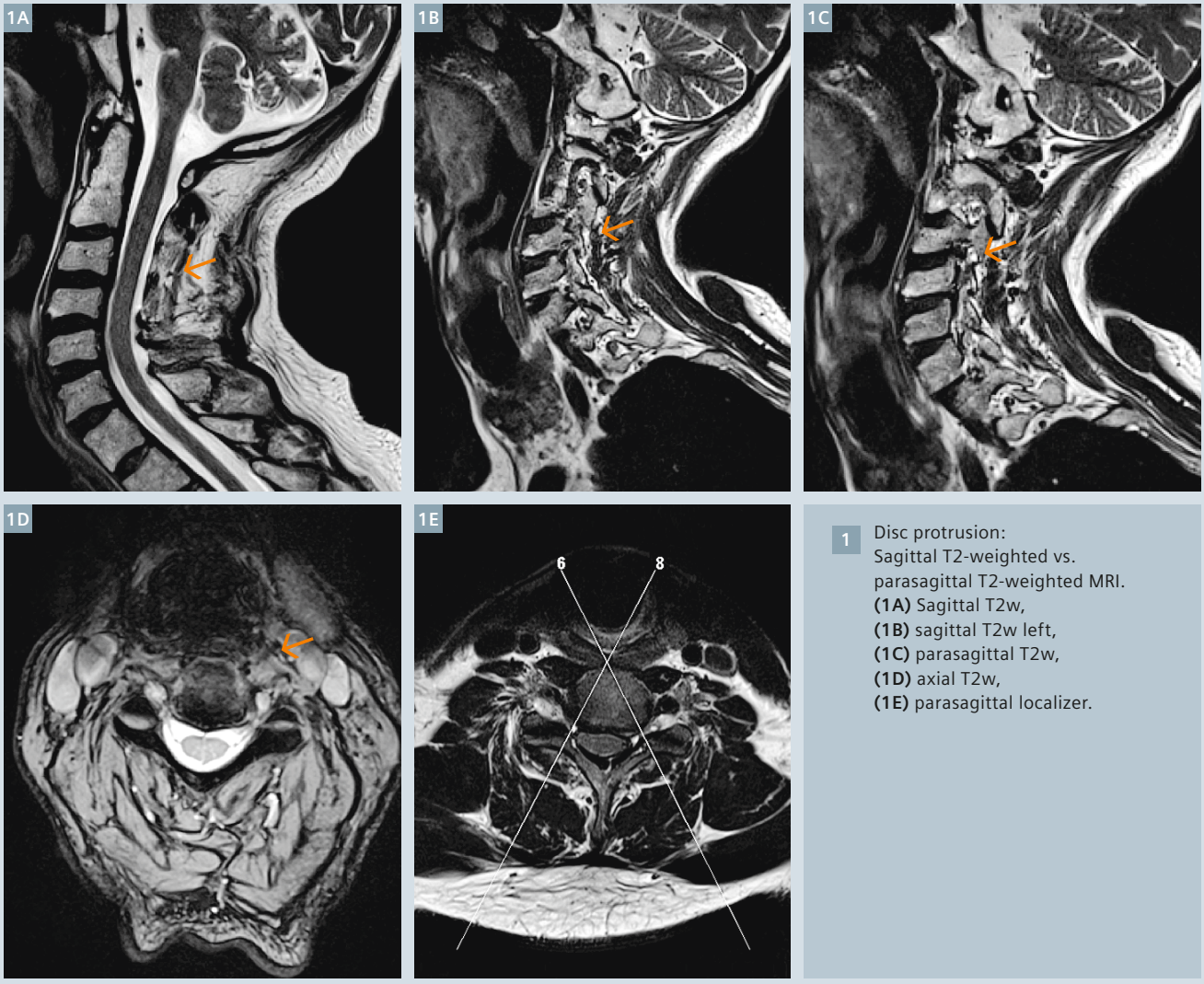

1 Disc protrusion:
Sagittal T2-weighted vs. parasagittal T2-weighted MRI.
(1A) Sagittal T2w,
(1B) sagittal T2w left,
(1C) parasagittal T2w,
(1D) axial T2w,
(1E) parasagittal localizer.

		TA [min]	Matrix	FOV [mm]	Slices	ST	TR [ms]	TE [ms]
Cervical spine	Parasagittal T2w TSE	2:13	384	260	11	2	2690	110

Table 1: Parasagittal T2-weighted TSE sequence used in this case for improved visualization of the neuroforamina.

Case 2: 3D T2-weighted sequences and parasagittal image plane reconstructions

In contrast to oblique-oriented 2D MR sequences, 3D MR sequences allow in retrospect any necessary reformation and are less dependent on accurate planning of the exam. Furthermore, there are obvious time benefits where multiple planes are needed. However, the differences in contrast and image impression (high resolution in-plane versus isotropic voxels resulting in thin slices with reduced in-plane resolution) compared with conventional 2D MRI sequences should be mentioned, even though they are not covered in this article.

In this case, MR images were made of a 52-year-old male who presented with pain in the lower back, radiating in the legs. Standard 2D MRI based on axial and (para-) sagittal planes showed disc protrusion of the L4-S1 vertebra with the maximum of the herniation at the L4/L5 segment. There was a narrowing more of the right neuroforamen than of the left neuroforamen at the L4/L5 segment due to the disc protrusion as well as spondylarthritis.

In addition to the standard MRI protocol, we used a balanced steady-state free precession sequence (TrueFISP), which provides a high signal intensity of the cerebrospinal fluid. As shown in figure 2B, the oblique reconstruction improves the confidence of the finding. With its short acquisition time, this TrueFISP sequence is also less sensitive to motion artifacts. To achieve a similar contrast of the cerebrospinal fluid other sequences can also be used, e.g. 3D CISS sequences. However, it should be pointed out that at 3T we must also keep the flip angles under observation because of their effect on the specific absorption rate (SAR) [3].

One drawback of the TrueFISP sequence is the so-called dark banding artifact which can be met by acquiring images at different phase offset angles. Another alternative would be the application of the SPACE sequence for T2w 3D imaging at 3T.

By allowing multiplanar oblique reconstructions, the additional 3D sequence reduces the risk of missing neuroforamen encroachment, without the need for further sequences and without increasing the complexity of the procedure for the MR scan. Although the lumbar neuroforamina have a nearly sagittal orientation to the lumbar spine and are in most cases well depicted with traditional location of planes, these additional images provided by the TrueFISP that depict the neuroforamina en face facilitate the detection of even minor encroachments. In addition, the higher spatial resolution can improve the diagnostic confidence for the conventional planes e.g. as shown in this case, for a strictly axial orientation (Fig. 2C).

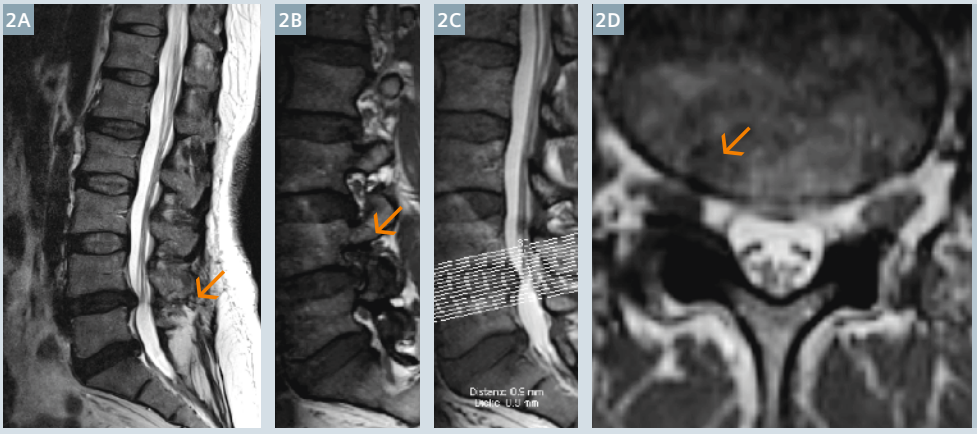

2 Disc protrusion: Sagittal T2-weighted sequence vs. parasagittal TrueFISP reconstructions and strictly axial reconstructions along the disc. **(2A)** Sagittal T2w, **(2B)** parasagittal reconstruction, **(2C)** localizer, **(2D)** axial reconstruction.

		TA [min]	Matrix	FOV [mm]	Slices	ST	TR [ms]	TE [ms]
Sequence	Cor TrueFISP 3D	4:26	256	220	80	0.9	4.86	2.43
Lumbar spine reconstructions	Axial		256		Variable	1	4.86	2.43
	Parasagittal reconstruction angulated towards the neuroforamina		256		Variable 30	1	4.86	2.43

Table 2: TrueFISP sequence and parasagittal reconstructions.

Case 3: Parasagittal and oblique oriented MR sequences in case of indwelling metal

In this case MRI images were made of a 76-year-old female who presented with a one-year history of back pain spreading more in her right than her left leg. Two years ago a spacer between the spinous processes L4/L5 had been implanted at another hospital.

In this case, a conventional parasagittal plane represents a good option for postoperative imaging, since metal susceptibility artifacts are avoided. But depending on the implant used and its configuration, the usage of double oblique planes offers the opportunity that the artifact generated by the osteosynthesis instrumentation moves out of the field-of-view. We prefer conventional T2-weighted TSE sequences in patients with surgical hardware and in combination with different angulations: Often good, robust imaging is feasible even with the pronounced sensitivity of 3T towards artifacts introduced by these implants. Since 3D gradient echo sequences, like the MEDIC, are more prone to susceptibility artifacts, they do not represent the backbone of our protocol. However, for instance 3D SPACE sequences have the advantage of post-imaging reconstructions which may be required especially in very complex cases and instrumentation e.g. severe scoliosis and rotation of the spine. As demonstrated in figure 4, the instrumentation does not affect the diagnostic quality of the MR scan and the neuroforamina can be assessed adequately.

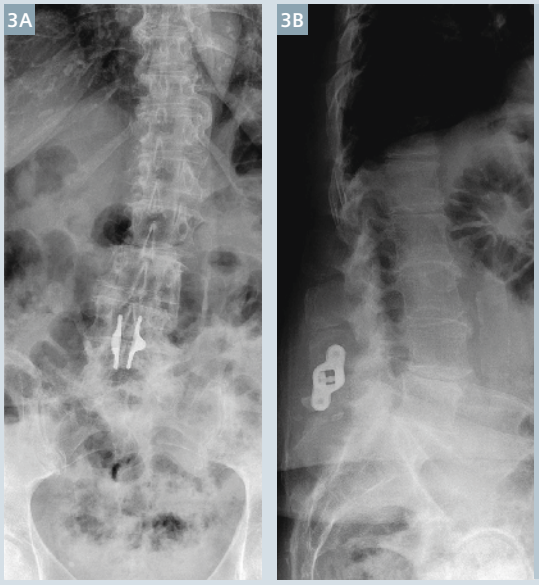

3 X-rays of lumbar spine with osteosynthesis material between the spinous process L4/L5.

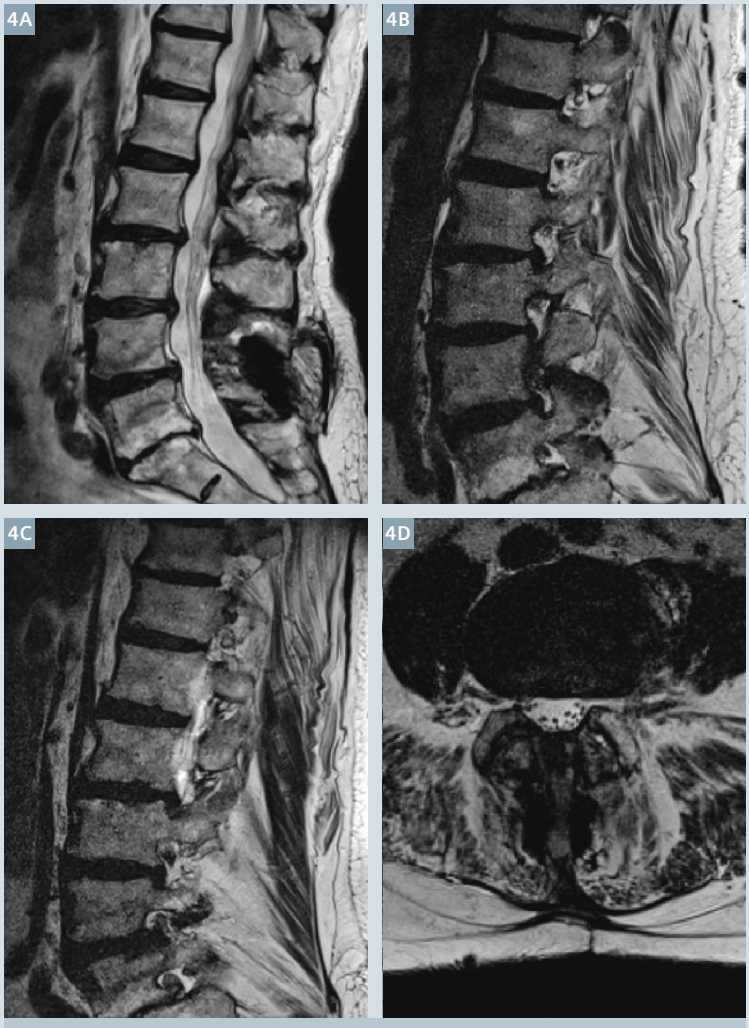

4 Sagittal vs. parasagittal oriented T2-weighted TSE sequences. **(4A)** Sagittal T2w, **(4B)** parasagittal T2w left, **(4C)** parasagittal T2w right, **(4D)** axial T2w.

Case 4: Additional value of dynamic MRI sequences

For the evaluation of pathologies of the cervical spine in particular, dynamic MRI sequences can add important clinical information, obtained within a routine clinical setting. In this case, a 42-year-old man with persisting pain in the cervical spine presented for MR reevaluation after a car accident two years ago. He has no focal paresis, only paresthesia in his left thumb. The kinematic MRI comprised of ultrafast sequences (e.g. T2-weighted HASTE) at 30° inclination and reclination. At the neutral position a disc bulge and myelopathy signal are denoted at the C6/C7 level indicating the cause of the symptoms. The disc bulge was significantly increased in extension (reclination) position (Fig. 5C).
This case illustrates well the valuable information obtained by adding a 30-second sequence to the standard MRI protocol. Sometimes abnormalities can only be depicted – or are better depicted – by flexion or extension of the spine so that the symptoms are at their maximum. This method may be restricted, apart from contraindications, if there is severe pain that renders the patient unable to bear this position. Nevertheless, the application of a HASTE sequence represents a good approach that allows in most cases such a dynamic scan. Other sequences, like conventional 2D TSE, or even 3D sequences like SPACE or TrueFISP do, of course, offer all the advantages discussed above, but they are coupled with longer examination times and sequence-dependant challenges such as sensitivity to metal artifacts [4].

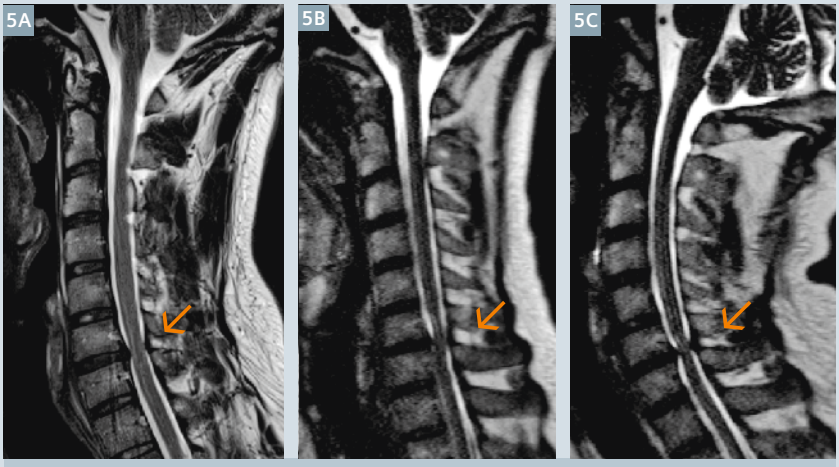

5 Conventional sagittal T2w vs. dynamic T2w MRI.
(5A) Sagittal T2w, **(5B)** T2w HASTE inclination, **(5C)** T2w HASTE reclination.

		TA [min]	Matrix	FOV [mm]	Slices	ST	TR [ms]	TE [ms]
Cervical spine inclination	T2w HASTE sag	0:30	320	250	15	3	1000	249
reclination	T2w HASTE sag	0:30	320	250	15	3	1000	249

Table 3: Dynamic sequences.

References

1 Bartynski, W.S. and L. Lin, Lumbar root compression in the lateral recess: MR imaging, conventional myelography, and CT myelography comparison with surgical confirmation. AJNR Am J Neuroradiol, 2003. 24(3): p. 348-60.
2 Yang, J., et al., Application of MPR in sacral nerve injury during sacral fracture. J Trauma, 2011. 70(6): p. 1489-94.
3 Baskaran, V., et al., Myelographic MR imaging of the cervical spine with a 3D true fast imaging with steady-state precession technique: initial experience. Radiology, 2003. 227(2): p. 585-92.
4 Gerigk, L., et al., Dynamic magnetic resonance imaging of the cervical spine with high-resolution 3-dimensional T2-imaging. Clin Neuroradiol, 2012. 22(1): p. 93-9.
5 Shapiro, M., Imaging of the spine at 3 tesla. Neuroimaging Clin N Am, 2012. 22(2): p. 315-41, xi-xii.

Thuy D. Do

Marc-André Weber

Contact

Marc-André Weber, M.D., M.Sc.
Professor of Radiology
Heidelberg University Hospital
Diagnostic and Interventional Radiology
Im Neuenheimer Feld 110
69120 Heidelberg, Germany
MarcAndre.Weber@med.uni-heidelberg.de

Save the Date

Heidelberg Summer School

Musculoskeletal Cross Sectional Imaging 2015

July 24th / 25th 2015
Heidelberg, Germany

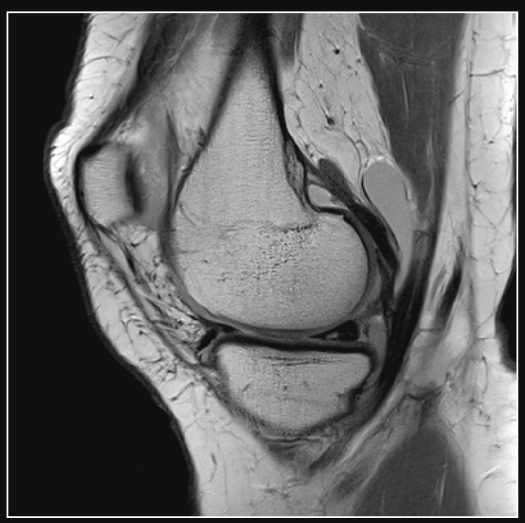

The Heidelberg Summer School offers advanced learning opportunities and promotes the academic exchange of knowledge, ideas, and experiences by bringing together physicians and professional staff from all over the world. Excellent speakers will cover a wide range of medical, physical, and technical topics in musculoskeletal imaging. All lectures are in English.

Course director

Marc-André Weber, M.D., M.Sc.

Professor of Radiology, Section Head Musculoskeletal Radiology at the University Hospital Heidelberg

CME Accreditation

The symposium will be accredited by the 'Landesärztekammer Baden-Württemberg' with CME credits (category A).
Also, the symposium is accredited for 1 category 3 credit point for the ESSR diploma by the European Society of Musculoskeletal Radiology.

Registration

Mrs. Marianne Krebs, Secretary of the Section Musculoskeletal Radiology

Marianne.Krebs@med.uni-heidelberg.de

For further information please visit:

www.heidelbergsummerschool.de

Can MRI Estimate the Cortical Bone Quality? A Feasibility Study Employing Short-TE MRI

Atena Akbari[1,2]; Shahrokh Abbasi-Rad[1,2]; Niloofar Tondro[3]; Mohsen Shojaee-Moghaddam[3]; Hamidreza Saligheh Rad[1,2]

[1] Quantitative MR Imaging and Spectroscopy Group, Research Center for Molecular and Cellular Imaging, Tehran University of Medical Sciences, Iran
[2] Department of Medical Physics and Biomedical Engineering, School of Medicine, Tehran University of Medical Sciences, Iran
[3] Imaging center, Payambaran Hospital, Tehran, Iran

Background

Pore size and distribution in the cortical bone structure represent its mechanical competence and consequently its quality [1]. Through aging, several natural processes such as bone remodeling and trabecularization will incur significant alterations in the porosity of cortical bone, in the way that the size and number of pores increase with the concomitant cortical thickness decrease. Therefore, a direct relationship between age and porosity is expected [2]; meaning that the older an individual is, the more porous its cortical bone is.

Pores of the cortical bone can be categorized into three types: Haversian canals, lacunae, and canalicular network [3-8], in all of which there exists a significant amount of water. By the same token, to investigate the cortical bone porosity, quantification of the fluids, essentially water, which reside in these microscopic pores can be considered as a promising and growing strategy [2]. Magnetic Resonance Imaging (MRI), due to its sensitivity to the proton microenvironments, has proved to be a good candidate for this quantification purpose. As pores become larger during aging, their surface-to-volume ratio (S/V) and consequently the mobility of the residing water molecules will increase [9]. As a result, the energy transfer mechanism between free water molecules and surrounding lattice will be prolonged, which will lead to an increase in their longitudinal relaxation time (T1). Hence, cortical bone free water T1 can be probably a desired feature to extract the aforementioned relationship between cortical bone porosity (free water content) and age [10, 11].

MR pulse sequences employing Echo Time (TE) in the order of microseconds, known as Ultra-short Echo Time (UTE) imaging, are capable of acquiring signal from cortical bone water molecules [12]. But due to its being time-consuming and lack of availability in daily clinics, it is not a suitable clinical method for cortical bone free water T1 measurement. Short Echo Time (STE) pulse sequence with TE in the range of 1-1.5 ms has been shown to be an applicable and clinical alternative for the quantification of cortical bone free water T1 [10, 11].

In this work as a first step, a cohort of subjects including 20 healthy normal volunteers (8 males and 12 females) in the age range of 20-70 years underwent STE-MR free water T1 quantification procedure for the purpose of establishing the aforesaid relationship between free water T1 and age. In the next step, we considered the obtained regression line equation as a baseline on which a new insight into the cortical bone quality can be predicated. To pursue

1

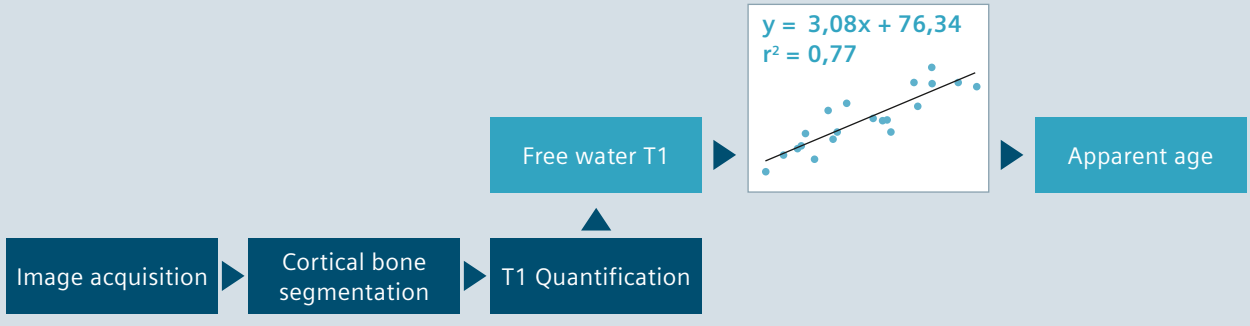

1 Flow diagram for the whole procedure of case analysis for calculation of cortical bone apparent age.

this goal, we quantified the free water T1 of new individual and introduced it as an input to the extracted regression line equation. The output of these numerical calculations is a type of age differing from an individual's actual age and would be named as the 'apparent age' with the potential of giving information about cortical bone quality. In the sequel, the stepwise process of apparent age calculation is illustrated for two cases and six examples are discussed.

Case analysis: cortical bone apparent age vs. actual age

Calculation of the cortical bone apparent age of each individual accomplishes by introducing cortical bone free water T1 as input to the regression line equation extracted from the cohort of subjects. The general steps towards apparent age calculation are illustrated as a flow diagram in figure 1.

For further clarification, the exact steps can be recapitulated as follows:

- **Image acquisition:** Acquiring two STE-MR images with identical imaging parameters except for TR (TR1 = 20 ms / TR2 = 60 ms).
- **Segmentation:** Placing region-of-interest (ROI) on the whole cortical bone area drawn manually using polygon tool in ImageJ software (http://imagej.net).
- **T1 Quantification:** Solving a non-linear equation obtained by dividing two gradient echo signal equations using MATLAB (The Mathworks, Natick, MA, USA).
- **Apparent Age Calculation:** Using cortical bone free water T1 as input to the obtained regression line equation.

Case analysis 1

Actual age: 34 years
Apparent age: 46.77 years

This individual was a female with actual age of 34 years, whose apparent age was calculated to be 46.77 years, meaning that her cortical bone porosity status is similar to that of a 46-year-old female.

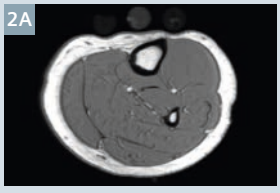

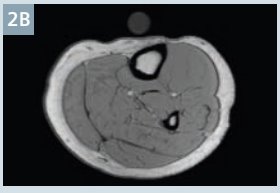

Step 1: Image acquisition

2 Two STE-MR images acquired from a 34-year-old female subject with two different TRs. **(2A)** TR = 20 ms, **(2B)** TR = 60 ms.

In order to enhance the accuracy of the proposed method 10 slices were acquired resulted in a stack of 20 STE images.

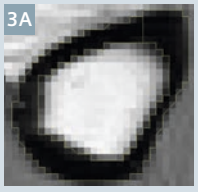

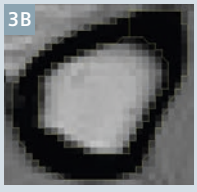

Step 2: Cortical bone segmentation

3 Manually segmented cortical bone drawn out of two STE-MR images shown in figure 2. **(3A)** TR = 20 ms, **(3B)** TR = 60 ms.

TR = 20 ms
$\overline{SI}$ = 160.22

TR = 60 ms
$\overline{SI}$ = 286.93

Step 3: T1 quantification

$$\frac{286.93}{160.22} = \frac{1 - \exp(-60/T1)}{1 - 0.88\exp(-60/T1)} \Big/ \frac{1 - \exp(-20/T1)}{1 - 0.88\exp(-20/T1)} \Rightarrow T1 = 220.37 \text{ ms}$$

$$\text{Apparent age} = \frac{(220.37 - 76.33)}{(3.08)} = 46.77 \text{ years}$$

Step 4: Apparent age calculation

Case analysis 2

Actual age: 67 years
Apparent age: 59.28 years

This individual was a male with actual age of 67 years whose apparent age was calculated to be 59.28 years, meaning that his cortical bone porosity status is similar to that of a 59-year-old male.

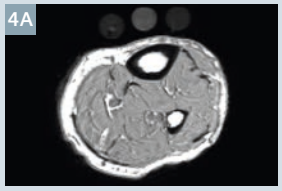

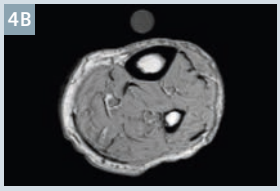

Step 1: Image acquisition

4 Two STE-MR images acquired from a 67-year-old male subject with two different TRs. **(4A)** TR = 20 ms, **(4B)** TR = 60 ms.

In order to enhance the accuracy of the proposed method 10 slices were acquired resulted in a stack of 20 STE images.

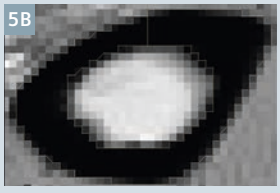

Step 2: Cortical bone segmentation

5 Manually segmented cortical bone drawn out of two STE-MR images shown in figure 4. **(5A)** TR = 20 ms, **(5B)** TR = 60 ms.

TR = 20 ms
$\overline{SI}$ = 122.34

TR = 60 ms
$\overline{SI}$ = 237.04

Step 3: T1 quantification

$$\frac{237.04}{122.34} = \frac{1 - \exp(-60/T1)}{1 - 0.88\exp(-60/T1)} \Big/ \frac{1 - \exp(-20/T1)}{1 - 0.88\exp(-20/T1)} \Rightarrow T1 = 258.92 \text{ ms}$$

$$\text{Apparent age} = \frac{(258.92 - 76.33)}{(3.08)} = 59.28 \text{ years}$$

Step 4: Apparent age calculation

Method

Subjects

In order to establish the postulated relationship between free water T1 and actual age of individuals, we have performed cortical bone free water T1 quantification method on a cohort of normal subjects including 20 healthy (12 females and 8 males) volunteers covering the age range of 20–70 years. For subject recruitment, health criteria were defined as BMI < 30 kg/m^2, lacking any medical histories that indicate disorders, surgery, or treatments (e.g. glucocorticoid therapy or antiepileptic drugs).

Imaging protocol

The imaging site was selected to be at 38% of the tibia length measured from the medial malleolus. The rationale for considering this site was the fact that cortical bone has the maximum thickness in this site and hence is more straightforward for the analysis procedure. Each subject's leg was kept fixed as much as possible in order to avoid any motion during imaging. Subjects were placed in the MR magnet for the total scan time of about twenty minutes to acquire a stack of 20 STE-MR images (10 slices with TR = 20 ms, and 10 slices with TR = 60 ms) using dual-TR gradient echo imaging strategy. Image acquisition was performed on a 1.5 Tesla MR scanner (MAGNETOM Avanto, Siemens Healthcare, Erlangen, Germany) using an 8-channel knee coil. Since capturing signal from cortical bone microscopic pores occupied by water molecules is challenging due to their very short T2*~ (μs) [13-16], selecting the echo time of imaging protocol is highly crucial. With respect to such small T2*, it seems that the TE values in the range of 1–1.5 ms would be satisfying for the ultimate goal of cortical bone free water quantification. Regarding the trade-off between TE value, SNR, and spatial resolution, 1.29 ms was determined to be the optimal value. Summary of imaging parameters is listed in table 1.

Image analysis and T1 quantification

Whole cortical bone was segmented manually in each slice from the obtained STE images using polygon tool in ImageJ software based on visual discrimination of cortical bone from marrow and muscle. The quantification process was done by dividing the two gradient echo signal equations, which yield a ratio by which the T1 values of cortical bone free

Table 1

Repetition Time	Echo Time	Field-of-View (FOV)	Spatial Resolution	Slice Thickness	Flip Angle	Total Scan Time
TR1 = 20 ms TR2 = 60 ms	1.29 ms	267 × 267 mm²	0.8 x 0.8 mm²	5 mm	20°	20 minutes

STE-MR imaging parameters.

6

7

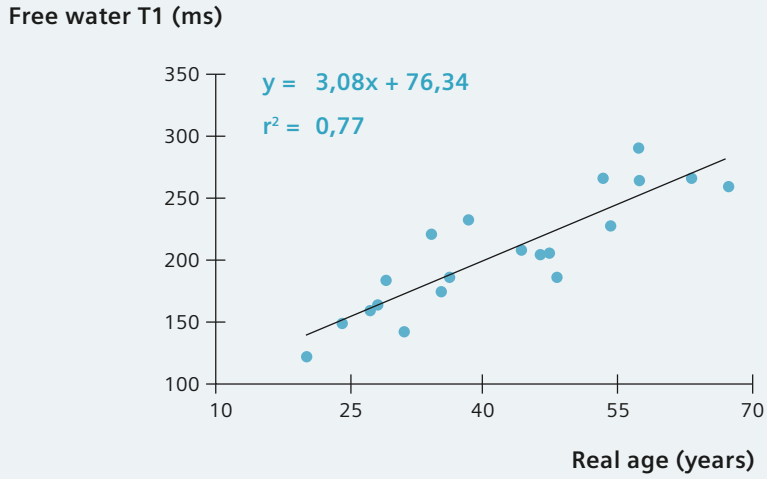

7 Correlation between cortical bone free water longitudinal relaxation time (T1) and 'actual age' in twenty healthy volunteers covering the age range of 20-70 years ($r^2 = 0.77$, $p < 0.0001$).

water were calculated. They were computed in all ten slices and were pooled for statistical validity.

Establishment of baseline equation from a cohort of healthy subjects

In order to compute cortical bone apparent age as a potential marker for bone quality, a baseline equation (regression line equation) was needed, which can be extracted by probing a relationship between cortical bone free water T1 values and actual age in a cohort of healthy subjects with an acceptable diversity of age. The r^2 value was calculated as a measure of accuracy of the computed baseline.

Apparent age calculation

To calculate the apparent age of an individual the cortical bone free water T1 value was simply used as an input to the regression line equation obtained in the previous step. The observed discrepancy between actual and apparent ages would be a probable representative of cortical bone quality of individual.

The summary of all steps is shown as a flow diagram in figure 6.

Result and discussion

Cortical bone free water T1 values which were quantified among twenty normal healthy volunteers were proved to have a direct relationship with actual age plotted in figure 7. In the sense that by aging the volume of cortical bone pores increases which ensues a concomitant increase in the mobility of free water molecules. These alterations are simultaneous with the increase of T1 values of cortical bone free water.

The linear regression line obtained from this study provides us with the relationship between cortical bone free water and apparent age which can be considered as an indicator for cortical bone quality. Equation 1 is the foundation for apparent age calculation in the way that by considering the cortical bone free water T1 as input, the output would be the apparent age.

Equation 1	**Free water T1 = 3.08 * (Apparent age) + 76.33**

During aging, size and number of cortical bone pores increase as the result of several natural processes such as bone remodeling and trabecularization (i.e. changes caused by actual aging), while other factors (e.g. lifestyle, genetics, etc.) may accelerate or decelerate the process of cortical bone micro-architectural degradation (i.e. changes caused by apparent aging). The cortical bone apparent age of six different subjects are reported in figure 8 and described in the sequel.

For three subjects (8A, 8B, and 8C) their apparent ages were reported to be lower than their actual ages. In other words, the trend in the architectural changes of cortical bone has been progressed in a way that the bone quality is better than what would have been expected from their actual age.

For three subjects (8D, 8E, and 8F), their apparent ages were reported to be higher than their actual ages. This difference indicates that pore structure deterioration has developed faster than the normal rate of cortical bone pore architectural alterations. As is visible from six different subjects shown in figure 8, cortical bone trabecularization has occurred with higher speed in the first three cases (8A, 8B, and 8C) than in the second three (8D, 8E, and 8F), which in turn is a proof of the concept for apparent age definition. It should be noted that in order to augment the authenticity of proposed concept, other variables (e.g. gender, genetics, etc.) besides the age must be taken into account, while in this pilot study we have only considered the alterations of cortical bone pores by aging.

The concepts and information presented in this article are based on research and are not commercially available. Its future availability cannot be ensured.

Contact

Dr. Hamidreza Saligheh Rad, Ph.D.
Quantitative MR Imaging and Spectroscopy Group
Research Center for Molecular and Cellular Imaging
Institute for Advanced Medical Technologies
Tehran University of Medical Sciences, Tehran, Iran
Phone: (+98) 218 897 3653 – 108
Fax: (+98) 216.648.2654
h-salighehrad@tums.ac.ir

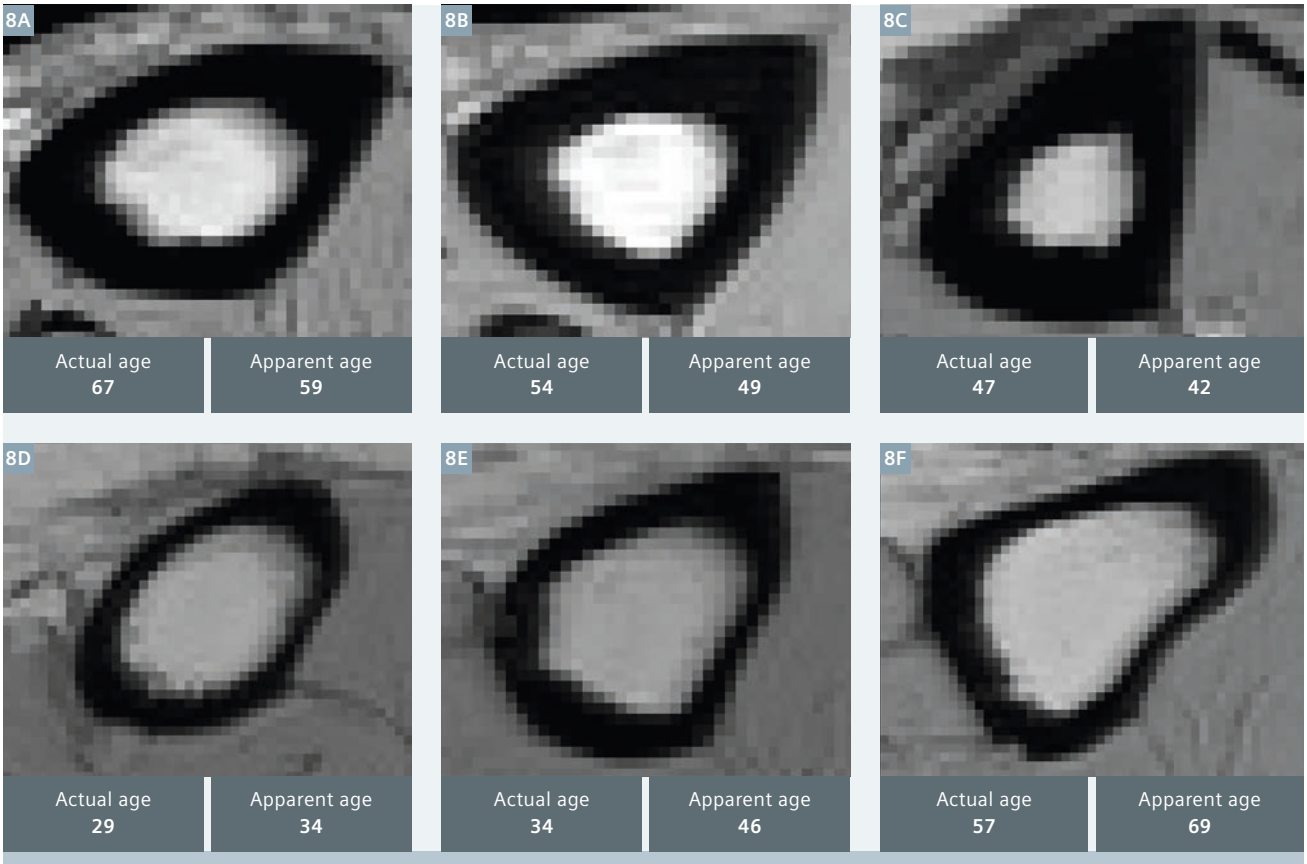

8 Actual versus apparent age of six healthy volunteers.
Three subjects (**8A:** male, **8B:** male, **8C:** female) had apparent ages lower than their actual ages and three subjects (**8D:** female, **8E:** female, **8F:** male) had apparent ages higher than their actual ages.

Acknowledgement

We would like to thank Shaahin Mehdipour, MRI modality manager at Fanavarihaye Azmayeshgahi, Iran Siemens Advanced Partner, for his great help and support; Payambaran Imaging Center, Tehran, for their cooperation in clinical research.

References

1 Nyman, J.S., et al. Measurements of mobile and bound water by nuclear magnetic resonance correlate with mechanical properties of bone. Bone, 2008. 42.1: p.193-199.
2 Bae, Won C., et al. Magnetic resonance imaging assessed cortical porosity is highly correlated with μCT porosity. Bone, 2014. 66: p.56-61.
3 Wu, Y., et al. Density of organic matrix of native mineralized bone measured by water- and fat-suppressed proton projection MRI. Magn Reson Med, 2003. 50: p.59 -68.
4 Cao, H., et al. Quantitative bone matrix density measurement by water- and fat-suppressed proton projection MRI (WASPI) with polymer calibration phantoms. Magn Reson Med, 2008. 60: p.1433-1443.
5 Cao, H., et al. Quantitative 31P NMR spectroscopy and 1H MRI measurements of bone mineral and matrix density differentiate metabolic bone diseases in rat models. Bone, 2010. 46: p.1582-1590.
6 Techawiboonwong, A., et al. In vivo MRI of submillisecond T2 species with two-dimensional and three-dimensional radial sequences and applications to the measurement of cortical bone water. NMR in Biomed, 2008. 21: p.59-70.
7 Techawiboonwong, A., et al. Cortial bone water: in vivo quantification with ultrashort echo-time MR imaging. Radiology, 2008. 248: p.824-833.
8 Du, J., et al. Qualitative and quantitative ultrashort echo time (UTE) imaging of cortical bone. J Magn Reson, 2010. 207: p.304-311.
9 Fantazzini, P., et al. Bone tissue and porous media: common features and differences studied by NMR relaxation. Magnetic resonance imaging, 2003. 21.3: p.227-234.
10 Akbari, A., et al. Investigation of Relationship between Free-Water T1 and Age in Human Cortical Bone Employing Short-TE 1H-MRI at 1.5T. International Society for Magnetic Resonance in Medicine, 2014, Italy.
11 Akbari, A., et al. Introducing a Novel Clinical Biomarker to Assess Human Bone Health Employing Conventional MRI. Asia oceanic Congress of Radiology, 2014, Japan.
12 Robson, M.D., et al. Magnetic resonance: an introduction to ultrashort TE (UTE) imaging. Journal of computer assisted tomography, 2003, 27.6: p. 825-846.
13 Nyman, J.S., et al. Measurements of mobile and bound water by nuclear magnetic resonance correlate with mechanical properties of bone. Bone, 2008, 42: p.193-199.
14 Horch, R.A., et al. Characterization of 1H NMR signal in human cortical bone for magnetization resonance imaging. Magn Reson Med, 2010, 64: p.680-687.
15 Horch, R., et al. Clinically-compatible MRI strategies for discriminating bound and pore water in cortical bone. Magn Reson Med, 2012, (Epub Jan 31).
16 Ong, H.H., et al. Deuterium nuclear magnetic resonance unambiguously quantifies pore and collagen-bound water in cortical bone. JBone Miner Res,2012, in press.

Learn more!

Don't miss the talks of experienced and renowned experts on all aspects of musculoskeletal MR imaging at:

www.siemens.com/magnetom-world

Accelerated High-Resolution MRI of Joints and Metal Implants

Jan Fritz

Johns Hopkins University
(Baltimore, USA)

Cartilage Evaluation

Darshana Sanghvi

Kokilaben Dhirubhai Ambani
(Mumbai, India)

Imaging Sports Trauma

James M. Linklater

Castlereagh Imaging
(St. Leonards, Australia)

Anatomical and Functional MRI for Radiotherapy Planning of Head and Neck Cancers

Maria A. Schmidt, Ph.D.; Rafal Panek, Ph.D.; Erica Scurr, DCR(R), MSc; Angela Riddell, MD FRCS FRCR; Kate Newbold, MD MRCP FRCR; Dow-Mu Koh, MD MRCP FRCR; Martin O. Leach, Ph.D. FMedSci

Cancer Imaging Centre, Royal Marsden NHS Foundation Trust and Institute of Cancer Research, Sutton, UK

Introduction

Head and Neck cancers are relatively common: squamous cell carcinoma of the head and neck (SCCHN) has a worldwide incidence of approximately 500,000 cases per annum [1]. Treatment is a combination of surgery, chemotherapy and radiotherapy (RT), devised to maximize the probability of eradicating the disease while retaining organ function [2-5]. Recent technical advances in RT include high-precision conformal techniques such as intensity-modulated RT (IMRT) and volumetric intensity modulated arc therapy (VMAT), which enable dose escalation to lesions without exceeding recommended exposure levels for organs at risk (OAR). However, these techniques require accurate anatomical information to contribute towards improving disease control.

High-resolution Magnetic Resonance Imaging (MRI) has increasingly been used to plan Head and Neck RT [6-10]. MRI and CT images are registered, combining the advantageous soft tissue contrast of MRI examinations and the required CT-based electron density. However, MR images are often distorted due to magnetic field inhomogeneity and non-uniform gradients [11-13], and the use of CT-MR fusion requires geometrically accurate MRI datasets. This article describes the equipment, protocols and techniques used in Head and Neck MRI at the Royal Marsden NHS Foundation Trust to ensure that the MRI examinations undertaken for RT planning purposes achieve the required geometric accuracy.

1 Receiver coil arrangement used at the Royal Marsden NHS Foundation Trust to perform Head and Neck MRI for RT planning. A standard MR-compatible baseboard is employed, enabling the use of a thermoplastic mask. The large flex-coil is positioned above the neck and used in conjunction with elements of the spine array.

High resolution anatomical imaging in the radiotherapy planning position

At the Royal Marsden NHS Foundation Trust clinical Head and Neck MRI examinations for RT planning are undertaken at 1.5T in the 70 cm bore MAGNETOM Aera (Siemens Healthcare, Erlangen, Germany). Patients are scanned in the RT position using an appropriate head rest and thermoplastic shell immobilisation attached to an MR-compatible headboard, modified to remain accurately positioned on the Aera patient couch. In addition to the elements of the posterior spine coil selected at the level of the lesion, a large flex-coil is also placed anteriorly, in line with the tumor, employing a custom-built plastic device to keep the coil curved, following the neck anatomy. This arrangement achieves a high signal-to-noise ratio, allows effective use of parallel imaging and keeps patient comfort in the RT planning position (Fig. 1).

The MRI protocol covers the primary tumor and neck lymph nodes with approximately isotropic T1-weighted sagittal 3D acquisition (TE 1.8 ms, TR 880 ms, 160 x 1 mm slices, 250 mm x 250 mm FOV, 256 x 256 image matrix). Images are acquired post contrast-agent injection (single dose). This dataset is subsequently registered with the RT planning CT examination, and for this reason its geometric integrity is checked periodically with a large linear test object, previously described [14], consisting of sets of straight tubes in three

orthogonal directions. Figure 2 shows images of the test object without and with post processing to correct image distortion. The 3D distortion correction built into the scanner software is essential for RT planning, and always used. The maximum displacement found within the volume encompassed by head and neck examinations is less than 1 mm. In addition, the imaging protocol employs a 500 Hz/pixel bandwidth, ensuring chemical shift related displacements in the readout direction remain under 0.5 mm.

Having characterized the geometric integrity of the protocol employed, it is also essential to characterize any further distortion associated with the distribution of magnetic susceptibility values within the subjects. In Head and Neck a large number of air-tissue interfaces in the vicinity of the tumors gives rise to localized magnetic field inhomogeneity, detrimental to the geometric integrity of the images. For this purpose, the field inhomogeneity in this region was estimated in five Head and Neck subjects. Transaxial gradient-echo images were acquired with fat and water in phase (TE values 4.76 and 9.53 ms), and the phase images were subtracted. The local field inhomogeneity was measured after phase unwrapping. Displacements associated with the airways were mostly under 0.5 mm with this sequence. Displacements only reach 1 mm in the vicinity of dental implants, and only very few pixels are affected.

Functional imaging

In addition to the clinical service providing anatomical images for RT planning, functional MRI is also employed to characterize lesions pre and post treatment and to investigate prediction of treatment response both at 1.5T (MAGNETOM Aera) and 3T (MAGNETOM Skyra). In RT planning, the ultimate aim of functional imaging techniques is to identify radioresistant disease and thus provide a biological target volume for dose boosting. Geometric accuracy is therefore essential to allow correct registration of functional MR images with anatomical MRI and CT datasets. In Head and Neck cancers, both diffusion-weighted imaging (DWI) and Dynamic Contrast-Enhanced (DCE) MRI have been explored [15-21].

Diffusion-weighted imaging with readout segmentation of long variable echo-trains (RESOLVE): EPI-based DWI is sensitive to the mobility of water molecules and to their environment. In cancer, cell proliferation is often associated with an increase in cell density and in extracellular space tortuosity. This leads to lower values of the Apparent Diffusion Coefficient (ADC), compared to healthy tissues [22-23]. ADC values have thus been used for tumor detection, prediction and assessment of treatment response.

EPI in regions adjacent to air-tissue interfaces is known to suffer from poor geometric integrity [24]. Because this affects Head and Neck studies, strategies to reduce the echo-train length were sought. In addition to parallel imaging, the RESOLVE technique was also employed to acquire multi-shot DWI using a navigator signal to enable accurate multi-echo combinations. In Head and Neck studies, DWI with RESOLVE was employed, covering the volume of interest to identify restricted diffusion within primary lesions and affected lymph nodes.

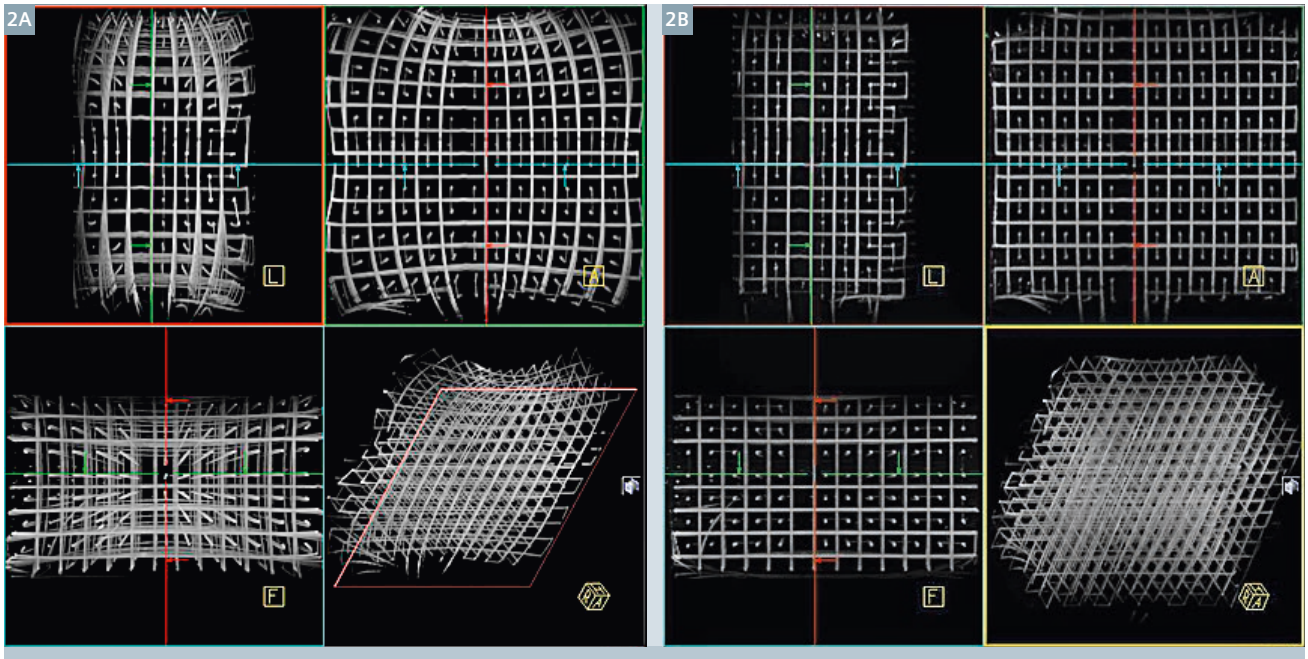

2 Images of the Linear Test Object (described by Doran et al. [14]) acquired using a 3D T1-weighted sequence with bandwidth 500 Hz/pixel, without distortion correction **(2A)** and with 3D distortion correction **(2B)**. Each picture shows three maximum intensity projections (sagittal, coronal and transaxial) and a 3D view of the test object.

3 A comparison of conventional single shot DWI **(3A)** and RESOLVE DWI **(3B)** in a head examination. The ADC calculated with the RESOLVE DWI **(3C)** retains the geometric integrity. Standard DWI parameters: TE 98 ms, TR 7000 ms, receiver bandwidth 1040 Hz/pixel, matrix 192 x 192, FOV 230 mm x 230 mm, 3 averages, slice thickness 4 mm. RESOLVE DWI parameters: TE 58 ms, TR 5700 ms, receiver bandwidth 950 Hz/pixel, matrix 128 x 128, FOV 240 mm x 240 mm, slice thickness 4 mm.

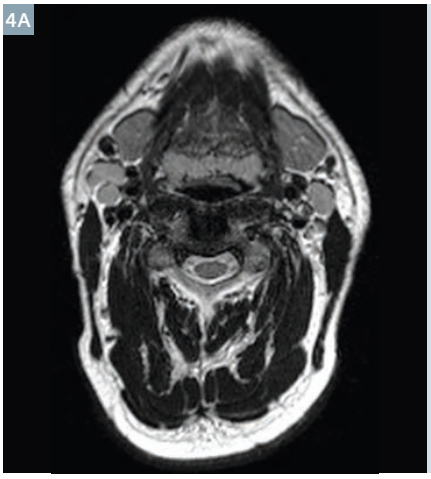

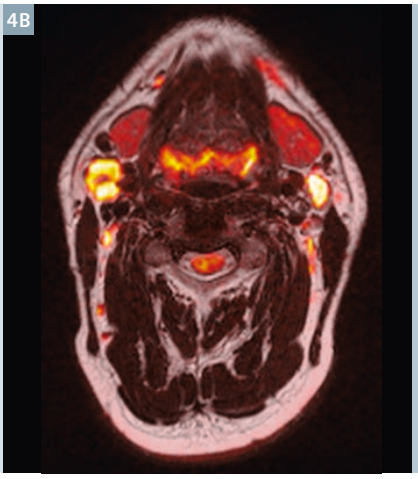

4 Head and Neck T2-weighted image **(4A)** with co-registered RESOLVE diffusion-weighted image **(4B)**. Restricted diffusion (high intensity) can be observed in nodes, spinal cord, tonsils and submandibular glands with no apparent geometrical distortion.

Figure 3 compares DWI acquired without and with the RESOLVE technique for a Head subject, in a slice comprising air spaces. The clear improvement in geometric integrity achieved with RESOLVE DWI allows the registration of anatomical and functional images, thus allowing the use of DWI in RT planning for Head and Neck cancers (Fig. 4).

Dynamic contrast-enhanced MRI with CAIPIRINHA-VIBE and TWIST view-sharing:

In dynamic contrast-enhanced (DCE)-MRI a series of 3D T1-weighted images is acquired to monitor contrast-agent uptake following an intravenous injection of contrast-agent. Using reference images, this technique can be quantitative and provide a dynamic calculation of T1 for each voxel. This enables pharmacokinetic modelling, providing information on tumor microcirculation, vascularity, blood volume and vessel permeability [25, 26]. This quantitative approach to DCE requires high temporal resolution to maintain accuracy. However, this conflicts with the need for high spatial resolution in RT planning applications.

The combination of flex-coil and spine coil elements has been used for DCE employing TWIST view-sharing and CAIPIRINHA reconstruction to produce high resolution images (voxel size 2 mm isotropic x 44 slices, CAIPIRINHA parameters: 2x2) with 2.5 s temporal resolution (TWIST parameters: A = 33% B = 33%). An example of TWIST/CAIPIRINHA DCE with a generous superior/inferior coverage to include both primary site and local involved lymph nodes is shown in figure 5. Isotropic voxels allow for a good 3D delineation of a biological target volume. In addition, Dixon reconstruction of fat and water images also provides information on fat content within the imaged volume, which might be important in the context of tumor response to treatment. Figure 6 shows T1-weighted water-Dixon signal change after Gd injection for a given representative slice containing a primary tumor. Last frame shows K^{trans} map within the region of interest.

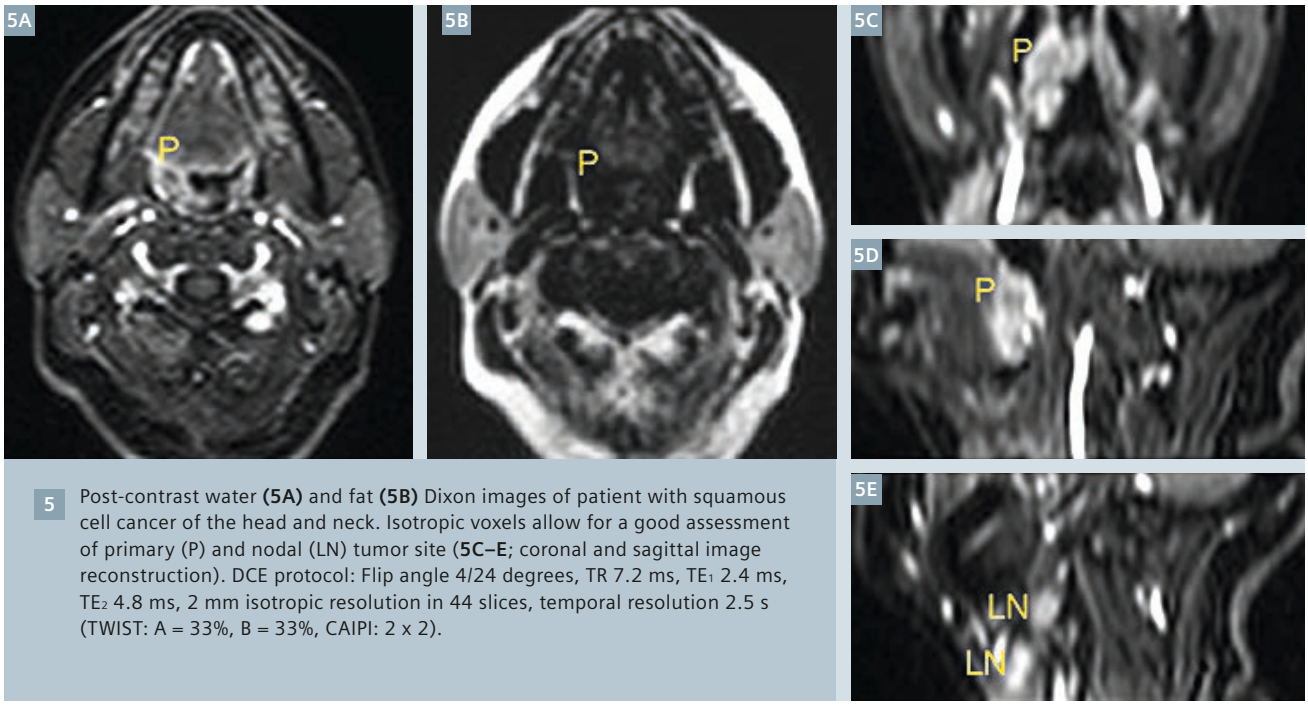

5 Post-contrast water **(5A)** and fat **(5B)** Dixon images of patient with squamous cell cancer of the head and neck. Isotropic voxels allow for a good assessment of primary (P) and nodal (LN) tumor site (**5C–E**; coronal and sagittal image reconstruction). DCE protocol: Flip angle 4/24 degrees, TR 7.2 ms, TE_1 2.4 ms, TE_2 4.8 ms, 2 mm isotropic resolution in 44 slices, temporal resolution 2.5 s (TWIST: A = 33%, B = 33%, CAIPI: 2 x 2).

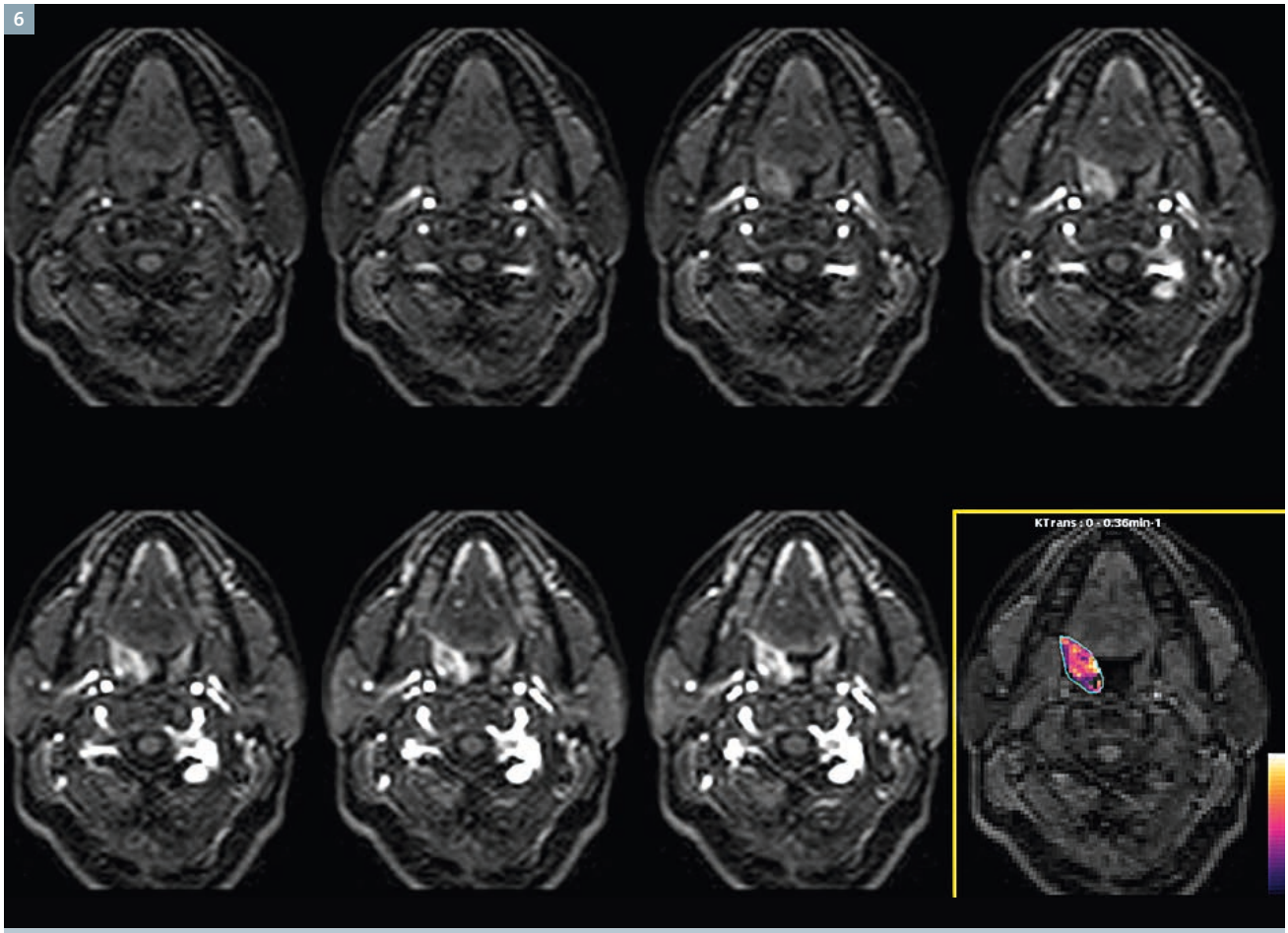

6 T1-weighted Dixon/water signal change after contrast agent injection, showing progressive enhancement and washout of Head and Neck cancer lesion. Last frame shows K^{trans} for a region of interest over a primary tumor site.

Conclusion

Geometrically accurate anatomical and functional imaging for RT planning of Head and Neck cancers were acquired in the RT planning position in standard clinical scanners; this service was developed to meet the clinical and research needs of the users, using custom built coil positioning devices and test objects.

Acknowledgments

The authors wish to thank D. Nickel, R. Kroeker and P. Ravell (Siemens Healthcare) for the provision of the works-in-progress package WIP771 (VIBE with View Sharing TWIST). The authors acknowledge the support of CRUK and EPSRC to the Cancer Imaging Centre at ICR and RMH in association with MRC & Department of Health C1060/A10334, C1060/A16464 and NHS funding to the NIHR Biomedicine Research Centre and the Clinical Research Facility in Imaging. This work was also supported in part by Cancer Research UK Programme Grants C46/A10588 and C7224/A13407. MOL is an NIHR Senior Investigator.

Radiotherapy Planning where MR data is the only imaging information is ongoing research. The concepts and information presented in this article are based on research and are not commercially available. Its future availability cannot be ensured.

Contact

Dr. Maria A. Schmidt
MRI Unit
Royal Marsden NHS
Foundation Trust
Downs Rd
Sutton SM2 5PT
UK
Phone: +44 (0)20 8661 3353
maria.schmidt@icr.ac.uk

References

1 Parkin DM, Bray F, Ferlay J, Pisani P. Estimating the world cancer burden: Globocan 2000. International Journal of Cancer. 2001;94(2):153–6.
2 Bentzen SM, Trotti A. Evaluation of early and late toxicities in chemoradiation trials. J Clin Oncol 2007; 25:4096-4103.
3 Harrington KJ, et al. Interactions between ionising radiation and drugs in head and neck cancer: how can we maximise the therapeutic index? Curr Opin. Investig Drugs 2002; 3: 807-11.
4 Lefebvre JL, et al. Larynx preservation clinical trial design: key issues and recommendations - a consensus panel summary. Int J Radiat Oncol Bioi Phys. 2009; 73: 1293-303.
5 Kazi R, et al. Electroglottographic comparison of voice outcomes in patients with advanced laryngopharyngeal cancer treated by chemoradiotherapy or total laryngectomy. Int J Radiat Oncol Bioi Phys. 2008; 70: 344-52.
6 Ahmed M, Schmidt M, Sohaib A, Kong C, Burke K, Richardson C, Usher M, Brennan S, Riddell A, Davies M, Newbold K, Harrington KJ & Nutting CM. The value of magnetic resonance imaging in target volume delineation of base of tongue tumours – a study using flexible surface coils. Radiother Oncol 2010; 94, 161-7.
7 Bhide SA, Ahmed M, Barbachano Y, Newbold K, Harrington KJ & Nutting CM. Sequential induction chemotherapy followed by radical chemo-radiation in the treatment of locoregionally advanced head-and-neck cancer. Br J Cancer 2008; 99, 57-62.
8 Gregoire V et al. Radiotherapy for head and neck tumours in 2012 and beyond: conformal, tailored, and adaptive? Lancet Oncol. 2012; 13(7), pp.e292-300.
9 Nuyts S. Defining the target for radiotherapy of head and neck cancer. Cancer Imaging.2007;7(Special Issue A):S50–S55.
10 Newbold K, Partridge M, Cook G, Sohaib SA, Charles-Edwards E, Rhys-Evans P, et al. Advanced imaging applied to radiotherapy planning in head and neck cancer: a clinical review. Br J Radiol. 2006 Jul 1;79(943):554–61.
11 Wang D & Doddrell DM. Geometric distortion in structural magnetic resonance imaging. Current Medical Imaging Reviews 2005; 1: 49-60.
12 Wang H, Balter J & Cao Y. Patient-induced susceptibility effect on geometric distortion of clinical brain MRI for radiation treatment planning on a 3T scanner. Phys Med Biol. 2013; 58: 465-77.
13 Reinsberg SA, Doran SJ, Charles-Edwards EM & Leach MO. A complete distortion correction for MR images: II. Rectification of static-field inhomogeneities by similarity-based profile mapping. Phys Med Biol 2005; 50: 2651-61.
14 Doran SJ, Charles-Edwards L, Reinsberg SA & Leach MO. A complete distortion correction for MR images: I. Gradient warp correction. Phys Med Biol. 2005; 50: 1343-61.
15 Thoeny HC, de Keyzer F & King AD. Diffusion-weighted MR imaging in the head and neck. Radiology, 2012; 263(1): pp.19-32.
16 Vandecaveye, V. et al. Evaluation of the larynx for tumour recurrence by diffusion weighted MRI after radiotherapy: initial experience in four cases. The British Journal of Radiology 2006; 79: 681-687.
17 Sumi M, Sakihama N, Sumi T, Morikawa M, Uetani M, Kabasawa H, et al. Discrimination of metastatic cervical lymph nodes with diffusion-weighted MR imaging in patients with head and neck cancer. AJNR Am J Neuroradiol 2003; 24(8):1627-34.
18 Powell C, Schmidt M, Borri M, Koh DM, Partridge M, Riddell A, Cook G, Bhide S A, Nutting CM, Harrington KJ & Newbold KL. Changes in functional imaging parameters following induction chemotherapy have important implications for individualised patient-based treatment regimens for advanced head and neck cancer. Radiother Oncol. 2013; 106, 112-
19 Quon H, Brizel DM. Predictive and prognostic role of functional imaging of head and neck squamous cell carcinomas. Semin Radiat Oncol. 2012 Jul; 22(3):220–32.
20 Wang P, Popovtzer A, Eisbruch A, Cao Y. An approach to identify, from DCE MRI, significant subvolumes of tumours related to outcomes in advanced head-and-neck cancer. Medical Physics. 2012; 39(8):5277–85.
21 Srinivasan A, Mohan S & Mukherji SK. Biological imaging of head and neck cancer: the present and the future. AJNR Am J Neuroradiol. 2012; 33(4), pp. 1-9.
22 Padhani et al. Diffusion-Weighted Magnetic Resonance Imaging as a Cancer Biomarker: Consensus and Recommendations, Neoplasia 2009; 11(2):102-125.
23 Galbán CJ et al. The parametric response map is an imaging biomarker for early cancer treatment outcome. Nature medicine, 2009;15(5): pp.572-6.
24 Jezzard P. Correction of geometric distortion in fMRI data. Neuroimage 2012; 62: 648-51.
25 Walker-Samuel S, Leach MO, Collins DJ. Evaluation of response to treatment using DCE-MRI: the relationship between initial area under the gadolinium curve (IAUGC) and quantitative pharmacokinetic analysis. Phys Med Biol. 2006 Jul 21; 51(14):3593–602.
26 O'Connor J P B, Jackson A , Parker G J M and Jayson G C. DCE-MRI biomarkers in the clinical evaluation of antiangiogenic and vascular disrupting agents. British Journal of Cancer 2007; 96: 189–195. doi:10.1038/sj.bjc.6603515.

Advance your clinical capabilities with the MAGNETOM RT Pro edition

For more information please visit us at: www.siemens.com/mri-in-rt

Development of MR-only Planning for Prostate Radiation Therapy Using Synthetic CT

Peter Greer, Ph.D.[1]; Jason Dowling, Ph.D.[2]; Peter Pichler, M.P.H.[3]; Jidi Sun, M.Sc.[3]; Haylea Richardson, B.Med.Rad.Sc.[3]; David Rivest-Henault, Ph.D.[2]; Soumya Ghose, Ph.D.[2]; Jarad Martin, M.D.[1]; Chris Wratten, FRANZCR[1]; Jameen Arm, MSc[4]; Leah Best, MSc[4]; Jim Denham, M.D.[1]; Peter Lau, FRANZCR[4]

[1] Calvary Mater Newcastle, Newcastle, New South Wales, Australia and University of Newcastle, Newcastle, New South Wales, Australia
[2] CSIRO, Australian e-Health Research Centre, Brisbane, Queensland, Australia
[3] Calvary Mater Newcastle, Newcastle, New South Wales, Australia

Introduction

The department of Radiation Oncology at Calvary Mater Newcastle, treats approximately 1,800 new patients per year. When it comes to prostate treatments, MR scans are used in addition to CT for treatment planning. Having to undergo two scans however is a burden both to patients as well as the health system. We have looked into addressing this by replacing the CT by an MR-only[1] workflow when treating patients with prostate cancer.

Description of the current treatment process

In the conventional CT based workflow the patient undergoes two imaging sessions, an MR imaging session and a CT imaging session. The MR dataset with its high soft tissue contrast enables precise visualization of the prostate target and adjacent rectum and bladder organs at risk, while the CT dataset provides electron density information for dose calculations. The two image sets are registered in the Varian Eclipse™ treatment planning system (TPS) and the anatomical target and normal tissue contours delineated on the MR scan are transferred to the CT scan. Dose calculation and beam definition are then performed on the CT scan. Virtual or digitally reconstructed radiographs (DRRs) are also generated from the CT scan which shows the location of implanted fiducial gold markers in the prostate relative to the beam isocenter. These are used as reference images to align the patient using orthogonal X-rays before treatment in one of our five Varian (Trilogy™ and TrueBeam™) linear accelerators.

MR-only workflow[1]

The MR-only workflow differs in that the only imaging session is the MR and a synthetic CT scan is produced for dose calculations and DRR generation [1]. This workflow reduces the patient and health system burden and reduces systematic errors in treatment planning introduced by image registration uncertainties. This project is a collaboration between the clinical/academic site the Department of Radiation Oncology, Calvary Mater Newcastle and the Biomedical Imaging Research Group of the Commonwealth

[1] Radiotherapy Planning where MR data is the only imaging information is ongoing research. The concepts and information presented in this article are based on research and are not commercially available. Its future availability cannot be ensured.

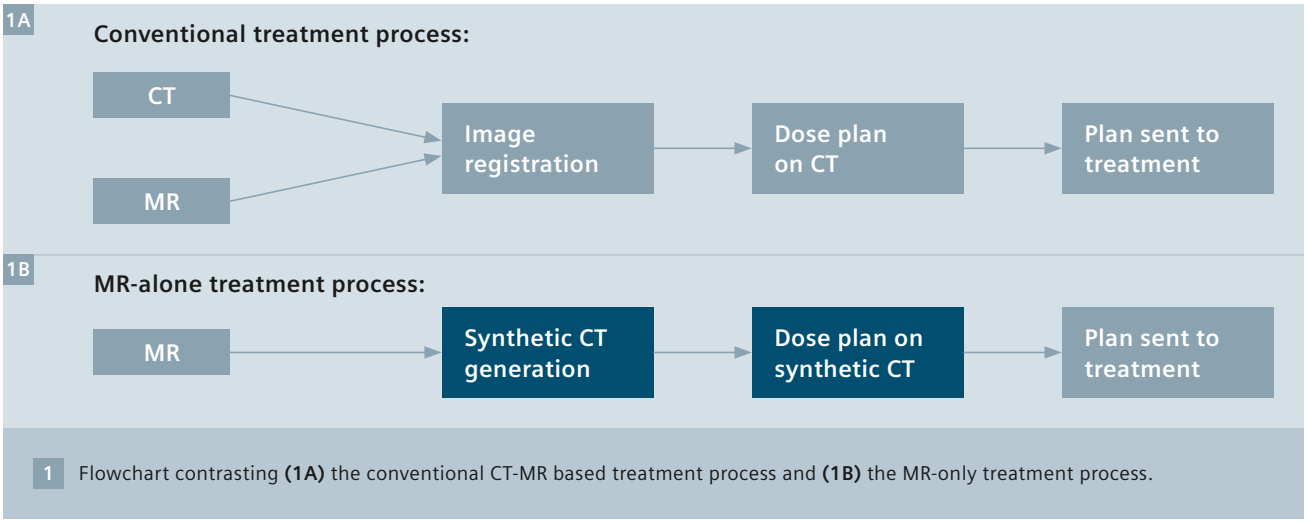

1 Flowchart contrasting **(1A)** the conventional CT-MR based treatment process and **(1B)** the MR-only treatment process.

Scientific and Industrial Research Organisation (CSIRO).

The major technical steps in the treatment process are setup and imaging of the patient in the 3T MAGNETOM Skyra suite, production of synthetic CT scans; contouring of relevant organs; beam definition and dose calculation in Eclipse; setup, image-guided positioning and treatment at the Linac.

To date 40 men with ages ranging from 58 to 78, undergoing prostate cancer radiation therapy treatment have been scanned under a research protocol. All prostate patients undergoing long fractionation treatment were eligible except that patients with hip prostheses were excluded due to distortions induced by metallic implants. Synthetic CT scans were produced for treatment planning comparisons to conventional CT based dose calculations.

Conventional MR scanning sequences are currently used for the MR-only workflow. Three sequences are used. The planning MR is a 3D, T2-weighted 1.6 mm isotropic voxel SPACE sequence with field-of-view (FOV) to cover the entire pelvis (ranging from 380-450 mm^2). The prostate delineation sequence is a 2D axial T2-weighted sequence with FOV approximately 200 × 200 mm^2. A further T1-weighted gradient echo sequence with flip angle 80 degrees is used to image the implanted prostate fiducial markers (gold seeds 1 × 3 mm). These sequences were acquired in 12-15 minutes total with 340 s for the planning MR, 235 s for the small FOV T2 scan and 186 s for the T1 flip 80 scan. Patients were MR imaged prior to treatment as close as possible to the acquisition of the conventional planning CT scan so that dose comparisons on synthetic CT and conventional CT could be made. Although not necessary for treatment planning a further set of weekly MR scans was obtained for each patient to examine patient anatomical and dose variations. Therefore the data set consists of one MR session of three sequences for RT planning and seven MR scanning sessions of three sequences throughout the duration of treatment.

Seven field intensity modulated treatment delivery is used at our Center for prostate treatments. The treatments are delivered in 39 fractions of 2 Gy per fraction. Typical margins are 7 mm with 5 mm posteriorly.

Simulation at the MR

The patient is positioned at MR in the treatment position. This is achieved with an MR compatible laser bridge for patient rotation alignment, a radiation therapy specific couch top and coil mounts (CIVCO, Rotterdam, The Netherlands) which hold the coils away from the patient surface so they do not disturb the patient position. The 3T images are utilized for both delineation of the target and normal tissues using the MR patient model and for the production of the synthetic CT for dose calculation and DRRs for image-guidance at treatment.

The synthetic CT scans are created using an enhancement of our previous single atlas method [2] that combines multi-atlas deformable registration to the patient MR scan and local weighted voting to assign a CT value to each voxel of the MR planning scan. Firstly an atlas database is created in two steps:

1. A set of matching patient MR and CT planning scans are acquired;
2. The patient CT scan is deformably registered to the corresponding patient MR scan to form conjugate MR-CT pairs with matching geometry.

Then to create synthetic CT scans from a subsequent patient planning MR scan the following steps are used:

1. Each atlas MR scan is deformably registered to the patient planning MR scan;
2. For each small region of the patient planning MR, the intensity is compared to the same region in all the registered atlas MR scans;
3. Each atlas scan is assigned a weighting according to the similarity of the region values with the most similar having the highest weighting (all assigned weights sum to 1);
4. The CT values from the corresponding region of the conjugate CT atlas scans are added together using the previously determined weightings to provide the CT intensity value of that region of the synthetic CT scan. Methods to automatically segment both prostate and normal tissues are also being developed which will further increase treatment planning efficiency [3, 4]. The bone contours on the MR scans can be segmented very accurately with the deformable image registration method.

2 Patient positioning for MR scanning showing the coil bridges.

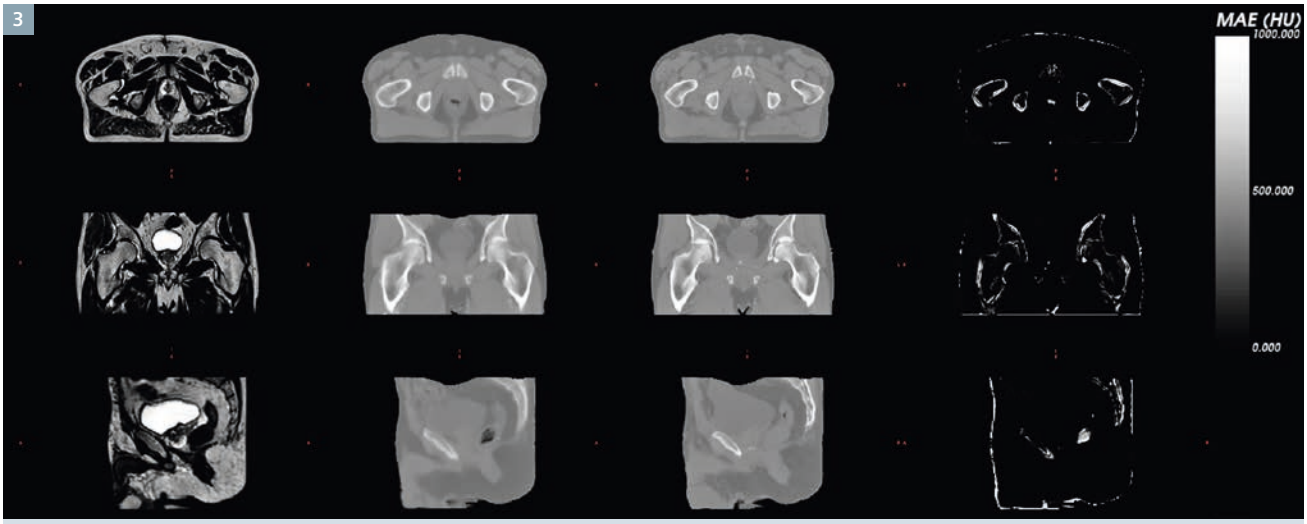

3 Shows axial, coronal and sagittal views from an original MR image of a 67-year-old study participant. The second column shows the automatically generated synthetic CT (sCT) with the original patient CT shown in the third column. The final column shows the difference between the synthetic and actual CT.

Treatment planning

The synthetic CT and MR images are imported to the Eclipse TPS with the AAA algorithm. The synthetic CT is first written to DICOM format with the header details written so that Eclipse interprets this as a CT scan for the patient. As the synthetic CT is created from the MR image data the scans are inherently registered. Target and normal tissue anatomy are delineated by the radiation oncologist on the MR scans. A treatment plan and dose calculation is then developed by the radiation therapist using the synthetic CT scan. The dose is then displayed for the radiation oncologist on the MR scan. The image guidance is performed using the Varian On-Board-Imager® and the treatment plan is delivered using the Varian Trilogy Linac.

Doses calculated on the synthetic CT scans were compared to gold standard doses calculated on the conventional CT scan with an average difference of 0.3% on average. A major advantage of the technique is that it does not require specialized sequences such as ultra-short echo time sequences. Only the single 3D SPACE sequence is required for synthetic CT generation which reduces the potential for patient motion compared with multi-sequence methods of generating synthetic CT that have been proposed [5, 6].

Conclusion

This study has shown that synthetic CT scans can be generated from MR scans using conventional T2-weighted sequences and that dose calculations are comparable to conventional CT scan dose calculations. Investigations of MR image distortion were also performed using test phantoms. Distortions in the region of the prostate were found to be sub-mm and distortions at the periphery were a maximum of 1.7 mm with the MAGNETOM Skyra 3D distortion correction applied. The MR-only workflow is efficient and only requires one imaging session for the patient. The next stage of our work is a prospective study where treatment will be performed using the MR-based treatment plan for a group of patients. MR-only prostate treatment planning is feasible and represents an improved process in radiation therapy planning.

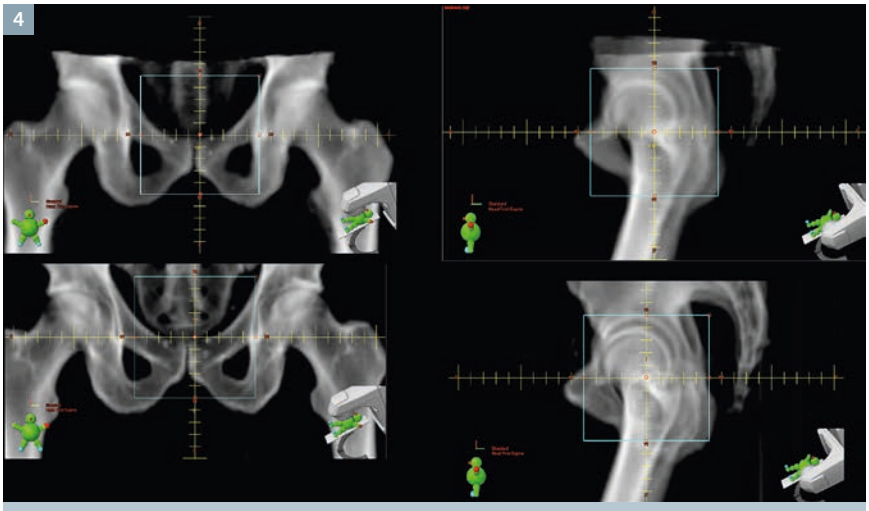

4 Anterior-posterior (AP) (left) and lateral (right) Digitally Reconstructed Radiographs (DRRs) generated from the MRI derived synthetic CT volume (top row) and actual planning CT (bottom row) for the same patient as in figure 3.

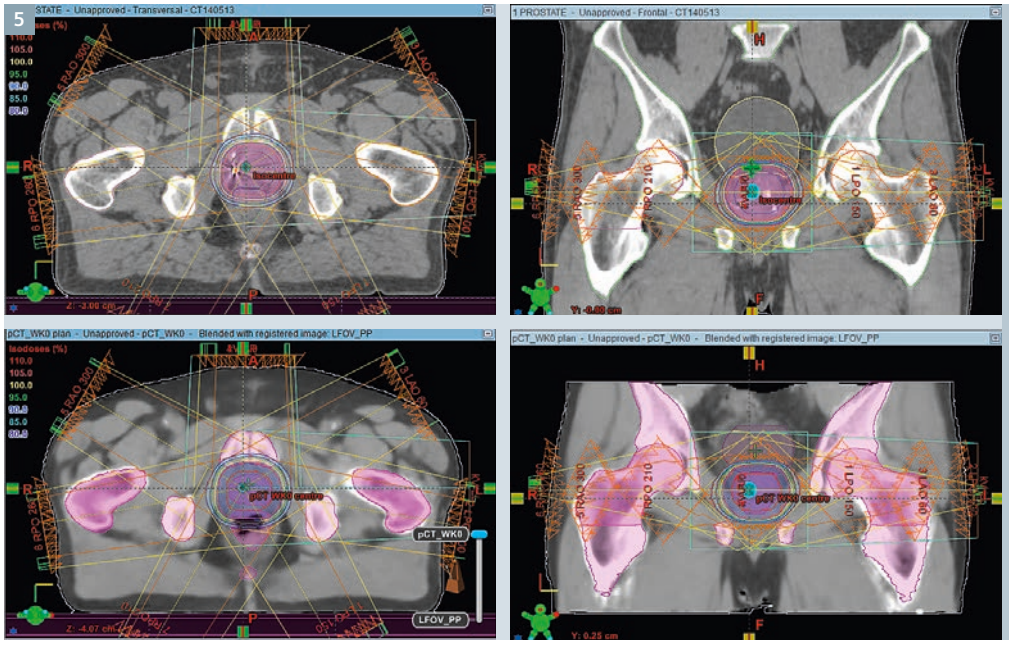

5 Screenshots from Eclipse TPS for the same patient as in figures 3, 4 showing comparison of dose calculation on conventional CT (top) and on synthetic CT (bottom). Contours displayed on the synthetic CT are the MR defined contours.

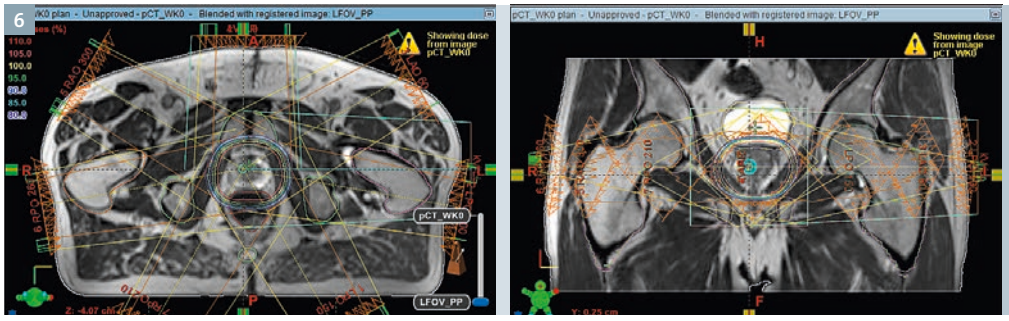

6 Screenshot from Eclipse TPS showing dose calculated on the synthetic CT scan displayed on the MRI scan.

Acknowledgments

This work was supported by Cancer Council New South Wales research grant RG11-05, the Prostate Cancer Foundation of Australia (Movember Young Investigator Grant YI2011) and Cure Cancer Australia.

References

1 Greer P, Dowling J, Lambert J, Fripp J, Parker J, Denham J, et al. A magnetic resonance imaging-based workflow for planning radiation therapy for prostate cancer. Med. J. Aust. 2011;194:S24.

2 Dowling JA, Lambert J, Parker J, Salvado O, Fripp J, Capp A, et al. An atlas-based electron density mapping method for magnetic resonance imaging (MRI)-alone treatment planning and adaptive MRI-based prostate radiation therapy. Int. J. Radiat. Oncol. Biol. Phys. 2012;83:e5–11.

3 Dowling JA, Fripp J, Chandra S, Pluim JPW, Lambert J, Parker J, et al. Fast automatic multi-atlas segmentation of the prostate from 3D MR images. Prostate Cancer Imaging. Image Analysis and Image-Guided Interventions. Springer; 2011. p. 10–21.

4 Chandra S, Dowling J, Shen K, Raniga P, Pluim J, Greer P, et al. Patient Specific Prostate Segmentation in 3D Magnetic Resonance Images. IEEE Transactions on Medical Imaging. 2012 Aug 2;31.

5 Johansson A, Karlsson M and Nyholm T, CT substitute derived from MRI sequences with ultrashort echo time, Med. Phys. 2011;2708-2714

6 Hsu, S-H, Cao Y, Huang K, Feng M, Balter JM, Investigation of a method for generating synthetic CTmodels from MRI scans of the head and neck for radiation therapy, Phys. Med. Biol. 2013;8419-8435.

Contact

Peter Greer
Principal Physicist
Calvary Mater Newcastle
Corner of Edith & Platt Streets
Waratah, NSW, 2298 Australia
Phone: +61 2 4014 3689
peter.greer@newcastle.edu.au

Contact

Jason Dowling
Research Scientist
CSIRO, Australian e-Health Research Centre
Level 5 – UQ Health Sciences Building
Royal Brisbane and Women's Hospital
Herston, QLD, 4029 Australia
Phone: +61 7 3253 3634
Jason.Dowling@csiro.au

4D-MRI: Future of Radiotherapy of Moving Targets?

Kinga Barbara Bernatowicz; Rosalind Lucy Perrin; Marta Peroni; Damien Charles Weber; Antony John Lomax

Center for Proton Therapy (CPT), Paul Scherrer Institut, Villigen PSI, Switzerland

Background

4D-CT imaging is widely used in radiotherapy planning of moving tumors to account for motion, and to provide the physical properties of tissue for dose calculations, e.g. electron density for conventional radiation therapy or proton stopping power for proton therapy. However, it is limited to representing only a single, averaged breathing cycle, often contains imaging artifacts, and contributes a substantial dose exposure for the patient. To overcome these issues, a 4D-MRI imaging protocol applied to evaluating respiratory motion of the liver was proposed by von Siebenthal et al. [1].

This approach is capable of resolving irregular respiratory motion, with the added benefit of delivering no imaging dose to the patient. Unfortunately, whilst being a promising technique, MR imaging alone does not provide the physical properties of tissue required for accurate dose calculations. However, by combining the motion information provided by 4D-MRI, with the density data provided by single phase CT data, the advantages of motion imaging with 4D-MRI can now be applied to radiotherapy applications.

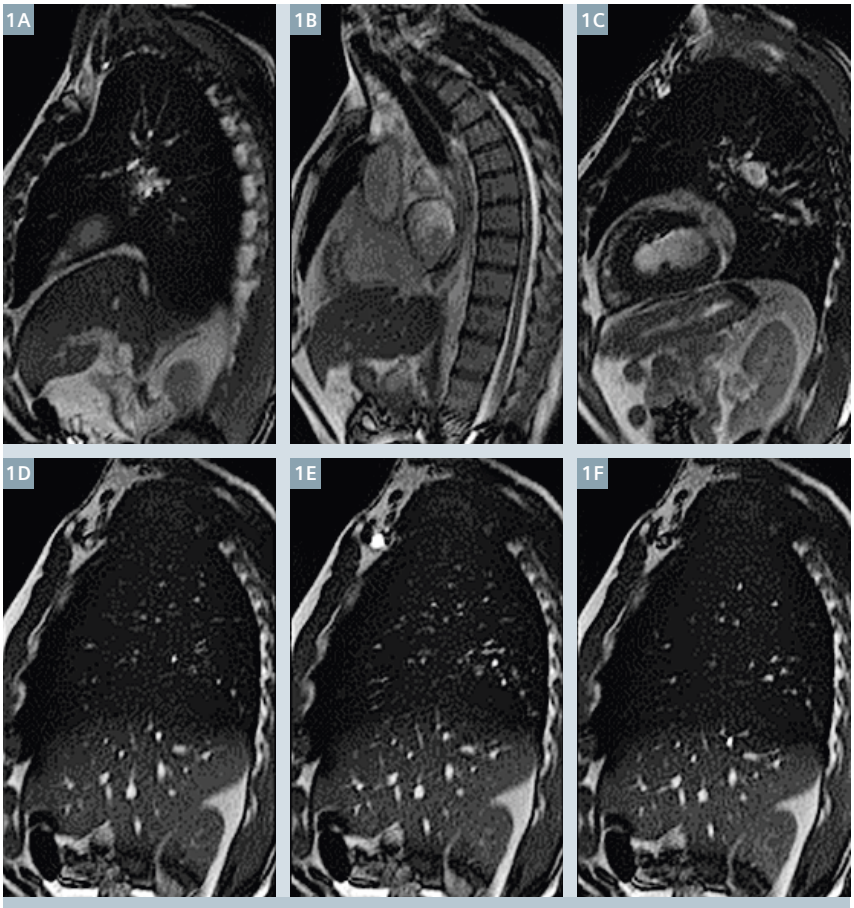

1 Sagittal slices through the thorax and upper abdomen, showing image slices **(1A–C)** and navigator slices **(1D–F)** acquired with the experimental 4D-MRI protocol*.

4D-MRI acquisition

The 4D-MRI protocol relies on the interleaved acquisition of a 'navigator' and different image slices in the sagittal plane (Fig. 1). The navigator is fixed at a single position throughout the acquisition time, and describes the motion state of the volume of interest at any instant during the acquisition. The actual 2D image slice is then scanned through the planned field-of-view (FOV).

This experimental sequence* does not make any assumptions about the breathing amplitude, its regularity, or the number of reconstructed phases. In contrast, commonly used methods for 4D imaging use a one-dimensional respiratory signal for sorting the 2D images, whereas 4D-MRI images can be retrospectively sorted based directly on the acquired navigator frames. The correspondence of the imaging slices is then established by comparing the two temporally embracing navigator frames (see Fig. 2). If these navigator frames are similar, the image slices can be stacked into a (3D) volume with the same time stamp and therefore, a complete 4D image data set with the same temporal resolution as the navigator frames can be reconstructed.

This approach has now been implemented on a 1.5T MAGNETOM Aera MR system (Siemens Healthcare, Erlan-

* Work in progress, the product is currently under development and is not for sale in the US and in other countries. Its future availability cannot be ensured. The product is not yet licensed for sale in Canada, in accordance with Canadian Law. Performance claims have not been reviewed by Health Canada, and are subject to change. Its future availability cannot be guaranteed.

2

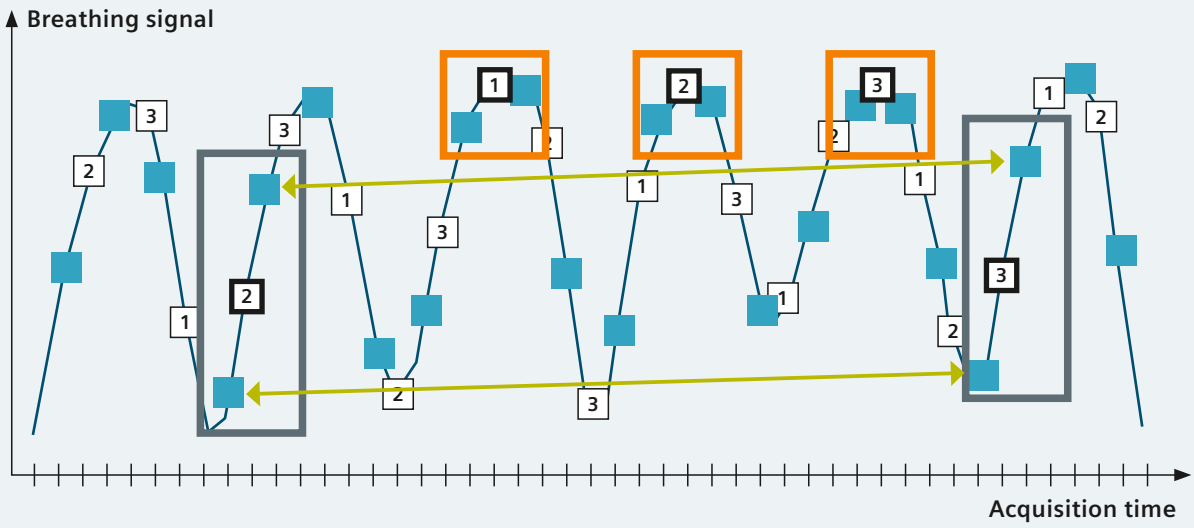

2 Acquisition of slices (white boxes) and embracing navigator frames (blue boxes). Slices associated with the same volume are matched by comparing navigator pairs (green arrows) [2].

gen, Germany) using an experimental version of the balanced steady state free precession sequence (TrueFISP)*. Images are acquired in batches of 3-5 minute duration, with up to one hour of total acquisition time and with image slice thicknesses of 4 to 6 mm. Recent advances in the field are now looking at the simultaneous acquisition of navigator and data slices, with use of other advanced sequences, for example CAIPIRINHA [3].

Applications

- **Intra- and inter-fraction motion studies**
  Since MRI involves no radiation dose to patients or volunteers, 4D-MRI protocols allow for repeated studies on the same subject and/or for longer time period acquisitions in order to capture breathing variability (Fig. 3). Motion deformation fields can also be extracted using deformable image registration.
- **Mapping motion from MRI-CT**
  The 4D-CT (MRI) method has now been developed within our group for simulating many 4D-CT data sets from a single, static reference CT and a data-base of motion deformation fields extracted from 4D-MRI studies [4]. The mapping of motion information from 4D-MRI onto CT images is thereby achieved using subject-specific or population-based models, based on the establishment of mechanical correspondences between structures of interest (e.g. the liver). The resulting 4D-CT (MRI) images are of good quality when compared to 4D-CT (Fig. 4), and now represent the tissue properties necessary for dose calculations, whilst incorporating the motion information provided by 4D-MRI.
- **4D dose calculations in radiotherapy**
  Including the realistic, variable respiratory motion in provided by 4D-CT (MRI) data into 4D dose calculations, opens the door to novel future applications. Based on such data sets, advanced imaging and delivery methods, such as beam tracking (Fig. 5), can now be evaluated and comprehensive 4D planning studies and robustness evaluations performed.

3

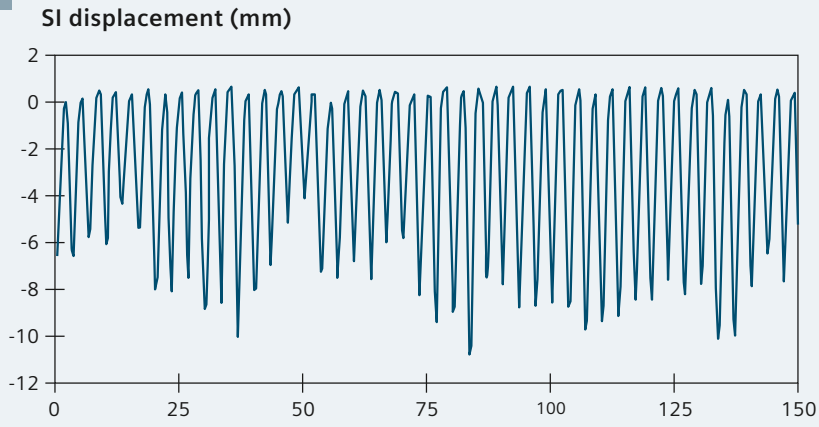

3 Example of extracted 2.5 minute trace of the average liver SI motion [2].

* Work in progress, the product is currently under development and is not for sale in the US and in other countries. Its future availability cannot be ensured. The product is not yet licensed for sale in Canada, in accordance with Canadian Law. Performance claims have not been reviewed by Health Canada, and are subject to change. Its future availability cannot be guaranteed.

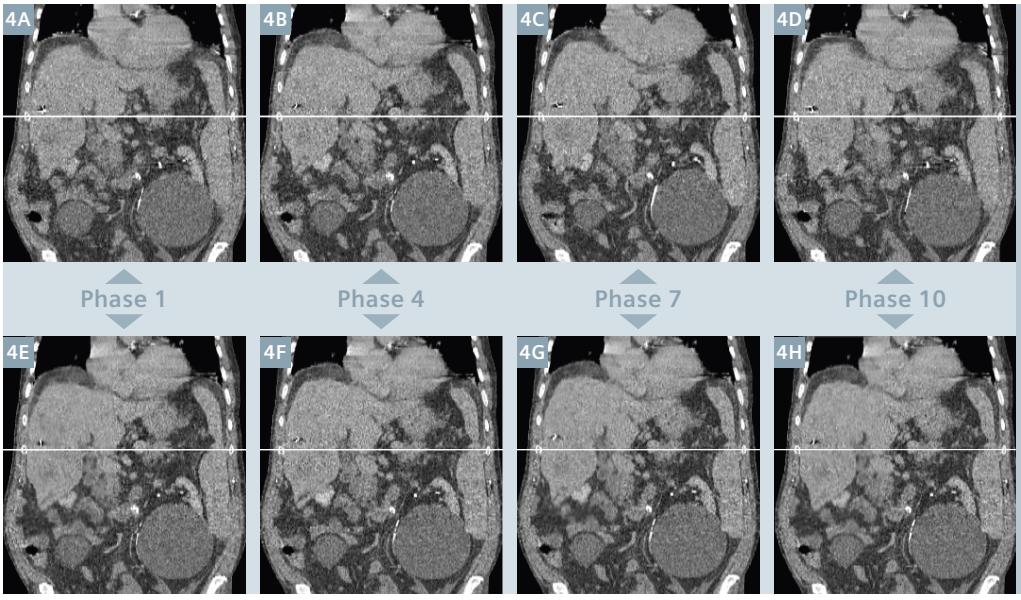

4 Comparison of different breathing phases of 4D-CT **(4A–D)** and 4D-CT (MRI) image sets **(4E–H)** simulated from the 4D-MRI motion library and a reference CT [4].

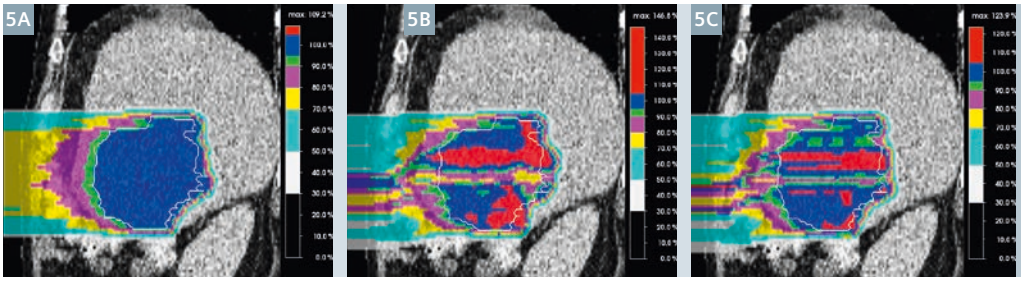

5 4D dose calculation results for different scanned proton tracking techniques based on 4D-CT (MRI) [5, 6].

Summary

4D-MRI, combined with CT data to produce 4D-CT (MRI) data sets, is a powerful new technique for imaging and modeling motion for radiotherapy applications. It allows for accurate modeling of motion variability, an important limitation of current 4D-CT techniques, and will allow in the future for the acquisition of patient specific motion libraries for advanced motion mitigation techniques such as tracking and re-tracking [5, 6].

References

1 von Siebenthal M, Székely G, Gamper U, Boesiger P, Lomax A, Cattin P., 4D MR imaging of respiratory organ motion and its variability., Phys Med Biol. 2007 Mar 21;52(6):1547-64. Epub 2007 Feb 16.

2 PhD Thesis, von Siebenthal, M. 2008, http://www.vision.ee.ethz.ch/~organmot/chapter_publications.shtml

3 Celicanin Z, Bieri O, Preiswerk F, Cattin P, Scheffler K, Santini F., Simultaneous acquisition of image and navigator slices using CAIPIRINHA for 4D MRI., Magn Reson Med. 2014 Feb 24. doi: 10.1002/mrm.25134. [Epub ahead of print].

4 Boye D, Lomax T, Knopf A., Mapping motion from 4D-MRI to 3D-CT for use in 4D dose calculations: a technical feasibility study. Med Phys. 2013 Jun;40(6):061702. doi: 10.1118/1.4801914.

5 Zhang Y., Knopf A, Tanner C, Boye D, Lomax AJ., Deformable motion reconstruction for scanned proton beam therapy using on-line x-ray imaging., Phys Med Biol. 2013 Dec 21;58(24):8621-45. doi: 10.1088/0031-9155/58/24/8621. Epub 2013 Nov 21.

6 Zhang Y, Knopf A, Tanner C, Lomax AJ., Online image guided tumour tracking with scanned proton beams: a comprehensive simulation study., Phys Med Biol. 2014 Nov 24;59(24):7793-7817. doi:10.1088/0031-9155/59/24/7793.

Contact

Kinga Barbara Bernatowicz
Paul Scherrer Institute
5323 Villigen PSI
Switzerland
kinga.bernatowicz@psi.ch

SIEMENS

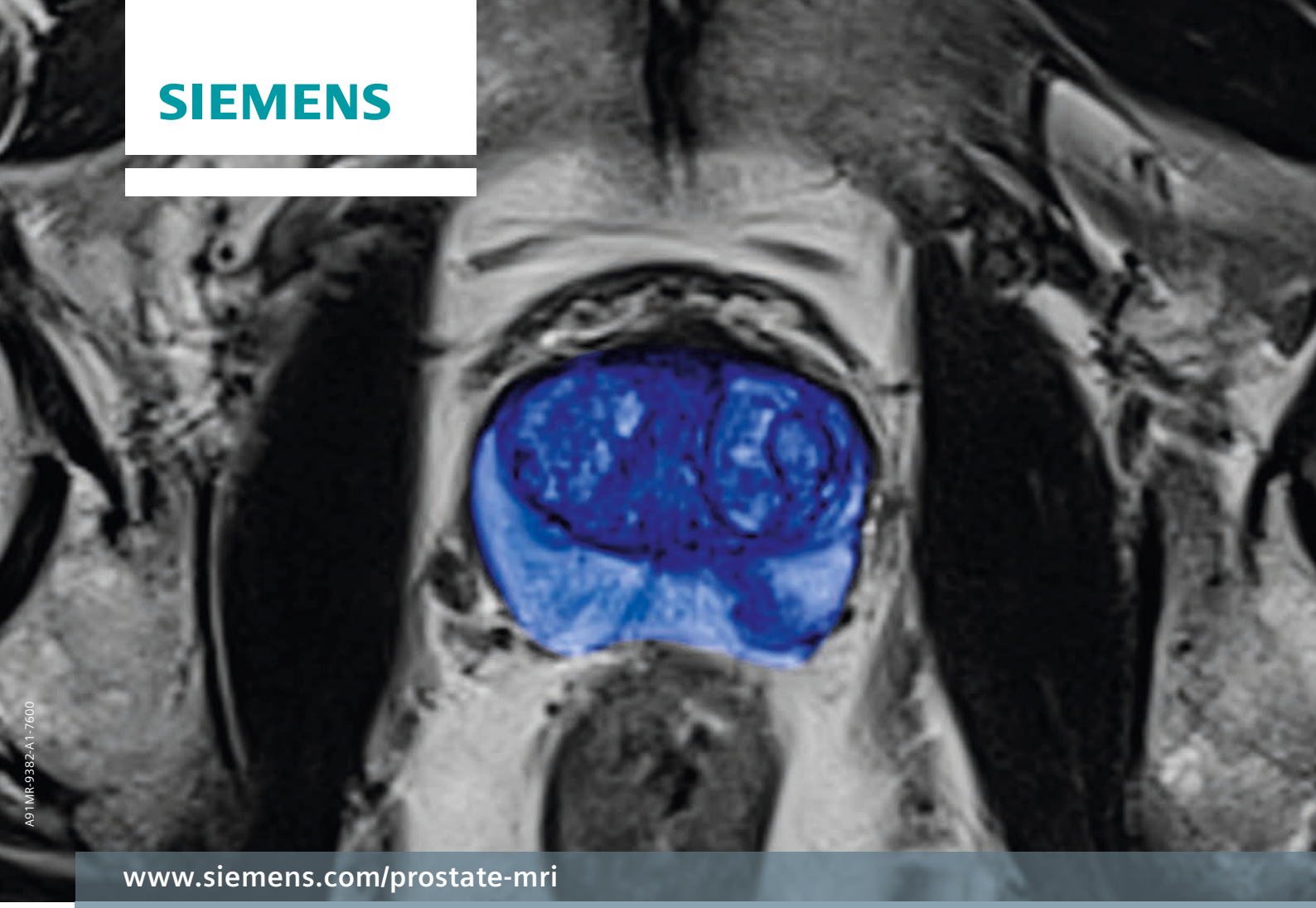

A91MR-9382-A1-7600

www.siemens.com/prostate-mri

SEEit – accelerate accuracy

New certainty in prostate cancer assessment.

One out of six men will develop prostate cancer during their lifetime.[1] Conventional diagnosis via trans rectal ultrasound-guided biopsy is not only a painful invasive procedure, it is also "blind" and misses cancer in up to 20% of all cases.[2]

In contrast, **MRI can exclude life-threatening cancer with more than 89% certainty and help reduce the need for biopsy in patients with suspected prostate cancer by up to 51%.**[3] This makes MRI currently the most sensitive technique to diagnose prostate cancer.

SEEit[4] was designed to increase clinical and financial performance.

It allows for accelerated non-invasive Prostate MRI in **10 minutes.** To further increase process efficiency, Siemens offers standardized reporting tools to communicate the findings in an easy and standardized manner.

[1] http://seer.cancer.gov/statfacts/html/prost.html

[2] http://www.nhs.uk/Conditions/Cancer-of-the-prostate/Pages/Diagnosis.aspx

[3] Pokorny et al. EUR UROL 2014:66:22–29; Abd-Alazeez Nature PCAN 2014:17:40–46

[4] The product is still under development and not commercially available yet. Its future availability cannot be ensured.

Answers for life.

Technical Aspects of MR-only Radiotherapy

Tufve Nyholm, Joakim Jonsson

Umeå University, Sweden

Introduction

Magnetic resonance imaging (MRI) has emerged as a key component in modern radiotherapy. The superior soft tissue contrast compared to computed tomography (CT) allows for increased accuracy in the definition of both target and organs at risk [7] using commonplace sequences [29]. Functional imaging techniques, primarily diffusion-weighted imaging and dynamic contrast enhanced imaging, are currently studied as a means of identifying areas within a tumor that require a higher dose in dose-painting trials [41]. Several current studies also aim to evaluate the possibilities of early treatment response assessment using MRI [25], which could enable treatment adaptation. At present, the main rationale of integrating MRI into the radiotherapy workflow is the gain in accuracy in target volume definitions. For several major patient groups, MR imaging is preferable from a medical point of view, i.e. for tumor definition [5, 27, 30]. CT or CT equivalent information is still, however, required for the technical aspects of treatment planning such as:

- accurate dose calculations, which depend on knowledge of the attenuation properties of the tissue measured in a CT exam and
- generation of reference images which are used for patient positioning based on in-room X-ray imaging.

Therefore, it is common practice to acquire both CT and MR data and align these image series in the same coordinate system, or frame of reference, through image registration. The MR data is used to define the target volume and the CT data to plan the treatment and serve as a reference for patient positioning. This workflow is, however, not optimal for several reasons. Besides the increase in cost and workload when using multiple imaging modalities, there is also an introduction of additional geometrical uncertainty due to the image registration.

Image registration is commonly performed at many clinics in order to align two image sets within a common frame of reference. Depending on the purpose of the image registration and the properties of the available image data, the registration can be performed in several ways. Mutual information rigid registration, based either on the full image volume or a smaller sub-volume, is available in most clinical treatment planning systems. For prostate cancer cases, where gold fiducial markers are commonly used, landmark registration methods can be employed in order to co-register MRI data to the planning CT. Manual registration, which is a robust but time-consuming method, is also an option. Regardless of method, image registration is a tricky business for several reasons. First off, for clinical cases we never know the correct alignment of two images, which makes it difficult to assess the uncertainties of a specific method. Phantom studies and purely digital experiments are unlikely to reflect the full complexity of the clinical case. Secondly, and related to the aforementioned problem, is the lack of robust quality measures for individual registrations. Finally, the task may actually be close to impossible, regardless of registration method. An example could be a prostate case without implanted fiducial markers. MRI is the imaging modality of choice for target definition, due to the greater soft tissue contrast. The prostate behaves much in the same way as other soft tissue tumors, i.e. its position in the body is not fixed and the spatial relation to surrounding bony anatomy may vary. This implies that a sub-volume based registration algorithm would be suitable in order to avoid any negative influence the surrounding anatomy may have on the registration. Although there are limited references regarding the matter, it is reasonable to assume that the limited soft tissue contrast in, and in close proximity to, the prostate gland in the CT image set would degrade the quality of a multi-modal sub-volume

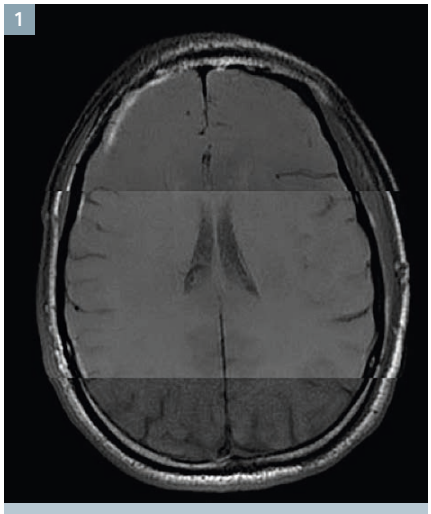

1 Top 40 Hz/pixel, mid 100 Hz/pixel, bottom 400 Hz/pixel. Notice differences in signal-to-noise but especially geometrical differences.

registration. In other words, the reason that soft tissue registrations between MR and CT images will be associated with substantial uncertainties is exactly the same reason why we need MR image data to begin with; we lack sufficient anatomical information on soft tissue in the CT images. For the sake of balance, it should be said that for some indications, such as intracranial lesions, including larger volumes in the registration is not associated with any added uncertainty since the soft tissue is relatively fixed with respect to the bony anatomy. Even in those cases, however, image registration uncertainty is still a factor to consider. Ulin et al. [42] investigated the clinical variability of MR-CT registrations for one patient with an intracranial lesion for 45 clinics. The analysis revealed a standard deviation of 2.2 mm, which only accounts for the variability among the observers. There may still be a systematic component on top of this.

In summary, MR imaging has been shown to increase the geometrical accuracy in the definition of target volume. The challenge today is to make sure that we can radiate this target volume in an accurate and precise manner. This problem can be reduced into several sub-problems, e.g. control over geometrical distortions in the MR images; differences in the patient setup in the MR scanner compared to treatment; and registration uncertainties introduced when MR and CT data is placed in the same coordinate system. In this article we provide a brief overview of the current knowledge regarding geometrical distortions and patient setup in the radiotherapy context and describe the problems and proposed solutions for MR only radiotherapy.

MR image distortions

Geometric distortions in MR images can be caused by the system itself, from nonlinearities in the magnetic gradients or inhomogeneities in the static magnetic field. Nonlinearities in the gradients can be characterized and corrected using spherical harmonics expansions of the fields generated by the gradient coils and can be accurately corrected using software supplied by the MR vendors.

Distortions can also be caused by the imaged object in the form of chemical shift or magnetic susceptibility artefacts. Image distortions due to susceptibility effects and chemical shift in conventional MR imaging are inversely proportional to the gradient field strength, so that stronger gradients will minimize such distortions at a cost of more image noise. Phantom studies have shown the residual distortion for clinical sequences to be within 1 mm [18, 31]. Object-induced distortion effects have also been investigated in clinical data and the effect proved to be small for internal structures relevant for prostate treatments [28]. In general, anatomical imaging sequences using relatively high bandwidths reduce distortions caused by susceptibility effects and chemical shift to an acceptable level for radiotherapy [26, 40]. Methods using post-processing corrections [35] or special modes of acquisition [6] have also been studied.

Some MR protocols are more sensitive to geometric distortions, echo planar imaging being one example. Such sequences can display significant geometric distortions due to susceptibility effects, and must be handled with care when used for radiotherapy purposes.

MR imaging using immobilization equipment

Planning CT scans are normally acquired using flat table tops to match the flat treatment couch used at the accelerator. The standard patient support is concave in most MRI scanners, although some have flat couches. The problem of concave patient supports is easily surmounted, either by manufacturing a flat table top insert at the hospital or by purchasing a commercial solution. Flat table tops are necessary if patient immobilization is to be used at the MRI scanner.

A more intricate problem is MRI compatibility of the immobilization equipment, both in material properties and size. MR safe materials must be used for base-plates, nuts, bolts and other fittings. A traditional plastic face mask for head and neck immobilization is normally constructed in MR safe materials; however, a standard MRI head coil will not be able to accommodate it. By using surface coils (i.e. flex coils) instead, imaging of the immobilized head and neck is possible, although a dedicated head coil still provides higher quality images [10]. When using surface coils for radiotherapy planning, care must be taken not to place the coils directly on the skin of the patient since the external anatomy may be distorted. Instead, the coils should be placed either hanging from a frame or on top of a holder close to the patient surface, without touching it. Nowadays, MRI compatible immobilization equipment and coil holders are commercially available.

MR-only radiotherapy[1]

In this article, we define MR-only radiotherapy as external beam radiotherapy where MR data is the only imaging information that is used for the planning and preparation of the treatment. Arguments for an MR-only workflow commonly include the avoidance of image registration in the planning stage of the treatment [1, 4, 8, 15, 18, 19, 20, 23, 31, 33, 39], reduced costs due to less imaging or a simplified workflow [1, 4, 8, 24, 39], and reduced exposure to unspecifically aimed radiation [4, 18, 39].

[1] Radiotherapy Planning where MR data is the only imaging information is ongoing research. The concepts and information presented in this article are based on research and are not commercially available. Its future availability cannot be ensured.

2

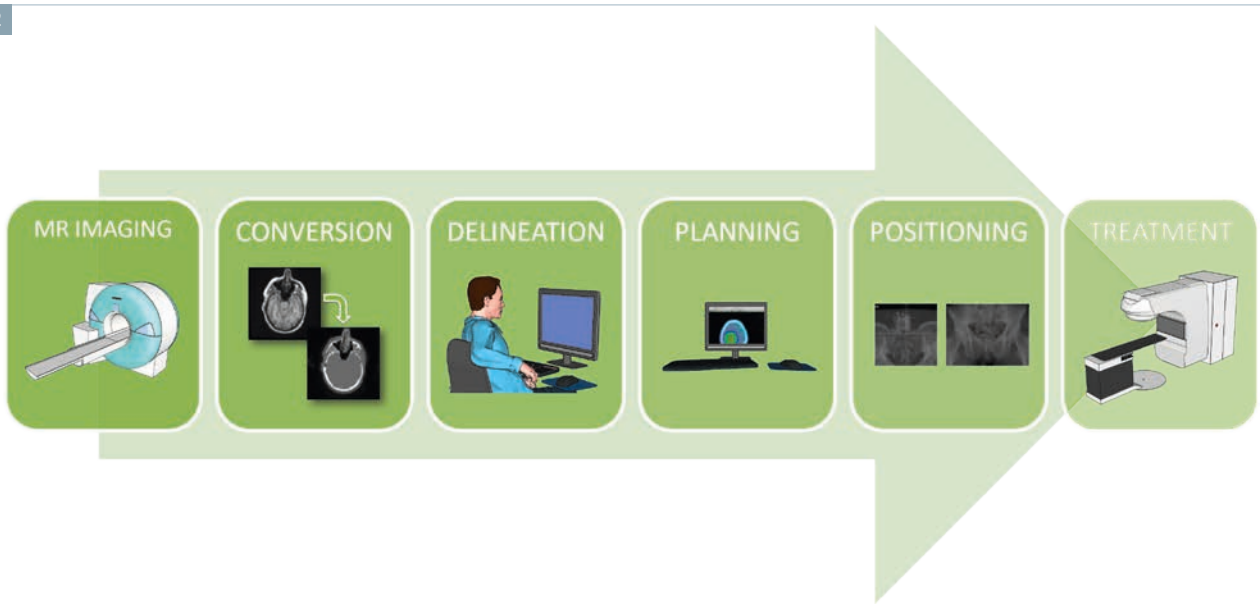

2 Simple schematic displaying the MR-only radiotherapy workflow. The difference from the traditional radiotherapy workflow is mainly the exclusion of CT imaging and registration and the addition of the conversion step.

Current methods of accurate dose calculations rely heavily on CT (or CT equivalent) information due to the relationship between Hounsfield units and electron density, and will probably continue to do so for the foreseeable future. Therefore, a reliable conversion method from MR information to CT equivalent information will be necessary for an MR-only workflow in radiotherapy. Several methods have been investigated by multiple research teams.

Manual bulk density assignment

A method that has been researched extensively is segmentation, i.e. dividing the image into classes with different attenuation properties. The simplest form of segmentation is to only use one tissue class and assign a bulk density to the entire patient, typically that of water or a mixture of adipose tissue and muscle. Even though this is an extremely simplified version of reality, it yields acceptable dosimetric results. Typical dosimetric differences from inhomogeneity corrected CT based dose calculations using this approach have been reported to be within 2-3% for prostate and intracranial target volumes [9, 17, 22, 23, 32, 33, 38]. A significant problem with this approach is that the traditional method of patient positioning at treatment depends on anatomical reference images that visualize bony anatomy. To overcome this issue, the number of tissue classes can be increased to include e.g. bone, soft tissue, lung tissue and air, and assign each tissue class an appropriate bulk density. In addition to making the creation of anatomical reference images possible, this also increases the dosimetric accuracy to around 1% for intracranial targets volumes [17, 22, 38] and between 1-2% for prostate treatments [17, 23].

Although the dosimetric results are relatively accurate, the method of manual density assignment has problems – the method relies on the precision of the operator that defines the anatomy in the MR images. This is of limited importance in the dosimetric aspect, but may have substantial impact on the subsequently generated positioning references. Also, the method is so labor intensive and time consuming that it is not feasible for widespread clinical implementation. In order to accomplish such a development, automated conversion methods from MR to s-CT data are needed.

Atlas methods

One method for automatically generating s-CT data is the combined MR-label image atlas. By deformably registering the atlas MR image to a new patient MR image and applying the resulting deformation field to the corresponding label image, a new image can be created based on the data in the label image. The label image can contain any information, e.g. CT or attenuation data. This approach has been used for attenuation correction applications in PET/MRI [37] as well as for dose calculation purposes in radiotherapy [8]. Atlas methods do not normally rely on tissue segmentation; instead, the full complexity atlas label image is warped onto the patient shape. Dosimetric results indicate accuracy comparable to bulk density assignment; for the radiotherapy application, Dowling et al. [8] reported point dose differences between atlas label image and CT based calculations of about

2%. Atlas based methods are normally sensitive to atypical anatomy; e.g. in the study by Dowling et al., 2 out of 39 patients had to be excluded for this reason. Although atlas based methods are fairly robust and automatic, an argument can be made that the deformable image registration is associated with a considerable geometric uncertainty. This uncertainty is introduced into the treatment if the deformed label image is used to create the positing reference image and not solely for dose calculations.

Direct conversion

With the advent of ultra-short echo time imaging (UTE), interest has increased for direct conversion of MR image intensities to Hounsfield units. Since cortical bone appears as a signal void in traditional MR imaging, it has been impossible to distinguish it from air. UTE imaging samples the signal during the free induction decay, before the signal from cortical bone and other tissues with short T2 relaxation times has vanished [36], making it possible to discriminate such tissues from air. Even though UTE images renders signal from bone, it is not presently possible to find any single MR sequence which is directly convertible to Hounsfield units – more information is necessary. Several researchers have suggested using UTE sequences with several different echo-times to segment soft-tissue, air and bone [2, 3, 21]. This technique is fully automatic and preserves the geometric integrity of the input image. UTE images suffer from the same system related distortions as traditional MR sequences; however, the fast radial sampling makes it less sensitive to common object related distortions such as chemical shift and susceptibility effects. An alternative to the previously mentioned segmentation approach is to build a statistical model that relates MR voxel intensities to Hounsfield units [12, 34]. Such an approach yields an s-CT image with a continuous Hounsfield unit distribution, as well as making it possible to estimate the uncertainties in the conversion [13]. Recent studies

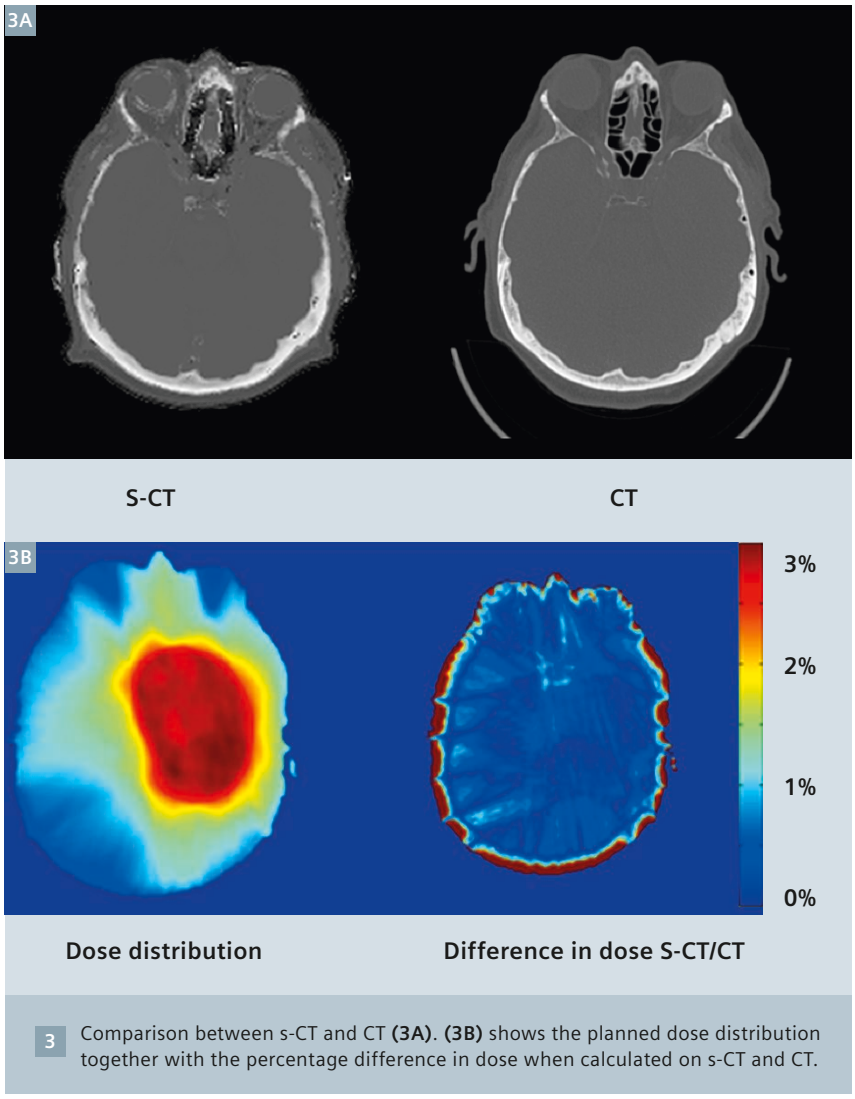

3 Comparison between s-CT and CT **(3A)**. **(3B)** shows the planned dose distribution together with the percentage difference in dose when calculated on s-CT and CT.

compared dose calculations on s-CT data with CT data, and found statistically insignificant dose differences of less than ±0.5% for intracranial targets [14, 16].

It is also possible to combine segmentation methods with direct conversion. A recent study [19] investigated the accuracy of a conversion method were the pelvic bone structures were first delineated manually. These delineations then served as input for a direct conversion method which could successfully convert the image intensities from standard MRI sequences to Hounsfield units. When the entire remaining anatomy was set to a bulk density, all points within the prostate PTV were within ±1.3% of the dose calculated on the standard CT input data.

The atlas registration approach can also produce segmentations that can serve as input for a later stage direct conversion. Hoffman et al. [11], which employed this approach for attenuation correction of PET/MR images, demonstrated that the method could accurately predict the attenuation map of a patient from MR input data. No systematic differences were found between PET images corrected with s-CT data and actual CT data. These combined methods ease the demand on the local accuracy of the segmentation, since the final conversion is performed using direct voxel wise conversion.

Summary

Radiotherapy is a local treatment modality that is highly dependent on image guidance. Over the last decade there has been an increased clinical use of both MRI and PET to enable accurate delineation of the target volume. However, the radiotherapy workflow does still depend on CT information as the treatment planning softwares require attenuation data to be able to perform accurate dose calculation and to generate reference images for positioning. It has been shown that it is possible to generate CT equivalent information based on MR data, and with this technology it will be possible to abandon the CT in the future for those diagnoses where MR is the modality of choice for target delineation. Imaging in treatment position and risk of geometrical distortions are two other areas that need to be addressed when introducing an MR scanner in the radiotherapy environment.

Contact

Tufve Nyholm
Department of Radiation Sciences
Umeå University
Umeå
Sweden
Phone: +46 90 785 8432
tufve.nyholm@umu.se

References

1 Beavis, A W, P Gibbs, R A Dealey, and V J Whitton. 1998. "Radiotherapy Treatment Planning of Brain Tumours Using MRI Alone." The British Journal of Radiology 71 (845): 544–48.

2 Berker, Yannick, Jochen Franke, André Salomon, Moritz Palmowski, Henk C W Donker, Yavuz Temur, Felix M Mottaghy, et al. 2012. "MRI-Based Attenuation Correction for Hybrid PET/MRI Systems: A 4-Class Tissue Segmentation Technique Using a Combined Ultrashort-Echo-time/Dixon MRI Sequence." Journal of Nuclear Medicine 53 (5): 796–804. doi:10.2967/jnumed.111.092577.

3 Catana, Ciprian, Andre van der Kouwe, Thomas Benner, Christian J Michel, Michael Hamm, Matthias Fenchel, Bruce Fischl, Bruce Rosen, Matthias Schmand, and A Gregory Sorensen. 2010. "Toward Implementing an MRI-Based PET Attenuation-Correction Method for Neurologic Studies on the MR-PET Brain Prototype." Journal of Nuclear Medicine 51 (9): 1431–38. doi:10.2967/jnumed.109.069112.

4 Chen, Lili, Robert a Price, Lu Wang, Jinsheng Li, Lihong Qin, Shawn McNeeley, C-M Charlie Ma, Gary M Freedman, and Alan Pollack. 2004. "MRI-Based Treatment Planning for Radiotherapy: Dosimetric Verification for Prostate IMRT." Int J Radiat Oncol Biol Phys 60 (2): 636–47. doi:10.1016/j.ijrobp.2004.05.068.

5 Chung, Na Na, Lai Lei Ting, Wei Chung Hsu, Louis Tak Lui, and Po Ming Wang. 2004. "Impact of Magnetic Resonance Imaging versus CT on Nasopharyngeal Carcinoma: Primary Tumor Target Delineation for Radiotherapy." Head & Neck 26 (3): 241–46. doi:10.1002/hed.10378.

6 Crijns, S P M, C J G Bakker, P R Seevinck, H de Leeuw, J J W Lagendijk, and B W Raaymakers. 2012. "Towards Inherently Distortion-Free MR Images for Image-Guided Radiotherapy on an MRI Accelerator." Physics in Medicine and Biology 57 (5): 1349–58. doi:10.1088/0031-9155/57/5/1349.

7 Dirix, Piet, Karin Haustermans, and Vincent Vandecaveye. 2014. "The Value of Magnetic Resonance Imaging for Radiotherapy Planning." Seminars in Radiation Oncology 24 (3). Elsevier: 151–59. doi:10.1016/j.semradonc.2014.02.003.

8 Dowling, Jason A, Jonathan Lambert, Joel Parker, Olivier Salvado, Jurgen Fripp, Anne Capp, Chris Wratten, James W Denham, and Peter B Greer. 2012. "An Atlas-Based Electron Density Mapping Method for Magnetic Resonance Imaging (MRI)-Alone Treatment Planning and Adaptive MRI-Based Prostate Radiation Therapy." Int J Radiat Oncol Biol Phys 83 (1). Elsevier Inc: e5–11. doi:10.1016/j.ijrobp.2011.11.056.

9 Eilertsen, Karsten, Line Nilsen Tor Arne Vestad, Oliver Geier, and Arne Skretting. 2008. "A Simulation of MRI Based Dose Calculations on the Basis of Radiotherapy Planning CT Images." Acta Oncologica 47 (7): 1294–1302. doi:10.1080/02841860802256426.

10 Hanvey, S, M Glegg, and J Foster. 2009. "Magnetic Resonance Imaging for Radiotherapy Planning of Brain Cancer Patients Using Immobilization and Surface Coils." Physics in Medicine and Biology 54 (18): 5381–94. doi:10.1088/0031-9155/54/18/002.

11 Hofmann, Matthias, Florian Steinke, Verena Scheel, Guillaume Charpiat, Jason Farquhar, Philip Aschoff, Michael Brady, Bernhard Schölkopf, and Bernd J Pichler. 2008. "MRI-Based Attenuation Correction for PET/MRI: A Novel Approach Combining Pattern Recognition and Atlas Registration." Journal of Nuclear Medicine 49 (11): 1875–83. doi:10.2967/jnumed.107.049353.

12 Johansson, Adam, Mikael Karlsson, and Tufve Nyholm. 2011. "CT Substitute Derived from MRI Sequences with Ultrashort Echo Time." Medical Physics 38 (5): 2708. doi:10.1118/1.3578928.

13 Johansson, Adam, Yu Yun, Thomas Asklund, Mikael Karlsson, and Tufve Nyholm. 2012. "Voxel-Wise Uncertainty in CT Substitute Derived from MRI." Medical Physics 39 (6): 3283–90. doi:10.1118/1.4711807.

14 Jonsson, Joakim H, Mohammad M Akhtari, Magnus G Karlsson, Adam Johansson, Thomas Asklund, and Tufve Nyholm. 2015. "Accuracy of Inverse Treatment Planning on Substitute CT Images Derived from MR Data for Brain Lesions." Radiation Oncology (London, England) 10 (1): 13. doi:10.1186/s13014-014-0308-1.

15 Jonsson, Joakim H, Anders Garpebring, Magnus G Karlsson, and Tufve Nyholm. 2012. "Internal Fiducial Markers and Susceptibility Effects in MRI-Simulation and Measurement of Spatial Accuracy." Int J Radiat Oncol Biol Phys 82 (5): 1612–18. doi:10.1016/j.ijrobp.2011.01.046.

16 Jonsson, Joakim H, Adam Johansson, Karin Söderström, Thomas Asklund, and Tufve Nyholm. 2013. "Treatment Planning of Intracranial Targets on MRI Derived Substitute CT Data." Radiotherapy and Oncology 108: 118–22.

17 Jonsson, Joakim H, Magnus G Karlsson, Mikael Karlsson, and Tufve Nyholm. 2010. "Treatment Planning Using MRI Data: An Analysis of the Dose Calculation Accuracy for Different Treatment Regions." Radiation Oncology 5 (1): 62. doi:10.1186/1748-717X-5-62.

18 Kapanen, Mika, Juhani Collan, Annette Beule, Tiina Seppälä, Kauko Saarilahti, and Mikko Tenhunen. 2013. "Commissioning of MRI-Only Based Treatment Planning Procedure for External Beam Radiotherapy of Prostate." Magnetic Resonance in Medicine 70 (1): 127–35. doi:10.1002/mrm.24459.

19 Kapanen, Mika, and Mikko Tenhunen. 2013. "T1/T2*-Weighted MRI Provides Clinically Relevant Pseudo-CT Density Data for the Pelvic Bones in MRI-Only Based Radiotherapy Treatment Planning." Acta Oncologica (Stockholm, Sweden) 52 (3): 612–18. doi:10.3109/0284186X.2012.692883.

20 Karlsson, Mikael, Magnus G Karlsson, Tufve Nyholm, Christopher Amies, and Björn Zackrisson. 2009. "Dedicated Magnetic Resonance Imaging in the Radiotherapy Clinic." Int J Radiat Oncol Biol Phys 74 (2): 644–51. doi:10.1016/j.ijrobp.2009.01.065.

21 Keereman, Vincent, Yves Fierens, Tom Broux, Yves De Deene, Max Lonneux, and Stefaan Vandenberghe. 2010. "MRI-Based Attenuation Correction for PET/MRI Using Ultrashort Echo Time Sequences." Journal of Nuclear Medicine 51 (5): 812–18. doi:10.2967/jnumed.109.065425.

22 Kristensen, Brian Holch, Finn Jørgen Laursen, Vibeke Løgager, Poul Flemming Geertsen, and Anders Krarup-Hansen. 2008. "Dosimetric and Geometric Evaluation of an Open Low-Field Magnetic Resonance Simulator for Radiotherapy Treatment Planning of Brain Tumours." Radiotherapy and Oncology 87 (1): 100–109. doi:10.1016/j.radonc.2008.01.014.

23 Lambert, Jonathan, Peter B Greer, Fred Menk, Jackie Patterson, Joel Parker, Kara Dahl, Sanjiv Gupta, et al. 2011. "MRI-Guided Prostate Radiation Therapy Planning: Investigation of Dosimetric Accuracy of MRI-Based Dose Planning." Radiotherapy and Oncology : Journal of the European Society for Therapeutic Radiology and Oncology 98 (3). Elsevier Ireland Ltd: 330–34. doi:10.1016/j.radonc.2011.01.012.

24 Lee, Young K, Marc Bollet, Geoffrey Charles-Edwards, Maggie A Flower, Martin O Leach, Helen McNair, Elizabeth Moore, Carl Rowbottom, and Steve Webb. 2003. "Radiotherapy Treatment Planning of Prostate Cancer Using Magnetic Resonance Imaging Alone." Radiotherapy and Oncology 66 (2): 203–16. doi:10.1016/S0. doi:10.1088/0031-9155/57/5/1349.

25 Li, Sonia P, and Anwar R Padhani. 2012. "Tumor Response Assessments with Diffusion and Perfusion MRI." Journal of Magnetic Resonance Imaging 35 (4): 745–63. doi:10.1002/jmri.22838.

26 Liney, Gary P, and Marinus a Moerland. 2014. "Magnetic Resonance Imaging Acquisition Techniques for Radiotherapy Planning." Seminars in Radiation Oncology 24 (3). Elsevier: 160–68. doi:10.1016/j.semradonc.2014.02.014.

27 Milosevic, M, S Voruganti, R Blend, H Alasti, P Warde, M McLean, P Catton, C Catton, and M Gospodarowicz. 1998. "Magnetic Resonance Imaging (MRI) for Localization of the Prostatic Apex: Comparison to Computed Tomography (CT) and Urethrography." Radiotherapy and Oncology 47 (3): 277–84.

28 Pasquier, D, N Betrouni, M Vermandel, T Lacornerie, E Lartigau, and J Rousseau. 2006. "MRI Alone Simulation for Conformal Radiation Therapy of Prostate Cancer: Technical Aspects." IEEE EMBS, January, 160–63. doi:10.1109/IEMBS.2006.260341.

29 Paulson, Eric S., Beth Erickson, Chris Schultz, and X. Allen Li. 2015. "Comprehensive MRI Simulation Methodology Using a Dedicated MRI Scanner in Radiation Oncology for External Beam Radiation Treatment Planning." Medical Physics 42 (1): 28–39. doi:10.1118/1.4896096.

30 Prabhakar, R, K P Haresh, T Ganesh, R C Joshi, P K Julka, and G K Rath. 2007. "Comparison of Computed Tomography and Magnetic Resonance Based Target Volume in Brain Tumors." Journal of Cancer Research and Therapeutics 3 (2): 121–23.

31 Prabhakar, R, P K Julka, T Ganesh, a Munshi, R C Joshi, and G K Rath. 2007a. "Feasibility of Using MRI Alone for 3D Radiation Treatment Planning in Brain Tumors." Japanese Journal of Clinical Oncology 37 (6): 405–11. doi:10.1093/jjco/hym050.

32 Prabhakar, R, P K Julka, T Ganesh, A Munshi, R C Joshi, and G K Rath. 2007b. "Feasibility of Using MRI Alone for 3D Radiation Treatment Planning in Brain Tumors." Japanese Journal of Clinical Oncology 37 (6): 405–11. doi:10.1093/jjco/hym050.

33 Ramsey, C R, and A L Oliver. 1998. "Magnetic Resonance Imaging Based Digitally Reconstructed Radiographs, Virtual Simulation, and Three-Dimensional Treatment Planning for Brain Neoplasms." Medical Physics 25 (10): 1928–34.

34 Rank, Christopher M, Christoph Tremmel, Nora Hünemohr, Armin M Nagel, Oliver Jäkel, and Steffen Greilich. 2013. "MRI-Based Treatment Plan Simulation and Adaptation for Ion Radiotherapy Using a Classification-Based Approach." Radiation Oncology 8 (1): 51. doi:10.1186/1748-717X-8-51.

35 Reinsberg, Stefan a, Simon J Doran, Elizabeth M Charles-Edwards, and Martin O Leach. 2005. "A Complete Distortion Correction for MR Images: II. Rectification of Static-Field Inhomogeneities by Similarity-Based Profile Mapping." Physics in Medicine and Biology 50 (11): 2651–61. doi:10.1088/0031-9155/50/11/014.

36 Robson, Matthew D, Peter D Gatehouse, Mark Bydder, and Graeme M Bydder. 2003. "Magnetic Resonance: An Introduction to Ultrashort TE (UTE) Imaging." Journal of Computer Assisted Tomography 27 (6): 825–46.

37 Schreibmann, Eduard, Jonathon a. Nye, David M. Schuster, Diego R. Martin, John Votaw, and Tim Fox. 2010. "MR-Based Attenuation Correction for Hybrid PET-MR Brain Imaging Systems Using Deformable Image Registration." Medical Physics 37 (5): 2101–9. doi:10.1118/1.3377774.

38 Stanescu, T, H-S Jans, N Pervez, P Stavrev, and B G Fallone. 2008. "A Study on the Magnetic Resonance Imaging (MRI)-Based Radiation Treatment Planning of Intracranial Lesions." Physics in Medicine and Biology 53 (13): 3579–93. doi:10.1088/0031-9155/53/13/013.

39 Stanescu, Teodor, Jans Hans-sonke, Pavel Stavrev, and B Gino Fallone. 2006. "3T MR-Based Treatment Planning for Radiotherapy of Brain Lesions." Radiology and Oncology 40 (2): 125–32.

40 Walker, Amy, Gary Liney, Peter Metcalfe, and Lois Holloway. 2014. "MRI Distortion: Considerations for MRI Based Radiotherapy Treatment Planning." Australasian Physical & Engineering Sciences in Medicine / Supported by the Australasian College of Physical Scientists in Medicine and the Australasian Association of Physical Sciences in Medicine, February. doi:10.1007/s13246-014-0252-2.

41 Van der Heide, Uulke A, Antonetta C Houweling, Greetje Groenendaal, Regina G H Beets-Tan, and Philippe Lambin. 2012. "Functional MRI for Radiotherapy Dose Painting." Magnetic Resonance Imaging 30 (9). Elsevier Inc.: 1216–23. doi:10.1016/j.mri.2012.04.010.

42 Kenneth Ulin, Marcia Urie, Joel Cherlow. 2010. "Results of a Multi-Institutional Benchmark Test for Cranial CT/MR Image Registration" Int. J. Radiation Oncology Biol. Phys. 77 (5): 1584-1589.

syngo.via RT Image Suite: Empower Radiation Therapy with MRI Information

Elena Nioutsikou

Siemens Healthcare, Imaging & Therapy Division, Forchheim, Germany

What if you could bring your clinical capabilities to a higher level?

With cancer incidents expected to rise by as much as 45% by 2030, oncologists are under pressure to perform more efficiently [1]. This global healthcare trend affects, amongst others, Radiation Therapy (RT) providers who treat approximately one in every two patients presenting with cancer.

The last decade has seen a rapid growth in the utilization of MR images in treatment planning of radiation therapy. This is partially owing to the fact that MR information brings additional clarity to the clinical image, enabling more confident treatment decisions. But even when clinics have access to the latest imaging devices, making the most of imaging data remains cumbersome and time-consuming with current software solutions. Consequently, healthcare institutions could expand their clinical capabilities by introducing solutions that maximize RT imaging intelligence.

syngo.via RT Image Suite has been developed by Siemens to fulfill this need. It helps oncologists to devise and assess routine and complex treatment strategies. And by providing a comprehensive view of the patient, its flexible, intuitive design supports even the very complex cases. Efficient 3D and 4D image assessment, precise contouring and streamlined collaboration among physicians will help to advance the quality and efficiency of radiation therapy treatments.

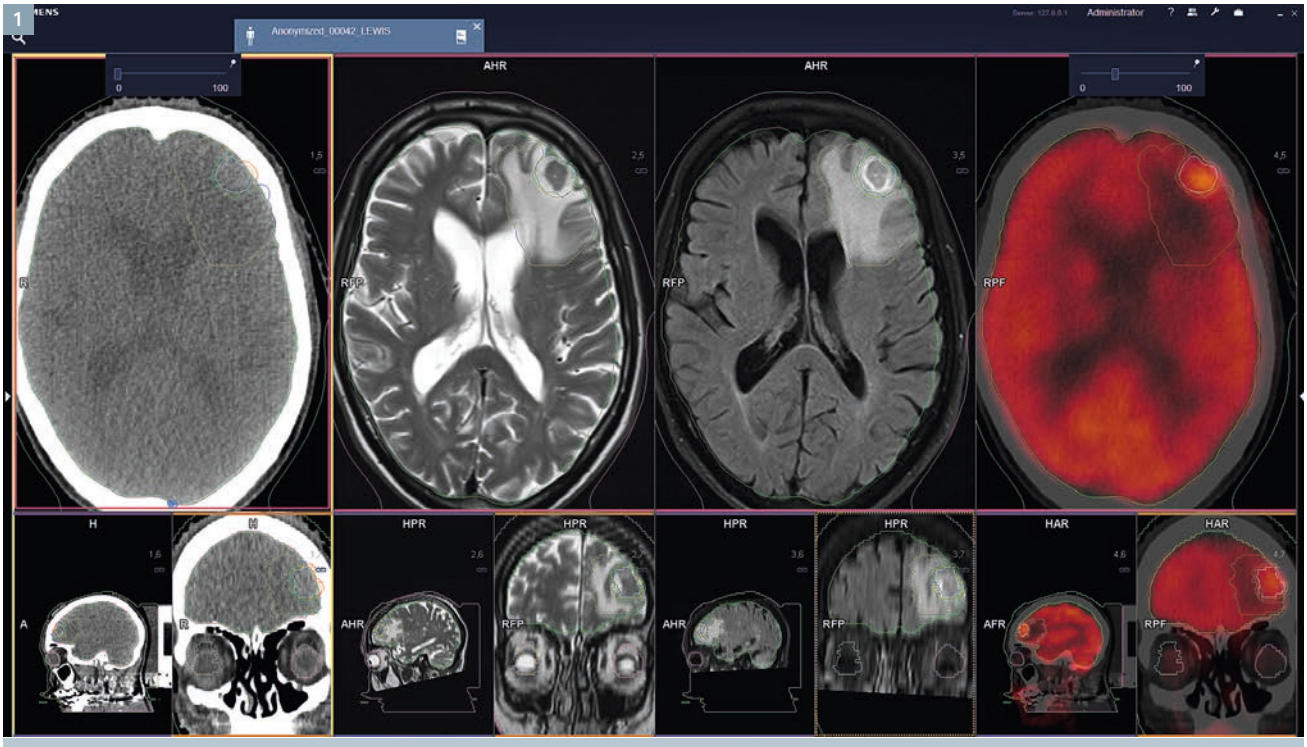

1 Exploiting all imaging information at hand to its full potential: A CT image of a brain tumor that will later be used for dose calculation, shown side-by-side with two MR contrasts. The contours were drawn on MR and are shown on all images.

What if you could drive improved outcomes with a comprehensive view of your patient?

See clearly
Your institution is striving to provide high-quality, tailor-made treatments. You have at your disposal a wide spectrum of images from 3D or 4D CT, to PET and MRI, which can form a basis for treatment decisions. And their optimal use will help meet the ultimate goal of optimizing outcomes for each patient.

With *syngo*.via RT Image Suite you can visualize a wide range of clinical images including anatomical and physiological images, for example through multiparametric MRI. A concurrent display of up to eight image series[1] (four single or four fused series) is possible on up to two monitors[2]. Rigid and state-of-the-art Deformable[3] Registration supports a confident inclusion of images, even if those were not acquired in treatment position. These powerful capabilities enable a comprehensive clinical view of the patient, for example when preparing initial consultations for a tumor board, during the course of consulting Radiotherapy on how to optimally plan their treatment strategy, or even when evaluating the progress of a particular patient.

By providing the complete picture at great clarity, you have a solution that enables easier and more intuitive clinical decision making.

What if you could streamline your contouring tasks with an elegant and easy-to-use solution?

Contour efficiently
Your institution is required to meet increasing quality demands and increasing patient numbers, despite budgetary and staffing constraints. Achieving these objectives requires you to adopt processes that are more efficient, a difficult challenge given the essential task of contouring.

Although contouring on CT images has been a task of Radiation Oncologists for over a decade, contouring on MRI is still an evolving field where cross-department collaboration is highly desirable.

syngo.via RT Image Suite is an intuitive and easy-to-use software solution that enables this collaboration, by facilitating the contouring of both routine as well as advanced cases efficiently. It can be deployed in a variety of ways, for instance as a server-based solution with one or more clients installed in Radiology. Simple import from CDs and DVDs, pre-fetching from PACS, and easy patient data reconciliation allow you to get started quickly. A set of modern tools including Deformable Registration[3] or 3D Smart Freehand Segmentation in any orientation, support fast 3D and 4D CT, MR and PET delineation. In particular, contour changes performed on any image are immediately reflected on all other images: this parallel contouring capability significantly accelerates the segmentation in multi-modality cases while letting you use all available information to their full extent. In cases where a multitude of images is available, the ability to simultaneously display on the screen up to eight[1] image series eases the otherwise cumbersome and time-consuming process of switching panes and exchanging data between applications.

Contouring for treatments that rely heavily on MRI information, such as radiosurgery and brachytherapy, is also supported. Figure 2 illustrates this with a clinical case of vaginal high-dose brachytherapy (explained in detail in MAGNETOM Flash #59, 4/2014, p14-19). Finally, the ability to configure for automatic send to TPS (Treatment Planning System) saves valuable time in completing cases.

From start to finish, *syngo*.via RT Image Suite supports you in achieving high-quality results, efficiently.

What if you could strengthen your clinical practice by enabling image-based cancer care pathways?

Advance your clinical practice
Your team constantly strives to advance its clinical capabilities. Imaging is frequently the critical factor, whether investigating the optimal treatment for a recurrence, adapting a strategy during the course of treatment, monitoring the progress of therapies, or simply exploring the added value of functional imaging in treatment planning. However, providing image-based care pathways seems impractical partially owing to the lack of adequate tools.

syngo.via RT Image Suite enables you to make imaging part of the daily clinical and research practice. To assess the need for re-contouring, you can visualize previously drawn structures on your current image series, supporting clear decision making. And when adaptation is needed, contour warping using Deformable Registration[3] supports new segmentation and further re-planning.

The application also aids in preparing the treatment of patients presenting with tumor recurrences. In this case, the ability to display images and visualize structure sets used during prior treatment on the current dataset guide new contouring smoothly.

All these cases profit greatly from the Advanced Visualization[1] functionality allowing you to compare and contour a variety of images such as diffusion-weighted and contrast-enhanced MRI, Dual Energy CT, 'Cone Beam CT-of the-day' or PET images acquired with different tracers. Additional *syngo*.via applications[2] support you in tasks such as quantification, aiding therapy prognosis and monitoring treatment

[1] Requires Advanced Visualization option
[2] Optional
[3] Requires Deformable Registration option

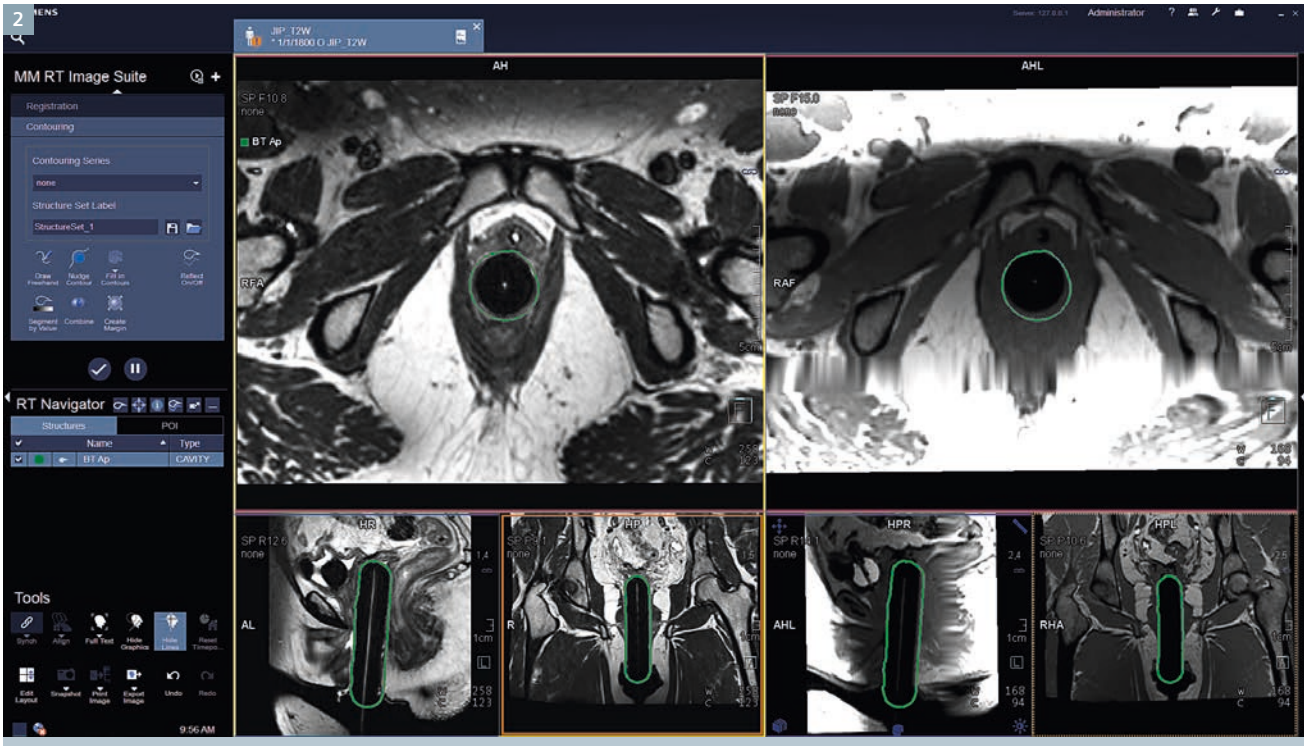

2 Contouring a vaginal cylinder in preparation for brachytherapy treatment planning. Left: 3D T2w SPACE, Right: 3D T1w MPRAGE. *Images courtesy of Dr. Prisciandaro, University of Michigan, Ann Arbor, MI, USA.*

response. Whether you are a Radiologist contouring for the Radiation Therapy department or a Radiation Oncologist with a dedicated MRI, the client-server architecture greatly facilitates efficient communication and teamwork.

From adaptive therapy, to treating recurrences and performing imaging in Radiation Therapy research, *syngo*.via RT Image Suite supports you and your team in advancing your clinical practice.

Clinical Example: Adding MRI soft tissue clarity to CT images of the prostate for reducing normal tissue toxicity in whole gland radiotherapy

Radiotherapy treatment to prostate tumors has traditionally targeted the whole prostatic gland, even when the extent of the disease was suspected to be confined to a smaller region. Today, state-of-the-art treatment planning is based on CT images, which are considered essential due to their capability to provide both the electron density information needed for dose calculation and the geometric accuracy that is expected for planning a precise treatment.

A number of clinical studies [2, 3, 4] have shown that adding the soft tissue information that MRI brings to the picture can help reduce the target volume which is often overestimated by CT alone. Furthermore, Villeirs et al. [5] have shown that the use of MRI in combination with CT improves the accuracy of prostate gland as well as organ-at-risk (OAR) delineation, with decreased inter-observer variability. It is anticipated that this will make an impact on the regions of the surrounding anatomy that would otherwise be exposed to the high-dose region. Reducing, for example, dose to healthy/functional tissue will have a direct effect on any treatment complications experienced by the patient, whether they are manifested as acute or late effects. Alternatively, a dose escalation of 2-7 Gy can be achieved for the same rectal wall dose when MRI is used in organ definition [6].

In the example illustrated below, (Fig. 3) the MR image was acquired in a radiology setting; the patient was not lying on a flat table-top[4] in the 'treatment position'. As a consequence, in order for MRI information to enhance that provided by CT, a Deformable Registration of the MR images was necessary. In figure 3A, the images prior to registration can be seen, while figure 3B shows the results of the registration.

Contouring of all ROI can then proceed on the image that carries the relevant information (e.g. femoral heads on CT, prostate, rectum and bladder on MRI) and those contours can be associated to the CT and sent to a treatment planning system (TPS) for further dosimetric planning.

Deformable registration is also often needed when the CT and MRI were acquired with a significant time difference between the two scans, without following the same protocols; this could give rise to diverse organ filling, making rigid registration lead to odd results.

[4] See [7] for further information.

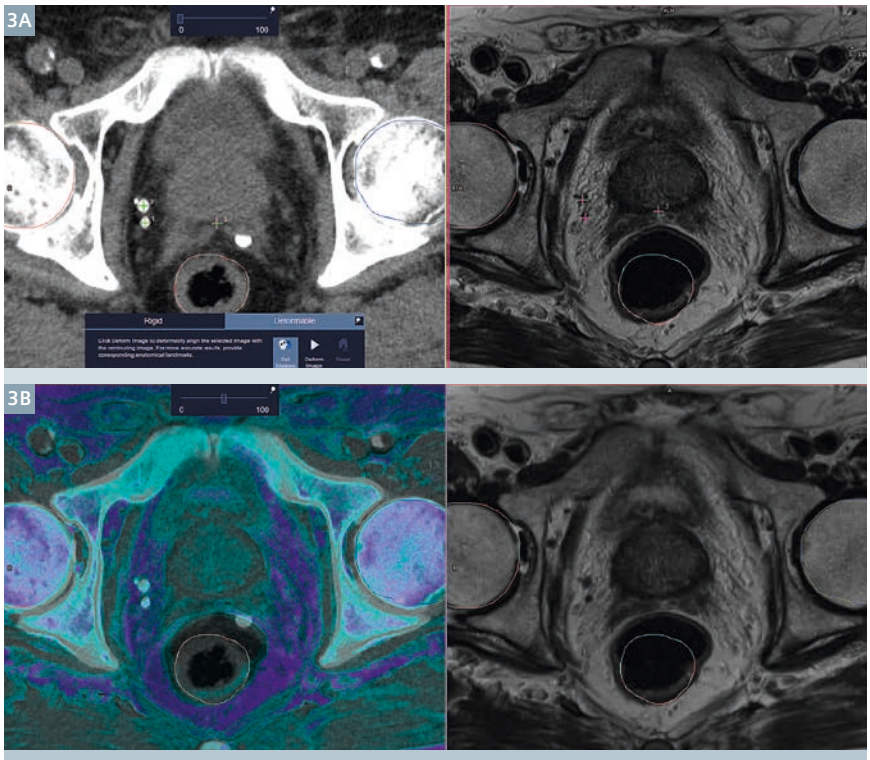

3 CT and MRI of the same patient acquired in different positions and therefore requiring Deformable Registration before proceeding to contouring. **(3A)** Landmarks selected to guide the registration and **(3B)** result of the registration with the MR overlaid on the planning CT.

References

1 Benjamin D. Smith, Grace L. Smith, Arti Hurria, Gabriel N. Hortobagyi, Thomas A. Buchholz. "Future of Cancer Incidence in the United States: Burdens Upon an Aging, Changing Nation", J Clin Oncol 27. 2009.

2 Debois M. et al. (1999). The contribution of magnetic resonance imaging to the three-dimensional treatment planning of localized prostate cancer. Int J Radiat Oncol Biol Phys. 45 (4), pp. 857-865.

3 Rasch C. et al. (1999). Definition of the prostate in CT and MRI: a multi-observer study. Int J Radiat.Oncol.Biol.Phys. 43(1), pp. 57-66.

4 Roach M. et al. (1996). Prostate volumes defined by magnetic resonance imaging and computerized tomographic scans for three-dimensional conformal radiotherapy. Int. J. Radiat. Oncol. Biol. Phys. 35(5), pp. 1011-1018.

5 Villeirs et al. (2005). Interobserver Delineation Variation Using CT versus Combined CT + MRI in Intensity–Modulated Radiotherapy for Prostate Cancer. Strahlenther Onkol 181 (7), pp. 424-430.

6 Steenbakkers et al. (2003). Reduction of dose delivered to the rectum and bulb of the penis using MRI delineation for radiotherapy of the prostate. Int J Radiat Oncol Biol Phys 57 (5), pp. 1269–1279.

7 MAGNETOM RT Pro edition. (s.d.). Available at http://www.healthcare.siemens.com/medical-imaging/magnetic-resonance-imaging/mri-guided-therapy/magnetom-rt-pro-edition

Conclusion

syngo.via RT Image Suite helps to leverage MRI and other multi-modality information in Radiation Therapy. *syngo*.via RT Image Suite improves decision-making with a clear and comprehensive view of your patients, efficient and precise contouring, as well as treatment monitoring and adaptation capabilities that enable personalized therapy.

Contact

Elena Nioutsikou
Siemens Healthcare
Imaging & Therapy Division
Forchheim
Germany
elena.nioutsikou@siemens.com

The product *syngo*.via RT Image Suite is based on *syngo*.via VB10. It is still under development and not yet commercially available. Its future availability cannot be ensured.

Further Reading

For further articles, application tips and clinical talks from experts focusing on the role of MRI in Radiation Therapy, please visit us at:

www.siemens.com/magnetom-world-rt

Case Series: 3T Prostate MRI With and Without the Use of an Endorectal Coil

Josephin Otto, M.D.; Harald Busse, Ph.D.

Department of Diagnostic and Interventional Radiology, Leipzig University Hospital, Leipzig, Germany

Introduction

Magnetic resonance imaging (MRI) has become a reliable technique for the detection, localization and local staging of prostate cancer [1]. Over the last decade, prostate MRI has clearly benefitted from advances in MRI hardware, most notably the introduction of 3 Tesla systems, and from the increased use of complementary functional imaging techniques in a multiparametric approach [2]. The use of endorectal coils will clearly improve the signal-to-noise ratio in the prostate, but the potential diagnostic gain is still open to debate [3]. Other factors that have to be considered are the extra time and effort needed, overall patient comfort, and reimbursement issues.

It is generally agreed that surface coils alone are sufficient for the detection and localization of significant prostate cancer [4], while local staging should ideally be performed with an endorectal coil or at a 3 Tesla system [5]. In an attempt to shed some light on that issue, the following three cases show axial, T2-weighted turbo spin-echo and diffusion-weighted images of the prostate at 3T (MAGNETOM Trio, A Tim System, Siemens Healthcare, Erlangen, Germany) that were acquired within the same patients, both with and without the use of an endorectal coil (eCoil, Medrad, Pittsburgh, PA, USA). Acquisition parameters were not adjusted between scans to facilitate comparison.

References

1 Dickinson L, Ahmed HU, Allen C, et al. Magnetic resonance imaging for the detection, localisation, and characterisation of prostate cancer: recommendations from a European consensus meeting. Eur Urol. 2011;59:477-94

2 Giannarini G, Zazzara M, Rossanese M, et al. Will Multi-Parametric Magnetic Resonance Imaging be the Future Tool to Detect Clinically Significant Prostate Cancer? Front Oncol. 2014;4:294

Case 1

59-year-old patient with prostate-specific antigen (PSA) level of 13 ng/ml and Gleason score (GS) 7 (3+4) prostate cancer in the apex with a diameter of about 1 cm. T2-weighted images acquired with surface coils only (Figs. 1A-C), combining a 6-channel body matrix coil placed ventrally at the pelvic level and selected elements of a 24-channel spine matrix coil integrated into the MR table, and with the addition of an endorectal coil (Figs. 1D-F) show focal hypointense MRI signals at the level of the apex. Diffusion-weighted images acquired with a b-value of 800 s/mm² reveal hyperintense focal areas (Figs. 1B, E) with a corresponding reduction of the apparent diffusion coefficient (ADC) (Figs. 1C, F).

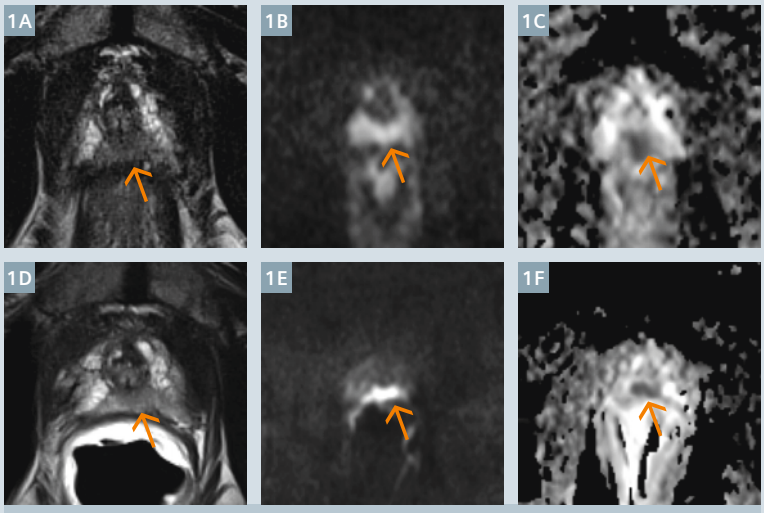

1 3T prostate MRI (MAGNETOM Trio, A Tim System). Images were acquired with surface coils only **(1A–C)** and in combination with an endorectal coil **(1D–F)**. **(1A, D)** Axial, T2-weighted fast spin-echo sequences with repetition time TR 4,400 – 4,600 ms, echo time TE 126 ms and flip angle FA 120 – 135°. **(1B, E)** Axial diffusion-weighted imaging (DWI) was performed with a single-shot echo planar imaging sequence with TR 3,000 ms, TE 85 ms, FA 90° and b-values of 50, 500, 800 and 1,500 s/mm². **(1C, F)** ADC maps were calculated from DWI images at b-values 50, 500 and 800 s/mm².

Case 2

65-year-old patient with PSA level of 56 ng/ml and GS 7 (3+4) prostate cancer with a diameter larger than 1.5 cm, mainly located in the right peripheral zone. The whole-mount histopathological section analysis revealed stage pT3b disease. The tumor is visible as a hypointense mass on T2-weighted images (Figs. 2A, D). The prostate capsule of the dorsolateral mid-gland shows an irregular bulging (Fig. 2D). Features on diffusion-weighted images (Figs. 2B, E) are less pronounced while ADC maps indicate a small corresponding region with restricted diffusion independent of the choice of imaging coils (Figs. 2C, F).

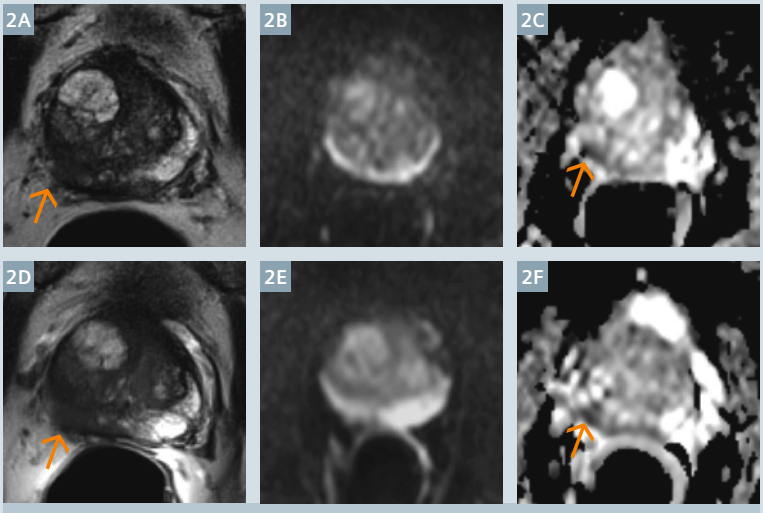

2 3T prostate MRI using axial, T2-weighted fast spin-echo and diffusion-weighted imaging (see figure 1 for MR imaging parameters).

Case 3

71-year-old patient with PSA level of 8.2 ng/ml and GS 7 (3+4) prostate cancer in the left transitional zone, ventrolateral. The tumor is visible as an irregular hypointense mass on (Figs. 3A, D) T2-weighted images with (Figs. 3B, E) focal signal increase on DWI with b-value of 800 s/mm² and (Figs. 3C, F) corresponding low values on ADC maps. The prostate capsule shows an irregular bulging ventrolaterally and the length of the tumor contact is larger than 1 cm, suggesting extracapsular tumor growth, which was confirmed by histopathology (stage pT3a).

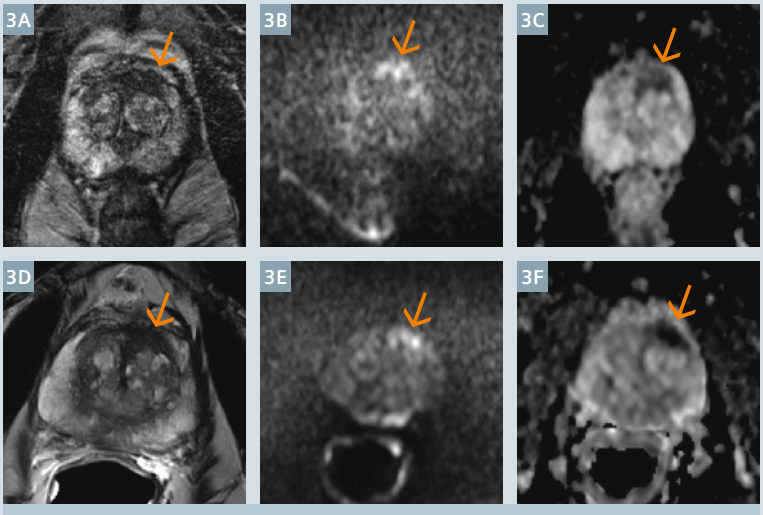

3 3T prostate MRI using axial, T2-weighted fast spin-echo and diffusion-weighted imaging (see figure 1 for MRI parameters).

3 Somford DM, Hamoen EH, Fütterer JJ, et al. The predictive value of endorectal 3 Tesla multiparametric magnetic resonance imaging for extraprostatic extension in patients with low, intermediate and high risk prostate cancer. J Urol. 2013;190:1728-34

4 Abd-Alazeez M, Kirkham A, Ahmed HU, et al. Performance of multiparametric MRI in men at risk of prostate cancer before the first biopsy: a paired validating cohort study using template prostate mapping biopsies as the reference standard. Prostate Cancer Prostatic Dis. 2014;17:40-46.

5 Otto J, Thörmer G, Seiwerts M,et al. Value of endorectal magnetic resonance imaging at 3T for the local staging of prostate cancer. Rofo. 2014;186:795-802

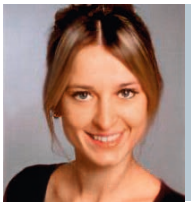

Josephin Otto

Harald Busse

Contact

Josephin Otto, M.D.
Department of Diagnostic and Interventional Radiology
Leipzig University Hospital
Liebigstraße 20
04103 Leipzig
Germany
josephin.otto@medizin.uni-leipzig.de

60-Channel Body Coil for 1.5T and 3T

Gregor Thörmer, Ph.D.

Global Segment Manager Men's and Women's Health, Siemens Healthcare, Magnetic Resonance Imaging, Erlangen, Germany

Introduction

The development of head (and neck) coils with large numbers of independent coil elements and channels (e.g. the 64-channel Head & Neck coil) has proven that both substantial signal-to-noise ratio (SNR) improvements and significant improvements in the quality of accelerated imaging techniques are possible.

Consequently, the new Body 60 coil[1] design extends these capabilities to the emerging field of abdominal and pelvic MRI.

Technical specifications

The Body 60 coil consists of a 30-channel anterior and a 30-channel posterior part, which are typically used in a sandwich mode (Fig. 1A). The anterior part, Body 30 coil, can be used separately and in flexible combination with coils like the integrated Spine coil (Fig. 1B). Furthermore, the two 30-channel coils can be positioned consecutively on the chest and pelvis in order to perform whole-body examinations with maximum coil coverage of approximately 130 cm[2] (Fig. 1C).

The coils are made of a novel visco-elastic foam material and are each equipped with 5 rows of 6 elements.

Compared to a conventional coil setup on a Tim 4G system with 48 channels, this represents a 78% increase in coil element density along the z-direction and at least a two-fold increase compared to competitive systems[3]. The Body 60 allows a max. coverage of 46 cm in z-direction. As shown in figure 2, the SNR gain for abdominal applications in the 'sandwich' mode is 38% on average and still 20% at the center of the phantom.

[1] 510(k) pending
[2] Coverage in combination with the standard 20-channel Head coil
[3] Data on file

1 The Body 60 coil is designed to serve a broad range of clinical applications. **(1A)** 'Sandwich' mode, i.e. for pelvic, abdominal or lung exams. **(1B)** Individual operation as a single Body 30 coil, also possible with 48-channel systems. **(1C)** Whole-body setup, in combination with the integrated 32ch Spine coil and a 20ch Head coil (not shown here).

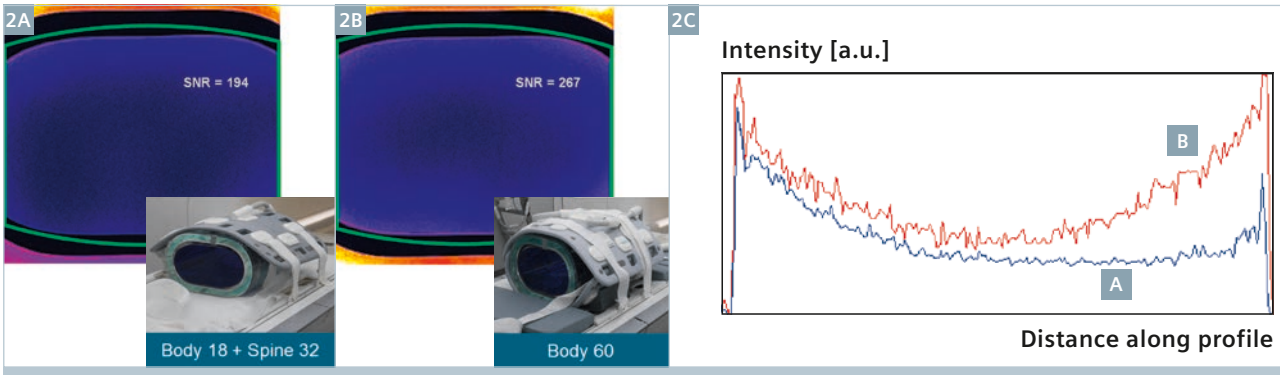

2 SNR maps of **(2A)** the combination of the Body 18 and Spine 32 coil and **(2B)** the Body 60 coil. Within a ROI (green line) corresponding to whole abdominal coverage the SNR is increased by 38% with the 60 channel coil. The respective SNR profiles (blue = Body 18 & Spine 32; red = Body 60) vertically through the center of the phantom are shown in **(2C)**.

3 Liver imaging at 1.5T with 3D VIBE Dixon water, GRAPPA 8, 320 matrix, slice thickness 3 mm, 72 slices, TA 4.86 s, TR 4.0 ms, TE 1.3 ms. Under extreme iPAT conditions the standard combination of the Body 18 and Spine 32 **(3A)** shows the typical pattern of a central iPAT artifact. By combining Body 30 and Spine 32 **(3B)** the artifact is substantially reduced and not present at all with the Body 60 setup **(3C)**. Also note the very homogeneous image appearance in 3C.

4 Prostate MRI at 3T with 0.5 x 0.5 mm inplane resolution in 3:11 min. Imaging parameters: 2D T2 TSE, 320 matrix, FOV 160 x 160 mm, slice thickness 3 mm, 26 slices.

Image examples

An enclosed set of pads allows for comfortable patient positioning in different clinical situations. In addition the Body 60 features the DirectConnect Interface for optimized cable handling. One of the major applications is in abdominal imaging. As shown in figure 3, the unique iPAT performance of the Body 60 coil allows for routine scans with a PAT factor of 8 whilst maintaining excellent diagnostic image quality. In the case of prostate MRI, the coil can be used to either go for very efficient examinations (10-min protocol) or to increase the spatial resolution as shown in figure 4. Respective scan protocols may be found on the MAGNETOM World webpage. Figure 5 shows a whole-body scan performed with the Body 60 coil.

5 Whole-body examination at 1.5T in 4 stations. Imaging parameters per station: 384 matrix, slice thickness 5 mm, 35 slices, FOV 309 x 450 mm, total TA 17:11 min.

Download .edx-files at www.siemens.com/magnetom-world

Go to: Clinical Corner > Protocols > SEEit Prostate Protocols

Contact

Gregor Thörmer, Ph.D.
Global Segment Manager
Men's and Women's Health
Siemens Healthcare
Postbox 32 60
91050 Erlangen
Germany
gregor.thoermer@siemens.com

Siemens Healthcare Publications

Our publications offer the latest information and background for every healthcare field. From the hospital director to the radiological assistant – here, you can quickly find information relevant to your needs.

MAGNETOM Flash
Everything from the world of magnetic resonance imaging.

SOMATOM Sessions
Everything from the world of computed tomography.

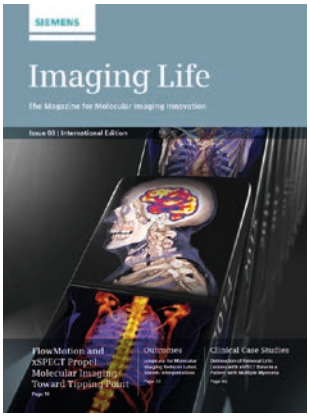

Imaging Life
Everything from the world of molecular imaging innovations.

AXIOM Innovations
Everything from the world of interventional radiology, cardiology, and surgery.

Heartbeat
Everything from the world of sustainable cardiovascular care.

Medical Solutions Online
The online version includes additional video features and greater depth to the articles in the printed healthcare leadership magazine. Read online at:
www.siemens.com/medical-solutions

For current and past issues and to order the magazines, please visit
www.siemens.com/healthcare-magazine

The entire editorial staff at Siemens Healthcare extends their appreciation to all the radiologists, technologists, physicists, experts and scholars who donate their time and energy – without payment – in order to share their expertise with the readers of MAGNETOM Flash.

MAGNETOM Flash – Imprint

© 2015 by Siemens AG,
Berlin and Munich,
All Rights Reserved

Publisher:
Siemens AG
Medical Solutions
Business Unit Magnetic Resonance,
Karl-Schall-Straße 6, D-91052 Erlangen,
Germany

Editor-in-chief:
Antje Hellwich
(antje.hellwich@siemens.com)

Editorial Board:
Wellesley Were; Ralph Strecker;
Sven Zühlsdorff, Ph.D.;
Gary R. McNeal, MS (BME);
Peter Kreisler, Ph.D.

Production:
Norbert Moser, Siemens AG,
Medical Solutions

Layout:
Agentur Baumgärtner,
Friedrichstraße 4, D-90762 Fürth,
Germany

Printer:
G. Peschke Druckerei GmbH,
Taxetstrasse 4,
D-85599 Parsdorf b. Munich,
Germany

Note in accordance with § 33 Para.1 of the German Federal Data Protection Law: Despatch is made using an address file which is maintained with the aid of an automated data processing system.

MAGNETOM Flash is sent free of charge to Siemens MR customers, qualified physicians, technologists, physicists and radiology departments throughout the world. It includes reports in the English language on magnetic resonance: diagnostic and therapeutic methods and their application as well as results and experience gained with corresponding systems and solutions. It introduces from case to case new principles and procedures and discusses their clinical potential. The statements and views of the authors in the individual contributions do not necessarily reflect the opinion of the publisher.

The information presented in these articles and case reports is for illustration only and is not intended to be relied upon by the reader for instruction as to the practice of medicine. Any health care practitioner reading this information is reminded that they must use their own learning, training and expertise in dealing with their individual patients. This material does not substitute for that duty and is not intended by Siemens Medical Solutions to be used for any purpose in that regard. The drugs and doses mentioned herein are consistent with the approval labeling for uses and/or indications of the drug. The treating physician bears the sole responsibility for the diagnosis and treatment of patients, including drugs and doses prescribed in connection with such use. The Operating Instructions must always be strictly followed when operating the MR system. The sources for the technical data are the corresponding data sheets. Results may vary.

Partial reproduction in printed form of individual contributions is permitted, provided the customary bibliographical data such as author's name and title of the contribution as well as year, issue number and pages of MAGNETOM Flash are named, but the editors request that two copies be sent to them. The written consent of the authors and publisher is required for the complete reprinting of an article.

We welcome your questions and comments about the editorial content of MAGNETOM Flash. Please contact us at magnetomworld.med@siemens.com.

Manuscripts as well as suggestions, proposals and information are always welcome; they are carefully examined and submitted to the editorial board for attention. MAGNETOM Flash is not responsible for loss, damage, or any other injury to unsolicited manuscripts or other materials. We reserve the right to edit for clarity, accuracy, and space. Include your name, address, and phone number and send to the editors, address above.

MAGNETOM Flash is also available on the internet:

www.siemens.com/magnetom-world

SIEMENS

MAGNETOM Flash

The Magazine of MRI

Issue Number 2/2015 | ISMRM Edition

Not for distribution in the US

62

7T Image Gallery: Translate MRI Research Power into Clinical Care
Page 8

fit-Upgrade: A Success Story
Stephan Zangos, Thomas J. Vogl
Page 16

Hepatic Fat Quantification in Pediatric Patients
Jie Deng, Cynthia K. Rigsby, et al.
Page 23

Dot Configuration with the Dot Cockpit
Bart Schraa
Page 38

4D-MRI: Radiotherapy of Moving Targets
Kinga B. Bernatowicz, Antony J. Lomax, et al.
Page 74

Please enter your business address

Institution

Department

Function

Title

Name

Street

Postal Code

City

State

Country

MR system used

Please include me in your mailing list for the following Siemens Healthcare customer magazine(s):

☐ Medical Solutions

☐ MAGNETOM Flash

☐ SOMATOM Sessions

☐ AXIOM Innovations

Stay up to date with the latest information

Register for:

E-mail

☐ Yes, I consent to the above information being used for future contact regarding product updates and other important news from Siemens.

☐ unsubscribe from info service

Please print clearly!

MAGNETOM Flash

Siemens AG
Healthcare
Magnetic Resonance
Antje Hellwich – Marketing
P.O. Box 32 60
D-91050 Erlangen
Germany

→Visit www.siemens.com/magnetom-world for case reports, clinical methods, application tips, talks and much more clinical information.

SUBSCRIBE NOW!

– and get your free copy of future MAGNETOM Flash! Interesting information from the world of magnetic resonance – gratis to your desk. Send us this postcard, or subscribe online at www.siemens.com/MAGNETOM-World

On account of certain regional limitations of sales rights and service availability, we cannot guarantee that all products included in this brochure are available through the Siemens sales organization worldwide. Availability and packaging may vary by country and is subject to change without prior notice. Some/All of the features and products described herein may not be available in the United States.

The information in this document contains general technical descriptions of specifications and options as well as standard and optional features which do not always have to be present in individual cases, and which may not be commercially available in all countries. Due to regulatory reasons their future availability cannot be guaranteed. Please contact your local Siemens organization for further details.

Siemens reserves the right to modify the design, packaging, specifications, and options described herein without prior notice. Please contact your local Siemens sales representative for the most current information.

Note: Any technical data contained in this document may vary within defined tolerances. Original images always lose a certain amount of detail when reproduced.

Not for distribution in the US

Global Business Unit

Siemens AG
Medical Solutions
Magnetic Resonance
Henkestraße 127
DE-91052 Erlangen
Germany
Phone: +49 9131 84-0
www.siemens.com/healthcare

Local Contact Information

Asia/Pacific:
Siemens Medical Solutions
Asia Pacific Headquarters
The Siemens Center
60 MacPherson Road
Singapore 348615
Phone: +65 6490 6000

Canada:
Siemens Canada Limited
Healthcare
1550 Appleby Lane
Burlington, ON L7L 6X7, Canada
Phone +1 905 315-6868

Europe/Africa/Middle East:
Siemens AG, Healthcare
Henkestraße 127
91052 Erlangen, Germany
Phone: +49 9131 84-0

Latin America:
Siemens S.A., Medical Solutions
Avenida de Pte. Julio A. Roca No 516, Piso
C1067 ABN Buenos Aires, Argentina
Phone: +54 11 4340-8400

USA:
Siemens Medical Solutions USA, Inc.
51 Valley Stream Parkway
Malvern, PA 19355-1406, USA
Phone: +1 888 826-9702

Global Siemens Headquarters

Siemens AG
Wittelsbacherplatz 2
80333 Muenchen
Germany

Global Siemens Healthcare Headquarters

Siemens AG
Healthcare
Henkestraße 127
91052 Erlangen
Germany
Phone: +49 9131 84-0
www.siemens.com/healthcare

Order No. A91MR-1000-113C-7600 | Printed in Germany | CG MR 2743 051515. | © 05.15, Siemens AG

www.siemens.com/magnetom-world